Saline structure, circulation and suspended sediment transport in a channelized salt-wedge estuary : the Adour river estuary

Sophie Defontaine

THÈSE

PRÉSENTÉE À

L'UNIVERSITÉ DE PAU ET DES PAYS DE L'ADOUR

ÉCOLE DOCTORALE DES SCIENCES EXACTES ET DE LEURS APPLICATIONS

par

Sophie Defontaine

POUR L'OBTENTION DU GRADE DE

DOCTEUR

Spécialité : Mathématiques

2019

Saline structure, circulation and suspended sediment transport in a channelized salt-wedge estuary : the Adour river estuary

---

Structure saline, circulation et transport des sédiments en suspension dans un estuaire à coin salé chenalisé : l'estuaire de l'Adour

---

Composition du jury :

Isabelle Brenon	Rapporteur
Sylvain Ouillon	Rapporteur
David Amouroux	Examinateur
Aldo Sottolichio	Examinateur
Arnoldo Valle-Levinson	Examinateur
Romaric Verney	Examinateur
Benoit Liquet	Directeur de thèse
Damien Sous	Directeur de thèse

Abstract

Estuaries constitute unique habitats for a large variety of living organisms and essential nurseries for many marine species. However, they are also very vulnerable. In the overall context of climate change and a growing anthropogenic pressure, the preservation of estuarine and marine ecosystems is a key issue. It is therefore essential to improve our knowledge of the hydrodynamical processes controlling the dynamics and renewal of water masses in estuaries and their ability to transport, expel or retain sediments, contaminants, nutrients and living organisms. The present study is mainly based on a series of field experimental campaigns, complemented by 3D numerical modeling, in order to investigate the Adour estuary functioning. The field campaigns combined long-term bottom-mooring and b3.5oat surveys, during which velocity, turbulence, salinity and suspended sediment concentration data were collected. The data processing is focused on the analysis of estuarine circulation and suspended sediment dynamics. The estuarine circulation is characterized by a strong variability of velocity and salinity fields, which results in a time-dependent salt-wedge regime. It was shown that river flow and tides are the main drivers of the Adour estuary dynamics. The suspended sediment dynamics is strongly related to the circulation of water-masses, and thus varies with the tidal amplitude and the river flow. No ETM was observed during this study, and SSC values are very low compared to other tidal estuaries. A 3D realistic numerical modeling of the Adour estuary was developed with the TELEMAC-MASCARET suite of solvers. This model was calibrated and validated based on the field data collected during this study. Such a complex hydrodynamics is not easy to reproduce numerically, especially the unsteady vertical density gradient.

Résumé

Les estuaires constituent un habitat unique pour une grande variété d'organismes vivants et des aires d'alevinage pour de nombreuses espèces marines. Cependant ils sont aussi très vulnérables. Dans le contexte global de changement climatique et d'augmentation de la pression anthropique, la préservation des écosystèmes marins et estuariens est une question fondamentale. Il est donc essentiel d'améliorer notre connaissance des processus hydrodynamiques qui contrôlent la dynamique et le renouvellement des masses d'eau dans les estuaires, ainsi que leur capacité à transporter, expulser ou retenir les sédiments, les contaminants, les nutriments et les organismes vivants. Cette étude est principalement basée sur des données collectées dans l'estuaire de l'Adour, ainsi que d'un modèle numérique en trois dimensions, et a pour but d'étudier le fonctionnement de cet estuaire. Les campagnes de terrain ont combiné des instruments ancrés au fond de l'estuaire sur des périodes longues et des mesures depuis un bateau, durant lesquels des données de vitesse, turbulence, salinité et concentration de sédiment en suspension ont été collectées. L'analyse des données s'est concentrée sur la circulation à l'intérieur de l'estuaire et le transport des sédiments en suspension. La circulation estuarienne est caractérisée par une grande variabilité de des champs de vitesse et de salinité, qui donne lieu à un régime de coin-salé non-permanent. Il a été montré que la marée et le 3.5débit de la rivière sont les forçages principaux de la dynamique de l'estuaire de l'Adour. La dynamique des sédiments en suspension est fortement liée à la circulation des masses d'eau, et varie donc avec l'amplitude des marées et le débit du fleuve. Aucun bouchon vaseux n'a été observé lors de cette étude, et les valeurs de concentration en sédiment observées sont très faibles comparées à celles collectées dans d'autres estuaires tidaux. Un modèle numérique 3D réaliste de l'estuaire de l'Adour a été développé avec TELEMAC-MASCARET. Ce modèle a été calibré et validé grâce aux données collectées lors de cette étude. Une dynamique aussi complexe que celle de l'estuaire de l'Adour n'est pas facile à reproduire numériquement, en particulier le gradient de densité non-permanent.

Résumé étendu

Les estuaires sont des masses d'eau localisées à la jointure entre continent et océan. Leur dynamique généralement très complexe est propre à chaque système. Les forçages varient selon différentes échelles de temps et d'espace et indépendamment les uns des autres. L'onde de marée varie en amplitude au cours du cycle de marée, mais également sur un cycle de 28 jours avec une alternance de maximums d'amplitude appelés vives-eaux et de minimums appelés mortes-eaux. Cette onde de marée se déforme lorsqu'elle se propage dans l'estuaire. Elle peut augmentée en amplitude due à la convergence de l'estuaire ou diminuée en amplitude par frottement. Cette onde peut également devenir asymétrique. De même, le débit du fleuve peut être très variable en fonction des saisons et sur des épisodes de crue intenses et courts. Si un fleuve possède différents affluents, cela peut créer une variation du débit dans l'espace. Cette rencontre entre les eaux douces et saumâtres provenant du continent et les eaux salées provenant de l'océan est à l'origine d'importants gradients de densité, qui influencent très largement la dynamique estuarienne. Ces gradients de densité et les interactions entre l'onde de marée et la morphologie de l'estuaire sont généralement les forçages principaux de la dynamique estuarienne et sont à l'origine de mécanismes tels que la circulation gravitationnelle et le pompage tidal. Néanmoins, d'autres forçages peuvent contribuer à cette dynamique, notamment le vent, les vagues, la rotation de la Terre. Bien que la dynamique estuarienne ait été très largement étudiée à travers le monde ces dernières années pour des questions principalement environnementales (i.e. pollution) et économiques (e.g. dragage), le déplacement des masses d'eau, la stratification et le transport sédimentaire à l'intérieur de l'estuaire de l'Adour était jusqu'à lors méconnue. Les problèmes de pollution de la zone côtière (plages d'Anglet et zone de pêche) et d'envasement du port de Bayonne à l'embouchure de l'estuaire ont donné lieu à des études hydrodynamiques ou chimiques. Néanmoins, les précédentes études hydrodynamiques se sont uniquement portées sur la zone côtière et aucune étude couplant hydrodynamique et paramètres physico-chimiques n'avait été réalisée dans l'estuaire jusqu'à lors.

Cette étude a donc pour but d'investiguer le fonctionnement hydro-sédimentaire de la partie aval de l'estuaire de l'Adour, qui est représentatif d'un type d'estuaire méconnu. L'estuaire de l'Adour a une morphologie très particulière, qui est plus proche d'un chenal de navigation que d'une embouchure de fleuve. L'embouchure de l'estuaire est totalement artificielle, endiguée et régulièrement draguée pour les besoins du port de Bayonne. De plus, cet estuaire est soumit à la fois à des forçages maritime et fluvial importants. Dans cette étude, on a voulu répondre à un certain nombre d'interrogations concernant: l'influence du cycle de marée et de débit de la rivière sur la dynamique estuarienne, l'alternance du forçage dominant la dynamique estuarienne au cours du cycle mortes-eaux vives-eaux, les conséquences de cette dynamique sur le transport sédimentaire, et finalement la possibilité de reproduire cette dynamique numériquement. Une double approche expérimentale et numérique a été mise en œuvre pour répondre à ces questionnements. La partie expérimentale s'est concentrée sur la bas estuaire, c'est-à-dire les 6 derniers kilomètres de l'Adour entre la confluence de la Nive et l'embouchure. Une analyse des données des précédentes campagnes de mesure a été effectuée, avant de pouvoir définir les informations manquantes et de pouvoir y pallier par de nouvelles campagnes de mesure. Des paramètres physico-chimiques et hydrodynamiques ont donc été collectés simultanément à haute fréquence et sous différentes conditions de marnage et de débit. L'approche numérique quant à elle fut composée premièrement d'un cas test qui nous a permis d'examiner la capacité du modèle TELEMAC3D à reproduire un écoulement stratifié. Dans un second temps, un modèle numérique réaliste en 3 dimensions de l'estuaire de l'Adour et de sa zone côtière a été développé. Le modèle numérique TELEMAC3D résout les équations de Navier-Stokes pour les écoulements à surface libre et des équations d'advection-diffusion pour les différents traceurs. Bien que la partie expérimentale ait été centrée sur la zone avale de l'estuaire, l'amplitude géographique du modèle numérique est elle bien plus grande, elle comprend une partie océanique et amont importante.

Les données collectées lors des quatre campagnes de mesure qui ont eut lieu entre septembre 2017 et septembre 2018 nous ont permis de mettre en évidence le fait que la marée et le débit soient les forçages principaux qui s'exercent sur l'estuaire de l'Adour. Il en résulte une dynamique complexe et de forts gradients de densité. Les eaux denses marines entrent dans l'estuaire par le fond de la colonne sous forme de coin salé durant le flot, et sont expulsées de l'estuaire durant le jusant. Ces estuaires sont appelés « estuaires à coin salé non permanent » pour les différentiés des « estuaires à coin salé stagnant ». Cependant, la circulation à l'intérieur de l'estuaire varie largement avec les conditions de forçage. Un fort débit a tendance à renforcer la stratification et à limiter l'entrée des eaux marines dans l'estuaire. Un fort marnage au contraire aura tendance à augmenter le mélange et à diminuer voire à détruire la stratification, avec un fonctionnement qui serait similaire aux estuaires partiellement mélangés. Un coin salé stagnant peut être observé dans des conditions de mortes-eaux à étiage. L'estuaire de l'Adour a donc une grande variabilité de fonctionnement, qui dépend principalement de la marée et du débit du fleuve. La viscosité cinématique montre une forte réponse aux variations de la structure saline. Contrairement à beaucoup d'estuaires où le mécanisme de « tidal straining » est responsable de pics de mélange au flot et d'une stratification maximale au jusant, les estuaires à coin salé non-permanent comme l'estuaire de l'Adour sont caractérisés par des valeurs maximales de viscosité cinématique au jusant, c-à-d quand la stratification est minimale. Grâce aux données collectées, le fonctionnement de l'estuaire de l'Adour a pu être mis en perspective à travers le schéma de classification de Geyer et MacCready (2014) où un certain nombre d'estuaire bien documentés sont déjà représentés. La grande variabilité de fonctionnement de l'estuaire de l'Adour a été confirmé par ce schéma de classification, bien que l'utilisation de valeurs moyenne sur un cycle de marée reste discutable dans le cas des estuaires à coin salé non-permanent.

Dans cette étude, il a également été démontré que le transport de sédiment en suspension est très largement influencé par la structure saline et le mélange turbulent. Les mécanismes de remise en suspension, de déposition et d'advection s'alternent tout au long du cycle de marée et leur intensité est directement corrélée à l'intensité des forçages maritime et fluvial. Les sédiments sont donc remis en suspension, advectés vers l'amont puis déposés pendant le flot, pour ensuite être de nouveau remis en suspension, advectés vers l'aval et expulsés ou re-déposés dans l'estuaire aval. D'autre phénomènes ont pu être observés, tel que : (i) la chute des sédiments de la couche d'eau douce s'écoulant en surface vers la couche salée du fond due à l'atténuation de la turbulence par la stratification, (ii) la convergence des sédiments au niveau du point nodal de salinité. D'après la littérature, les deux mécanismes principaux à l'origine de la création d'un bouchon vaseux sont le pompage tidal et la circulation résiduelle. Aucun de ces deux mécanismes ne se manifeste dans le bas estuaire et les apports en sédiment de la rivière sont faible, ce qui expliquerait pourquoi aucun bouchon vaseux n'a pu être observé dans la partie aval de l'estuaire de l'Adour. Néanmoins, le mécanisme de pompage tidal qui semble avoir lieu dans la partie amont de l'estuaire pourrait être à l'origine d'un bouchon vaseux. Des campagnes de mesure supplémentaires seraient nécessaires pour vérifier cette hypothèse.

La partie numérique de ce travail a commencé par l'étude d'un cas test connu sous le nom d'expérience de Viollet, qui se base sur des expériences réalisées en laboratoire dans un canal. L'expérience mise en place par Viollet en 1980 est un écoulement à 2 couches dans un canal très faiblement incliné. La couche supérieure est plus chaude donc moins dense et s'écoule plus vite que la couche inférieure. Après comparaison entre les mesures (i.e. profils de vitesse et de température) et les résultats de simulations, il semble que TELEMAC3D soit capable de reproduire un écoulement stratifié en densité de manière satisfaisante. Par la suite, un modèle numérique 3D réaliste de l'estuaire de l'Adour et sa partie côtière a été développé. Ce modèle numérique a été calibré et validé grâce aux données collectées lors des quatre campagnes de mesure. La calibration et la validation du niveau d'eau sont basées sur les données collectées par les différents marégraphes placés le long de l'Adour et de la Nive, et montrent une bonne concordance entre simulation et mesure. La vitesse a quand à elle été calibrée et validée avec

les données des ADCPs qui ont été ancrés dans l'estuaire sur une période d'un mois. Un des points spécifiques de la circulation à l'intérieur de l'Adour est donc le gradient de salinité vertical. La stratification observée dans l'estuaire de l'Adour est bien plus complexe que celle produite dans l'expérience de Viollet, car elle n'est pas constante dans le temps ni dans l'espace. De plus, la géométrie de l'estuaire de l'Adour est bien plus complexe que celle d'un simple canal. Cette stratification est donc bien plus difficile à reproduire numériquement. Un grand nombre de paramètres physiques et numériques ont été testés afin de reproduire la stratification qui a été observée, comme par exemple les différents modèles de turbulence ou les différents schémas d'advection. Même si certain paramétrages permettent de reproduire la dynamique de l'estuaire de l'Adour de manière satisfaisante sous certaines conditions hydrologiques, aucun paramétrage ne reproduit correctement tous les cas de figure observés. Il semble qu'un excès de diffusion numérique pourrait expliquer en partie les différences entre mesures et résultats numériques.

En conclusion, cette étude décrit une série de campagnes de mesures et le développement d'un modèle numérique ayant pour but de caractériser le fonctionnement d'un estuaire aménagé et exposé à d'important forçages maritime et fluvial: l'estuaire de l'Adour. Une série de processus hydrodynamiques ont été documentés à travers des mesures faites par des instruments ancrés au fond de l'estuaire, mis sur un treuils, fixés à la coque du bateau et tractés par le bateau. Il a été démontré que les forçages maritime et fluvial importants sont à l'origine d'une stratification en densité très variable allant du régime d'estuaire partiellement mélangé au régime d'estuaire à coin salé. Il a été mis en évidence que la stratification est renforcée durant le flot et atténuée durant le jusant. Cette variabilité de fonctionnement a une grande influence sur la capacité de vidange de l'estuaire. L'analyse des propriétés turbulentes a mis en lumière une forte corrélation entre stratification et mélange. Le flot est caractérisé par une stratification stable et un faible mélange turbulent, alors que le jusant est associé à un fort mélange turbulent et une faible stratification. D'après les données de stratification et de mélange, le changement de régime pourrait être attribué à un échange de forçage dominant en fonction des conditions hydrologiques. En se basant sur les données de concentration de particules en suspension, il a été établi que le cycle de marée est responsable d'un cycle de remise en suspension-advection-déposition. L'amplitude de marée tend à renforcer ou diminuer ces différents processus tout au long du cycle de vives-eaux/mortes-eaux. De même, l'intensité du débit de la rivière va influencer ce cycle de remise en suspension-advection-déposition. De manière générale un forçage important, qu'il soit maritime ou fluvial, va renforcer les processus de remise en suspension et d'advection et diminuer le dépôt et inversement lors des périodes de forçage faible. Aucun bouchon vaseux n'a pu être observé lors de nos campagnes de mesure. L'influence des aménagements du bas estuaire sur la capacité de l'estuaire à évacuer les sédiments est discutable et mériterait d'être approfondit. L'hypothèse de la présence d'un bouchon vaseux dans la partie amont de l'estuaire nécessiterait de nouvelles campagnes de mesure pour être confirmée ou invalidée. La complexité de ce système estuarien en fait un vrai défi numérique. Bien que le modèle numérique est encore besoin de quelques améliorations afin entre autre de diminuer la diffusion numérique, les premiers résultats sont très encourageants. Car si le niveau d'eau et les vitesses sont correctement reproduits par le modèle, les différentes structures salines verticales et le mélange associé restent un défi numérique.

To my family
for supporting and believing
in me throughout this Ph.D.

"See what you did to make the water clean. You let it be ... and the mud settled down on its own - and you got clear water. Your mind is also like that! When it is disturbed, just let it be. Give it a little time. It will settle down on its own. You don't have to put in any effort to calm it down. It will happen. It is effortless." Buddha

Acknowledgement

A Ph. D. is a complex journey, during which the contribution, help and support of many people are essential to reach the destination despite doubts, hesitations, errors and nervous breakdowns. I am indebted to all of the people who supported me with good advice, a smile, a hug and/or a beer during the past three years.

First, I would like to express my sincere thanks to my Ph. D. supervisors ***Benoit Liquet*** *and* ***Damien Sous*** *for their support, trust and patience. Prof.* ***Benoit Liquet*** *always kept a close eye on me and my work, and he always kept his door open to talk about my Ph.D. I wish also to express my warm and sincere thanks to Dr.* ***Damien Sous****, without whom none of this work would have been possible. His continuous support of my Ph.D. study and research work, his patience and his invaluable advice and assistance helped me throughout the research and writing of this thesis.*

Besides my advisors, I would like to thank the rest of my thesis committee: Dr. ***Isabelle Brenon****, Dr.* ***Sylvain Ouillon****, Prof.* ***David Amouroux****, Dr.* ***Aldo Sottolichio****, Prof.* ***Arnoldo Valle-Levinson*** *and Dr.* ***Romaric Verney****, for their insightful comments and encouragement. They helped me widen my research and gave me new perspectives.*

In addition to my committee, I am grateful to all the scientists I worked with or discussed with at the Laboratory or during the summer schools and conferences that I participated in. I would like to express my thanks and appreciation to ***Philippe Maron*** *for his invaluable advice and assistance with my numerical work. My gratitude also goes to Dr.* ***Romaric Verney****, who patiently and from a distance helped me with the completion of the paper.*

I also acknowledge the European Regional Development Fund (ERDF) and the Agence de l'Eau Adour-Garonne (AGWA) who funded the ***MICROPOLIT project*** *in relation to which this research work was carried out. Experimentations were sponsored by the EC2CO PANACHE program (CNRS INSU) with the* ***PANACHE project****.*

I am grateful to all contributors involved in field experimentations : the port of Bayonne, the Gladys group, MIO and EPOC laboratories, and in particular to ***Stéphane Gubert*** *whose efforts were essential to the deployment. I would like to thanks the ship crew members who were involved in our field experimentations :* ***Nathalie****,* ***Marcel*** *and* ***Benoit****, it was pleasure to work with them and their knowledge of the field site was priceless. I should also acknowledge many people who help me during the field campaigns by being with me and helping me on the boat and/or in the lab:* ***Nagib****,* ***Aurore****,* ***Jonathan****,* ***Laurent*** *and* ***Florian****.*

I thank my fellow labmates for the stimulating discussions, support before deadlines, and for all the fun we had in the last three years. Special thanks go to the colleagues with whom I shared an office : ***Iñaki****,* ***Manu****,* ***Lulu****,* ***Floflo****,* ***Delphine****,* ***Amaia****,* ***PA****,* ***Florian****,* ***Ana****,* ***Ali****,* ***Rafik****,* ***Ximun*** *and* ***Omar****. I would like to also thank* ***Youssef*** *and* ***Fariza*** *with whom I shared a lot of coffee/smoke breaks very late a night for their unfailing support, especially during last summer, when I was writing this manuscript. I also extend my gratitude to ISABTP staff with whom it was a pleasure to share my lunch break every day. Your sympathy, cheerfulness and jokes will miss me.*

I warmly thank the team of MICROPOLIT Project for their friendliness and all the good times shared together: ***Aurore****,* ***Carole****,* ***Sandra****,* ***Jonathan****,* ***Laura****,* ***Alyssa****,* ***Alexis*** *and* ***Tiphaine****, in particular to the girls of the knitting team.*

I would like to express my deepest gratitude to my long-time friend ***Jeanne*** *for her invaluable work of proofreading on my manuscript and also for her cheering and untiring help during my difficult moments.*

A special thank goes to my boyfriend ***Fabrice*** *who endured my sudden mood changes, my*

anxiety and irritability day after day, and still stands by my side.

Finally I would like to thank my family. The encouragement and support from my parents and my sister was a powerful source of energy. A special thought is devoted to my grand-mother for her never-ending support and love.

Contents

List of Figures

List of Tables

Acronyms

ADCP Acoustic Doppler Current Profiler

ADV Acoustic Doppler Velocimeter

AGWA Agence de l'Eau Adour-Garonne

BPB CCI Bayonne - Pays Basque Chamber of Commerce and Industry

EPOC Environnements et Paléoenvironnements Océaniques et Continentaux

ERDF European Regional Development Fund

ETM Estuary Turbidity Maximum

GFF Glass Fiber Filter

HW High Water

LISST Laser In-situ Scattering and Transmissometry

LW Low Water

MIO Mediterranean Institute of Oceanography

PSD Particle Size Distribution

RMSE Root Mean Square Error

RSSI Received Signal Strength Indicator

SIPS Strain-Induced Periodic Stratification

SPM Suspended Particulate Matter

SSC Suspended Sediment Concentration

General Introduction

Context

Estuaries are complex transfer areas of water mass and Suspended Particulate Matter (SPM) between ocean, land and continental waters [33]. They constitute unique habitats for a large variety of living organisms and essential nurseries for many marine species. Estuarine areas are also characterized by urbanization, industrialization and agricultural intensification, leading to riverine, estuarine and marine water contamination. In the overall context of climate change and a growing anthropogenic pressure, the preservation of estuarine ecosystems is a key issue. In the last decades, various European regulations have been implemented to preserve and improve water quality, but also to protect marine and estuarine ecosystems, as well as human health, and to reduce our impact on those systems: the European Water framework Directive, the Marine Strategy Framework Directive, and the Bathing Water Directive. Their common goals are to establish an overview of water quality, then study its evolution and finally prevent and get rid of pollution. To achieve these goals, it is paramount to improve our knowledge of the hydrodynamical processes controlling the dynamics and renewal of water masses in estuaries and their ability to transport, expel or retain sediments, contaminants, nutrients and living organisms.

Estuarine dynamics largely influence chemical and biological processes. Reaction rates are challenged by the different estuarine dynamic time-scales (i.e., tidal cycle, fortnightly cycle, seasonal variations): a chemical reaction with a kinetic longer than the tidal period would not reach an equilibrium [35]. The residence time of waters and sediment will also impact biological productivity. Rapid flushing will generally be associated with high biological productivity, while long residence time leads to nutrient recycling, hypoxia and water acidification. To preserve estuarine and marine ecosystems, decisions have to be made despite conflicting interests. A quality management system based on quantitative decision-making tools such as observations and numerical modeling predictions is highly needed.

A significant research effort has been engaged in the last decades to investigate estuarine dynamics from in-situ measurements and/or numerical modeling. River flow, tidal motion and wind stresses have been identified as the major drivers of estuarine dynamics. The competition between these drivers differs significantly from site to site and according to time-scales. Improving our knowledge on estuarine dynamics requires the study of such competition and switching between drivers.

MICROPOLIT project

MICROPOLIT is a multidisciplinary project, co-funded by the European Founding for Regional Development (ERDF) and the Adour-Garonne Water Agency (AGWA). This project aimed to study the state and the evolution of the marine water quality of the Basque Country coastline. Three specific study sites were selected for field experimentations: the Adour estuary, the Capbreton canyon and the Basque rocky coast. The purpose of this project is a better understanding of the water's quality in the area of study, the identification and quantification of

the pollution sources, as well as the capacity of ecosystems to get rid of pollution. To determine the overall effects, gaining knowledge of the interactions between physical, biological and chemical processes is paramount. Researchers from different laboratories pooled their resources for this project: IPREM-LCABIE, IFREMER-LRHA, IPREM-ECP, IPREM-EEM, SIAME-IVS, INRA-ECOBIOP, LMAP, IMA, centre de la Mer de Biarritz. the MICROPOLIT project is composed of 5 ACTIONS, namely: ACTION I : Establishing the state of knowledge about the biodiversity and chemical quality, ACTION II: increasing the knowledge about the sources, the reactivity and impacts of micro-pollutants, ACTION III : Establishing monitoring systems and link development with existing systems, ACTION IV : Modeling of the pollutant dispersion, and simulation of the impacts, ACTION V : Reducing sources (treatment vs natural purification capacity). This Ph. D was funded by the MICROPOLIT project and was part of ACTION IV dedicated to modeling pollution dispersion and simulating the impacts. This action aimed to understand and predict water mass and suspended sediment displacement as well as their dispersion in the coastal area.

Objectives and methods

Study site

The goal of the present study is to gain knowledge of hydrodynamics and sediment transport in a man-engineered channel-shape estuary, subjected to strong tidal and riverine forcing, with few inter-tidal areas and a small watershed, as very little is known about such estuaries. The selected field site is the Adour river estuary, located at the bottom of the Bay of Biscay. It is a highly developed estuary with several kilometers of its downstream part that have been entirely channelized in order to secure the Bayonne harbor operations. This specific morphology is reinforced by a man-engineered reduction of the section at the last reach, in order to ease the expulsion of water and sediment. The dynamics of estuarine water masses and sediments is further affected by human interventions aiming to facilitate the navigation by dredging activities and wave protection. In addition to this very specific morphology, the Adour estuary is also subjected to important riverine and tidal forcing, due to its location near the Pyrénées (which implies heavy rainfall and snow melt freshet) and the Atlantic ocean. Despite serious economic and environmental issues related to water quality and sediment supply, very little is known about the functioning of the Adour estuary and the influence of human interventions on its internal dynamics. Previous studies have focused on the dynamics of the turbid plume and its area of influence in ocean waters [9, 23, 32, 65, 88].

Objectives

The overall objective of this study is to characterize the current and salinity structures within the lower Adour estuary, as well as their respective influences on the suspended sediment dynamics, in a type of estuary that has been largely unexplored. This type of estuary has very complex hydrodynamics, which vary in space and in time. In such estuaries, it has been shown that the dynamics are mainly driven by tides and river discharge. The density structure created by the fresh riverine waters flowing into the dense marine waters can be responsible for a gravitational circulation. The tidal wave propagation inside an estuary generates a barotropic pressure gradient and tidal stresses. The sediment dynamics are largely influenced by the estuarine hydrodynamics. A striking feature of sediment dynamics in estuaries is the formation of what we call an Estuary Turbidity Maximum (ETM), which is an area of particularly high concentration of suspended sediment. In order to gain detailed insight into the Adour estuarine dynamics, we addressed five specific questions :

- 1) What is the tidal cycle influence on the Adour estuary hydrodynamics?

- 2) How does the river discharge impact the estuarine dynamics ?
- 3) Does the fortnightly cycle induce a switch of drivers ?
- 4) How are the suspended sediment dynamics controlled by the estuarine drivers?
- 5) To what extent is it possible to reproduce such a complex hydrodynamics with a state-of-the-art numerical model ?

Methodology

In order to address the objectives above mentioned, a dual experimental/numerical approach was developed. Both approaches are complementary and necessary to the development of a reliable numerical model capable of predicting and simulating estuarine dynamics. Field experiments were used to address objectives 1) to 4), as well as to calibrate and validate the numerical model. The numerical model was developed to address objective 5) and complement the understanding gained with the field experiments.

Existing data sets were collected and analyzed to design our field campaigns. Our field experiments focused first on the dry season (Sept. 2017), to address objectives 1), 2) and 4). Experiments spanned two fortnightly cycles as we carried out tidal cycle surveys during spring and neap tides, and deployed moored instruments over one month. This data set was complemented by a one-tidal cycle survey on September 2018. In order to address objectives 3) and 4), an additional one-tidal cycle survey was undertaken during a freshet event (June 2018).

A realistic 3D numerical model of the Adour estuary was developed with the TELEMAC suite of solvers, based on recent bathymetry data. One-month simulations were run under the same hydrological conditions as those encountered during the field campaigns, in order to address objective 5).

Manuscript structure

The manuscript is divided into 4 parts. First part is dedicated to the state of the art about saline structure, circulation and sediment transport in salt-wedge estuaries and a presentation of the study site. Part II details the methods and tools developed during our field experimentations and to analyse the collected data, in order to understand the hydrodynamics and sediment transport in a strongly anthropized salt-wedge estuary. We start with a presentation of the field experimentations carried out in the lower estuary, before introducing the complex salinity structure and circulation taking place inside the lower estuary, and finally clarifying the link between the circulation of water masses, salinity structure, turbulent mixing processes and the variability of the suspended sediment concentration inside the Adour estuary. Part III explains the numerical approach developed during thid Ph. D. A presentation of the numerical tool, TELEMAC 3D, is followed by a benchmark study of density stratification with TELEMAC3D. Finally, the 3D numerical model of the Adour estuary is presented, as well as its calibration and validation based on the field data collected during this Ph. D.. Part IV is devoted to the conclusions of this Ph. D. work and prospects for future work.

Part I

State of the Art

Chapter 1

Hydro-sedimentary functioning of salt-wedge estuaries

1.1 Definition and Classification schemes of estuaries

Throughout the years, "estuary" has been given a number of different definitions, depending on the field of study at hand. It is thus challenging to find a common way to classify or categorize estuaries. Various definitions and classification schemes have been developed. In this section, we will focus on one commonly accepted definition, as well as some well-known classification schemes used in Estuarine Physics.

1.1.1 Definition of an estuary

The term "estuary" comes from the Latin word "*aestus*", which means "tide". Estuaries have been defined and classified in a variety of ways, on the basis of several criteria: water balance, geomorphology, hydrodynamics, vertical structure of salinity, among others. One of the most commonly used definitions was given by Cameron and Pritchard [18]: "*a semi-enclosed coastal body of water having free connection to the open sea, and within which sea water is measurably diluted with fresh water deriving from land drainage.*" As per this definition, the estuary is a "semi-enclosed coastal body". It means that the lateral boundaries have a significant impact on the estuarine circulation. The "free connection to the open sea" means that the saline entrance is of great importance in the estuarine circulation patterns. Another crucial notion of this definition is the dilution of sea water by fresh water, implying that this definition only covers positive estuaries, where the salinity in the estuary is lower than ocean salinity. Inverse estuaries, where evaporation exceeds the fresh water inputs, as well as neutral estuaries, where neither the fresh water inflow nor the evaporation dominates, are not covered by this definition. It also underlines the importance of the salinity gradient in estuarine circulation [104].

A growing interest in classifying estuaries has developed along the years, with the aim of gaining a unified view on common processes characterizing each type of estuaries. Different classification schemes have been proposed based on : tidal forcing [25, 56], geomorphology [91, 104] [91, 104], vertical salinity structure [18], and hydrodynamics[55, 120, 46].

1.1.2 Classification according to geological origin

From a geological point of view, it is very interesting to classify estuaries according to their origin. Different natural mechanisms can generate estuaries, such as a rise in sea level or tectonic activity. On the basis of geomorphological structure, estuaries may be divided into four groups [91, 104]. **Coastal plain estuaries** have been formed either from subsidence of the land or from a rise in sea level, resulting in **drowning of a former river valley**. They are typically wide (several km) and shallow (around 10 m), with a V-shaped cross section (Fig. 1.1). Cheasapeak

Bay with its tributaries is a good example of a coast plain estuary. A second type of estuary is the **Fjord type**, formed by the action of glaciers, carving out steep side valleys. They are generally elongated deep channels with a glacial till at the mouth and a U-shaped cross section. For example, Puget sound's estuaries are very deep, narrow, and have inflows from local rivers. A third large group of estuaries, named **bar-built estuaries**, result from the development of a sand spit along the coast due to a littoral drift. A good example is the Pamlico sounds in North Carolina. They are generally shallow, with a narrow channel which connects the estuary to the ocean. Lastly, **tectonic estuaries** have been formed by plate boundaries faulting or folding. Resulting basins are filled up by the ocean. San Franscico Bay is an example of this type of estuary.

Unfortunately, such classification scheme based on geomorphology structure does not take into account the human intervention, which can highly modify the original morphology of an estuary.

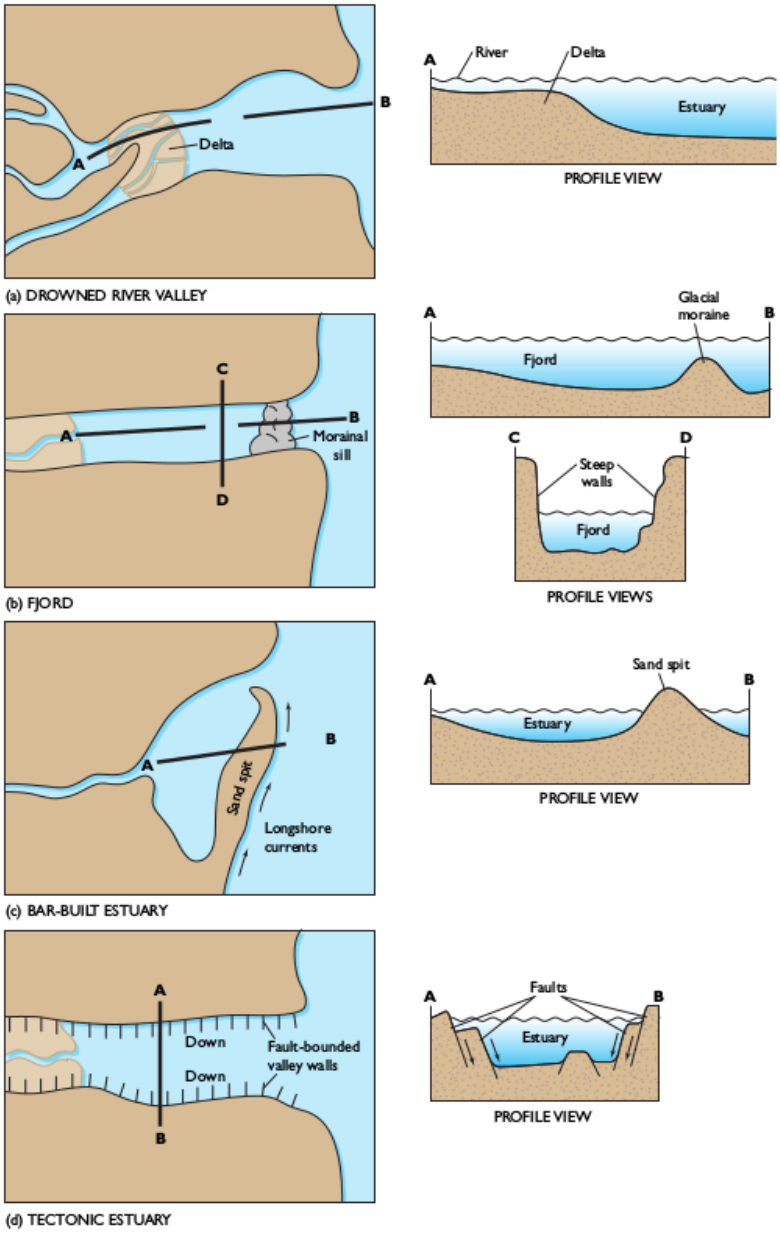

Figure 1.1: Classification of estuaries according to geomorphological struture. Extracted from Pinet, 2009 [89].

1.1.3 Classification according to tidal forcing

Estuaries can also be classified based on their tidal amplitude [25, 56], as microtidal ($< 2m$), mesotidal (2m to 4m) and macrotidal ($> 4m$). Wind and wave forcing are dominant in **microtidal estuaries**. In such estuaries, sand bodies are generally generated by storm and waves (e.g. wind tidal flats, bay beaches, recurved spits and cuspate spits) [56]. For instance, the Rhone river is characterized by a microtidal estuary (about 20 cm). In **mesotidal estuaries**, tidal forcing is dominant. Tidal deltas are the principal sand accumulation forms occurring in such estuaries [56]. The Fraser estuary is considered to be a mesotidal estuary. In **macrotidal estuaries**, tidal forcing is even more important. Such estuaries are generally characterized by a broad mouth and a funnel shape. Tidal flats can be formed at the center of the estuary. Sand deposits are generally long, linear, and oriented parallel to tidal currents [56]. The Gironde estuary is a typical macrotidal estuary.

1.1.4 Classification according to tidal propagation

One major feature of estuaries is the tidal influence, and the subsequent variation of water elevation inside the estuary. The morphology of the estuary will affect the propagation of the tidal wave along the estuary. The amplitude of the tide along the estuary is subjected to two constraints: bed friction and section reduction. A classification scheme was proposed, based on the competition between the effects of convergence and friction in the estuary [34]. When the tidal wave propagates inside the estuary, the convergence of the estuary will focus the energy, leading to an increase in water elevation, while the friction at the bed and on the wall will tend to dissipate the energy in decreasing the water elevation. When the effect of convergence is prevalent over the friction in the estuary, the tidal amplitude is increasing landward. In this case, the estuary is named **hyper-synchronous**. The Gironde estuary is mainly hyper-synchronous, with a maximal amplitude of 6 m in Bordeaux during spring tide [5]. In **hypo-synchronous** estuaries, such as the Rotterdam waterway, the friction is prevalent over the convergence effect and thus the tidal amplitude decreases in the upstream direction. In the case of a balance between both effects, the tidal amplitude remaining mostly uniform, the estuary is named **synchronous**. The Elbe river is known to be a synchronous estuary [66].

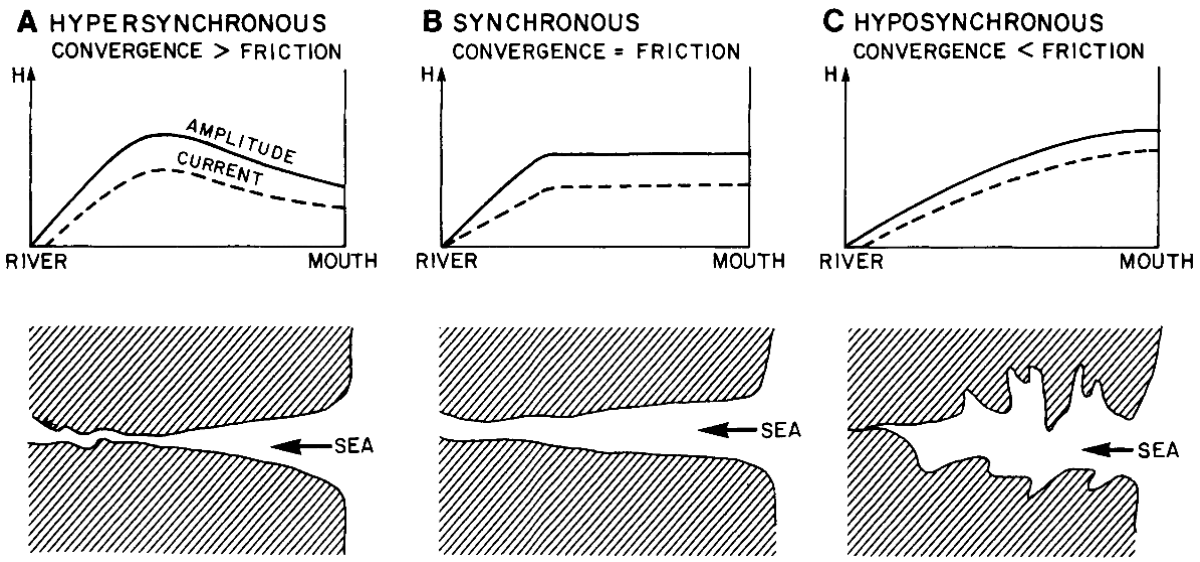

Figure 1.2: Classification of estuaries according to their tidal propagation. Source : Coastal Sedimentary Environments [85]

A switching between hyper-synchronous and synchronous or even hypo-synchronous can occur

during the fortnightly cycle. During spring tides, the higher current velocities increase the energy dissipation by friction, resulting in some cases in hyposynchronous conditions. On the other hand, neap tides favor the hypersynchronous conditions [5].

1.1.5 Descriptive classification according to stratification structure

The combined effects of tide and river discharge inside the estuary lead to the generation of a density stratification. Inside an estuary the density variability will be greatly dominated by the salinity gradients, the temperature distribution influence on the water density can be neglected. A classification scheme based on water column salinity stratification has been developed [18, 93, 104], in which estuaries can be classified as salt-wedge, strongly stratified, weakly stratified, or well mixed. Stratification is the result of a competition between buoyancy forcing due to river freshwater inflow and turbulent mixing from tidal forcing.

Salt-wedge estuaries (or highly stratified estuaries) are characterized by a river flow strong enough to sustain a strong density gradient with a sharp pycnocline, against the tidal mixing tendency. This leads to a two-layer flow with almost uniform layers and a thin interface, where the upper layer has a salinity close to nil, and the lower layer has a salinity identical to marine waters. A classical example of a salt-wedge estuary is the Southwest Pass of the Mississippi river.

When the tidal forcing is sufficient to avoid a river-dominated configuration, a strong stratification remains throughout the tidal cycle. Such estuaries are named **strongly stratified**. The pycnocline is well developed with both layers being almost homogeneous.

If the tidally-generated turbulence is strong enough to challenge the vertical density gradient, then the stratification is smoothed compared to salt-wedge estuaries. These weakly stratified estuaries are also named **partially mixed estuaries**. The weak pycnocline is due to advection and turbulent mixing taking place at the interface. The stratification is generally stronger during neap tides. The Coriolis force may produce a tilt of the interface, and a slight lateral salinity gradient. Chesapeake Bay is known to be a partially mixed estuary.

When the tidal mixing is sufficient to overwhelm the vertical saline structure, we refer to this as **well-mixed estuaries**. Turbulent mixing applies on the full water column and it is particularly strong at the bottom of the water column. A longitudinal salinity gradient is produced, with salinity decreasing landward. Because of the Coriolis force, a lateral salinity gradient may develop, e.g. in the Northern hemisphere, higher salinity water moves landward along the left bank and fresher water moves seaward along the right bank. The Delaware Bay is an example of well-mixed estuaries.

However, the horizontal and vertical salinity gradients can show important variations in time (e.g. from neap to spring tide, or from wet to dry season) and space (from mouth to the head of the estuary), and as such, the same estuary can be classified differently depending on the forcing conditions. This classification scheme might not be systematically used to classify estuaries.

1.1.6 Toward a quantitative classification according to hydrodynamics

The classification schemes presented above are very descriptive and general, and have been gradually replaced with more recent, quantitative schemes, that generally focus on the competition between buoyancy generated by the river discharge and mixing produced by the tide. Estuaries are therefore categorized according to their hydrodynamic processes.

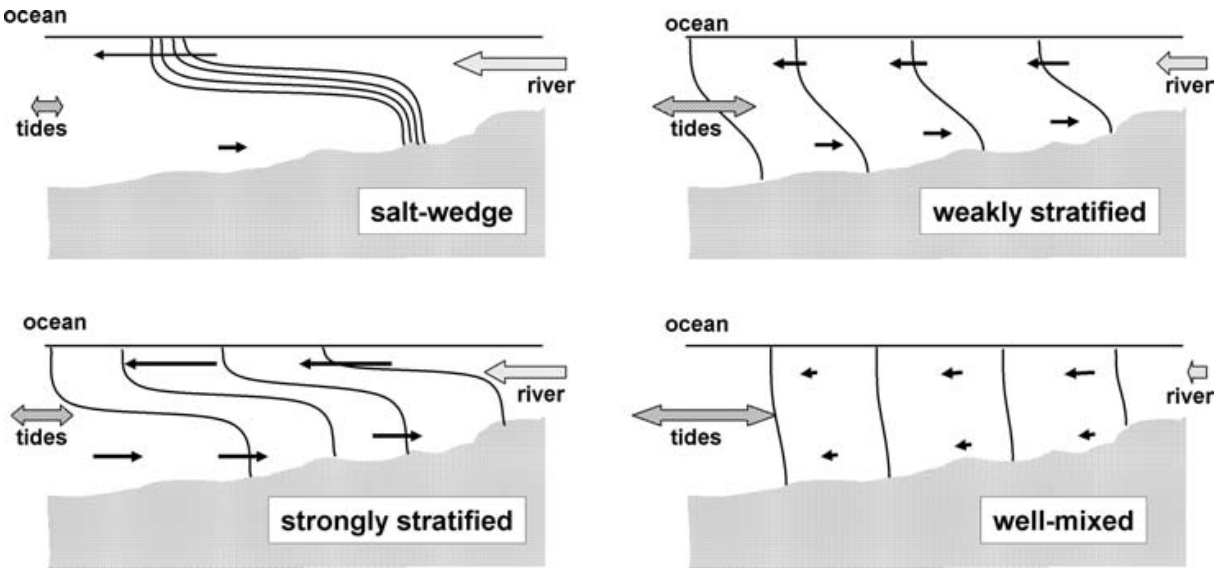

Figure 1.3: Classification of estuaries according to their saline structure. Figure extracted from Contemporary issues in estuarine physics edited by Arnoldo Valle-Levinson [121]

1.1.6.1 Classification in terms of stratification and circulation

A widely adopted classification scheme, in which estuarine dynamics is included, was proposed by Hansen and Rattray [55]. This classification is based on two dimensionless parameters: the circulation parameter and the stratification parameter. Those parameters are based on tidally and cross-sectionally averaged variables. The circulation parameter is the ratio of the net surface velocity u_s to the mean freshwater velocity $U_f = Q/S$, where Q is the river flow and S the section. A strong gravitational circulation would generally be reflected by a high value of the circulation parameter. The stratification parameter is the ratio of the top-to-bottom salinity difference ∂S to the mean salinity over the section S_0. As expected, a low value of the stratification parameter means a weak vertical stratification of the water column. The comparison between stratification and gravitational circulation brings out the relative importance of horizonal diffusion and advection of the salt flux. Hansen and Rattray defined a parameter ν, as the diffuse fraction of total horizontal salt transfer in a rectangular channel. When ν tends to zero, the gravitational circulation is responsible for the upstream salt flux, whereas, when $\nu = 1$ the upstream salt flux is entirely due to diffusion processes. Figure 1.4 displays the diffusive fraction of total upstream salt transfer in relation to both circulation and stratification parameters. We can see that advection is not directly related to stratification. Advection processes dominate the salt flux for the high circulation parameter no matter the stratification values, whereas the flux is dominated by diffusion only under low circulation parameters.

Based on this stratification-circulation diagram, seven types of estuaries have been identified. In the case of type 1 estuaries, the net flow is seaward within the full water column, and the diffuse processes dominate the salt flux. Type 1 estuaries are divided into subclasses 1a, in which stratification is slight, and 1b in which stratification is appreciable. Type 2 estuaries are characterized by a net flow reversing at depth, and both advection and diffusion contributing to salt transport. The specificity of Type 3 estuaries is the dominance of advection in the upstream salt transfer. Similarly to type 1, type 2 and 3 estuaries are divided into two subclasses according to their stratification. Salt-wedge estuaries are part of type 4 estuaries described by a two-layer flow and a strong stratification. As the stratification and the circulation may vary in time and space inside an estuary, each estuary is thus represented by a line instead of a point in this classification scheme.

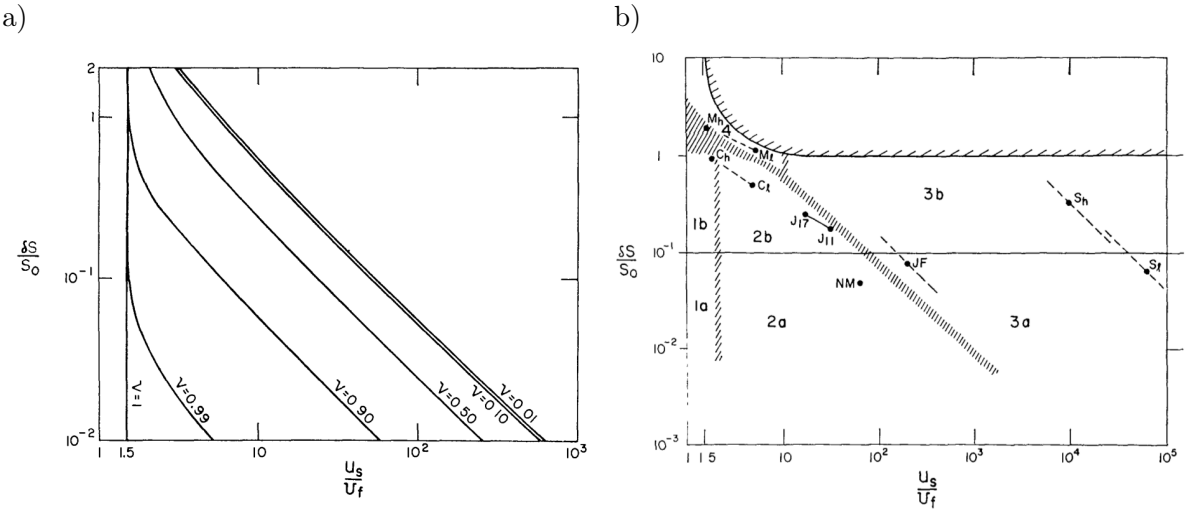

Figure 1.4: a) Fraction of horizontal salt balance by diffusion, as a function of salinity stratification and convective circulation in a rectangular channel, b) Proposed classification with some examples. (Station code: M, Mississippi River mouth; C, Columbia River estuary; J, James River estuary; NM, Narrows of the Mersey estuary; JF, Strait of Juan de Fuca; S, Silver Bay. Subscripts h and l refer to high and low river discharge; numbers indicate distance (in miles) from mouth of the James River estuary.) Extracted from Hansen and Rattray 1966 [55].

1.1.6.2 Classification scheme in term of mixing and stratification

One recent approach has been proposed by Geyer and MacCready [46], discussing the respective contributions of tide and river flow in mixing and stratification processes. It is based on a two-parameter space. The first is the freshwater Froude number $Fr_f = U_R/(\beta g s_{ocean} H)^{1/2}$ [50] which compares the net velocity due to river flow to the maximum possible front propagation speed. It expresses the ratio between river flow inertia and buoyancy due to salinity gradient. The second is the mixing parameter $M = \sqrt{(C_D U_T^2)/(\omega N_0 H^2)}$ which quantifies the effectiveness of tidal mixing in stratified estuaries, where U_R is the net velocity due to river flow, β is the coefficient of saline contraction, g is the acceleration due to gravity, s_{ocean} is the ocean salinity, H is the water depth, C_D is the drag coefficient, U_T is the amplitude of the tidal velocity, ω is the tidal frequency and $N_0 = (\beta g s_{ocean}/H)^{1/2}$ is the buoyancy frequency for maximum top-to-bottom salinity variation in an estuary.

Due to spring/neap variations and wet/dry season changes, estuaries are not represented by a point or a line in this classification scheme, but rather by rectangles covering the range of observed regimes. Authors have mapped various estuaries (see Fig. 1.5) based on those two parameters, demonstrating the efficiency of discriminating different classes of estuaries. For example, salt wedge estuaries, such as the Mississippi, the Fraser and the Ebro rivers, are located near the top of the diagram (i.e. high values of Fr_f), while partially stratified estuaries are at the center of the diagram (e.g. James river and San Fransisco Bay), and fjords and well mixed estuaries are on the bottom part (e.g. Puget Sound).

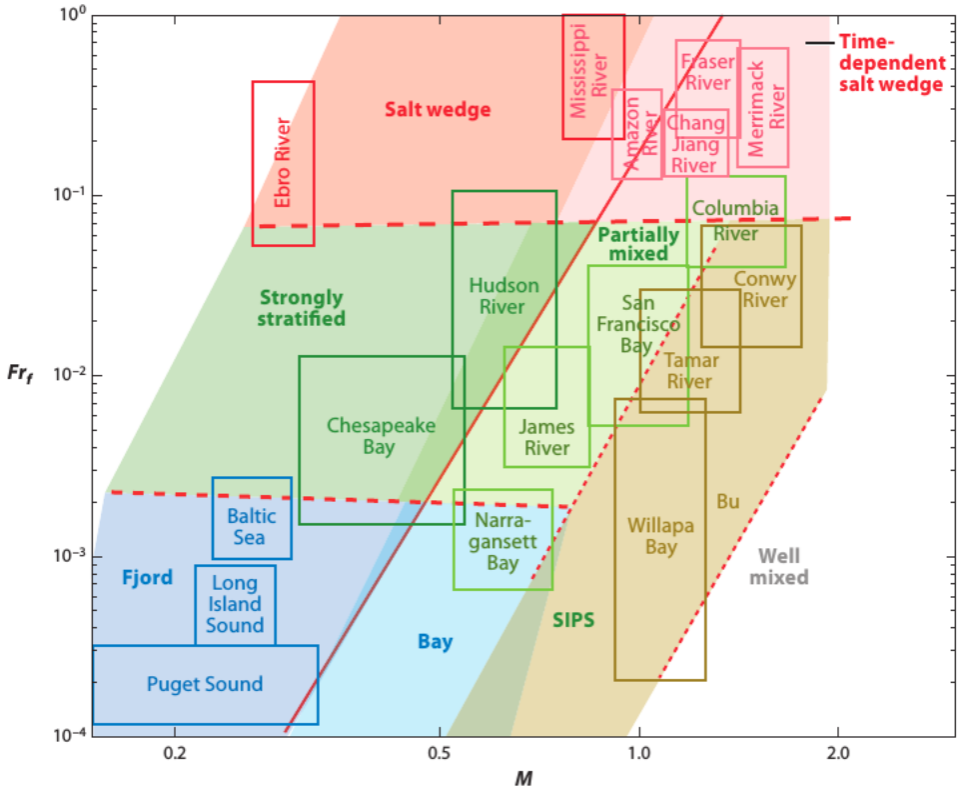

Figure 1.5: Classification of estuaries based on their freshwater Froude number and mixing number. Extracted from Geyer and MacCready 2014 [46].

1.2 Hydrodynamic processes in salt-wedge estuaries

In the past decades, many studies investigated estuarine dynamics from *in-situ* measurements [28, 36, 105, 107] and/or numerical modeling [14, 27, 74, 95]. From a physical point of view, estuaries are exchange areas between fresh brackish continental water and salty marine waters, mainly driven by river run-off and tide. Density gradients generated by continental waters interplaying with marine waters, and interactions between tides and estuarine morphology have been shown to be the major mechanisms governing estuarine dynamics. The buoyancy forcing is generated by the freshwater discharge, and results in horizontal density gradient and horizontal pressure gradient. The turbulent mixing, due to tidal and wind forcing, has been shown to be the second major factor in estuarine dynamics.

Our study will focus on the complex hydrodynamics of salt-wedge estuaries, and mostly on those subjected to energetic tidal forcing. Salt-wedge estuaries are characterized by a river discharge sufficient to maintain a strong density gradient against the tidal mixing [45]. Such estuaries have a very complex hydrodynamics which requires further investigation to be fully understood. We can differentiate the "**arrested salt-wedges**" from the "**time-dependent salt-wedges**". When tidal velocities are very weak, tidal motions do not alter the estuarine structure. In these arrested salt-wedges, the baroclinic pressure gradient is compensated by inertial and frictional forces. The salt-wedge is only advected to and fro. This estuarine structure can be found in microtidal estuaries, such as the Ebro and the Rhone rivers [60]. When salt-wedges estuaries are strongly forced by tides and river flow, density and velocity fields are highly variable throughout the tidal cycle and the estuarine structure is reset at each tidal cycle. Such estuaries are named "time-dependent salt-wedge estuaries". Strong tidal and river forcing result generally in a short estuary, i.e. a salinity intrusion that is of similar length to the tidal excursion [95]. The Fraser river is a typical example of a time dependent salt-wedge estuary [45]. The

strong interaction between tidal and riverine forcing, as well as estuarine morphology make time-dependent salt-wedge estuaries of the most energetic and variable. Hydrodynamics and sediment transport in such estuaries are strongly variable in both time and space. Despite the complexity and the variability of such estuarine dynamics, several key mechanisms emerge as common to many systems.

In this section, a brief survey of the state of knowledge of the hydrodynamic processes taking place into salt-wedge estuaries will be provided, with a specific focus on tidally energetic salt-wedge estuaries.

1.2.1 Major forcing

Tides and river flow are the major forcing of estuarine dynamics. The river flow brings fresh waters into marines waters, generating buoyancy and stratification, while tides produces turbulent mixing. The competition between gravity and turbulent mixing is the driving mechanism of estuarine dynamics. Both are fluctuating in time (tidal cycle, fortnightly cycle, seasons and decades), but the tidal forcing is also changing in space (i.e. during the propagation inside the estuary), resulting in variable interactions.

1.2.1.1 Riverine forcing

Estuaries are areas of interaction between waters of different composition. One of the most noticeable difference is the salinity, but others such as temperature, pH, or suspended sediment concentration may be important and may impact the estuarine system. This difference in salinity will play a major role in the vertical density stratification (halocline) that may develop inside the estuary. Temperature variations may also create density stratification, however, in estuarine systems, the salinity gradient generally dominates the density variation. This vertical stratification may greatly impact the estuarine dynamics by generating a two-layer flow and a baroclinic pressure gradient. The bottom layer, composed of dense marine waters, flows landward during the flood and seaward during the ebb. The top layer, composed of light freshwater, always flows seaward. This structure of light waters flowing on top of dense waters is stable from a gravitational point of view.

The river flow is strongly season-dependent, with high values during wet seasons (i.e. winter and spring) characterized by rainfall and snowmelts, and reduced discharge during dry season (summer). The river flow variation can be very slow (over a season) or very fast (freshet event). Extreme freshet events can create steep variations of river discharge (i.e. several hundred cubic meter per second) in few hours. These sudden variations deeply influence the estuarine dynamics. High river discharge periods are generally associated with a reduction of the tidal wave propagation and of the saline water entrance and with a increase in ebbing currents. The stratification is generally larger and the mixing rate weaker. It is all the more prevalent in salt-wedge estuaries, where the river forcing is dominant in front of the tidal mixing.

1.2.1.2 Tidal forcing

Variations of ocean levels around the world are the result of the gravitational pull of the Moon and the Sun. Their positions can be easily estimated and predicted. The moon revolves around the Earth in 28 days, thus the Moon, the Earth and the Sun are aligned every 14 days. In this configuration the gravitational pull of the Sun and the Moon are working together, generating periods of high tidal range, named spring tides. The larger tides occur one day or two after the new moon and the full moon. In between, tides of minimal amplitude occur, called neap tides. Tidal amplitude is then correlated to the distance and alignment of those stars (Fig. 1.6). Water elevation varies periodically with periods ranging from 12.25 to 24.5 hours. Around the world, tides vary in both range and shape, due to the presence of continents and the seabed morphology. The tidal wave can not turn freely around the world, it is distorted when

it encounters an obstacle such as a cap, a strait, an island or a continent. The sinusoidal shape of the tidal wave is also distorted by interaction with the seabed. Additional forces can affect the ocean surface elevation, such as the rotation of the Earth by centrifugal effects, or some meteorological conditions by pressure gradients. The tide is then also dependent on the latitude.

Tide is not restricted to the variation of ocean surface elevation, but it also generates tidal currents. They are just as variable as water elevation.

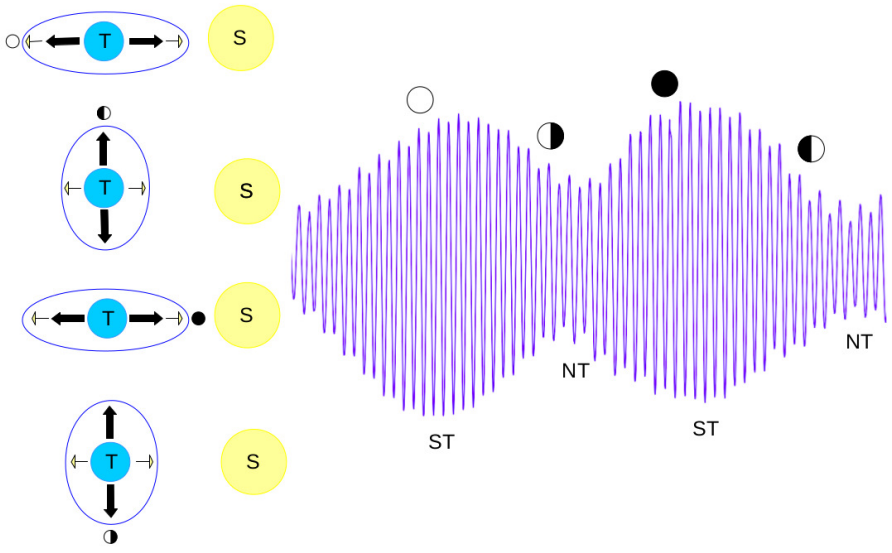

Figure 1.6: Earth, Moon and Sun positions during the fortnightly cycle. Inspired by Lemoine and Verney, 2015 [73]

As stated previously, salt-wedge estuaries can be divided into two classes, those with a stagnant salt-wedge and those with a time-dependent salt-wedge. The distinction between the two comes from the strength of tidal forcing compared with the river discharge. The stagnant salt-wedge type is typically associated with microtidal systems (i.e. tidal amplitude $< 2m$), when time-dependent salt-wedge estuaries are generally subjected to mesotidal or macrotidal forcing. In tidally energetic salt-wedge estuaries, the tidal forcing is the most important. Tidal velocities are comparable to, or even larger than, freshwater velocities.

Propagating into the estuary, the tidal wave can be greatly distorted by the bed friction and the convergence of the estuary banks. The bed friction will tend to reduce the tidal wave amplitude and the tidal velocity. The bed friction is highly dependent on the water depth. At the beginning of the flood, the water depth is small, the bed friction will then be greater than latter on the flood. On the other hand, the convergence of the estuary increases the tidal amplitude, the water slope and the speed of propagation. This causes the flood to become shorter and the ebb longer, generating what is named a "tidal asymmetry". Slack time associated with high tide is longer than the one associated with low tide. The tidal currents are also stronger during the flood than during the ebb. This asymmetry will increase landward. Such estuaries are described as **flood dominant**. Modification of the estuarine morphology by human intervention may impact the tidal wave propagation. For example, embankments are made generally in order to increase ebbing velocities and then ease sediment evacuation. They also produce lower levels of low tide.

The tidal wave propagation should be distinguished from the entrance of marine water. The limit of the saline entrance is generally shorter than the limit of tidal wave propagation. When

both are comparable, the estuary is said to be short.

1.2.2 Density driven flow

Estuaries can be distinguished from most of other aquatic environments by their horizontal and vertical salinity gradients. This makes their hydrodynamics very complex. Different factors will influence this dynamics such as river flow, tidal motion, wind, waves, or Earth rotation, among others. These gradients are generated by the interaction between fresh waters from the river and salty marine waters. The salinity distribution in estuaries governs the dynamic structure.

1.2.2.1 Estuarine circulation

As presented in the previous section, estuaries have different characteristics of shape, origin, stratification and mechanisms driving their hydrodynamics. However, one common feature is the horizontal gradient of salinity. Salinity increases progressively from the river to the ocean. Pritchard in 1952 [92] was the first to correlate the horizontal salinity gradients to the estuarine circulation. Based on his observations in the James river (Chesapeake Bay), he demonstrated that when the tidally averaged velocity is considered, the estuarine circulation structure may be regarded as having two layers, with a upper less saline layer moving seaward and a more saline bottom layer moving landward (Fig. 1.7). Nevertheless, the velocity profile changes throughout the tidal cycle. At the end of the ebb, the near-surface velocity reaches a maximum and the velocity decreases linearly with depth, while at the end of the flood, the near-surface velocity is relatively small and the velocity increases with depth until the bottom boundary layer. The horizontal salinity gradient $\partial s/\partial x$ has been shown to be the cornerstone of the estuarine circulation. The estuarine circulation has also been named "residual circulation" or "exchange flow" in other studies.

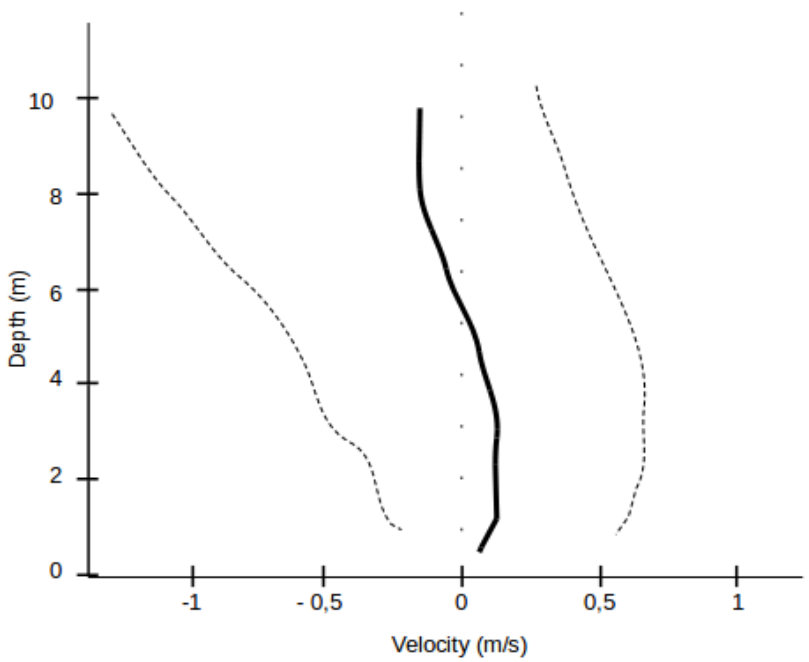

Figure 1.7: Schematic of the estuarine circulation. The full line represent the tidally averaged velocity. The dashed lines represent the maximum ebbing velocity (on the left) and the maximum flooding velocity (on the right).

This horizontal salinity gradient generates a pressure gradient. This pressure gradient is

composed of the influence of the surface slope and the horizontal gradient of salinity :

$$\frac{1}{\rho}\frac{\partial p}{\partial x} = g\frac{\partial \eta}{\partial x} + \beta g\frac{\partial s}{\partial x}(h - z) \tag{1.1}$$

where ρ is the water density, β is the coefficient of saline contraction, g is the acceleration due to gravity, h is the water depth, and z is the vertical coordinate measured upward from the bottom [50].

The pressure induced by the density gradient is greater at the mouth than at the head of the estuary, resulting in the landward displacement of marine waters. Near the surface, the second term on the right-hand side of equation (1.1) is zero, and the tidally averaged surface slope tilts in the opposite of the salinity gradient. Then near surface fresh water flows seaward. The pressure gradient tends to flatten both the horizontal gradients and the free surface, in order to achieve a stable configuration.

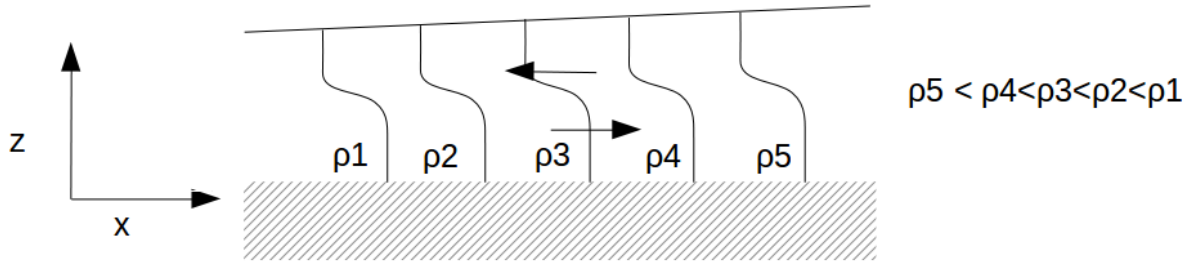

Figure 1.8: Schematic of the estuarine circulation pattern due to horizontal density gradient

The estuarine circulation is a small residue of the tidal current. Typical values (e.g. 0.2 $m.s^{-1}$) are of one order of magnitude smaller than tidal or riverine currents (e.g. 1.5 $m.s^{-1}$).

1.2.2.2 Stratification

As it has been shown in the previous section, the stratification (i.e. vertical density gradients) may vary strongly from one estuary to another. The stratification can also change during the tidal cycle, the fortnightly cycle or due to the seasonal variations. An estuary can vary from strongly stratified to well mixed depending on the forcing conditions. Estuarine stratification plays a crucial role in estuarine dynamics, mostly by damping vertical turbulence, thus reducing mixing across the interface. For example, in neap tide the stratification is maximal and tidal mixing is minimal. Such conditions of reduced mixing between both layers may lead to stagnant bottom waters and to hypoxia in the lower saline layer. In most estuaries, light fresh water is flowing over heavy salty water, except in inverse estuaries. This configuration is very stable and considerable work is necessary to overcome this stratification.

The fresh water from the river tends to generate and maintain the stratification, while the tidal motion tries to mix marine and riverine waters. Advection by the river flow will decrease the salinity of the upper layer, while vertical mixing will carry salt to the upper layer.

The well-known parameter to estimate the relative importance of stratification on mixing is the **gradient Richardson number**. It gives us the ratio between available turbulent mixing energy and the required potential energy :

$$Ri = -\frac{g}{\rho}\frac{\partial \rho/\partial z}{(\partial \overline{u}/\partial z)^2}, \tag{1.2}$$

where g is the acceleration due to gravity, ρ is the water density and $\overline{u}$ the mean longitudinal component of the velocity. The density stratification is supposed to be predominant on the

mixing for values of Ri above the threshold value of 0.25. Otherwise, the mixing overcomes the buoyancy force generated by the vertical density gradient.

The strength of the stratification is then represented by the buoyancy frequency or **Brunt-Väisälä frequency** :

$$N = \sqrt{-\frac{g}{\rho}\frac{\partial \rho}{\partial z}}. \tag{1.3}$$

The steepness of the density interface is related to the speed of the surface currents in the estuary. A strong river discharge is generally associated with a steep interface. Instead, in case of intense tidal forcing, the bottom-generated turbulence will be responsible for a vertically-mixed system. The stratification is the steepest in salt-wedge estuaries, where the river flow prevails over the tidal currents. The turbulent mixing is insufficient to breakdown the stratification. The interface tilts downward in the upstream direction due to friction, creating the wedge shape at the bottom layer front. The stratification tends to strengthen the estuarine circulation.

In tidally energetic salt-wedge estuaries, such as the Fraser river, maximum stratification is reached at the end of the flood tide, when minimum stratification occurs at the end of the ebb tide [45].

1.2.3 Mixing

One effect of tidal motion inside the estuary entrance is the generation of turbulence on the bed and at the interface between fresh and salt water. The mixing between fresh and salty waters originates from velocity shear and bottom stress. When mixing occurs in an estuary, the surface layer thickens and its salinity increases, the interface becomes less steeplike, and the bottom layer seems to be depleted.

For strongly stratified estuaries with a marked density interface and a two-layer flow, there are three major mechanisms responsible for turbulence : friction at the bed, internal waves and billow turbulence at a density interface due to shear instabilities. The bulk Richardson number can be used to estimate which mixing process is likely to take place in the estuary (Fig. 1.9):

$$Ri_B = \frac{gh\Delta\rho}{\rho_m u_m^2}, \tag{1.4}$$

where h is the total water depth, $\Delta\rho$ is the difference between top-to-bottom density, ρ_m is the depth averaged water density and u_m is the depth averaged velocity. An internal wave may form over a sill for $Ri_B > 1$, and when the mean flow velocity decreases the wave can propagate, enhancing the shear at the density interface. For values of the bulk Richardson number lower than one, shear due to bed friction is reduced, but the buoyant waters flowing over saline waters can generate strong interfacial shear, resulting in billow formation [75].

In almost stagnant salt-wedge estuaries generally subjected to microtidal forcing, the small tidal motions are unlikely to be sufficient to generate turbulence by bottom friction capable to penetrate the density interface. Only when the lower layer is thinner than the bottom boundary layer, mixing can occur at the density interface [35]. In tidally energetic salt-wedge estuaries, turbulence generated by both bed friction and interfacial shear may be able to overcome the stratification.

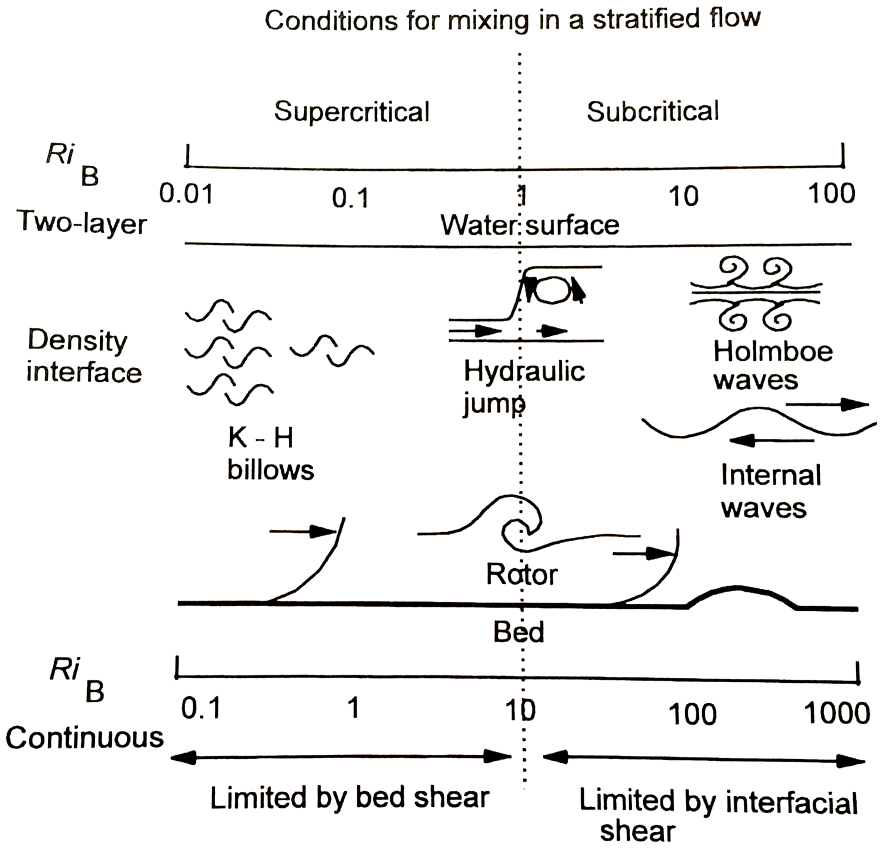

Figure 1.9: Schematic diagram of various mixing processes in a stratified flow. Extracted from Lewis, 1997 [75]

1.2.3.1 Shear instability at the interface

The velocity shear at the interface generates entrainment processes. Transfer of salt-water into the upper layer, through wave-like perturbations, is produced by the shear. The transfer of salt is a one-way process, therefore no freshwater is moving downward. In the upper layer, salt-water is moved downstream by advection by the river flow. A slow inflow of marine water compensates the upward downstream movement of the salt water across the halocline [35]. This process tends to reinforce the estuarine circulation.

Interaction with bottom bathymetry, or wind velocity variations can generate internal waves. When the velocity shear increases, internal waves can cause mixing when propagating. When those internal waves are breaking, there is salt water moving upward to the fresh water surface layer.

Geyer and Farmer [45] showed that, in the Fraser estuary, when strong shears develop across the interface, Kelvin-Helmoltz (K-H) instabilities (i.e. billows) occur. The K-H instabilities entrains water transfer from above and below.

1.2.3.2 Bottom friction

Tidal motion on the sea-bed produces bottom stress and shear. When the bottom boundary layer is thin enough, the bed turbulence will only affect the bottom part, creating a well-mixed layer (Fig. 1.10 b), while when the bottom boundary layer is thick, interaction between bottom shear and internal shear may occur (Fig. 1.10 a). Mixing processes are then produced at the interface.

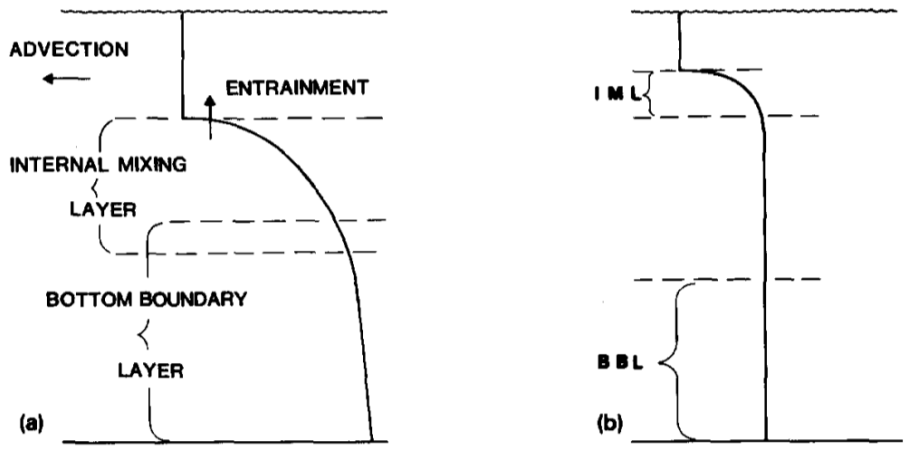

Figure 1.10: The salinity profile produced by the combination of internal mixing at the density interface and in the bottom boundary layer, in case of interaction between layers (a) and without interactions (b). Extracted from Dyer, 1991 [35]

1.2.3.3 Mixing in the salt-wedge estuaries

The degree of mixing is correlated to the tidal cycle. In tidally energetic salt-wedge estuaries, intense periods of mixing have been noticed during the ebb tide, while strong stratification occurs during the flood tide. Variations of mixing conditions along the tidal cycle can be explained by the fluctuation of the bottom stress and shear instabilities. At the end of the flood, the salt-wedge is almost arrested and stratification is strong. The freshwater flows over the salt-wedge resulting in intense shear across the interface. As the surface elevation decreases at the mouth of the estuary, the pressure gradient increases until it is strong enough to drive the salt-wedge out of the estuary. Bottom friction resists the salt-wedge displacement and significant shears are generated across the interface, leading to K-H instabilities. The pycnocline thickens and salt is transfered to the upper layer. A strong mixing is able to overcome the stratification and the estuary goes from being a two-layer flow to a well mixed structure. If the combined effect of tidal and riverine forcing is sufficient, the salt-wedge can be fully flushed at the end of the ebb tide. The variations in the degree of mixing are also related to the tidal range, with stronger mixing during spring tides and reduced mixing during neap tides [75].

1.2.4 Interactions

The tidal wave, when propagating inside an estuary, interacts with the estuarine morphology, stratification and circulation. These interactions can strongly modify the water masses circulation and mixing and also the sediment transport.

1.2.4.1 Tidal straining

In 1990, Simpson et al. introduced the notion of **Strain-Induced Periodic Stratification (SIPS)** based on observations made in a region of the Liverpool Bay. They noticed a cyclic stratification correlated to the tidal motion, with complete vertical mixing ($\Delta S = 0$) during the flood tide and stratified conditions ($\Delta S > 0.4$) during the ebb. It has been attributed to the influence of the vertical shear in the tidal current [108].

In a horizontally stratified estuary, during the flood, surface waters are advected faster than the near bed waters. The isohalines become more vertical, i.e. the stratification $\partial\rho/\partial z$ is highly reduced (Fig. 1.11). Flood current intensity decreases with the increasing distance to the mouth of the estuary. The isohalines are then more advected at the entrance than at the head of the

estuary, resulting in an increasing horizontal density gradient $\partial\rho/\partial x$ (Fig. 1.11 third panel). During the ebb, surface water advection is stronger than bottom water advection, increasing the density stratification $\partial\rho/\partial z$. Denser waters are more advected than lighter waters, decreasing the horizontal density gradient $\partial\rho/\partial x$ (Fig. 1.11). The stratification is maximal at the end of the ebb tide. [61].

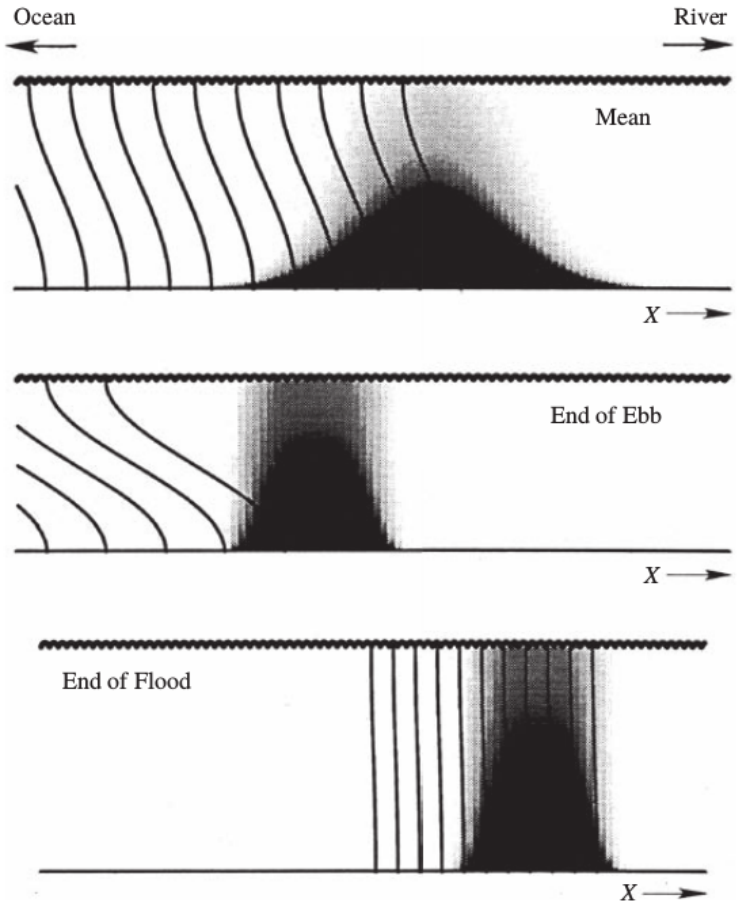

Figure 1.11: Conceptual sketch of tidal straining, and its influence on an estuarine turbidity maximum. Salinity is shown as contours, suspended particulate matter as shading. Extracted from Jay, 2010 [61]

In some studies, these stratification variations due to tidal straining have been referred to as **tidal mixing asymmetry**. The stratification plays a crucial role in the cycle of turbulence inside an estuary. The stratification tends to inhibit vertical mixing. In an estuary with tidal straining, during the ebb, the structure with surface waters flowing seaward over denser waters is particularly stable, deeply reducing the vertical mixing, while during the flood, important mixing occurs. The eddy viscosity, which quantifies the magnitude of momentum diffusion by turbulence, is greater during the flood tide than during the ebb tide. In an estuary, the horizontal density gradient always has the same sign and the baroclinic pressure gradient is always positive. However, the barotropic pressure gradient changes sign : it is positive during the flood and negative during the ebb. Therefore, barotropic and baroclinic pressure gradients works together during the flood and oppose each other during the ebb. The velocity profile is then relatively uniform during the flood, and severely sheared during the ebb (Fig. 1.12).

Stacey & Ralston's study [112] showed that tidal straining is restricted by the vertical extent of the boundary layer. In highly stratified estuaries, such as salt-wedge estuaries, the tidal straining is thus restricted by the pycnocline, while in weakly stratified estuaries, it extends to

the surface water. In salt-wedge estuaries, the tidal straining has generally no influence on the dynamics. An opposite pattern is usually observed, with maximum stratification during the flood (i.e. during the salt-wedge entrance) and maximum mixing during the ebb [45, 76, 95].

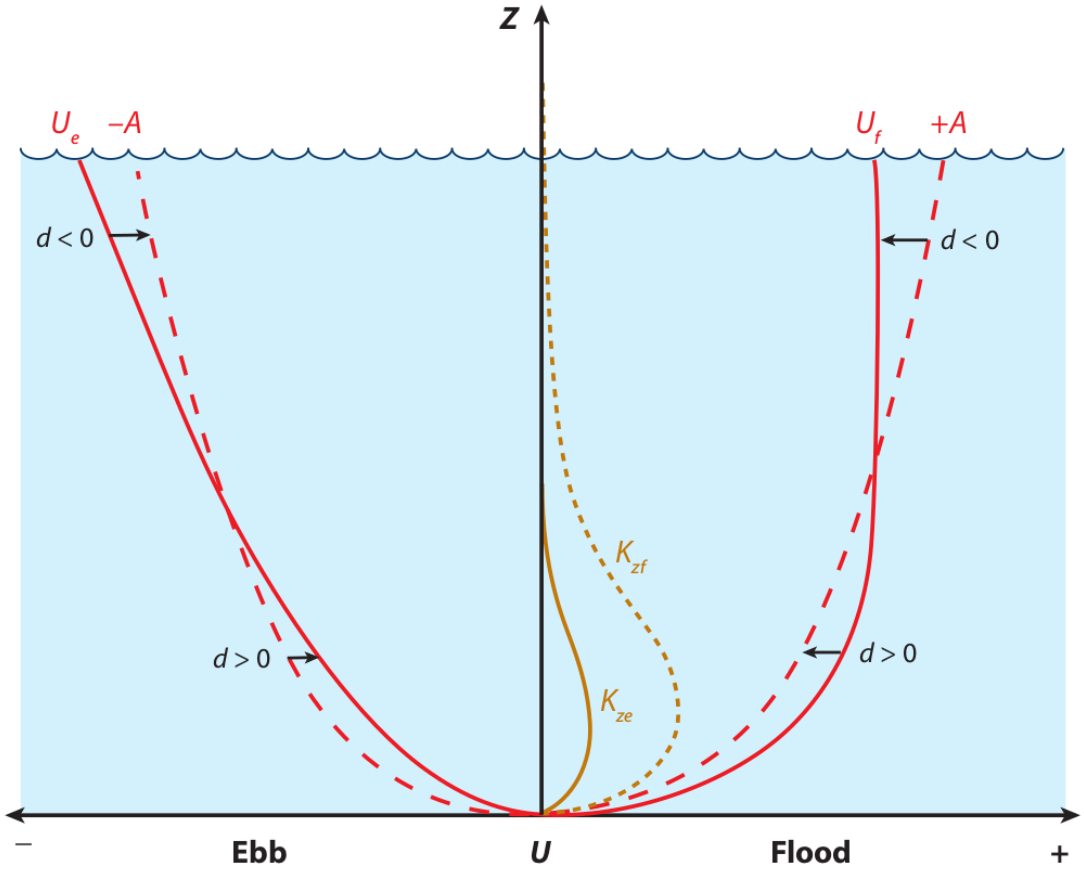

Figure 1.12: Vertical profiles of velocity and eddy mixing coefficients, demonstrating tidal asymmetry (based on Jay & Musiak 1994). The thick solid lines (U_f and U_e) are the ebb and flood velocity profiles, and the thick dashed lines ($-A$ and $+A$) indicate the semidiurnal velocity structure. The thin solid and dashed lines are eddy viscosity profiles for flood and ebb, with stronger mixing during the flood. The difference δ between the semidiurnal and actual velocity is the signal of tidal asymmetry. This is made up of a quarterdiurnal component and the mean (landward near the bottom and seaward near the surface).

1.2.4.2 Tidal pumping

The notion of tidal pumping was introduced by Allen et al. in 1980 [5], based on observation made in the Gironde and the Aulne estuaries. Authors presented the net tidal transport due to tidal velocity asymmetry and its influence on the trapping of sediment.

The tidal wave, when propagating in a shallow estuary, interacts with the bed. The tidal wave celerity depends on the water depth, therefore tidal wave celerity is stronger on the flood than on the ebb. This phenomenon is even more marked in estuaries with a large tidal amplitude (i.e. macrotidal estuaries). As the wave propagates inside the estuary, the asymmetry is more pronounced, with a steeper slope, stronger flood current and a shorter flood tide duration (Fig. 1.13). The bed shear tends to amplify this asymmetry. The flood predominance increases landward, until the loss of energy by friction is sufficient to reduce the amplitude of the tidal wave.

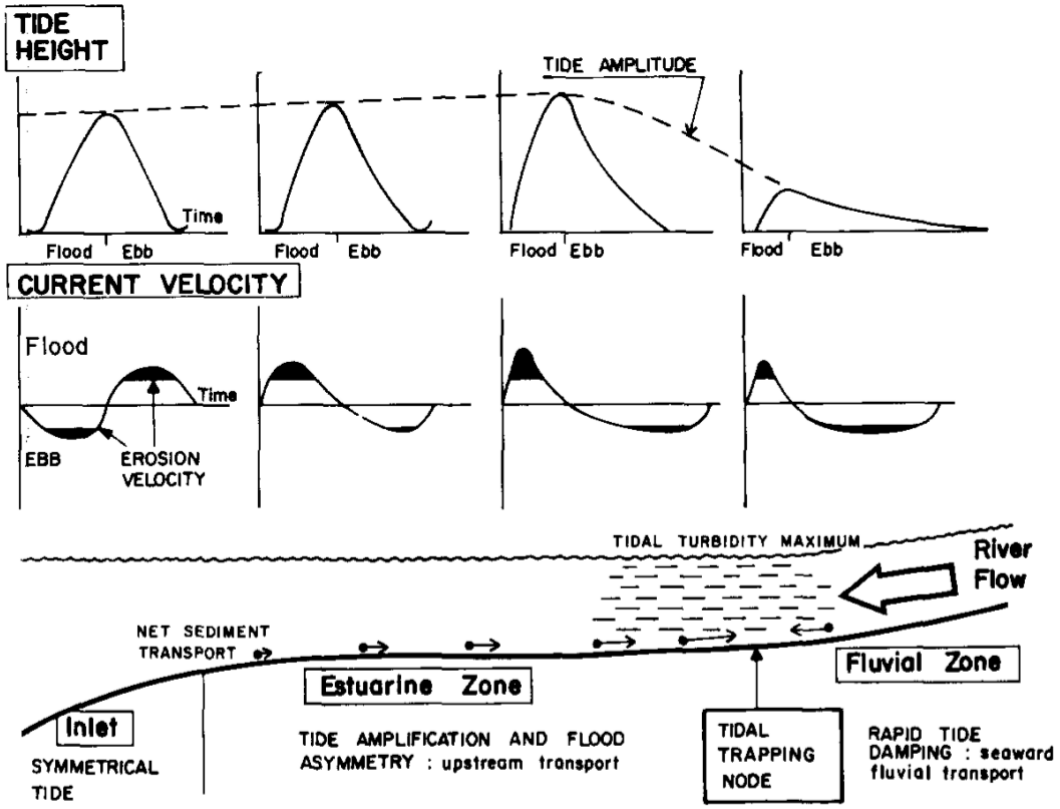

Figure 1.13: Schematic of the tidal pumping and its effects on trapping of suspended sediment. Extracted from Allen et al, 1990 [5]

1.3 Suspended sediment dynamics in estuaries

Riverine waters generally contain a high level of suspended sediments due to the watershed drainage by fresh water run-off. Estuaries are recognized as powerful traps of sediments, particularly those characterized by an ETM and an associated mobile pool of sediment. The increasing human activity in estuarine and coastal areas, such as waste discharge, urbanization, and agricultural intensification, leads to an increased pressure on ecosystems. Sediments can be associated with organic matter leading to hypernutrification, oxygen consumption and even hypoxia. High turbidity in ETM prevents sun light from reaching the bottom of the water column, inhibiting primary production. Sediments being efficient carriers of contaminant, estuaries can also be considered as contaminant traps [47]. The accumulation of contaminated sediments can impact dramatically estuarine and marine ecosystems, leading to major environmental issues. It has been shown in the Penobscot estuary that contaminants such as mercury can be trapped during several decades [47]. The recovery time for a given estuary after contamination is directly linked to the water and sediment flushing capacity. Water quality and contamination have motivated numerous studies of estuarine hydrodynamics and suspended matter dispersion [3, 38, 47, 64, 135].

In addition to environmental issues, one of the major economical stakes regarding suspended sediment in estuaries is the siltation in harbors. Estuaries facilitates connections between international offshore maritime trade and national inland trade. Harbors are generally located in protected areas at the entrance of estuaries. They are then exposed to siltation of suspended sediment from the river waters. In order to help navigation inside the estuary mouth and harbor, dredging operations are generally carried out to create a navigation channel and to maintain the depth along the docks. These operations are extremely expensive and the modification of the

depth inside the channel and along the banks considerably modifies the sediment dynamics inside the estuary. Dredging operations may even be counterproductive and favor siltation [81, 86, 110].

Therefore, a major issue of estuarine dynamics is to understand the fate of the sediment load. Under the competing effects of turbulent suspension and gravitational settling, strong variations of Suspended Sediment Concentration (SSC) are observed in both time (throughout the tidal cycle), and space (along the estuary).

1.3.1 Suspended sediment in estuaries

Sediments in suspension are of different natures, sources, and characteristic features. Particles in suspension are generally differentiated from dissolved material by a threshold size of 0.45 μm. Within the category of suspended sediment, fine sediments can be distinguished from coarse sediments by their size of less than 63 μm. In more detail, sediments have been classified by Wentworth in 1922 from coarsest : boulder (gravel) to finest : clay [133] (Tab. 1.1).

Table 1.1: The distribution of particle size based on Wentworth classification [133].

Sediment Class	**Composition**	**Dimension (mm)**	**Transport**
Gravel	Boulder	> 256	Rolling
	Cobble	256 - 64	
	Pebbled	64 - 4	
	Granule	4 - 2	
Sand	Very coarse sand	2 - 1	Saltation
	Coarse sand	1 - 0.5	
	Medium sand	0.5 - 0.25	
	Fine sand	0.25 - 0.125	
	Very fine sand	0.125 - 0.063	
Clay	Silt	0.063 - 0.004	Suspension
	Clay	< 0.004	

The diameter is not the only parameter which characterizes particles in suspension: their density ρ or excess density, and also their cohesion can be used. Fine sediment, i.e. $< 63\mu m$, are generally considered "cohesive", while coarser sediment are named "non-cohesive". Cohesive sediments are composed of a high fraction of clay minerals and can easily bind together. These sediments are also characterized by a low settling velocity: they are easily carried by the river flow and will settle down in calm areas such as harbors. In case of contamination, cohesive sediments will be good carriers of organic and mineral contaminants.

1.3.1.1 Transport in suspension

Particles in movement can be transported in different ways : rolling, salting, or in suspension. The means of transportation depends on the flow (i.e. velocity) and on the type of sediment (i.e. nature of sediment, dimensions and settling velocity). In general, fine sediment will be transported in suspension while coarser and denser sediment will be transporting by saltation (e.g. sand) or by rolling (e.g. gravel) (Tab. 1.1). In this section, as we consider only fine sediment, transport will focus only on the suspended load transport mechanism. Bed load transport mechanisms such as saltation and rolling will not be presented.

Transport in suspension occurs when the flow velocity and turbulence are sufficient to overcome the gravitational sinking of the particles. The turbulence induces a vertical mixing of the sediment inside the water column. When transported in suspension, the sediment velocity is comparable to the flow velocity. The quantity of sediment transported is expressed in mass concentration (i.e. in gram per liter), named Suspended Sediment Concentration (SSC). The

distribution of particles in suspension is not, or rarely, homogeneous inside the water column. The SSC is higher on the bottom of the water column because the river bed is the major sediment supply and the weight of particles tends to make them sink. The finest particles will be able to reach the surface water. Strong turbulence inside the water column will induce more homogeneity.

1.3.1.2 Erosion

In a river, the surface water flows faster than the bottom water due to bottom friction, which results in a gradient of velocity and shear stress on the bed. When the bed-shear stress is sufficient to overcome the sediment weight and the bed friction, the sediment can be suspended. The critical value of the bed shear velocity to suspend sediment depends on the density of the sediment. As we consider fine sediment, i.e. predominantly made up of cohesive particles, three types of erosion can be distinguished : entrainment of the fluid mud layer recently deposited, detachment of aggregates of mud under consolidation, and pull-out of blocks of consolidated mud. The critical bed shear stress for pulling out consolidated mud blocks is greater than the one required for entrainment of fluid mud.

1.3.1.3 Deposition processes

When the flow velocity decreases, as well as the turbulence, suspended particles settle down under the effect of gravity and accumulate at the bottom of the water column. A fluid mud layer is created at the bottom. If no erosion process is interacting with this mud layer, it will consolidate by gravity effects. One of the uppermost parameters for suspended particle dynamics is the settling velocity. It is defined as the velocity of a particle to fall in quiescent water. It is difficult to estimate, as it depends on the dimensions and density of particles which can be affected by flocculation processes. Larger and/or denser particles will have a higher settling velocity. Small and light particles will easily be kept in suspension. A size sorting can be naturally done in estuaries, with different layers of deposited sediment from densest (falling fast) to lightest (falling slow). As the flow carries the sediments in estuaries, the sorting can also be done on the longitudinal way.

1.3.2 Variation of the SSC

In estuaries, suspended sediment concentration varies under different time scales, from hours (tidal cycle) to months or even years (seasonal variations). The tidal time scale ranges from 12 hours (ebb/flood variations) to 15 days (fortnightly cycle), while the seasonal variations time scale varies from days (flood event) to months (wet/dry season). These variations in forcing will generate variations in flow velocity, shear stress and supply in SPM. It will affect erosion and deposition processes and thus the SSC inside the water column.

1.3.2.1 Tidal variation

Throughout the tidal cycle, water masses circulation changes in intensity and orientation. During slack times, currents reverse and velocity is very low, leading to deposition of suspended sediment on the river bed. It results in a vertical movement of particles from the water column to the river bed. During the maximum velocity period sediments are re-suspended by shear stress on the bed and then advected along the estuary by the flow. Throughout the tidal cycle, sediments will then move back and forth. On the flood tide, sediment will be re-suspended and advected landward, while during the ebb tide, sediments are resuspended and advected seaward.

1.3.2.2 Fortnightly cycle

The back and forth movement of sediments throughout the tidal cycle is modulated by the varying tidal amplitude (i.e. fortnightly cycle). With the decreasing tidal range, the magnitude of current velocities decreases and so does the bottom shear and the erosion capacity. In addition, the duration of slack increases, as well as the sedimentation capacity. During neap tide, the velocities are strongly reduced. Gravitational sinking and consolidation processes prevail. Neap tides are characterized by low SSC. On the other hand, when the tidal amplitude increases, current velocities and bottom shear increase and slack time decreases, resulting in a strong erosion and reduced sedimentation. Spring tides are then associated with a high SSC in the estuaries. In case of huge tidal amplitude, ebbing currents can be sufficient to flow sediment out of the estuary. Hence, every two weeks, there is a switch between consolidation and expulsion phases.

1.3.2.3 Seasonal variations

River waters are generally rich in suspended sediment and they are the main supply of SPM for estuaries. However, this supply is not constant throughout the year. River flow suffers variations due to varying climatic conditions (e.g. rainfall, snow). In the Northern hemisphere, summer and fall are generally named the "dry season" due to sunny weather conditions and evaporation, while winter and spring are considered as the "wet season". The wet season is characterized by high river flow and strong drainage of the watershed, thus fluvial waters are generally richer in suspended sediment. On the contrary, the dry season is associated with low river flow and low SSC. Yet, even during the dry season freshets can occur and lead to a rapid (a few hours) and strong (by an order of magnitude over) increase in river flow and SSC. Both river discharge and SSC are not necessarily increasing together. Depending on the location of the sediment catchment, a peak of SSC can be reached before or after the river flow peak, leading to hysteresis cycles between discharge and SSC. It also depends on the antecedent conditions. The first freshets of the wet season carry more SPM than the last one, because the sediment catchment has been drained and may have been emptied by previous freshets.

River discharge also interacts with the tidal wave propagation. During high discharge, the tidal wave propagation in the estuary is shorter and flood current velocity is smaller. Landward advection of suspended sediment is thus more limited. However, ebbing currents are reinforced and suspended sediment are easily expelled from the estuary. On the other hand, during low river discharge, tidal wave propagation in the estuary is longer and suspended sediment are advected further upward.

The intensity of the river flow also affects the salinity intrusion and the vertical stratification inside the estuary. Trapping mechanisms associated with the salinity structure (presented in the previous subsection) will then be modulated by variations of the riverine forcing. The location of the trapping area and even the ability of trapping fluctuates with the river flow.

These variations of the hydrological conditions can cumulate with the tidal variation, generating extreme forcing conditions, such as a freshets during spring tide conditions.

1.3.2.4 Human interventions

The natural movements of suspended sediment presented above do not take into account human activities in the watershed and inside the estuary. In the watershed, sediment supply is deeply altered by dam building, sand extraction in rivers, and the changes in, and intensifications of agriculture. It may take a long time for the consequences of such interventions to be revealed. Inside the estuary, navigation is essential for the correct functioning of the harbor. To ease the docking and navigation, the estuary is generally dredged and embankments are constructed. Natural sediment transport is biased by a narrower and deeper estuary. Such changes can even

lead to an increase in the deposition rate of fine sediments [26, 68, 123] and an increased residence time of SPM and contaminants.

1.3.2.5 Influence of the salt-wedge displacement

In addition to the above mentioned mechanisms, the displacement of the salt-wedge may influence the sediment transport, in particular in time-dependent salt-wedge estuaries where the salt-wedge structure may be reset at the end of each tidal cycle. Li et al. investigated how the advection of the salt-wedge affects intratidal sediment resuspension and associated residual transport, based on observations in the Changjiang estuary [76]. The steep stratification due to the salt-wedge entrance during the flood tide restricts the turbulence and thus the resuspended sediments are contained below pycnocline. During the ebb, shear velocities results in strong turbulent mixing and the suspended sediments are elevated up to the surface. This study revealed a substantial landward tidal pumping of sediments near the bed, with a landward sediment flux in the bottom layer and a seaward flux in the upper layer.

In 1992, it has been shown by Kostaschuk et al. [69] that SSC is influenced by the actions of tide on the river current and by the passage of water over the salt-wedge, resulting in a seaward decrease in concentration. The rate of seaward decrease in concentration has shown a slight tendency to be greater at low tide than at high tide. This seaward decline is thought to result from four factors: cut-off exchanges of sediment between bed and the water column by the salt-wedge, reduced turbulence in the upper layer, flocculation of fine sediment, and dilution of sediment-water mixture.

Kostaschuk and Luternauer have shown that the salt-wedge advection also affects the nature of particles to be resuspended and deposited, based on on data collected in the Fraser river [70]. As the flow becomes stratified the percentage of sand (>0.062 mm) in suspension dramatically decline. It has been attributed to the loss of contact of the seaward flow with the river bed and turbulence damping in the surface layer. It results in a decrease of sediment size and SSC in the upper layer, with transport restricted to particles less than 0.062 mm during the flood tide. As the tide falls, the salt-wedge is flushed and shear velocity increases, generating entrainment of bed material. The SSC increases, as well as the percentage of sand and the mean grain size. The SSC follows the shear velocity pattern.

1.3.3 Estuarine Turbidity Maxima

The Glangeaud's study in 1938 [52] was one of the first to introduce the notion of Estuary Turbidity Maximum (ETM) and try to explain its mechanisms. Based on observations in the Gironde estuary, the author noticed that in the part of the estuary subjected to tidal forcing, the sediment discharge was 10 to 75 times bigger than the sediment discharge upstream in the river. It was revealed that the ETM can be split with areas of turbidity minimum in the middle. This phenomenon of simultaneous multiple ETMs has been observed in others estuaries, such as the Hudson [96] and the Columbia [62]. A recent study of Burchard et al. [15] extensively presents the different mechanisms involved in the sediment trapping inside estuaries, based on observational and modeling studies. A particular attention is paid here below on the two main mechanisms involved in ETM generation in salt-wedge estuaries.

1.3.3.1 Definition

The estuarine turbidity maximum is generally defined as an area of high concentration of suspended sediment or an area of convergence of suspended sediment transport. ETM is a common feature of estuaries. Those areas of convergence are at the intersection of opposite sediment fluxes, resulting in low to null velocity and particles falling down. Sediment concentrations are higher in the convergence zone than upstream in the river or downstream in the estuary. Similarly to SSC variations, ETMs vary in concentration and location inside the estuary. An ETM moves

with the tidal variation and the limit of tidal and saline entrance inside the estuary. But it also varies depending on the river discharge. During the dry season, the ETM tends to move upward and it moves downward during high river discharge periods. When a flood event is combined with a spring tide, ebbing velocity may be strong enough to expel the ETM from the estuary.

1.3.3.2 ETM generation

ETMs and their generation mechanisms have been in the spotlight of estuarine studies during the past decades [15, 63, 119]. These studies have revealed two major physical processes involved in the formation of ETM. First, the estuarine circulation, due to longitudinal salinity gradient, combined with the river run-off, drive a convergent SPM transport at the salt intrusion limit, that can lead to the formation of an ETM [39]. Second, the asymmetry between the ebb and flood duration and peak velocities can also contribute to the formation of an ETM in the freshwater zone [5].

In their 1955 study [90] on the ETMs occurring at the salt intrusion limit in the Elbe river, Postma and Kalle were the first to hypothesize that *"The peculiar water movement in such tidal estuaries form a sort of 'trap for suspended matter' which catches the turbid water from the river water in the mixing zones and makes them revolve continuously in a vertical circulation while the water itself flows to the sea, without hindrance."* They also noticed that a two-layer flow circulation exists in the estuary, with fresh water flowing seaward over salty marine water flowing landward. The first study to investigate in depth the estuarine circulation as a mechanism responsible for ETM formation is the one by Festa and Hansen in 1978 [39], based on a 2D numerical model. They concluded that the magnitude and location of the turbidity maximum depend mostly on the strength of the estuarine circulation and on the particle size of the sediment. In essence, the estuarine circulation drives a net landward transport of suspended matter, until the salt intrusion limit, i.e. where the baroclinic pressure gradient ceases. Upstream the river flow generates a net seaward transport of SPM, until it reaches the salt intrusion limit, leading to the convergence of SPM transport (Fig. 1.14).

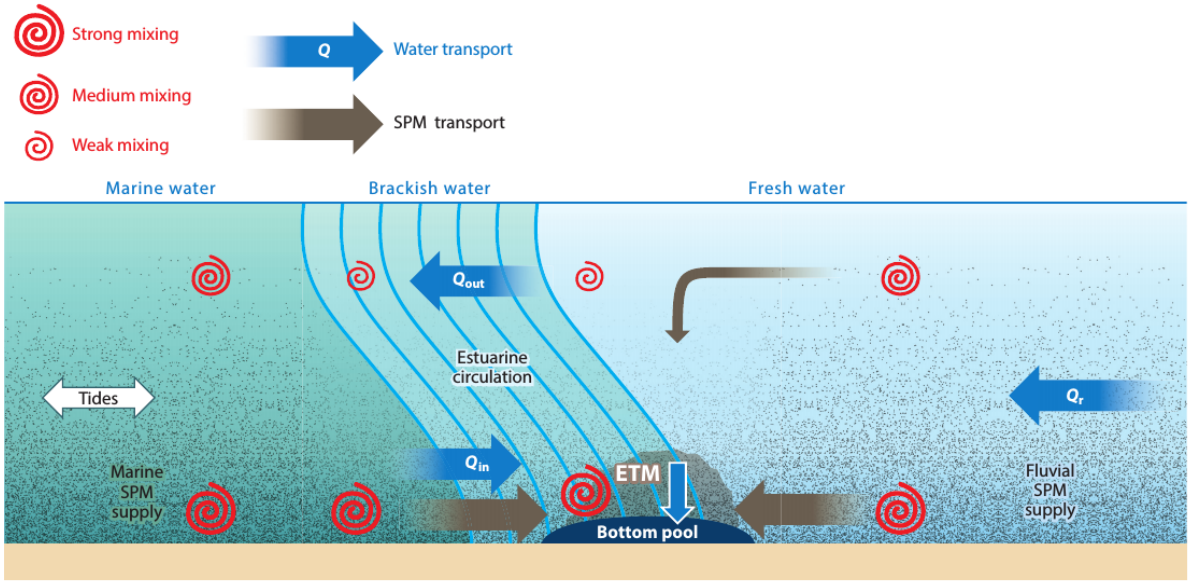

Figure 1.14: Schematic description of the major mechanisms responsible for ETM formation at the salt intrusion limit. Extracted from Burchard et al, 2018 [15]

The study of Allen et al. in 1980 [5] demonstrated that tidal processes alone could be the origin of SPM trapping. This phenomenon is particularly marked in macrotidal estuaries such as the Gironde and Aulne estuaries. Tidal pumping mechanism comes from the distortion of

the tidal wave during its propagation inside an estuary (cf. paragraph 1.2.4.2). This asymmetry contributes to the trapping of sediment at the nodal point of tidal influence by (1) a greater bottom erosion during flood and a large landward advection, (2) high sedimentation rate during longer flood slack (Fig. 1.13). The ebbing currents are not able to erode as many sediments as flood currents, leading to a net transport of sediment until the limit of tidal influence. This nodal point is generally located farther upstream in the estuary than the limit of saline intrusion, i.e. in the fresh water zone. Similarly to the saline intrusion limit, the limit of tidal influence location is subjected to riverine forcing. For example, an increase in river discharge makes it migrate seaward.

The two mechanisms are not incompatible, they can occur in the same estuary, depending on the forcing conditions. It has been shown that an estuary can go from being dominated by one process to being dominated by the other. On neap tides, estuaries are generally more stratified and the estuarine circulation prevails. In this configuration, the stratification may be the major mechanism in the ETM generation, resulting in an ETM located at the salinity front. On spring tides, the tidal asymmetry is more pronounced and the tidal pumping may become the major mechanism in the ETM formation, leading to an ETM at the limit of tidal influence. The river discharge can have a similar influence. During high river discharge, the stratification is strengthened and the tidal propagation is limited. The estuarine circulation is predominant and the ETM is located near to the mouth of the estuary, while during low river discharge, the tidal influence increases and the tidal pumping mechanism is reinforced (Fig. 1.15).

Many other mechanisms can be involved in ETM generation : tidal straining [62], stratification-induced turbulence damping [45], energetic wave conditions [54], topogaphy [62], or lateral trapping [49].

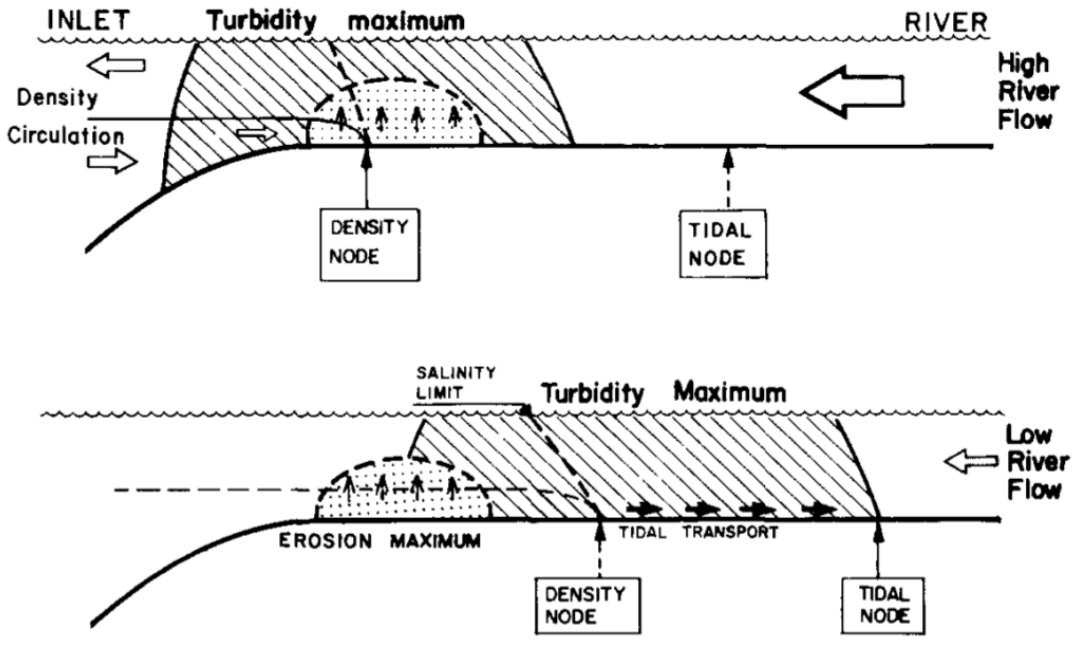

Figure 1.15: Schematic illustration of the varying mechanisms involved in ETM formation due to seasonal forcing changes. Extracted from Allen et al, 1990 [5]

For salt-wedge estuaries, the predominance of one of these mechanisms or the combined action of the two will strongly depends on the major forcing driving the estuarine dynamics. It can be expected the tidal asymmetry to be the major mechanism in macrotidal estuaries, while the convergence partly due to density circulation to be the major mechanism in microtidal estuary. In their numerical study [13], Burchard & Baumert focused on tidally energetic salt-

wedge estuaries and demonstrated that tidal asymmetry is of greater importance in the ETM formation than gravitational circulation, in an idealized macrotidal salt-wedge estuary. The gravitational circulation only plays a part in sustaining and stabilizing the ETM mass. Those results have been confirmed by observations in the Charente estuary (macrotidal salt-wedge estuary), where the tidal asymmetry is mostly responsible for the formation of the turbidity maximum, while the density gradient has an influence on its shape and its stratification [116]. In salt-wedge estuaries subjected to reduced tidal forcing, such as the Rotterdam waterway, the near-bed convergence as well as the abrupt change in turbulent mixing have been shown to be the mechanisms responsible for ETM entrapment [28].

Chapter 2

The lower Adour estuary

This study will focus on the Adour river estuary, located on the South-West coast of France. The Adour estuary has a very specific morphology and it is subjected to energetic forcing, which makes its hydrodynamics very complex. Previous hydrodynamic and sediment transport studies have focused on the dynamics of the turbid plume and on its area of influence in ocean waters [9, 23, 32, 65, 88]. In this chapter, an overview of the state of knowledge about the Adour estuary will be presented, with a peculiar attention to hydrodynamics and sediment transport.

2.1 Presentation of the study site

2.1.1 History of the Adour estuary

The estuary mouth used to be located at Cap Breton in front of the submarine canyon. Throughout the centuries, the Adour estuary mouth moved from Vieux-Boucau (North) to Pointe Saint Martin (South), passing by Cap Breton and Bayonne. In 1164, a strong freshet of the Nive river moved the mouth to Boucau, in front of Bayonne city. After few years, it moved back to Cap Breton and then to Vieux Boucau. In 1562, King Charles IX decided to fix the mouth of the estuary in front of Bayonne city, in order to relaunch the maritime trade of this declining city. After a strong freshets of the Nive river, engineers succeeded in diking the downstream part of the estuary in 1578. The former riverbed silted up, except what is now known as the Hossegor's lake. However, the estuary mouth was still unstable. A sand bar always developed across the estuary mouth. In 1810, Napoleon decided to reduce the entrance of the estuary to 150 m, in the aim of protecting the channel from sand accumulation due to the beach drift, and in order to focus the ebb energy [30]. However, sand continued to be accumulated in the channel. Therefore, dikes were extended between 1811 and 1816, and in 1896 the estuary begun to be dredged. Finally, in 1963, a 700-m-long jetty was constructed to avoid siltation inside the estuary entrance and to ease the navigation during swell conditions.

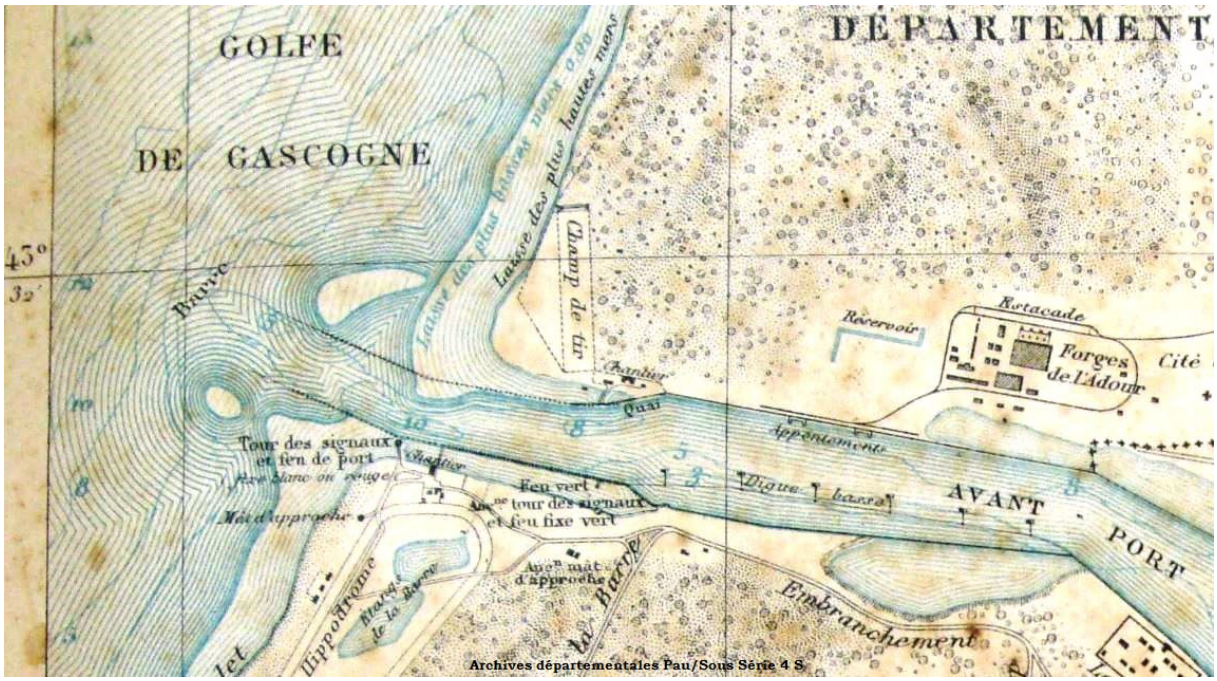

Figure 2.1: Former map of the Adour estuary entrance.

2.1.2 The Adour estuary and its watershed

The Adour river originates in the Pyrenées mountains at an altitude of 2200 m and flows for about 300 km before pouring into the Bay of Biscay (SW of France). The catchment area is of about 17000 km^2. The Adour runs through many agricultural areas, but also through cities and industrial areas. The Adour river has several tributaries, such as the Nive, the Gaves, the Bidouze among others. Some of them are considered torrential. The location of the Adour, between the Atlantic Ocean and the Pyrénées, leads to heavy rainfalls and freshets. The annual average rainfall is about 1400 mm/year [41]. In addition, the proximity with the Pyrénées generates freshets due to snow-melts events. Thus, the drainage capacity of the left bank (southern watershed)is a lot higher than that of the right bank.

The lower Adour estuary is characterized by its very specific morphology, which is closer to a navigation channel than a usual large estuary mouth (Fig. 2.2). The lower estuary is a fully engineered narrow channel, between 150 m and 400 m in width. The estuary mouth has been reduced by embankments to easily expel water and sediment from the estuary during the ebb. In order to facilitate navigation, the main channel is maintained by dredging to about 10 m depth along the dock and in the channel of the Bayonne harbor. A 700-meter-long jetty was constructed to protect the Bayonne harbor from swell conditions.

2.2 Majors forcing

Estuaries are generally subjected to a lot of external forcing, such as river flow, tides, wind, and waves, among others. Due to its specific location and thanks to man-engineered barriers, the Adour estuary is mostly subjected to two driving forces : river flow and tides. Wind and waves can be very energetic in this area and can have a huge impact on the shore erosion and plume dispersion, but the estuary is well protected by dikes and jetties, and is not too affected by such forcing.

Figure 2.2: Aerial picture of the Adour estuary mouth and its coastal area.

2.2.1 Riverine forcing

The river flow of the Adour river is hugely influenced by the adjacent Pyrénées mountains. One first obvious effect is the snowmelt events occurring during spring, which increase the river flow significantly. Another effect is the strong rainfalls (i.e. 1400 mm/years) caused by the blocking effect of the mountains on the clouds coming from the Atlantic Ocean. Water discharge data is available on the Banque Hydro website (http://www.hydro.eaufrance.fr/) for the Adour river and its tributaries. The annual average river discharge is about 300 $m^3.s^{-1}$, and can go up to more than 3000 $m^3.s^{-1}$, during extreme flood events (e.g. January 2014).

The river discharge varies greatly according to the season (Fig. 2.3). During summer (i.e. dry season), the river discharge is very low around 100 $m^3.s^{-1}$. August and September are the driest months of the year (Fig. 2.4). During winter and spring (i.e. wet season), the mean river discharge is stronger due to a lot of freshets, with river flow peaks over 1000 $m^3.s^{-1}$ and going up to 3000 $m^3.s^{-1}$ (Fig. 2.3). The river flow changes are abrupt, i.e. the river can go from 100 $m^3.s^{-1}$ to 800 $m^3.s^{-1}$ in few hours. February and April are the wettest months of the year. April is the month with the maximum discharge rate for the Gaves rivers, while February is the month with the bigger water amount for the rest of the tributaries. In February, the rainfall is strong in the Adour river watershed, which creates a huge fresh water input, while in April the snow melting is responsible for the strong fresh water input. Both Gave de Pau and Gave d'Oloron are the tributaries with the biggest influence on the Adour water discharge (respective mean contribution of 28.4% and 30.9%), which results in the left bank of the river having a higher capacity of drainage than the right bank. A strong variability of the river run off between years is also noticeable over the period 1969-2017, from one time to three times more important. The annual river discharge has had a slight tendency to decrease over the past 40 years.

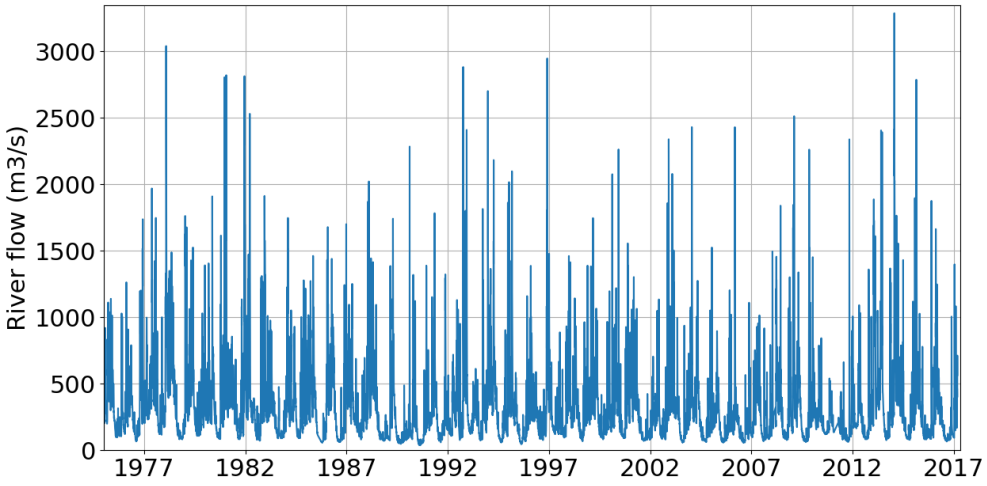

Figure 2.3: Variations of Adour river flow between 1975 and 2017, based on data from the Banque Hydro.

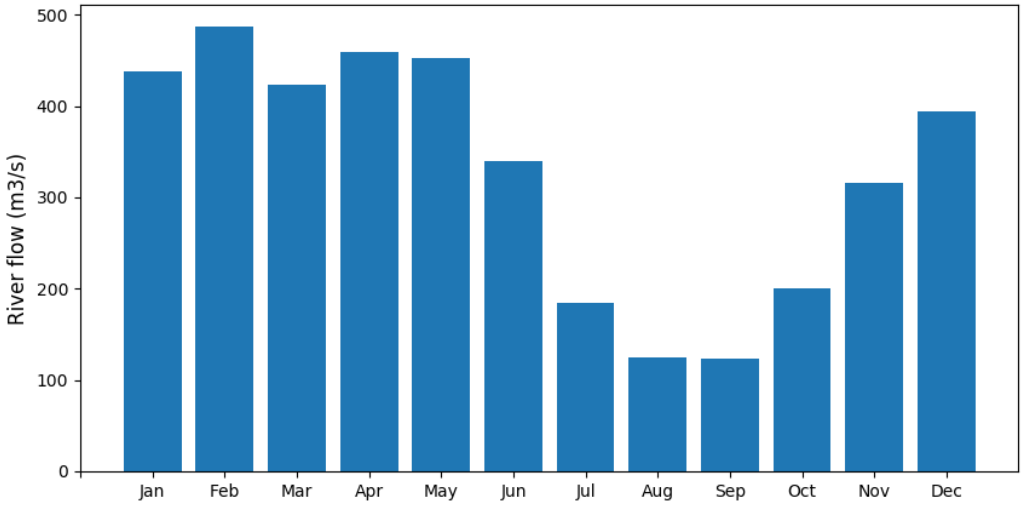

Figure 2.4: Monthly averaged water discharge of the Adour river, based on data collected between 1969 and 2017 (http://www.hydro.eaufrance.fr/).

2.2.2 Tidal forcing

The Adour estuary is flowing out into the Atlantic Ocean. The tidal wave reaching the French coast comes from the Atlantic ocean. This wave propagates from South to North. The tidal amplitude diminishes progressively from North to South, as the continental shelf extension decreases [22]. Based on data collected at the Convergent tidal gauge (https://data.shom.fr/donnees), the Adour estuary can be considered to be exposed to a semi-diurnal mesotidal regime, with a tidal range varying between 1 m to 4.5 m. The mean value of the sea level is about 2.5 m above chart datum. Based on data available on the Banque Hydro (http://www.hydro.eaufrance.fr/), the limit of intrusion of marine waters into the estuary is supposed to be no further than Urt village, which is located about 22 km from the estuary entrance. However, a study of the water elevation at different stations along the Adour river has shown that the limit of the tidal wave propagation

is Pontonx-sur-l'Adour, located about 70 km from the estuary mouth. Offshore tidal currents are relatively weak (i.e. less than 0.2 $m.s^{-1}$). They increase as they get closer to the shore, and can reach maximum velocities of 0.8 $m.s^{-1}$ during flood tide and 1.5 $m.s^{-1}$ during ebb tide [22].

Tidal forcing is not limited to a wave propagation inside the estuary, but it also induces a variation in salinity. Salinity in the Bay of Biscay varies throughout the year. In front of the Adour estuary, the salinity ranges from 34.5 to 35.5 PSU (Fig 2.5).

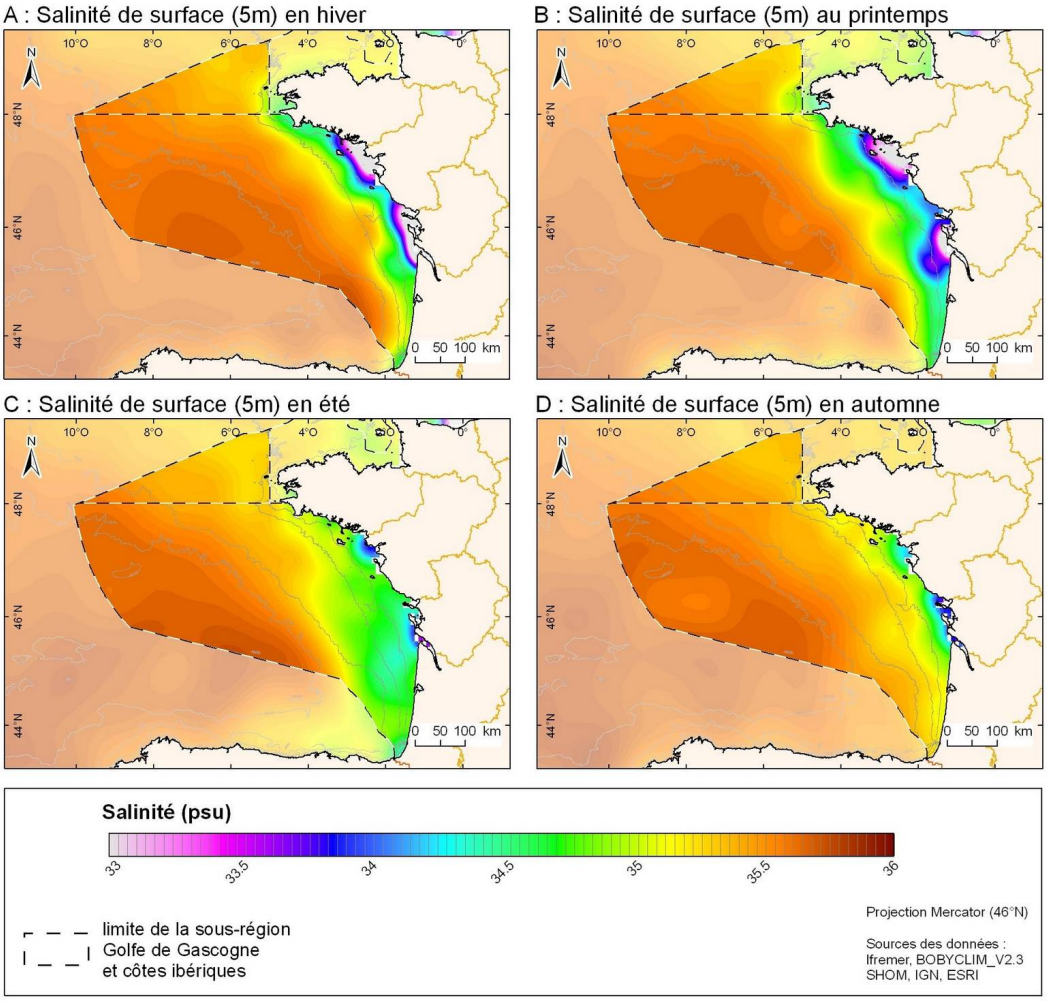

Figure 2.5: Salinity of surface waters in the Bay of Biscay during A) winter, B) spring, C) summer, and D) fall.

2.2.3 Wind and Waves

Even if Anglet is subjected to Northwest winds of 12.3 km/h in mean (Fig. 2.6), it suffers from a strong annual variability of wind orientation and strength [17]. During summer and spring, West to Northwest winds are mostly prevalent, whereas in fall and winter, strong Southwest winds and weak South winds are prevalent ([23]). According to the data provided by Météo France for the Biarritz airport station, winter is characterized by strong gusts of wind. From November to February, strong gusts of wind are registered more than 6 days per month. On the other hand, during summer (from June to Sept) less than 3 days per month are registered as having strong gusts of wind.

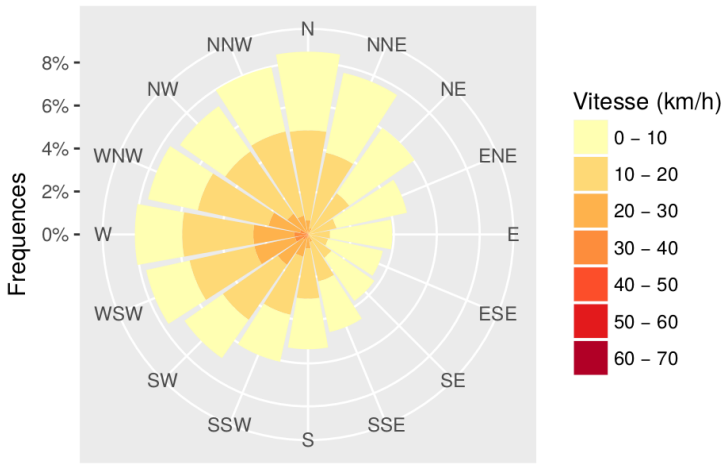

Figure 2.6: Wind rose for Anglet city, indicating strength and orientation of the winds. Based on data collected between 1949 and 2014. Extracted from Callens, 2017 [17]

Regarding waves forcing, Anglet is characterized by West-Northwest waves with significant wave height of 1.6 m (Fig. 2.7) and peak period of 10s [37]. However, it has been demonstrated that both jetties located at the estuary entrance protect efficiently the port against incoming swell and sea waves, with a reduction factor of 85 % compared to the offshore wave energy [6]. The weak remaining wave energy is then rapidly damped in the entrance of the estuary. Therefore, even if wind and waves have a significant influence on the coastal area, in particular on the plume dynamics, they have a reduced impact on the estuarine dynamics, and hence, they will not be taken into account in our numerical study.

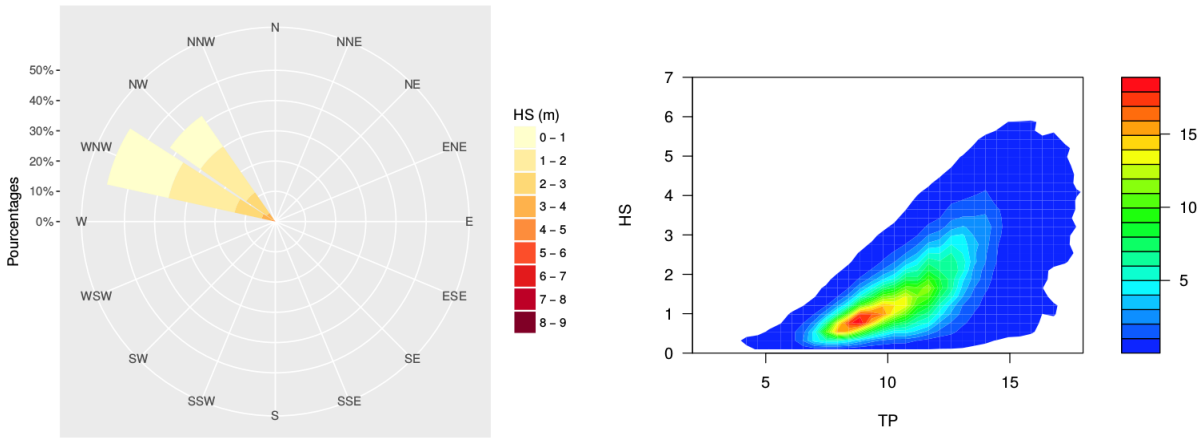

Figure 2.7: (a) Waves rose for Anglet city, indicating significant wave height and orientation. (b) Graphic representing the significant wave height in function of the peak period. Colors means the percentage of waves occurrence. Based on data collected between 1949 and 2014. Extracted from Callens, 2017 [17]

2.3 Water masses and salinity circulation

This section will briefly present the conclusions of the analysis of two former data sets. Those data sets were collected in 2008 and between 2011 and 2014, respectively. This analysis helped us to gain a better understanding of the physical processes involved in the estuarine dynamics. It was also used to comfort/question the design of our own measurement campaign.

2.3.1 Water masses circulation

During the summer of 2008, the Casagec engineering office carried out a field campaign to study the Adour river mouth hydrodynamics. An ADCP profiler was fixed on ship side to measure current velocity. The velocity was measured along 11 sections in the downstream estuary. These measurements were carried out over 6 days with specific tide coefficients : 30, 65 and 100, during summer time (i.e. the lowest water discharge period). The river flow during this period was of about 100 $m^3.s^{-1}$. This first set of data enabled us to analyze the tidal influence on the estuarine circulation.

In the Adour estuary, during the dry season, the maximum velocity is reached one hour before High Water (HW) with a value of more than 1 $m.s^{-1}$ and one hour before Low Water (LW) with a value of up to 2 $m.s^{-1}$. Minimum velocity is reached between one and two hours after HW and LW. The tidal wave cannot be fully considered as progressive. The higher velocity values are obtained in the narrower part of the estuary, such as the estuary mouth (width $<$ 150 m) for instance. It has been noticed that the bigger the tidal range, the faster the tidal currents were. At the beginning of the flood tide, marine waters enter the estuary at the bottom while the riverine waters still flow out of the estuary at the surface, resulting in a two-layer flow. At mid-flood tide, the riverine waters are "blocked" inside the estuary by the entering marine waters. The flood slack are shorter than ebb slack. On the ebb tide, the currents reverse and both marine and riverine waters flows out of the estuary. The ebbing velocity is very sheared while the flooding velocity profile is more logarithmic. Centrifugal forces affect the circulation of the bends.

2.3.2 Salinity circulation

Series of measurements carried out by the Casagec engineering office between 2011 and 2014 in the context of the "Observatoire de l'estuaire de l'Adour" project have shown a high level of stratification inside the estuary. Measurements of salinity, temperature, and water samples were carried out in the last 10 km of the river, at five stations, once a month during ebb tide. This second set of data gives us an insight into the riverine forcing influence on the saline circulation.

Looking at this data, it seems that the salt-wedge is not able to reach the upstream station (10 km from the entrance), when the river flow is above 300 $m^3.s^{-1}$. On the other hand, when the river flow is below 300 $m^3.s^{-1}$, we noticed stratification at the upstream station. When it comes to the two stations downstream, the exact opposite is noticeable: when the river flow is over 300 $m^3.s^{-1}$, stratification happens, and when the river discharge is below 300 $m^3.s^{-1}$, the water column is fully homogeneous and salty. These fully homogeneous and salty profiles also bring out the pulsed plume characteristic of the Adour river, already demonstrated by Dailloux [23].

This data also revealed a strong mixing area located in a sill downstream from the Grenet bridge, where the salinity profiles were never stratified, except during small tidal ranges.

2.4 SPM characteristics, SPM transport and exchange with coastal area

2.4.1 SPM characteristics

The SHOM database gives us access to maps of the sediment nature of the French coast. Following figure 2.8, the Adour estuary bottom is composed of mud in the upper part, and mostly composed sands and gravel in the lower part. This data appears coherent with the partial information given by the BPB CCI regarding the sediment dredged inside the Adour estuary. From data collecting in Spring 2017, sediments collected along the docks are mostly fine sediment easily suspended (more than 65% with D$<$200 μm), while in the navigation channel

sediments are mainly composed of coarse sand (more than 65% with D>200 μm). Coarse sand is likely to be transported by saltation or rolling.

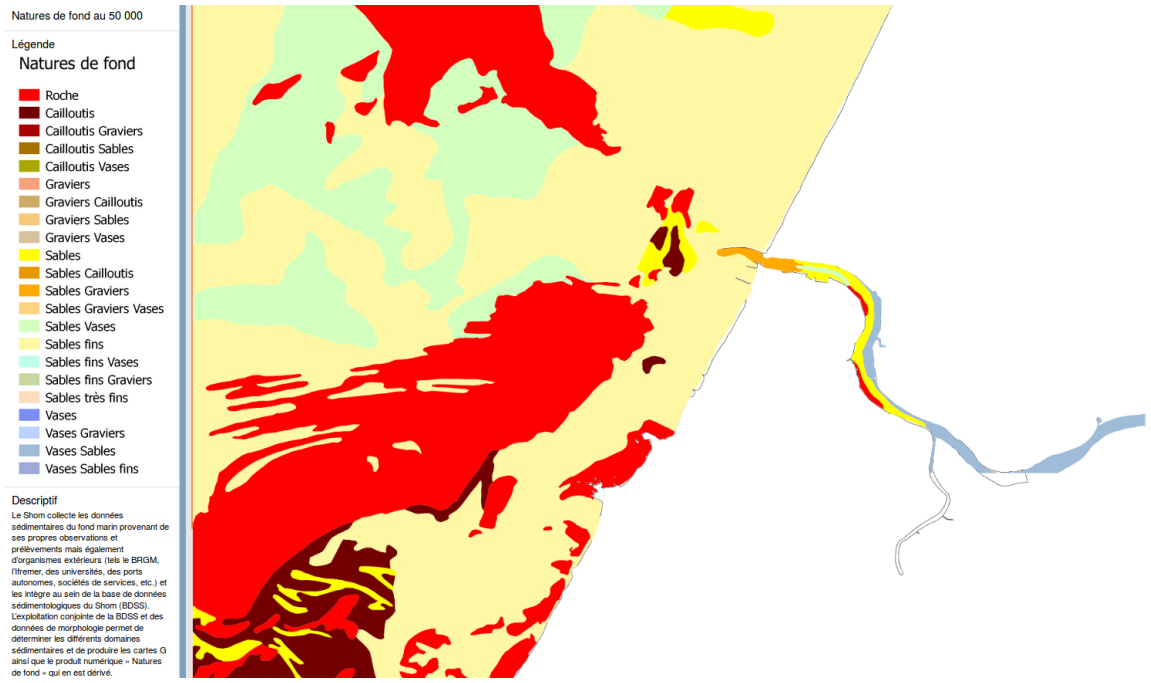

Figure 2.8: Nature of sediments along the Basque country coast and inside the Adour estuary. Extracted from the SHOM data base (https://data.shom.fr/donnees)

2.4.2 SPM dynamics inside the estuary

Different sets of data have been analyzed to map out the SPM dynamics inside the estuary. The first consists of SSC mesured at Urt station (about 20 km from the mouth) once a month over the period 2006-2015, and is available via the Agence de l'Eau Adour-Garonne (AGWA). However, it must be noted that this is low-frequency data and that the water samples were never collected during high river flow (probably for logistics purposes). The annual mean concentration is about 40 $mg.l^{-1}$. Maximums of concentration are reached during December/January and April. Minimums of concentration are reached during March and summer period. It appears that a huge quantity of suspended matter is washed away during winter (i.e. heavy rainfall period). In March, the quantity of available particles to be drained appears to be greatly reduced, even if the river discharge is important. In April (i.e. the beginning of the snow melting season), a new quantity of particles is available to be flushed by the fresh water.

The second data set was collected by the Casagec engineering office between 2011 and 2014 in the context of the "Observatoire de l'estuaire de l'Adour" project. One turbidity profile and two water samples were collected once a month, on the ebb tide, for 3 years, at each of the five stations located in the last 10 km of the estuary. In addition to this, a multi-parameter probe, named SMATCH, was fixed to the floating RO-RO terminal (about 6 km from the estuary mouth), about 1 m under the water surface. The probe collected the following data : temperature, salinity, turbidity and dissolved oxygen, over a period of 2 years (2012 - 2014). Unfortunately, the probe suffered some damage during this period (due to vandalism, ship collision, etc..), therefore the collection was not continuous. This data revealed a SSC varying from 10 $mg.l^{-1}$ to 350 $mg.l^{-1}$. These values are very low compared to other French estuaries where the SSC in the turbidity maximum zone can reach several grams per liter. Higher values of the river flow are generally correlated to higher values of SSC. But SSC does not vary linearly with the river flow. SSC peaks are larger when the freshets follow a dry period. A huge river discharge (e.g.

3000 $m^3.s^{-1}$ in January 2014) after a long period of rainfall will not lead to a large SSC peak (100 $mg.l^{-1}$ in January 2014). This can be explained by an empty sediment stock after a period of strong drainage. Hysteresis loops were made based on the SMATCH probe data (Fig. 2.9), showing a counter-clockwise behavior. It means that the peak of SSC lags behind the peak of river flow peak by several hours to days. Different explanations can be given to such behavior : (i) a distant catchment of SPM, (ii) some disturbance on the way which could slow down the dispersion of particles but not the water discharge, and (iii) the water discharge of one tributary, richer in SPM, is delayed from the others. The river flow is not the only forcing influencing the SSC in the last reach of the estuary, the bottom shear associated to tidal currents also affects the SSC. On figure 2.9, we notice several peaks of SSC per day, over a period of around 12 hours. We can hypothesize that the ebbing currents are strong enough to re-suspend sediment from the bed, during the freshets.

a) b)

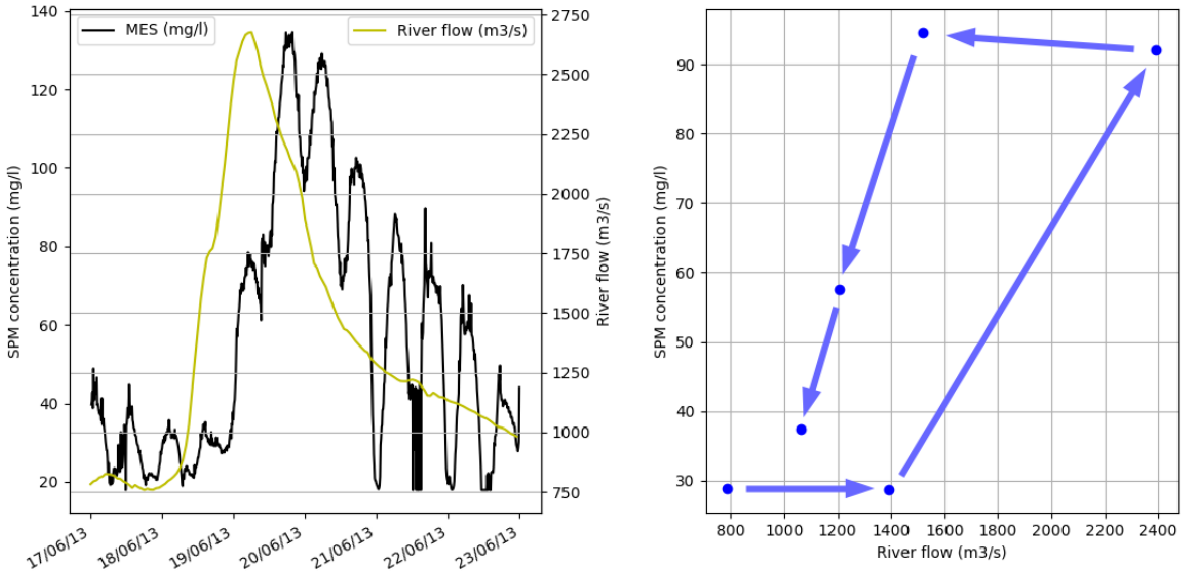

Figure 2.9: a) SPM concentration ($mg.l^{-1}$) in black, and river flow ($m^3.s^{-1}$) in yellow, along the freshet period, b) SPM concentration ($mg.l^{-1}$) in function of river flow ($m^3.s^{-1}$), on June, the 19th 2013.

The third set of data comes from the ACABIE team (IPREM laboratory), and was collected during the MAPEA project. A CTD was fixed to a floating pontoon, 1m under the surface, about 5km from the estuary mouth, continuously registering four parameters: temperature, conductivity, turbidity and pH. It stayed in place for about 3 months (between December, 21st 2006 and March, 17th 2007). The high frequency of this probe (data every 15 min) over about 80 days, allows us to highlight different phenomena, mostly consistent with those observed with the SMATCH probe. Hysteresis loops obtained with this set of data confirm the counter-clockwise behavior. A detailed study of the time series underlines some specificities of the SPM concentration evolution throughout the tide cycle (Fig. 2.10). The SPM concentration reaches a maximum after mid-ebb tide. This time matches a time of high velocity value. The out-flowing marine and continental waters create shear stress on the bed; the sediment are then re-suspended and expelled into the ocean. The larger the river flow, the sooner the peak of SSC occurs. As the tidal range increases, the value of the peak increases. SPM concentration reaches a minimum one hour after the high tide. This could be explained by the fact that the currents change direction one hour after the high tide, which results in a lowering velocity and particles settling down. It could also be due to the fact that the water column may be full of marine waters characterized

by low SSC.

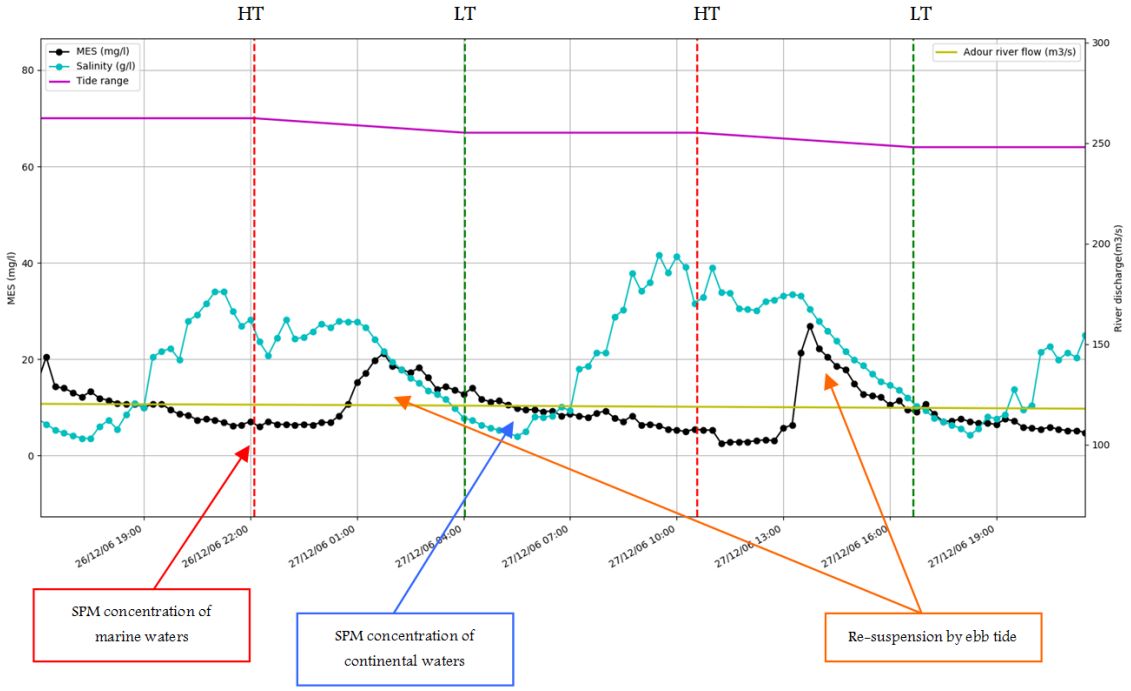

Figure 2.10: CTD data for December, 27th 2006 : Salinity ($g.l^{-1}$) in blue and SPM concentration ($mg.l^{-1}$) in black, Tide range in pink and River flow ($m^3.s^{-1}$) in yellow.

2.4.3 SPM exchange with coastal area

Before the construction of dikes and jetties, the southward beach drift created a sand spit in the Adour estuary mouth. The access to the Bayonne harbor was then regularly obstructed. In order to maintain navigation in the estuary entrance dikes, jetties and dredging activities were put in place. These structures and activities have jeopardized the natural drift of the sediment. Numerical studies [2] have shown that swell is responsible for a current oriented towards the estuary mouth, able to re-suspend and transport sediment under energetic wave conditions. In 1999, a sand pit was artificially created and maintained by dredging operations, in order to avoid sand accumulation in the estuary entrance under heavy swell conditions. Dubranna's numerical study [32] highlighted that the transport of sediment from the coastal area into the estuary is strongly limited by this man-engineered retention pit.

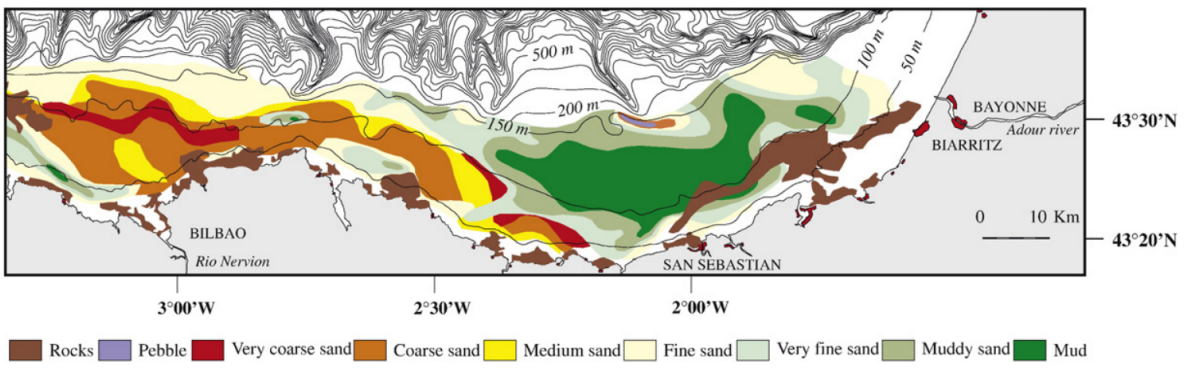

Figure 2.11: Sedimentary map of the Basque country shelf extracted from Jouanneau et al (2008) [65].

The sediment transport at the estuary mouth is not only in the estuary direction. Jouanneau et al (2008) [65] showed that one 50 km long mud patch, composed of very fine-grained particles, was located off the mouth of the Adour estuary, at a depth of 100m on the shelf (Fig. 2.11). It was hypothesized that sediments in the mud patch come from the Adour estuary. Video and satellite observations [23, 88] support this idea. Petus has revealed that the Adour river plume is present more than 60% of the time in front of the estuary mouth (Fig. 2.12) [88]. Dailloux has established that winds can overcome the Coriolis effect on the plume dispersion, and that wind has a huge influence on the plume direction.

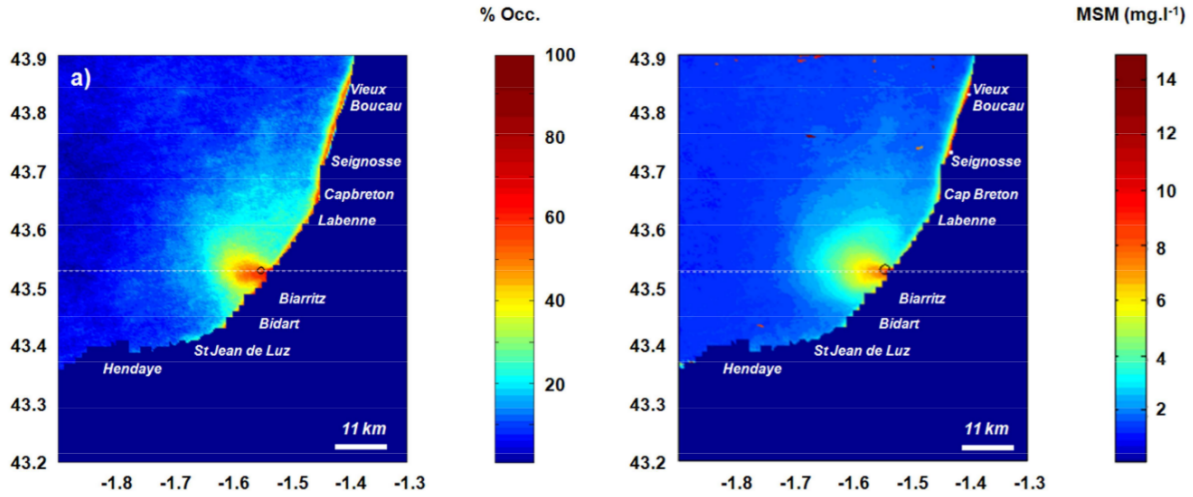

Figure 2.12: Area of Adour plume influence, based on 246 satellite images. On the left : the percent frequency of occurrence of SSC over 3 $mg.L^{-1}$. On the right : Mean SSC in $mg.L^{-1}$. Extracted from Petus 2009 [88].

2.5 Anthropogenic pressures

Estuarine areas are also characterized by a high level of human activity. A strong urbanization, industrialization and agricultural intensification lead to riverine, estuarine and then marine water contamination. Contamination of different origins can meet and react inside the estuary, which can lead to uncontrolled interactions (the "cocktail effect" phenomenon). The Adour estuary is a good example of this growing anthropogenic pressure, with the lower estuary nested in located Anglet, Boucau and Bayonne cities. The last 6 km of the estuary are occupied by the Bayonne harbor and associated activities. The increasing urban and industrial development within estuarine areas leads to degradation of the estuarine system.

2.5.1 Pollution

Several assessments of the Adour estuary water/sediment/biota quality were carried out between 2000 and 2003, aiming to determine the quantity of contaminant supplied by the Adour and Gaves rivers and discharged locally onto the estuary [117]. Pollution in the estuary was assessed as very worrisome for faecal bacteria, tributyltin (TBT), metal, polycyclic aromatic hydrocarbons (HAP) and polychlorobiphenyls (PCB). The main source of faecal bacteria was identified as the Nive river, the Aritxague stream and the drainage of the seawage treatment plant of Tarnos city. High levels of concentration of metals, TBT, HAP and PCB were observed in sediments inside the estuary close by the industrial sector of Boucau-Tarnos, the confluence with Maharin and Aritxague streams (i.e. Anglet and Bayonne agglomeration) and the Bacheforès and Mouguerre landfills.

Between 2011 and 2014, in the context of the "Observatoire de l'estuaire de l'Adour" project, water, sediment and biota quality were studied in the Adour estuary [12, 24]. The water was classified as low quality with regards to the concentration of suspended matter and faecal bacteria. This poor quality did not improve during the year, and the contamination in faecal bacteria was multiplied by two between 2013 and 2014. In the sediment compartment, the quality deemed good, except some episodic contamination in TBT and Pb. In the biota compartment, the quality was impaired by sporadic contamination of pyrene (HAP). An increase in metal contamination was noticed between 2013 and 2014, in the biota, even though the regulatory threshold was not reached.

2.5.2 Dredging activities

Harbors are generally protected areas and thus have a tendency to silt-up. Harbor depths are then maintained to improve accessibility and navigation. In the Bayonne harbor, located at the estuary mouth, the depth needs to be maintained between -9m and -5m (under the chart datum) depending of the dock (Fig. 2.13). For this reason, the lower Adour estuary is dredged since 1896.

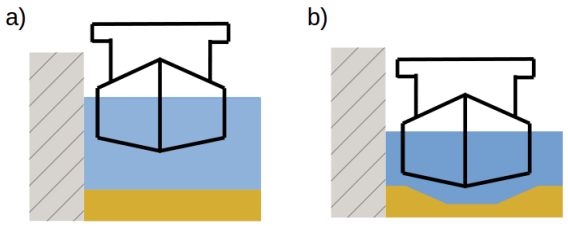

Figure 2.13: A schematic of a ship moored along one dock during high tide (a) and low tide (b).

Nowadays, the Bayonne - Pays Basque Chamber of Commerce and Industry (BPB CCI) is responsible for dredging activities in the harbor area located in the lower Adour estuary. In 2015, the BPB CCI purchased a dredger of 1200 m^3 capacity to maintain the depth in the internal channel, along the docks and in the retention pit. The harbor is divided into 10 areas (see Fig. 2.14). Areas 1 to 4 are dredged by suction, while areas 5 to 10 are dredged by grab hopper. The dredger operates about 200 days a year. Dredging by suction is allowed only between April and November, while dredging with the grab hopper is allowed year-round. In 2017, the maximum quantity of sediment to be dredged in the Harbor area was fixed to 525 000 m^3, and 500 000 m^3 in the coastal area per year. In areas 1 and 2, dredged sediments are mostly sandy, while dredged sediments inside the estuary are mostly muddy. There are three areas for piling (areas A, B and C in Fig. 2.14). Area A is the favored piling area throughout the year, while area B is only used to pile sand from Zone 1 from September to June. Piling in area C is only supposed to be occurred as an exception.

Dredging activities are not without consequences on the estuarine ecosystem. Resuspension of contaminated sediment inside the estuary may have adverse consequences on the estuarine fauna and flora. In addition, dredging by suction is responsible for killing of living organisms and piling activities can results in burying marine fauna and flora in the deposit area.

As a consequence, quality control is carried out in dredging and piling areas in the Adour estuary. The quality of the sediment to be dredged is checked twice a year. In 22 points between the Grenet Bridge and the estuary mouth, sediments are checked by a certified laboratory according to their granulometry, metal, PCBs and PAHs, organotin compounds, nutrients and bacteriology. A bio-sedimentary follow-up of the piling area is done once a year. Macroinvertebrate, granulometry, percentage of dry matter, aluminium and total organic carbon are controlled in the piling area. Between May 15th and September 30th, a bacteriological analysis

(Escherichia Coli) of the sediment to be piled in front of Anglet beaches (area B) is carried out once a month. Additionally, suction techniques are generally responsible for killing fish, which is why a follow-up of the piscicultural fauna sucked by the dredger is also carried out.

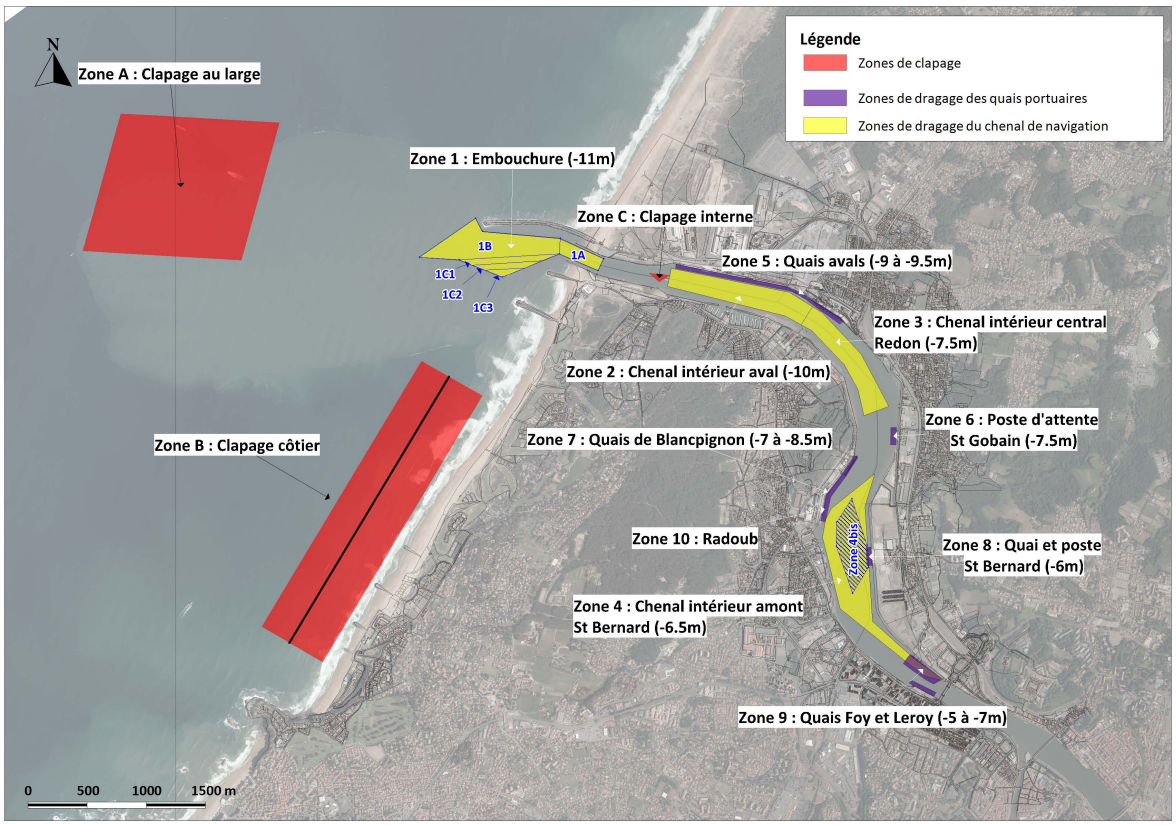

Figure 2.14: Map of the lower adour estuary and its coasal area. Piling areas (Area A, B and C) are represented in red. Dredging areas from 1 to 10 are displayed in yellow (internal channel) and purple (trench along the docks).

Part II

Estuarine circulation and suspended sediment dynamics

Chapter 1

Methodology

1.1 Analysis of available data sets

Before collecting our own set of data, a thorough analysis of several available data sets was carried out. This section presents all the available data sets that have been analyzed. Data sets are composed of different types of data (salinity, temperature, turbidity, SPM concentration, velocities etc ...), collected during different time periods, at different locations along the estuary. A correlation between this very low-frequency and decoupled data has not been easy to find. Major findings of this analysis have been presented in the previous chapter and have been carefully taken into consideration during the design of the new field campaign.

1.1.1 On line data sets

First, an analysis of the major forcing has been carried out based on data collected online. For the tidal forcing, the water elevation registered at the entrance of the estuary has been used. In the online SHOM database (https://data.shom.fr/), we have access to data from the Bayonne-Boucau tide gauge (longitude : -1.51483, latitude : 43.52732). The downloaded data is water depth in meter, at a frequency of 1 measurement every 10 min, over the following period: 20/09/2011-17/09/2014.

As to the riverine forcing, the river flow of the Adour river and of several tributaries is available online via the DREAL Aquitaine (http://www.hydro.eaufrance.fr/). The daily mean river flows for the period 01/01/1969 - 15/03/2017 has been studied. As the downstream station in the Adour river is located at Saint Vincent de Paul, all the river discharges from the downstream tributaries have been added : the Nive, the Bidouze, the Luy, the Gave de Pau and the Gave d'Oloron.

Further online data sets which have been analyzed, are the result of water samplings collected at Urt village between 2007-2015, available on the Agence de l'eau Adour-Garonne website (http://adour-garonne.eaufrance.fr/). Further analysis has been carried out on these water samples, but we focused only on the SPM concentration. Water samples were collected once a month, but not during the flood event (probably for logistic matters), between 2007 and 2015. Therefore values and mean values are probably underestimated. In addition to what the variability along day variations (tide cycle) or week variation (fortnightly cycle) have not been caught by those data.

1.1.2 Former field campaigns

Over the past decade, field campaigns have been carried out in the lower reach of the estuary. The results of three different field campaigns were analyzed. During the MAPEA project, the ACABIE team from the IPREM laboratory put in place a multi-parameter probe during 3 month. The probe was continuously registering temperature, conductivity, turbidity and pH, at

a frequency of one measurement every 15 minutes. This probe was secured at the naval base, to a floating pontoon about 1 m under the surface. It was left underwater for about 80 days (between December, 21st 2006 and March, 17th 2007). Water samples were collected and a linear regression was performed by the ACABIE team to deduce SPM concentration in $mg.L^{-1}$ from turbidity values. During the summer of 2008, the Casagec engineering office carried out a field campaign to study the Adour river mouth hydrodynamics. An ADCP profiler was fixed to ship side to measure current velocity. The velocity was measured along 11 sections in the downstream estuary. Those measurements were realized on 6 days with specific tide coefficients : 30, 65 and 100, during summer time (i.e. the lowest water discharge period). Finally, in the context of the Observatoire de l'estuaire de l'Adour project, a specific field campaign was designed in the last 10 km of the estuary. Five stations were selected along the Adour estuary and one in the Nive river. At each station, water samples were collected and CTD profiles were undertaken, once a month for about 3 years (from November 2011 to September 2014), always during ebb tide. In addition, a multi-parameter probe, named SMATCH, was fixed to the floating RO-RO terminal (6km from the estuary mouth), about 1 m under the water surface. The probe collected : temperature, salinity, turbidity and dissolved oxygen, every 10 min, over a period of 2 years (2012 - 2014). Unfortunately, the probe suffered difficulties and was damaged during this period (due to vandalism, ship collision etc..), therefore the data collection was not continuous.

1.2 New field experimentations

The available data sets presented above have shown different lacks in time resolution and space resolution, and the collected information were not identical. To complement the existing data sets, a new high-resolution/high-frequency field campaign was designed. The objective was to collect physical and chemical data simultaneously, on different time scales (tidal cycle, fortnightly cycle).

Table 1.1: Experimental conditions and measurements. LD/HD refer to low/high discharge conditions, respectively. ST/NT refer to spring/neap tide, respectively. T.R. and Disch. are the tidal range and river discharge, respectively. B.M, B.S. and MiniB refer to Bottom Moored velocity measurements at SF2 and SF4, anchored Boat Survey of velocity, salinity and turbidity profiles and longitudinal section with MiniBat underwater towed vehicle, respectively.

	Conditions			**Measurements**
	Date	T.R. (m)	Disch. (m^3/s)	
LD-ST17	Sept, 2017	3.2-3.8	84-86	B.M. + B.S. (SF1 to SF4)+ MiniB
LD-NT17	Sept, 2017	1.2-1.3	112-128	B.M. + B.S. (SF1 to SF4)+ MiniB
LD-ST18	Sept, 2018	3.3	103	B.S. (SF2)
HD-ST18	June, 2018	3.2	1421	B.S. (SF2)

The aim of the present field experiments is to study the tidally-driven hydrodynamics inside the lower estuary, including salt-wedge, stratification, mixing and SPM dynamics. The field campaigns are based on a series of operations aiming to investigate the effect of river discharge and tidal range on the estuarine dynamics. For the sake of simplicity, the experimental results have been organized and named following the forcing conditions: LD/HD refers to low/high river discharge and ST/NT refers to spring/neap tide conditions, respectively, while the year is added at the end. For instance, LD-ST17 refers to data recovered in low discharge and spring tide conditions in 2017. A summary of conditions during the boat survey measurements is given in Table 1.1, while each type of measurement is described below. The measurements were undertaken only in the last 6km of the estuary, between the mouth and the confluence with the Nive river (Fig. 1.10).

This new field campaign was sponsored by the EC2CO PANACHE program (CNRS INSU). The port of Bayonne, the Gladys group, MIO and EPOC supported the experimentation.

1.2.1 Instrumentation and calibration

Various instrumentation were deployed during the field campaign, with the support of the Gladys group, Mediterranean Institute of Oceanography (MIO) and Environnements et Paléoenvironnements Océaniques et Continentaux (EPOC) laboratories. For velocity and turbulence measurements ADCPs and ADVs were used. Salinity, temperature and turbidity data were collected with multi-parameters probes and CTDs. The granulometry of suspended material was analyzed with a LISST. Water samples were collected with a submerged pump and were filtered with portable filtration units. In this subsection, instrumentation will be quickly introduced, along with their limitations.

1.2.1.1 ADCPs and ADVs

Acoustic Doppler Current Profiler (ADCP) have been primarily designed to measure the flow velocity in a water column. Recently they have been used for the quantification of particulate matter in suspension in water [53, 97, 113]. ADCPs measure the acoustic signal reflected by the particle in suspension in the flow. The four ADCP transducers are used as transmitters and receivers. Acoustic pulse, named pings, are emitted by each transducer independently, and then the acoustic signal reflected by the particles is received by the transducers. The frequency of the reflected signal is linked to the particles velocity. If the reflected signal frequency is the same as the original signal, it means that the particles are not moving. If the particles are moving, the frequency is different: this is what is referred to as the Doppler effect. A blanking zone is defined between the head of the ADCP and the first cell. This distance is used to give the transducers time to settle before the echo returns to the receiver (Fig. 1.1).

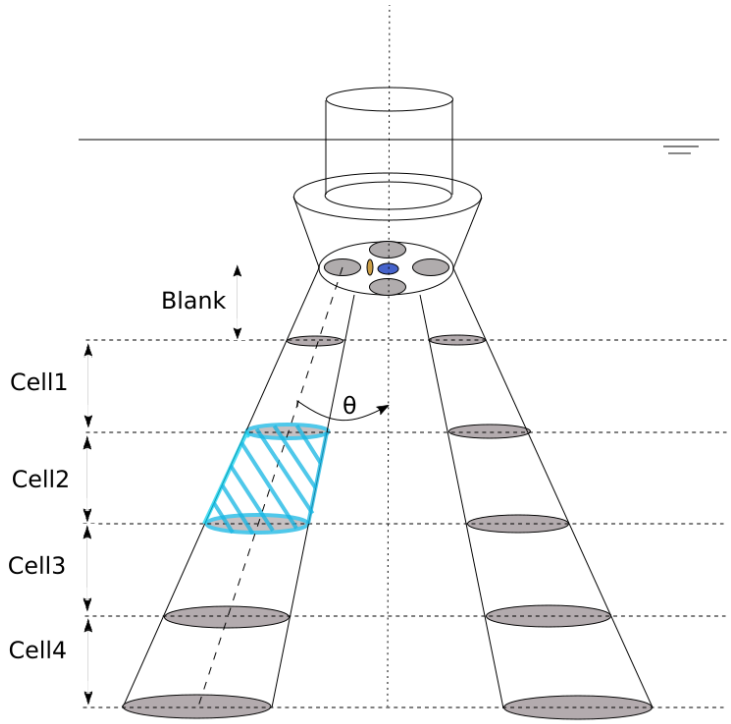

Figure 1.1: Schematic of ADCP functioning (looking down), with the four beams for velocity measurement (in grey), the 5th beam (in blue) for turbulence measurement and the pressure and temperature sensor (in yellow).

Only three beams are necessary to measure the three components of the velocity (U,V,W). The fourth beam is used to increase the accuracy of the measurement. The fifth beam is used to increase the accuracy of the velocity vertical component measurement. During each ping, the velocity is measured over the full cell (dashed in blue on Fig. 1.1) and a weighted average is calculated and associated to the center of the cell. The operator can define the cell size during the programing phase.

During our different field campaigns, various ADCPs were deployed : one RDI (Fig. 1.2 d)), one Flowquest FQ600 (Fig. 1.2 a)) and one Nortek Signature 1000 (Fig. 1.2 a)). Each of them has different characteristics (Tab. 1.2). These ADCPs have some inherent limitations due to their characteristics, e.g. the RDI has a huge blanking distance, then if bottom-moored the first 1.3 m are missed. If used "looking down" (i.e. secured on a boat hull), the loss of the first 1.3 m does not matter due to the boat draft. In the case of the FQ600, the large cell size makes it difficult for it to be deployed in very shallow water, but it will be very useful in deeper sea or in the ocean. The fifth beam of the Sig.1000 and its high frequency of measurement makes it very interesting for turbulence measurements. It was used primarily during short time measurement (i.e. a tidal cycle), rather than during long term measurement (i.e. one month) on bottom-moored station. The instrument characteristics should be carefully checked before any deployment. The memory and battery capacity are also scaling characteristics, they can be challenging during field campaign.

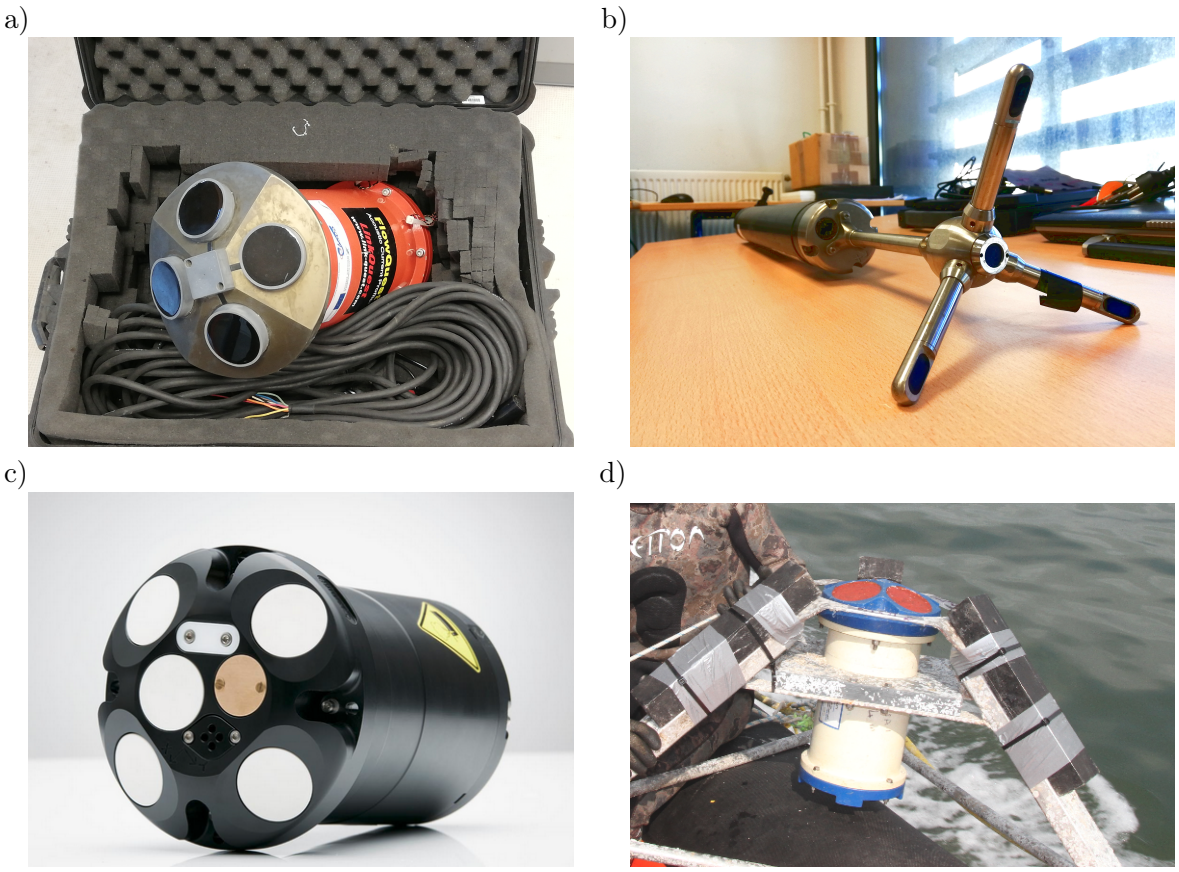

Figure 1.2: Velocty measurements have been done with different equipments : a) a Flowquest 600 Hz (FQ600) ADCP, b) two Nortek Vector ADVs, c) a Nortek Signature 1000 Hz ADCP and d) a RDI ADCP.

As stated above, the large blanking distance of the RDI makes it challenging to deploy in a moored station. In addition to the blanking distance, the size of the pyramid frame (onto which the ADCP has to be fixed) has to be considered. To compensate for this lack of information,

two Acoustic Doppler Velocimeter (ADV) were deployed in association of the RDI ADCP (Fig. 1.3 a)).

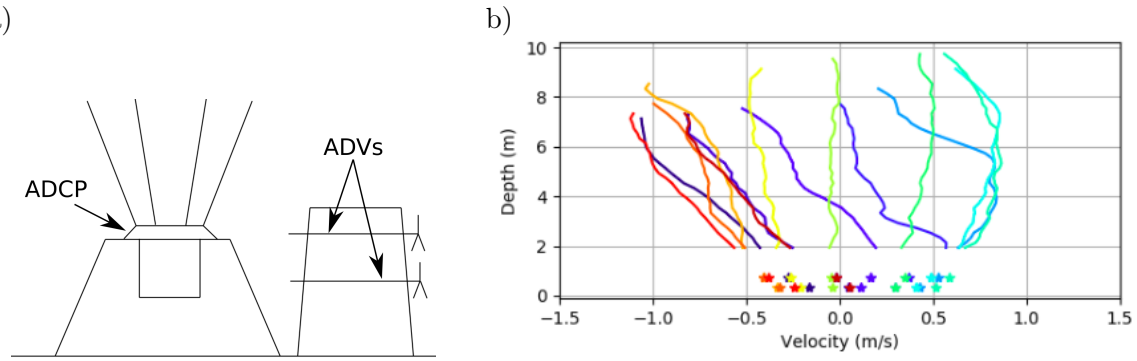

Figure 1.3: a) Schematic of the combined deployment of a bottom mounted RDI and two Vector ADVs. b) Velocity data collected by the bottom mounted RDI (full line) and the two Vectors (stars), colors correspond to time of measurement. It should be noticed the good agreement between ADCP and ADVs data.

ADVs (Fig.1.2 b) are single-point current meters capable of acquiring the three components of the velocity in a very small volume. The functioning is similar to the ADCP one, based on the Doppler effect on a reflected acoustic signal. ADVs are composed of three transducers used as transmitters and one transducer in the center used as a receiver. Its high data acquisition frequency of 64 Hz makes it useful for turbulence measurements.

Table 1.2: Characteristics of the deployed ADCPs : blanking distance in meter, the cell size in meter, the frequency in hertz, the beam angle in degree and the presence of a 5th beam.

	RDI	FQ600	SIG.1000
Blanking (m)	1.31	0.7	0.1
Cell size (m)	0.2	0.5	0.2/0.3
Frequency (Hz)	600	600	1000
Theta (°)	20	22	25
5th beam	NO	NO	YES

Only the compass has to be calibrated in an ADCP and an ADV. The calibration of the compass has to be done after each battery removal. This calibration can sometimes be challenging, as it has to be done away from any large ferrous structure. The ADCP has to be kept in the vertical position and has to be turned on 360°. The easiest solution we found was to "hang" it on a tree branch in order to ensure the verticality and be able to turn it easily.

1.2.1.2 Multi-parameters probes and CTD

During the field campaign, different type of multi-parameter probes and CTDs : one YSI 6920, one Seabird C19+ and three Diver CTDs.

The Diver CTDs were deployed to measure the Conductivity (in milliSiemens per centimeter), the Temperature (in degrees Celsius) and the Depth (in meter), as indicated by their name (Fig. 1.4). The frequency of acquisition is of 1Hz. Their body is made of ceramics to resist corrosive water, such as marine waters. They are very small, about 10 cm long, and they have an embedded battery and a large memory capacity. The data retrieval is facilitated by an optical connection. They came with pressure and temperature sensors, and one sensor with 4 electrodes to determine precisely the conductivity over a large range of value (0-120 $mS.cm^{-1}$). The calibration of the conductivity was realized with 5 standardized calibration solutions of 84

$\mu S.cm^{-1}$, 1413 $\mu S.cm^{-1}$, 5000 $\mu S.cm^{-1}$, 12880 $\mu S.cm^{-1}$ and 80000 $\mu S.cm^{-1}$, as recommended by the supplier. The calibration was undertaken before each deployment.

Figure 1.4: CTD DIVER with all the sensors embedded in the frame.

Conductivity (in milliSiemens per centimeter), temperature (in degrees Celsius) and turbidity (in nephelometric turbidity units - NTU) were collected by an YSI 6920 multiparameter probe (Fig. 1.14). Parameters are collected at a frequency of 1Hz. Due to the obsolescence of the probe (more than 13 years old), the pressure sensor and the internal clock were out of order and not repairable. It had to be combined with an independent pressure sensor or one of the Diver CTD, to be able to make turbidity profiles. Some port plugs were missing for the unused plugs, so we sealed them with liquid silicone. The conductivity was calibrated in a similar manner than with the CTD-DIVERs. An optical turbidity sensor 6136 was bought especially for this field campaign. The optical sensor emits a light wave with a specific frequency and wave-length into the water column. This wave is reflected and damped by the moving suspended particles. A receiver measures the reflected wave and converts it into an electric signal. This type of sensors are generally calibrated with standardized calibration solution in NTU. The calibration of the turbidity is generally done by the supplier. This calibration was done with three standardized calibration solutions of 10 NTU, 200 NTU and 1000 NTU, and was undertaken before each deployment. During the measurement campaign a probe guard was screwed on to protect the sensor from possible damage.

a) b)

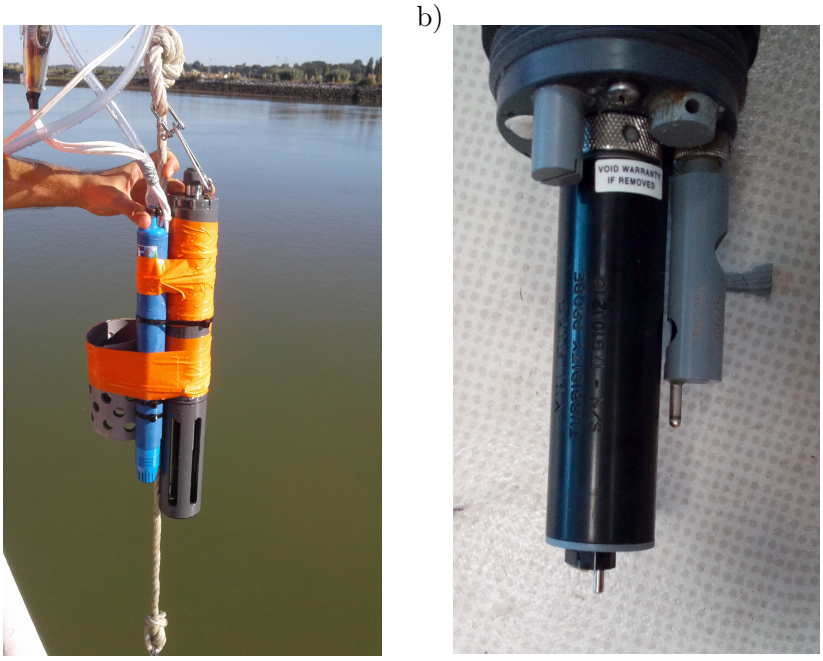

Figure 1.5: a) YSI multi-parameter probe with its guard during field deployment, b) Turbidity sensor on the left and Conductivity and Temperature sensor on the right mounted on the YSI probe.

The Seabird C19+ is equipped with a wide range of sensors: conductivity, temperature, pressure, turbidity, pH, fluorescence, dissolved oxygen and irradiance. All those parameters are measured at a frequency of 4Hz. All the sensors were on during deployments, however we focused only on the conductivity, temperature, pressure, and turbidity parameters. As it can be seen on figure 1.6, this probe is cumbersome, heavy and therefore not easy to manipulate. This probe was made available by Aurore Gueux (member of the MICROPOLIT Staff, responsible for data collection for the SOMLIT network). In this probe, all the sensors are embedded in the frame, except the pH sensor. The calibration has to be done in a Seabird certified Laboratory, every year (as per supplier's recommendation). As these calibrations are very expensive and make the probe unavailable during a long period, the SOMLIT protocol prescribes a Laboratory calibration at least every three years, except for the pH sensor, which is calibrated with three standardized calibration solutions before each deployment.

Figure 1.6: Seabird C19+ in its frame during the field campaign.

1.2.1.3 LISST

A SEQUOIA Laser In-situ Scattering and Transmissometry (LISST) 100X type B particle size analyzer was deployed. Various types of data can be retrieved from LISST measurements: Particle Size Distribution (PSD), the volume concentration for each size class, the total volume concentration, temperature, pressure, and the transmission signal intensity. The operating principle of laser diffraction is based on the fact that the light scattered by spherical particles with a specific size, composition and color can be computed and does not require any assumption. The LISST is composed of a collimated laser, a scattering volume where water and particle in suspension will pass through, a receiving lens, a special detector array composed of 32 rings of silicon and a photodiode. The laser operates at a 670 nm wavelength (Fig. 1.7). The light is

scattered by the particles in the scattering volume and it then collected by the receiving lens. The 32 rings of silicon are placed at the lens focal plane. The 32 detector rings cover 32 specific small ranges of angles over which the light scattering is measured. The angle of diffraction is inversely proportional to the particle size. Small particles diffract on the large angles. Behind the ring detector, a photodiode is placed to sense the power of the laser beam focused by a hole in the ring detector. An attenuation of the power due to the particle is measured and it is used to de-attenuate the light of the ring. The background measured with filtered water is then subtracted. Lastly an inversion procedure is carried out to produce the PSD. This mathematical inversion solves the 32 unknown concentrations based on the 32 known measurements. The particles are logarithmically spread over 32 size classes from 1 to 250 μm. The description and operating principle are detailed in Sequoia Scientific LISST-100X particle size analyser user manual and in the literature [4].

a) b)

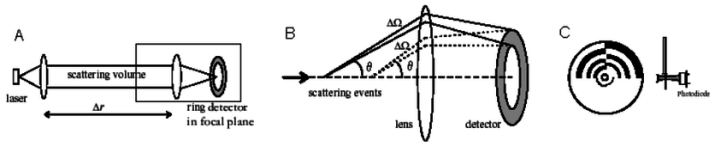

c)

Figure 1.7: a) The head of the LISST-100X type B, b) Conceptual diagrams of the Sequoia LISST extracted from Roesler & Boss, 2008 [101], c) The LISST-100X type B in its frame during the deployment.

Before and after any use of the LISST a measurement of the background should be carried out with ultra-pure water. It is used to verify the correct operational state of the instrument, e.g. the proper alignment of laser and lens or the absence of scratches on the lens. The LISST used during our field campaign is the property of the MIO laboratory, and the calibration was done by their technician Nagib Bhairy.

The LISST is a very convenient instrument, however it has some limitations in use. For SSC over 0.1 $g.L^{-1}$, the beam can be attenuated by the particles in suspension. No light is received by the lens. In this case, a path reduction module has to be used to reduce the scattering volume. Another drawback of the LISST is the fact that a density gradient can strongly alter the quality of the data by deviation of the optical path. In general, a salinity gradient of few $PSU.m^{-1}$ is considered too strong to obtain qualitative data from the LISST. This specificity of the LISST is a major drawback regarding its use in an salt wedge-estuary, where the density gradient is very sharp.

1.2.1.4 Water samples and filtrations

To determine the concentration of suspended material in the water, a commonly-used technique is the water samples collected on site, which are then filtered with a Glass Fiber Filter (GFF). This type of filter retains the particles with a size exceeding 0.45 μm. If the water samples have been collected simultaneously to turbidity measurement, and at the same location, these values of SSC can be correlated to turbidity measurements.

Filters were oven dried at 60°C for 48 hours before being weighed to the nearest 0.001 grams. During the dry season (slightly turbid samples), between 1L and 1.5L samples were passed through GFF filters, while during the wet season (highly turbid samples), 200mL water samples were used. GFF filters are supposed to retain only particulate matter of more than 45 μm. However, when marine waters are filtered, it is highly recommended to rinse with fresh ultra-pure water, in order to wash away any salt which may remain on the filter. The SOMLIT protocol recommends to pass at least 50 cl of ultra-pure water to wash away the salt. After filtration, filters are oven dried again at 60°C for 24h and then weighted again. The difference between the two weights associated to the volume of filtered water enables us to estimate the concentration of particulate matter in suspension.

During the first field campaign (September 2017), filtrations were undertaken in the laboratory, because triplicates were realized for half of the water samples. An error of 10 percent have been found in triplicates. The precision resulting from having triplicates was deemed unnecessary in light of the lab time saved. After which, when possible, filtration were carried out on board (Fig. 1.8).

a) b)

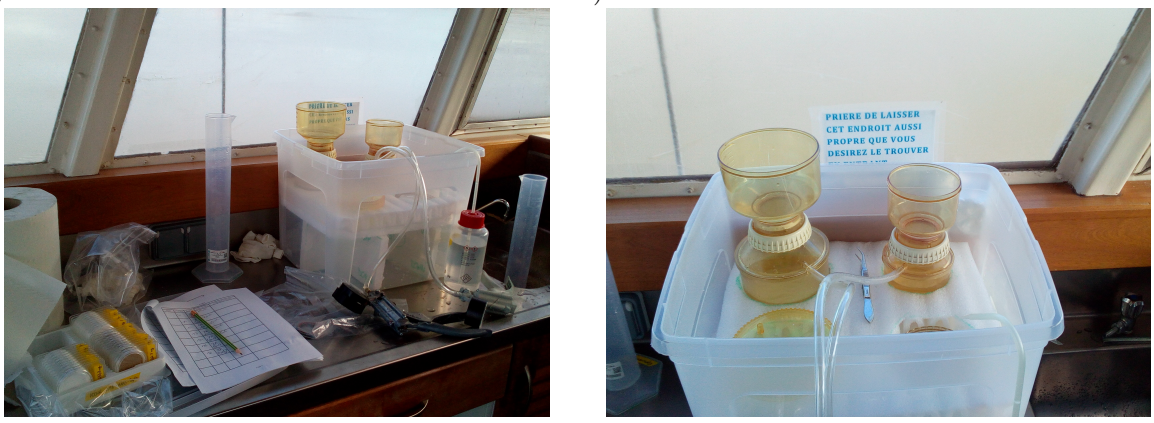

Figure 1.8: a) A laboratory is arranged on board the Ingenieur Lesbord. A part of the kitchen area and the sink are used for filtration during the experimentation. b) A box has been designed especially for both filtration units, in order to keep them straight even during navigation.

When a correlation has to be found between turbidity data and the SSC measured on site, a large range of value has to be covered. If only a small part of the range is covered, the correlation is not reliable. A laboratory calibration can be done to improve this correlation, by collecting sediment on site and making solution of known concentration. Turbidity measurements of these defined concentration solutions can be carried out, to be added to the linear regression.

1.2.1.5 Minibat

An under-water towed vehicle, named MINIBAT, equipped with a multi-parameter probe was deployed to carry out longitudinal sections inside the estuary. This instrument looks like a small plane, which can move up and down inside the water column with its two wings (Fig. 1.9). In order to keep the MINIBAT gliding, the ship has to keep a certain velocity in comparison to

the flow. Conductivity, temperature, pressure and turbidity were recorded by the probe fixed to the body of the MINIBAT. A GPS is associated to the MINIBAT, in order to track its position. Calibrations of the probe were undertaken by Nagib Bhairy, the technician at the MIO laboratory responsible for the instrument. Nagib came on board and piloted it during the field campaign.

a) b)

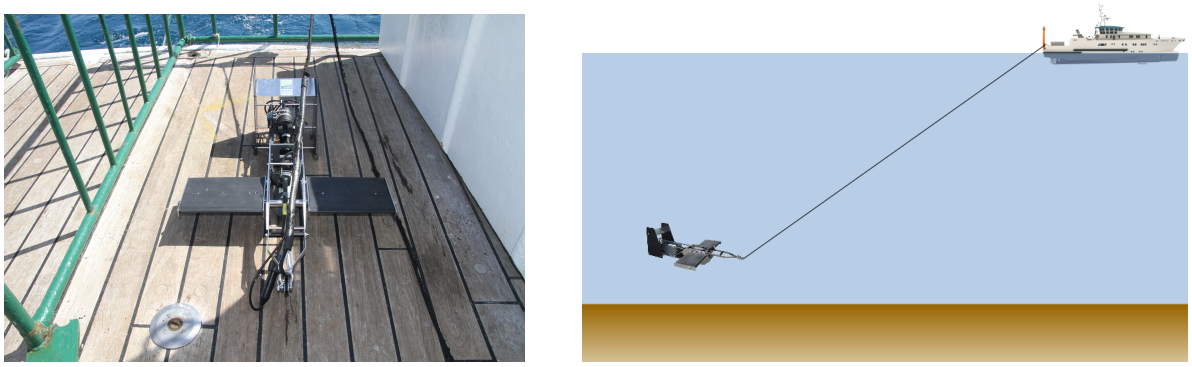

Figure 1.9: a) OSIL Minibat under-water towed vehicle equipped with a multi-parameter probe. b) Schematic of the under-water towed functioning.

1.2.2 Data collection

1.2.2.1 Sampling strategy

The goal of the field experiments was to study the tidally-driven hydrodynamics inside the lower estuary, including salt-wedge, stratification, mixing and SPM dynamics. The field campaigns were based on a series of operations aiming to highlight the effect of river discharge and tidal range on the estuary dynamics. Based on the analysis of the former field campaigns and for operational reasons, the measurements were undertaken only in the last 6km of the estuary, in between the mouth and the confluence with the Nive river (Fig. 1.10).

Figure 1.10: Map of the study site, where white stars named SF1 to SF4 represent the location of measurement, the ones named Boucau, Convergent and Urt represent the location of tide gauges. Colors represent depth in meter.

1.2.2.1.1 Moored stations

Two bottom-moored stations were deployed in Stations SF2 and SF4 (Fig. 1.10), near the center of the channel, for one month in September 2017. At station SF2, velocity profiles were recorded by a Flowquest ADCP (600 kHz) at 4Hz during 5 min every 15 min, with a vertical

resolution of 0.5m. The ADCP was located at 0.56 m above the bed. Salinity and temperature were recorded by a YSI 6920 probe at 0.52 m above the bed, every 15 min.

At Station SF4, a RDI Workhorse sentinel ADCP (600 kHz) recorded velocity profiles with similar acquisition parameters (4Hz during 5 min every 15 min) and a vertical resolution of 0.2m. The head of the ADCP was at 0.52 m above the bed. In addition, two Nortek Vector ADVs were added to the SF4 mooring frame at 0.75 m (hereinafter ADV1) and 0.36 m (hereinafter ADV2) above the bed, recording velocity at 16Hz during 5 min every 15 min and 30 min, respectively.

Both stations were secured by about 100 kg in weight, in order to be maintained on the bed in case of a collision with tree trunk or other debris, during freshets. A special mixture, mostly composed of chili pepper and grease, was put on the instruments to avoid marine fouling.

a) b)

Figure 1.11: a) Bottom moored pyramid frame equipped with the Flowquest ADCP and the YSI 6920 probe. b) Bottom moored pyramid frame equipped with the RDI Workhorse sentinel ADCP, and the associated another mooring frame with two Nortek ADVs and the OBS-3A.

1.2.2.1.2 Fixed boat stations

The fixed boat surveys were focused on the vertical structure of velocity, salinity, temperature and turbidity. Measurements were performed from an anchored boat (Fig. 1.10).

The salinity, temperature and turbidity measurements were carried out using a Seabird C19plus CTD sensor and/or a YSI 6920 probe. For each experiment, five-litters water samples were collected to calibrate the instruments. Forty-kilograms weights were attached to the measurements line in order to ensure its verticality. Probes measurements were recorded at 4Hz for the Seabird C19plus and 1Hz for the YSI 6920. Temperature data will not be discussed due to negligible contributions to the density variations compared to the salinity effect. In addition to the measurements of water properties, high-frequency velocity profiles were recorded, for LD-ST18 and HD-ST18 only, by a Nortek Signature 1000 current profiler (ADCP) secured along the hull. The ADCP was continuously sampling at a rate of 8Hz with 20 to 30 cm cells. Profiles were also carried out with a LISST-100X type B during LD-ST17 and LD-NT17.

a) b)

Figure 1.12: a) Frame used in September 2017 with a LISST-100X, a Seabird C19+, and a water pump. b): Frame used in June and September 2018 with a YSI 6920, a Seabird C19+, and a water pump.

1.2.2.1.3 Transversal sections

In order to catch the possible lateral circulation inside the estuary, ADCP transects were undertaken with a Nortek Signature 1000 fixed on a floating catamaran fastened along the semi-rigid craft (Fig. 1.13). Velocity profiles were continuously recorded at 4Hz, with a vertical resolution of 0.2 m. Transversal sections were undertaken across the estuary at the location of the 4 fixed boat stations (SF1 to SF4).

Figure 1.13: Catamaran equipped with a Nortek Signature 1000 and fastened to a semi-rigid craft, used during the field campaign in September 2017.

1.2.2.1.4 Longitudinal sections

Longitudinal transects were realized across the control area (i.e. between 1 km to 5.5 km from the entrance of the estuary) with an OSIL Minibat under-water towed vehicle, equipped with a multi-parameter probe. Salinity, temperature, pressure and turbidity were recorded by the Minibat. Deployments were carried out during the LD-ST17 and LD-NT17 experiments (see Fig. 2.4 and 2.7, respectively). While the Minibat provides useful spatial information, its deployment remains a very delicate operation in such a shallow and vertically sheared navigation channel. The sections were surveyed following the center axis of the estuary, i.e. not always in the main channel due to navigation constraints near the docks.

1.2.2.1.5 Long term measurements

In a long-term perspective, the YSI 6920 was fixed to a floating pontoon in March 2019; it is to remain there for months. As the flood conditions are particularly difficult to predict and it is not always possible to undertake measurements during such intense events, the long term probes are a good alternative to cover a large range of hydrological conditions. The probe is located on the port naval base (43.508228°N, 1.496170°W), close to the SF2 station on the left bank (Fig. 1.14 a)). The harbor staff had built a metallic structure to protect the YSI probe from floating tree trunks and others floating waste that can be adrift during energetic freshet conditions or eventual ship collision. The YSI has been placed in a bottom-closed squared pipe with a meshed bottom (Fig. 1.14 b)). The resolution has to be reduced to save memory space and battery power (data is collected every 15 min), and the measurement is limited to one position (1 m under the surface). The probe has to be checked every two or three months to retrieve data, change batteries and clean the probe from marine fouling.

a) b)

Figure 1.14: a) Panoramic view of the location where the YSI 6920 has been fixed, b) YSI probe inside its protecting structure.

1.2.2.2 Deployment and malfunctioning

Several field campaigns were carried out between September 2017 and September 2018, under different hydrological conditions. Some of them will not be presented due to the absence data resulting from malfunctioning instruments. Even if field campaigns do not always provide useful data, there is still something to learn from this malfunctioning, which is why I decided to include this section in the present thesis, in order to help other avoid similar problems.

1.2.2.2.1 Field campaigns

Thanks to the Bayonne harbor, which made the "Ingénieur Lesbordes" boat and crew available to us, we were able to deploy a wide range of instrumentation (presented in the previous section).

Figure 1.15: Ingénieur Lesbordes boat used during the field campaigns

September 2017
An extensive, one-month field experimentation with moored stations (from September 10th to October 5th) were undertaken during the dry season (100 $m^3.s^{-1}$). At the beginning of September, river flow was relatively high for the season (more than 300 $m^3.s^{-1}$) due to episodic rainfall. Boat surveys (including fixed boat station, transversal section and longitudinal section) were carried out on September 18th and 30th. The freshwater inflow decreased to about 100 $m^3.s^{-1}$. Boat survey was focused on neap-spring tide cycles. Measurements for spring tide cycle were made between September 18th and 20th, while measurements for neap tide cycle were made between September 28th and 30th. During fieldwork, large and small tides occurred (up to 3.76 m on September 21st 2017, and down to 1.12 m on September 29th 2017).

June 2018
A 8-hour boat survey was carried on June 12th 2018, during a flood event with a river discharge of about 1400 $m^3.s^{-1}$. The tidal range was of 3.18 m. The boat was anchored at station SF2, and profiling measurements of salinity, temperature, and turbidity were realized with a YSI 6920 probe. Velocity profiles were recorded by a Nortek Signature 1000 current profiler (ADCP) secured along the hull. The ADCP was continuously sampling at a rate of 8Hz with 30cm cells. Five-liters water samples were taken to calibrate the instruments.

September 2018
An additional campaign was carried out in September 2018 to complement the measurements performed during the dry season at spring tide (in September 2017), for similar hydrodynamics and tidal conditions. The measurements were similar to those carried out in June 2018.

March 2019
The YSI probe was deployed on the floating pontoon, as previously described. The day of the deployment, water samples were collected during 10 hours, to calibrate the probe. In May, June and August 2019, the probe was removed for about one hour, to retrieve the data, change the batteries and so that we could clean it.

1.2.2.2.2 Malfunctioning and setbacks

Malfunctioning of equipment is frequent. Sometimes it can be avoided, sometimes it cannot. In most cases, a single "in condition" test of the equipment before deployment can prevent a lot of mistakes or troubles.

During the first field campaign, ADCP transects were undertaken with a Nortek Signature 1000. The ADCP was shipped by Nortek only few days before deployment. When we tested it in the lab, we did not notice that the bottom tracking was malfunctioning and giving incorrect values. The data was therefore useless, without the correct ship velocity measurement. We should have tested it in real conditions to be sure that everything was working properly. A similar problem occurred with the new turbidity sensor delivered only a few hours before deployment, giving us no time to test and calibrate it properly. Consequently, the sensor collected incorrect data during the entire month of its deployment. Both events taught me that time management is crucial when preparing a field campaign, and that one should never deploy an instrument that has not been fully tested and calibrated.

The MINIBAT is a very powerful tool, but it requires a certain level of expertise. To keep it gliding, the ship has to maintain a certain velocity relative to the flow velocity. However, when we deployed the MINIBAT to catch the salt-wedge entrance, we did not realize that the two-layer flow would interfere. As the surface layer was flowing out the estuary and the bottom layer was flowing in, the MINIBAT went up and down from one layer to another, therefore it was almost impossible to maintain a constant velocity difference between the flow and the ship. Another difficulty was to work in shallow water with an highly variable bathymetry. As the MININBAT was piloted manually, there was a time lag between the time we requested it to go up and the time it actually went up. During the experimentations, the sonar is located on the boat and the MININBAT is located between 50 m and 100 m behind. As the bathymetry is very variable, the measurement done with the sonar does not correspond to the depth under the MINIABT (50/100m behind), consequently, we hit the bottom once or twice (without damaging the instrument). This experience taught me that instrumentation should be carefully selected to suit our field site, even though we were able to collect remarkable data with this instrument. I would like to thank Nagib Bhairy, who was piloting the MINIBAT. He did fantastic job, despite the tough conditions.

The obsolescence of the YSI 6920 was a set-back, firstly because of the lack of pressure sensor and the fact that new pressure sensors were not compatible with our probe, and secondly because the internal clock was out of service, and therefore when the battery is disconnected the clock is automatically reset to 01/01/2000. In addition, the springs which maintained the batteries in place were rusty, and so the smallest shock would disconnect the batteries, which would reset the clock back to 01/01/2000. In February 2018, we programmed the probe in autonomous mode and it was supposed to trigger itself at 8:00 AM. Unfortunately, the probe may have been shocked on the way to the field site, therefore no data was recorded and we lost a day of observation. Later on, I found a way to maintain the batteries inside their block with two small pieces of conductive metal. On this occasion, I learned to always take very good care of longstanding material and that there is always a way to make things work!

In June 2018, we tried to make turbulence measurements with an ADV at different depths in the water column (like a profile of turbulence). This kind of measurement is almost impossible to process and has been discarded by researchers in such energetic systems. The lesson here is that before undertaking any "non-conventional" instrumentation, you have to make sure that nobody has tried it before you, which will save you time.

1.2.3 Data processing

Data processing was carried out using Python 2.7.13 software. Python is a powerful, free tool, with a large community of users and developers.

1.2.3.1 ADCPs and ADVs data

Velocities

The raw data was post-processed with Python, i.e. no post-processing was carried out using any Instrument Software. For velocity measurements from moored stations, only the averages over the 5 min burst was memorized by the instrument. Similar averages were carried out with Python for the boat stations and ADVs data (with continuous sampling). Continuous sampling data were used for turbulence calculation.

To detect the end of the profile (surface for bottom moorings and bottom for boat stations), we used the echo intensity data recorded by ADCPs. The last few cells of the profile were removed for safety. The number of cell to be removed depends on instrument characteristics (i.e. cell size).

For each instrument, the velocity data was projected into a local coordinate system with the x axis directed along the channel with positive values upstream, the y axis directed laterally towards the right bank, and the z axis directed upward. For sake of simplicity, the generic term "velocity" refers henceforth to the x-component of velocity, unless otherwise specified.

Turbulent properties

During LD-ST18 and HD-ST18, a hull-mounted ADCP was used to monitor high-frequency velocity profiles. These measurements of the three components of the flow velocity enables us to quantify turbulent properties, such as the eddy viscosity ν_t and the rate of turbulent kinetic energy P_{tke}. These calculations were based on the **Covariance Method** [78, 107, 136]. The 8Hz, 1s averaged, ADCP data of opposing beams (b_i) were split into a mean ($\overline{b_i}$) and a fluctuating part (b_i'), using a sampling interval of 10 min. An additional high-pass filter was applied to remove low frequency fluctuations due to ship motion. The along-beam velocities were used to estimate the components of Reynolds stress, as follow :

$$-\overline{u'w'} = \frac{\overline{b_3'^2} - \overline{b_1'^2}}{4sin(\theta)cos(\theta)}, \tag{1.1}$$

$$-\overline{v'w'} = \frac{\overline{b_2'^2} - \overline{b_4'^2}}{4sin(\theta)cos(\theta)}, \tag{1.2}$$

where θ represents the angle of each beam from the axis of the instrument (e.g. $\theta = 25^o$ for Nortek Signature 1000 ADCP).

The eddy viscosity is classically computed following the flux-gradient hypothesis:

$$\nu_t = -\frac{\overline{u'w'}}{\partial\overline{u}/\partial z}. \tag{1.3}$$

The rate of Turbulent Kinetic Energy (TKE) production is expressed as a product of stress and shear :

$$P_{tke} = -\rho\overline{u'w'}\frac{\partial\overline{u}}{\partial z} - \rho\overline{v'w'}\frac{\partial\overline{v}}{\partial z}, \tag{1.4}$$

where ρ is the mean water column density.

Backscatter inversion

ADCP echo intensity data was used in an attempt to estimate the suspended sediment concentration inside the water column. Echo intensity reflects the backscattering strength of the water, which is due to the presence of backscatterers, such as solid particles, bubbles, and living organisms. To be related to the SSC in the water column, turbidity profiles and water samples from the boat survey were used. To link the echo amplitude to the quantity of particles in suspension, an energy balance was established through the Sonar Equation (1.5) [29].

$$RL = SL - 2TL + TI, \tag{1.5}$$

where RL is the received acoustic level measured by the ADCP, SL is the source level emitted by the ADCP, TL is the transmission loss due to attenuation of the acoustic signal by the estuarine waters, and TI is the target index.

To estimate the received intensity RL, we used the equation (1.6) proposed by Gostiaux and Van Haren (2010) [53]:

$$RL = 10log_{10}(10^{k_c E/10} - 10^{k_c E_0/10}), \tag{1.6}$$

where E is the Received Signal Strength Indicator (RSSI) by the ADCP, k_c is a scale factor used to convert RSSI counts to decibels, and E_0 is the reference noise level.

The transmission loss TL was calculated as a sum of the spherical spreading loss and the attenuation of acoustic signal by the estuarine waters, as defined by Equation 1.7. Due to low suspended sediment concentration ($< 100\ mg.L^{-1}$) during the field observations, the attenuation by the particles was neglected.

$$TL = 10log_{10}(\Psi R^2) + \int_0^R \alpha_w(r)dr, \tag{1.7}$$

where $10log_{10}(\Psi R^2)$ is the spherical spreading loss and $\int_0^R \alpha_w(r)dr$ is the water attenuation of acoustic signal.

The water attenuation α_w at frequency f was estimated by the formulation 1.8 given by François and Garrison (1982) [42, 43].

$$\alpha_w = \frac{A_1 P_1 f_1 f^2}{f_1^2 + f^2} + \frac{A_2 P_2 f_2 f^2}{f_2^2 + f^2} + A_3 P_3 f^2 \tag{1.8}$$

where P_1, P_2, P_3 are pressure dependencies, f_1 and f_2 are relaxation frequencies, and A_1, A_2, and A_3 are constants. The first two terms represent chemical relaxation processes for boric acid and for magnesium sulfate, respectively. The third term represents the absorption from pure water.

Finally, the target index TI can be expressed by Equation 1.9:

$$TI = BI + 10log_{10}(V), \tag{1.9}$$

with :

$$BI = 10log_{10}\Big(\frac{M\overline{\sigma}}{\rho_s \overline{\nu_s}}\Big) \qquad or \qquad BI = 10log_{10}(M) + cst, \tag{1.10}$$

where M is the suspended sediment concentration.

An empirical calibration can then be realized between $10log_{10}(M)$ and the backscatter index BI, such as : $10log_{10}(M) = a.BI + b$.

1.2.3.2 Mutli-parameters probes and CTDs data

Only the data collected on the way down was kept, essentially to avoid incorrect turbidity data. It is generally recommended to use the way back for conductivity data, due to the stabilization time necessary for this parameter. However, in our set of data the conductivity measured on the way down was consistent with the one measured on the way back.

Practical Salinity Scale

We used the formula adopted by UNESCO, named Practical Salinity Scale 1978 (PSS-78), to estimate the salinity from conductivity C ($mS.cm^{-1}$), temperature T (°C) and hydrostatic pressure p (dBar) measurement. This formula is based on a relation between the salinity and a ratio of the conductivity of a standard solution of potassium chloride (containing a mass of 32.4356 g KCl in a mass of 1 kg of solution) to the one of seawater at 15°C. Therefore, all waters with the same ratio of conductivity have the same salinity. Seawater has a conductivity ratio of one and a salinity of 35.

$$S = a_0 + a_1 R_T^{1/2} + a_2 R_T + a_3 R_T^{3/2} + a_4 R_T^2 + a_5 R_T^{3/2} + \frac{(T-15)}{1+k(T-15)}(b_0 + b_1 R_T^{1/2} + b_2 R_T + b_3 R_T^{3/2} + b_4 R_T^2 + b_5 R_T^{5/2}) \tag{1.11}$$

Where $a_0 = 0.008$, a_1 = -0.1692, $a_2 = 253851$, a_3=14.0941, a_4=-7.0261, a_5=2.7081, b_0=0.0005, b_1=-0.0056, b_2=-0.0066, b_3=-00375, b_4=0.0636, b_5=-0.0144, k=0.0162 and :

$$R_T = \frac{R}{r_T R_P}. \tag{1.12}$$

With the in-situ measurements of conductivity ratio given by :

$$R = \frac{C(S, T_{68}, P)}{C(35, 15_{68}, 0)} \tag{1.13}$$

And C(35,15$_6$8,0) = 42.914 $mS.cm^{-1}$ = 4.2914 $S.m^{-1}$.

The temperature coefficient of standard seawater can be expressed as follow :

$$r_T = c_0 + c_1 T + c_2 T^2 + c_3 T^3 + c_4 T^4 \tag{1.14}$$

Where c_0=6.766097 10^{-1}, c_1=2.00564 10^{-2}, c_2=1.104259 10^{-4}, c_3=-6.9698 10^{-7} and c_4=1.0031 10^{-9}.

And finally,

$$R_P = 1 + \frac{A_1 p + A_2 p^2 + A_3 p^3}{1 + B_1 T + B_2 T^2 + B_3 R + B_4 T R}, \tag{1.15}$$

where A_1= 2.070 10^{-5}, A_2 = -6.370 10^{-10}, A_3=3.989 10^{-15}, B_1=3.426 10^{-2}, B_2=4.464 10^{-4}, B_3=4.215 10^{-1} and B_4=-3.107 10^{-3}.

From the following equations, the practical salinity S ranges from 2 to 42. This formula is valid in a temperature range from -2°C to 35°C, and an hydrostatic pressure range from 0 to 10000 dBar. The determination of the coefficient values was based on existing seawaters, in order to ensure the conservative characteristics and reproducibility of salinity estimation.

Sea Water Density

From temperature, salinity and pressure, it is possible to determine the seawater density with another UNESCO formula. This formula is valid for temperature ranging between 0°C and 40°C and salinity ranging from 0 to 42.

The seawater density at atmospheric pressure can be expressed as follows:

$$\rho(S, T, 0) = \rho_{SMOW} + R_B S + R_C S^{3/2} + d_0 S^2 \tag{1.16}$$

The Standard Mean Ocean Water (SMOW) density can be given by :

$$\rho_{SMOW} = a_0 + a_1 T + a_2 T^2 + a_3 T^3 + a_4 T^4 + a_5 T^5 \tag{1.17}$$

Where a_0=999.842594, a_1=6.793953 10^{-2}, a_2=-9.095290 10^{-3}, a_3=1.001685 10^{-4}, a_4=-1.120083 10^{-6} and a_5=6.536332 10^{-9}.

The two temperature polynomials can be written as:

$$R_B = b_0 + b_1 T + b_2 T^2 + b_3 T^3 + b_4 T^4 \tag{1.18}$$

and

$$R_C = c_0 + c_1 T + c_2 T^2 \tag{1.19}$$

Where b_0=8.2449 10^{-1}, b_1=-4.0899 10^{-3}, b_2=7.6438 10^{-5}, b_3=-8.2467 10^{-7}, b_4=5.3875 10^{-9}, c_0=-5.7246 10^{-3}, c_1=1.0227 10^{-4}, c_2=-1.6546 10^{-6} and d_0=4.8314 10^{-4}.

From turbidity to SSC

When water samples are collected simultaneously to turbidity profiles, turbidity data can be "converted" to SSC. Over a same area and using the same equipment, a satisfying linear relation between turbidity and SSC can be found. The estimation of the SSC from turbidity values is subjected to simultaneous measurements of both parameters over a meaningful fraction of measurements. The data set should be large enough to provide a reliable correlation, and data should also be spread over the full range of turbidity values. If the data set is not sufficient to obtain a correct correlation, solutions of determined concentration can be produced in the laboratory with sediments collected on the field, on the day of the experimentation.

In the present study, turbidity profiles from boat surveys during LD-NT17, LD-ST17, LD-ST18 and HD-ST18 were converted into suspended sediment concentration (SSC) using a series of five-litters water samples and pre-weighted glass fiber filters. One calibration was realized for each day of deployment (e.g., Fig. 1.16).

The MINIBAT turbidity data was not converted into SSC, for evident operating limitations. As the MINIBAT was towed between 50m and 100m behind the ship, it was impossible to collect water samples at the exact same location and depth. We would have been able to do laboratory calibration with sediment collected on the field if the MINIBAT had not been shipped back the following day. MINIBAT turbidity data, even if not quantitative, is at least qualitative and gave us a lot of useful information.

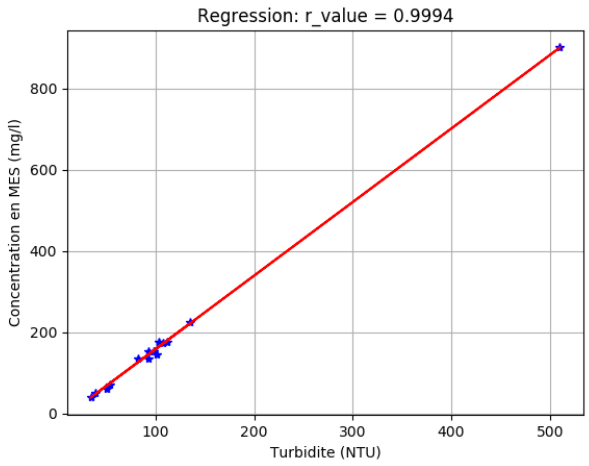

Figure 1.16: Linear regression between turbidity data measured on site and SSC calculated based on water sample filtrations collected on site.

Sediment fluxes

The computation of sediment fluxes would have required a complete cross-sectional monitoring of velocity and SSC profiles, which are not available in the present data set. The sediment fluxes per unit of cross-sectional area (referred as sediment fluxes in this study) are computed as the

product of velocity and SSC values measured along the vertical profile in a given horizontal position.

1.2.3.3 Richardson number

The non-dimensional Richardson number Ri is generally used to quantify the stability of the density stratification in a sheared flow [118]. A threshold value of 0.25 is commonly used to distinguish stable stratification from unstable configuration due to the breakdown of stratification by turbulent mixing. For high values of Ri, the buoyancy forces driven by the vertical density gradient are expected to overcome and suppress turbulent mixing. The Richardson number formulation was calculated from the ratio between density and mean velocity gradients:

$$Ri = -\frac{g}{\rho_0}\frac{\partial\rho/\partial z}{(\partial\overline{u}/\partial z)^2}, \tag{1.20}$$

where ρ_0 is the depth-averaged density. For the calculation of the Richardson number, density profiles were interpolated over the ADCP regular depths. Density and mean velocity profiles were slightly smoothed (over 6 points) to reduce unstable fluctuations before computing the gradients. In natural flow, gradient of velocity $\partial u/\partial z$ can often be almost nil, therefore Ri tends to infinity. This tendency was corrected by placing a minimum value of 0.02 s^{-1} for the vertical shear in computing Ri.

1.2.3.4 LISST data

A B-type LISST 100X was used to analyze the particle sizes in the water column during the boat survey. MATLAB routines provided by Romaric Verney were used to extract the following data from LISST binary files : the laser transmission, volume distribution, total volume concentration, temperature, median particle sizes, time and depth. Density gradients can strongly alter the quality of LISST data by deviation of the optical path. In general, a salinity gradient of few $PSU.m^{-1}$ is considered too strong to obtain qualitative data from the LISST. A criterion was implemented to retrieve unreliable data. This criterion was based on the Brunt-Väisälä frequency. The Brunt-Väisälä frequency N was computed based on Equation 1.21, the density gradient being estimated with Seabird data. After a visual analysis of the LISST data, the threshold value of N = 0.035 was selected.

$$N = \sqrt{-\frac{g}{\rho_0}\frac{\partial\rho}{\partial z}} \tag{1.21}$$

The excess density $\Delta\rho[kg.m^{-3}]$ can be défined as the difference between the density of the floc ρ_f and the water density ρ_w : $\Delta\rho = \rho_f - \rho_w$

The density of the floc is the ratio of the mass of the floc and its volume : $\rho_f = \frac{M_f}{V_f}$.

The floc mass can be considered as the sum of the mass of the water and the mass of the particle : $M_f = M_p + M_w$, similarly for the volume of the volume of the floc : $V_f = V_p + V_w$.

Therefore,

$$\Delta\rho = \rho_f - \rho_w = \frac{M_p + M_w}{V_p + V_w} - \frac{M_w}{V_w} = \frac{V_w(M_p + M_w) - M_w(V_p + V_w)}{V_w(V_p + V_w)} \tag{1.22}$$

$$= \frac{M_p}{V_p + V_w}\Big(\frac{V_w - M_w V_p/M_p}{V_w}\Big) \tag{1.23}$$

$$= \frac{M_p}{Vp + Vw}\left(1 - \frac{\rho_w}{\rho_p}\right) \tag{1.24}$$

With $\rho_w = 1g.cm^{-3}$ and $\rho_p = 2.65g.cm^{-3}$, the equation becomes : $\Delta\rho = \frac{M_p}{Vp+Vw}.0.6$.

According to Mikkelsen and Pejrup (2001) [82], the excess density of floc can be calculated with the total volumetric concentration C_{lisst} given by the LISST and the suspended particle concentration C_{obs} measured with the Seabird.

$$\Delta\rho = \frac{C_{obs}}{C_{lisst}}.0.6 \tag{1.25}$$

Chapter 2

Estuarine circulation

2.1 Structure and variability of the Adour estuary

In this chapter, we start by focusing on tidal forcing and tidal wave propagation inside the estuary, before moving on to salinity structure and circulation, based on the time evolution of the vertical profiles of the measured parameters (Figs. 2.3, 2.6 and 2.9 for LD-ST18, LD-NT17 and HD-ST18 cases, respectively), together with longitudinal sections (Figs. 2.4 and 2.7 for LD-ST17 and LD-NT17 cases, respectively). The LD-ST18 and HD-ST18 data is also depicted as temporal contour plots in Figures 2.11 and 2.12, respectively.

2.1.1 Tidal forcing and tidal asymmetry

Tides are one of the major forcing of estuarine dynamics. The type of tidal forcing an estuary is subjected to is highly variable and depends on the location of that particular estuary. When the tidal wave propagates in the estuary, it suffers distortion due to bathymetry, convergence, and friction effects. The tidal forcing then varies along the estuary. This section presents the tidal forcing and the tidal propagation in the Adour estuary.

2.1.1.1 Tidal forcing

An harmonic analysis of water elevation data collected over 5 years (from 2008 to 2013) with the "t_tide.py" Python function (inspired from "t_tide" MATLAB function), showed that the four major harmonics constituting our tidal forcing were: M2, S2, N2 and K2, with an amplitude of 1.22 m, 0.42 m, 0.25 m and 0.12 m amplitude, respectively. These four harmonics are all **semi-diurnal** with periods of 12.42, 12.00, 12.66 and 11.97 hours, respectively. The form factor is an indicator to classify tides as : semi-diurnal (0-0.25), mixed but mainly semi-diurnal (0.25-1.5), mixed but mainly diurnal (1.5-3), and diurnal (> 3). It is expressed as the ratio of main diurnal harmonics amplitudes to main semi-diurnal harmonics amplitudes (Eq. 2.1). Where 01 and M2 are harmonics generated by Moon's gravitational pull, with respective periods of 24h50 (i.e. 1 lunar day) and of 12h25 (i.e. 1/2 lunar day). And K1 and S2 are harmonics generated by the Sun's gravitational pull, with respective periods of 23h56 (i.e. 1 solar day), and of 11H58 (i.e. 1/2 solar day). The calculation of the Form factor clearly confirms that our tidal signal is semi-diurnal (F$<$ 0.25):

$$F = \frac{K1 + O1}{M2 + S2} = 0.077 \tag{2.1}$$

Based on the four major harmonics amplitudes, this system can be also considered as **mesotidal**. The tidal range varies between 1 m and 4.5 m, with a mean sea level of about 2.5 m above chart datum.

2.1.1.2 Tidal propagation into the Adour estuary

Due to the specific "channel shape" of the Adour estuary (i.e. no width reduction, only depth reduction), friction exceeds the effects of convergence. The tidal wave amplitude decreases as it moves landwards : it decreases by about 1.2m between Convergent and Urt and it decreases by 3.5 m between Convergent and St Vincent de Paul (Fig. 2.1). Such estuaries are named **hyposynchronous**. In the Adour river, the tidal wave propagates until Dax city (about 70 km from the mouth of the estuary), where it is damped out by a weir. This distance is called the "tidal limit", which should not be confused with the limit of saline water entrance. In the Nive river, it propagates until a weir located at Ustaritz village. A tidal phase lag of about 1h15 occurs between Convergent and Urt, and a phase lag of about 4 hours occurs between Convergent and St Vincent de Paul, during spring tides. This lag is attributable to the time required for the tidal wave to propagate upstream.

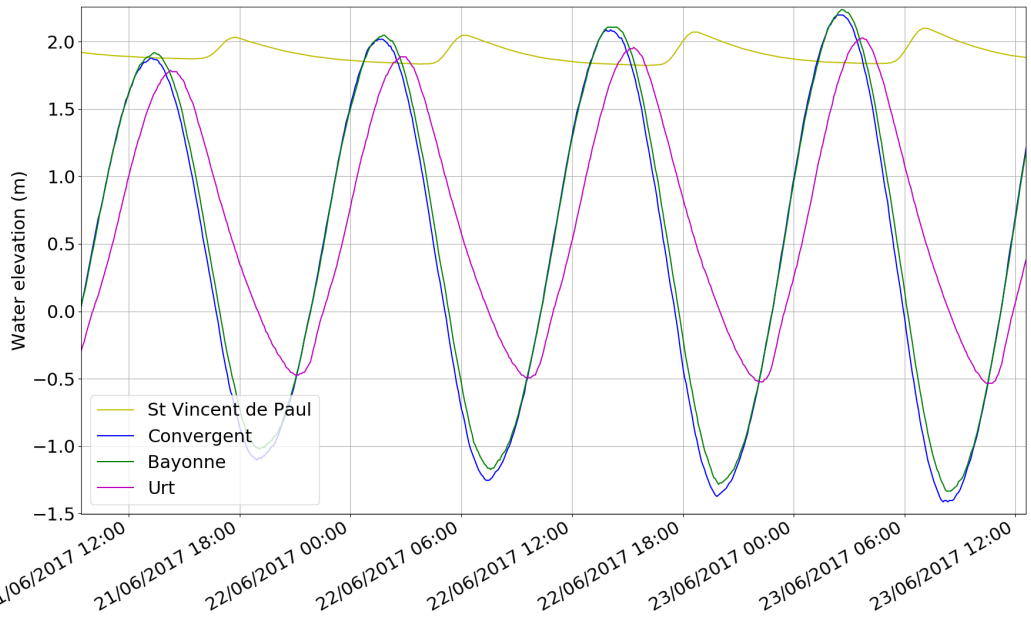

Figure 2.1: Water elevation collected at Convergent (i.e. at the estuary mouth, blue line), at Bayonne (i.e. at 6km from the estuary mouth, green line), at Urt (i.e. at about 20 km from the estuary mouth) and at St Vincent de Paul (i.e. at about 70 km from the estuary mouth), on spring tides.

The hyposynchronous characteristic of the estuary is largely reduced during neap tides, as the tidal amplitude is small and thus friction has a lower impact on the tidal wave propagation (Fig. 2.2). The tidal amplitude decreases by only 15 cm between Convergent and Urt. The estuary can be considered as close to be **synchronuous**, during neap tides. The tidal phase lag is also reduced to less than 1h between these two locations. In figure 2.2, we can also see that the tidal influence on the water elevation at St Vincent de Paul is negligible, due to very weak tidal forcing.

At the mouth of the estuary, the tidal wave is relatively symmetrical, i.e. the fall and the rise last approximately the same time. However, when the tidal wave propagates into the estuary, a distortion of the wave occurs (Fig. 2.1). When ebb and flood durations differ, it is referred to as an "**asymmetric tide**". In the Adour estuary, this phenomenon is visible at Urt village and even more so at St Vincent de Paul (Fig. 2.1). It is characterized by a shorter flood tide and an associated longer ebb: at Urt the flood lasts about 5h30, while the ebb lasts about 7h, and at St Vincent de Paul the difference is even more marked, with a flood of 2h and an ebb of 10h30. An

harmonic analysis of the water elevation data collected at Urt was carried out. It shown that these asymmetries are represented by compound tides. On neap tide, this asymmetry largely flattens (Fig. 2.2), as the tidal wave velocity can be expressed as the root square of the product of the depth by the gravity acceleration. On spring tide, the tidal amplitude is large, and thus the difference between flood and ebb velocities is large as well. However, on neap tide the tidal amplitude is weak and so is the difference between flood and ebb velocities. In Urt, during neap tide, the flood lasts 6h when the ebb lasts 6h30.

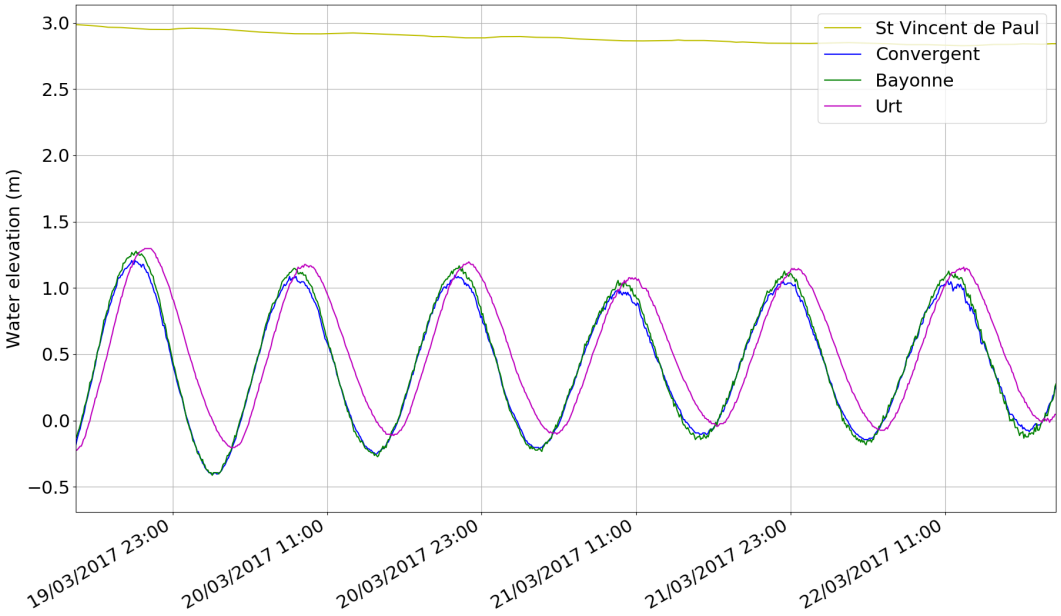

Figure 2.2: Water elevation collected at Convergent (i.e. at the estuary mouth, blue line), at Bayonne (i.e. at 6km from the estuary mouth, green line), at Urt (i.e. at about 20 km from the estuary mouth) and at St Vincent de Paul (i.e. at about 70 km from the estuary mouth), on neap tides.

2.1.2 Saline structure and circulation

2.1.2.1 Influence of tides

The data analysis first focuses on the dry season in order to analyze the influence of tides over the estuarine dynamics. Figures 2.3 and 2.6 present the tidal evolution of velocity, salinity and Suspended Sediment Concentration (SSC) profiles, during the dry season, for spring (LD-ST18) and neap (LD-NT17) tide conditions, respectively. Figures 2.4 and 2.7 display vertical salinity and turbidity structure along the last 6 km of the estuary, from the Minibat measurement during LD-ST17 and LD-NT17 experiments, respectively.

On the spring tide condition, the ebbing tide is characterized by a horizontal salinity gradient (Fig. 2.3 (c) and Fig. 2.4 (b)), with a homogeneous water column flowing out of the estuary. As the ebb progresses, the water column becomes fresher and flows faster. One hour before low water, the velocity reaches its maximum. At low water (11:36), the seaward current shows a strongly-sheared structure, with a nearly linear profile across the water column. Progressively, the water column slows down and the salinity still decreases homogeneously along the water column. As the tide rises, the salinity at the top of the water column still decreases, while at the bottom of the water column the salinity increases. Salinity profiles are not homogeneous anymore; a salinity gradient appears and isohalines begin to be sheared. The current reversal occurs around 13:30 (i.e. almost 2 h after the low water time). The velocity profile reveals a typical salt-wedge profile, when the salty marine waters flow into the estuary. A fast landward

salty bottom layer is observed in the lower 3m, while a fresh upper layer is still flowing seaward with a sheared profile. The salinity reaches its minimal value in the surface layer, when the salt wedge starts entering the estuary. The salty bottom layer, which is rather well-mixed, increases both in thickness and salinity as the tide rises. At the end of the flood tide (16:00), the full water column is salty and flows landward, blocking the fresh water inside the upper part of the estuary. The continental waters blocked inside the upper part of the estuary during the flood are then released during the ebb. This mechanism, named "pulsed plume mechanism", has already been highlighted by Dailloux [23].

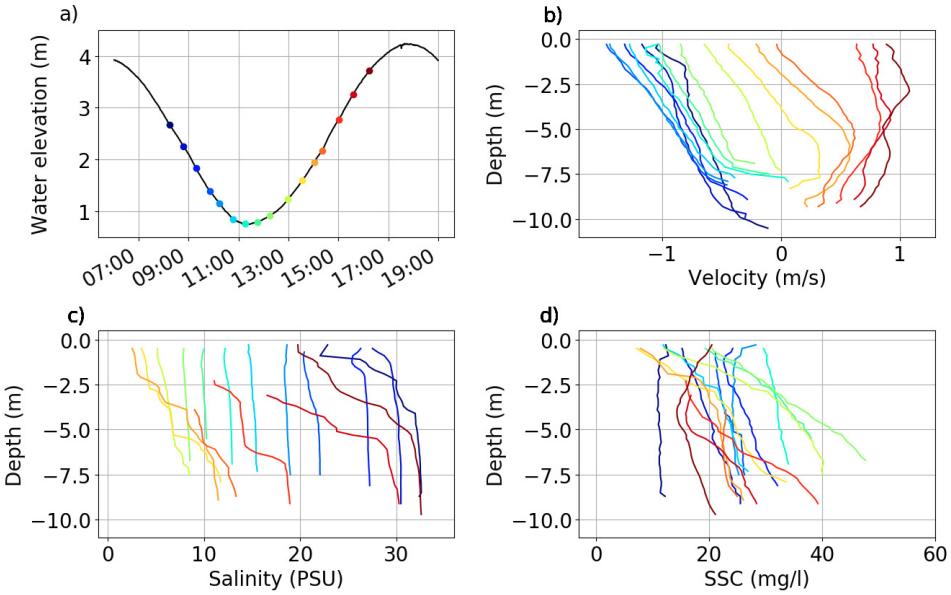

Figure 2.3: Tidal dynamics from LD-ST18 fixed boat surveys during low discharge spring tide conditions, at SF2 station. (a) Water level and timing of measurements. (b), (c), and (d): velocity, salinity and SSC profiles. Note that the same data is presented in contour plots in Figure 2.11.

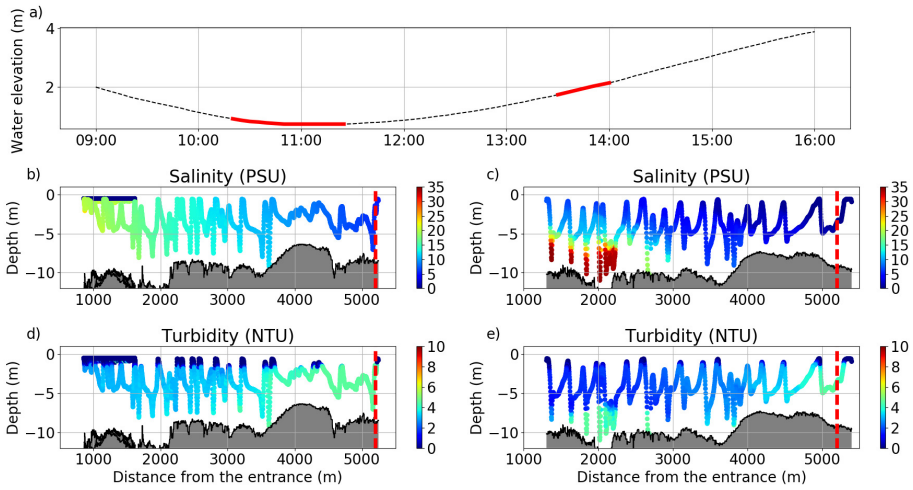

Figure 2.4: Longitudinal and vertical structure across the lower estuary from Minibat measurement during LD-ST17 experiment. (a): Water elevation with measurement periods highlighted in red. (b) and (c): salinity data for falling and rising tide. (d) and (e): turbidity data for falling and rising tide. The bed of the estuary is represented in grey. The red dashed line represents the SF2 station location.

The contrast between spring tide and neap tide (Fig. 2.6 and 2.7) is straightforward. During neap tide the salinity stratification is maintained throughout the tidal cycle and the velocity magnitudes are reduced. At the end of the flood (11:00), a sharp pycnocline separates a two-layer flow, with denser marine water flowing upstream underneath fresh continental waters. The bottom saline layer grows thicker until post-high tide slack water (14:00). Unlike spring tide, at neap tide the pycnocline is not able to reach the surface. There is a 3h time lag between the high water and the current reversal. As flow reverses seaward, the pycnocline thickens and deepens, while the surface and the bottom salinity remain relatively constant. In this case, the ebbing shear velocity profiles are associated with a vertical stratification. This permanent stratification leading to an inhibition of the salt-wedge flushing during neap tide is generally associated with stagnant waters and hypoxia [67, 11]. Indications of similar periods of continuous stratification has been observed in Liverpool Bay, during neap tides. It has been attributed to reduced tidal stirring and reinforced density currents [108]. Data from our bottom-moored YSI probe confirms that this continuous stratification may last 3 days (Fig. 2.5). We can see that between 28/09/2017 and 01/10/2017, the salinity at 0.52 cm above the bed was almost constant with a value of about 31 PSU.

During the fortnightly cycle, the volume of water stored in the estuary varies, as observed in the Gironde estuary by Allen et al in 1980 [5]. The level of high tide increases with the tidal amplitude everywhere inside the estuary. However, even if the level of the low tide decreases in the lower estuary, it increases upstream. It results in an increase in the average volume of water stored in the estuary during increasing tidal ranges (i.e. during the neap tide to spring tide phase). We observed this phenomenon in the Adour estuary, where the level of low tide during spring tide is higher than the level of low tide during neap tide (Fig. 2.8). It reveals the inability of the falling tide to expel the whole volume of stored water during the increasing tidal ranges. On the other hand, when the tidal range decreases (i.e. from spring to neap tide), both low and high tide levels decrease in the upper part of the estuary, while in the lower part of the estuary the high tide level decreases when the low tide level increases. The spring to neap phase is then associated with drainage of the water stored in the estuary. This cycle of drainage/storage of waters in the upper estuary occurs over a 2 week period, and the river flow in the lower estuary is thus modulated by the fortnightly cycle [5].

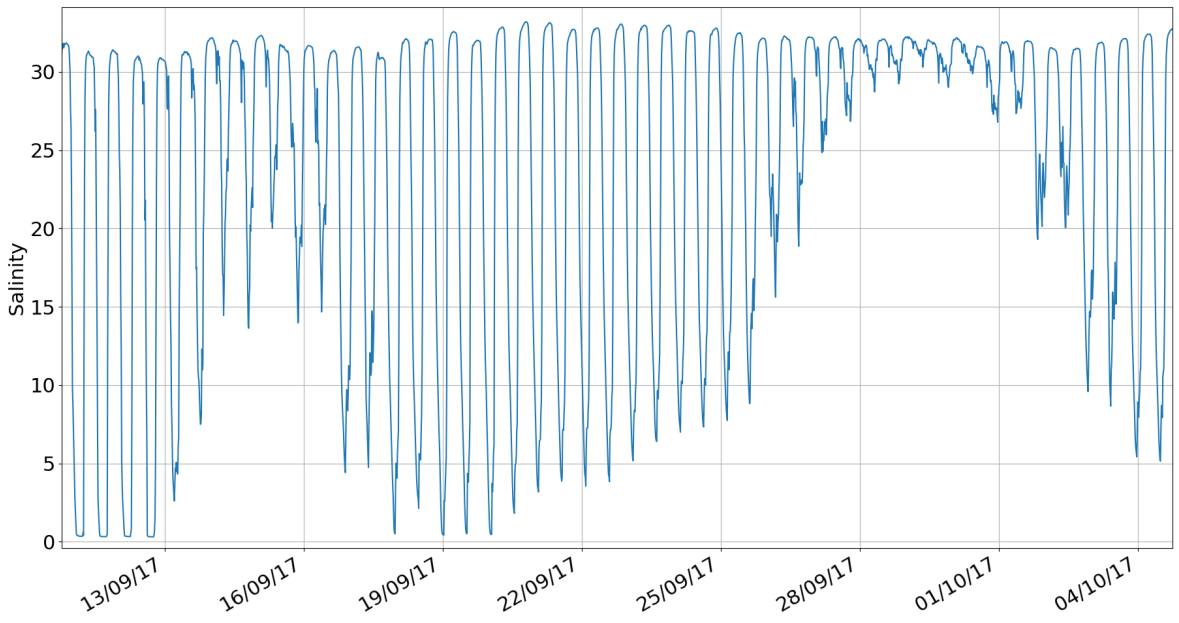

Figure 2.5: Salinity data recorded by the YSI probe at 0.52 m above the bed during our first field campaign (Sept/Oct 2017).

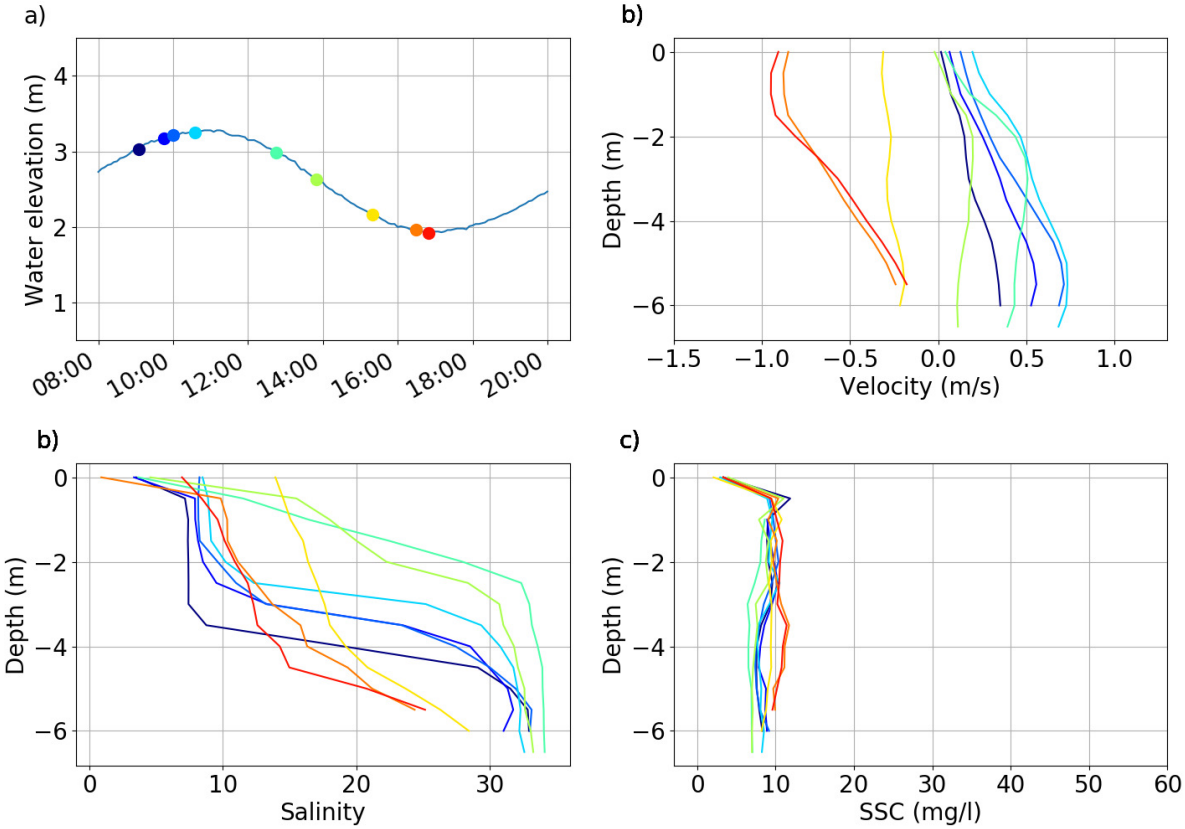

Figure 2.6: Tidal dynamics from LD-NT17 fixed boat surveys during low discharge neap tide conditions, at SF2 station. (a) Water level and timing of measurements. (b), (c), and (d): velocity, salinity and SSC profiles.

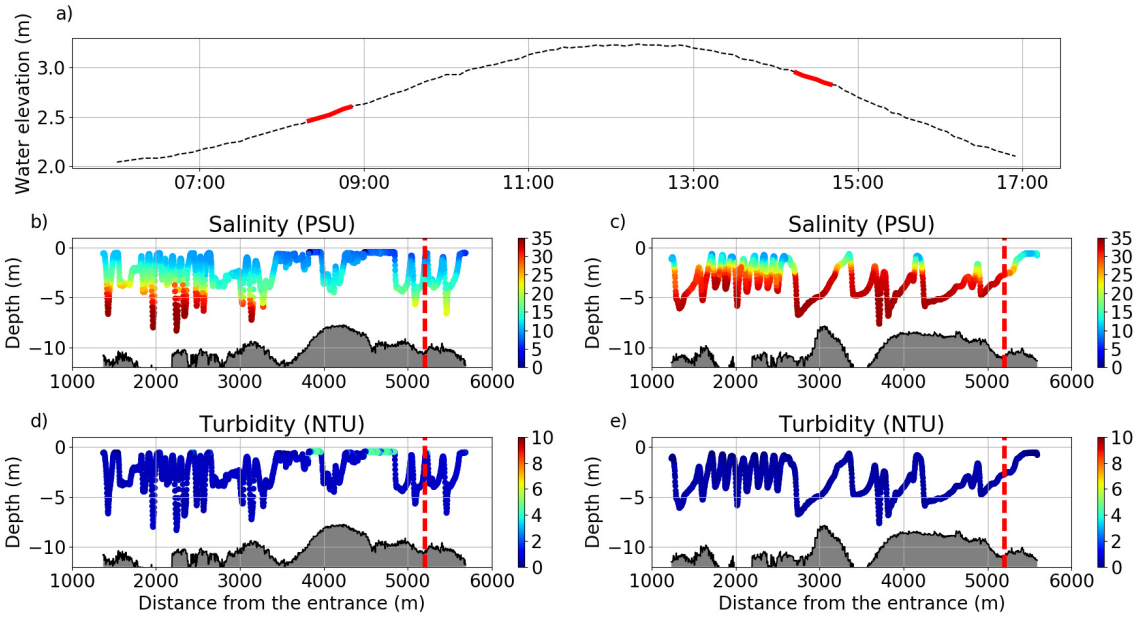

Figure 2.7: Longitudinal and vertical structure across the lower estuary from Minibat measurement during LD-NT17 experiment. (a): Water elevation with measurement periods highlighted in red. (b) and (c): salinity data for rising and falling tide. (d) and (e): turbidity data for falling and rising tide. The bed of the estuary is represented in grey. The red dashed line represents the SF2 station location.

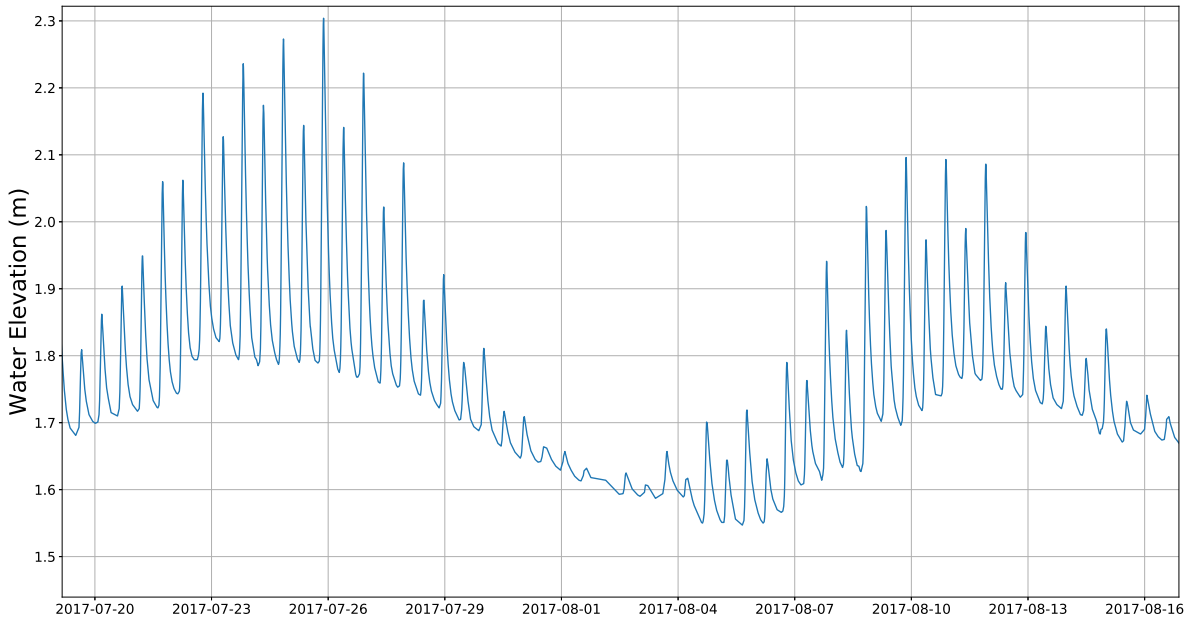

Figure 2.8: Fortnightly fluctuations of the water elevation at Dax village (in the upper part of the Adour estuary).

2.1.2.2 Influence of river

A dedicated experiment (HD-ST18) was carried out during a high discharge event in order to explore the role of river runoff in the hydro and sediment dynamics compared to the reference low river discharge dataset presented above. Figure 2.9 depicts the time evolution of velocity profiles, salinity and Suspended Sediment Concentration (SSC) profiles collected at SF2 station, during high river discharge conditions. The comparison with low discharge conditions presented in Figure 2.3 shows the drastic influence of the river run-off on estuarine dynamics. Similar maximal magnitudes are reached during the ebb, but the velocity profile is almost constant, and the water column is homogeneously fresh. As the tide rises, the water column shows a piston-like behavior, i.e. marine water impounding river water into the estuary with a quasi uniform velocity along the vertical. The current reversal (13:00) occurs much later in the high discharge case, i.e. almost three hours after the low water (09:58), than in the low discharge case. The piston-like behavior remains active throughout the flow reversal and during the main part of the flood tide. This greatly differs from the low discharge case for which a vertical shear of velocity is systematic at the early stage of the flood tide. At the very end of the flood (16:00), the salt-wedge is finally able to reach the measurement area. A 2 m thick bottom salty layer propagates upstream at about 0.5 $m.s^{-1}$. The high river discharge is once again responsible for a significant time lag compared to low discharge conditions in which case the salt-wedge is able to reach SF2 station about 2 h earlier. A remarkable observation, at the salt-wedge arrival, is the rapid seaward reversal of the overlying fresh water layer. The water column forms, therefore, a two-layer vertical structure with strong vertical shear in velocity and a sharp pycnocline. Note that the seaward/landward velocity maxima are reached in the upper parts of the pycnocline and of the salt-wedge, respectively.

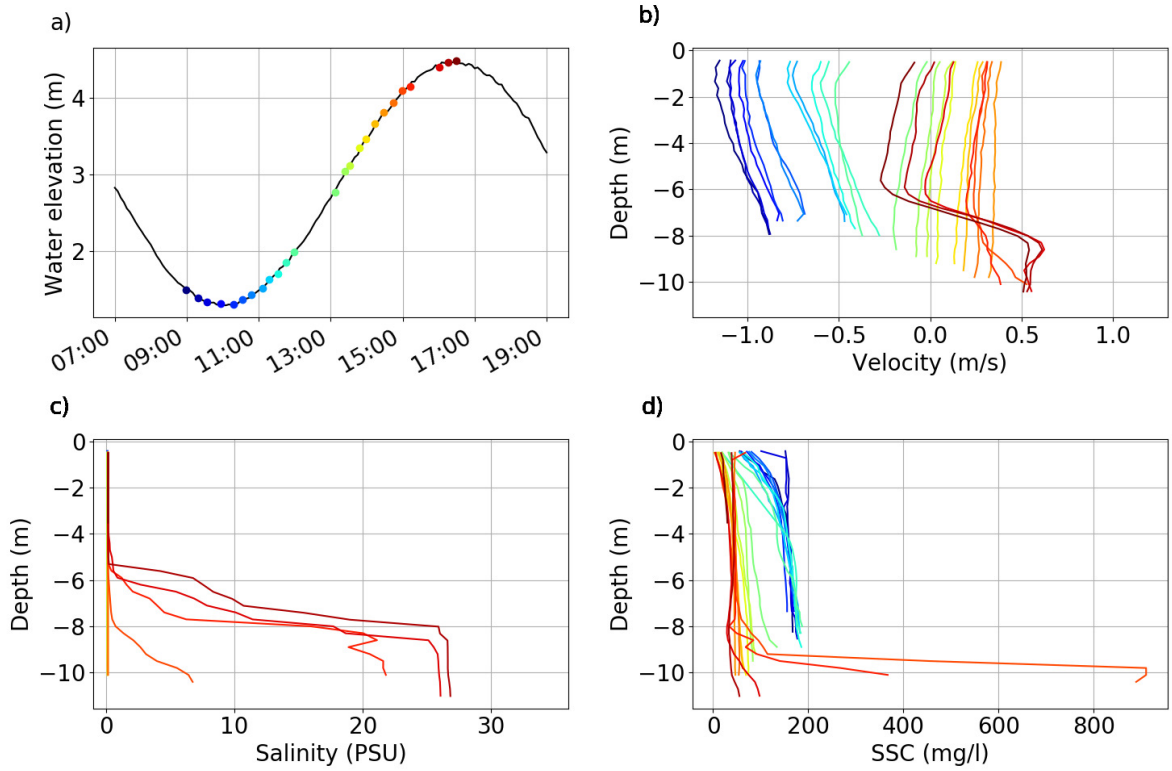

Figure 2.9: Tidal dynamics from HD-ST18 fixed boat surveys during high discharge spring tide conditions, at SF2 station. (a) Water level and timing of measurements. (b), (c), and (d): velocity, salinity and SSC profiles. Note that the same data is presented in contour plots in Figure 2.12.

2.1.2.3 Residual circulation

According to Pritchard [92], when the vertically varying currents are measured through the course of the tidal cycle and then averaged, the estuarine circulation can be revealed. Using the bottom mounted ADCPs velocity profiles collected over one month in September 2017 (i.e. dry season), we were able to highlight two different circulation patterns inside the Adour estuary depending on the tidal range (Fig. 2.10 a)). During neap tides, a two-layer flow appears with a landward bottom flow and a seaward surface flow. The strength of the estuarine circulation is 0.2 $m.s^{-1}$. This pattern seems to indicate that the horizontal salinity gradient is the driving force of the circulation under this configuration, i.e. neap tide and low river discharge. On the other hand, during spring tide, the salinity gradient is less marked, therefore the longitudinal baroclinic pressure reduces. Therefore, the barotropic component of the pressure gradient seems to prevail over the baroclinic component. It indicates that the tidal forcing drives the circulation in the estuary under these conditions. Similar findings of fortnightly switching in forcing, with density-driven flows in neaps and tidally forced flows in springs, has also been observed in the Gironde and Mossoro estuary [103, 122].

Figure 2.10 b) displays the influence of the river discharge on the estuarine circulation. It can be noticed that an increase in the river flow causes a subsequent increase of the seaward currents.

Nevertheless, the tidally-averaged parameters may be questioned in the case of time-dependent salt-wedge estuaries, as the longitudinal density gradient is strongly variable throughout the tidal cycle. We have shown in the previous section that the salt-wedge structure (i.e strong vertical density gradient) can totally break down during the ebb. For example in Figure 2.4, we can see that on spring tides the distance on the bottom between the 5 PSU and 20 PSU isohalines varies

from 500 m during the flood tide to 4 km during the ebb tide, even more so during a high river discharge, when the estuary can be mainly composed of fresh water during the major part of the tidal cycle (Fig. 2.9).

a) b)

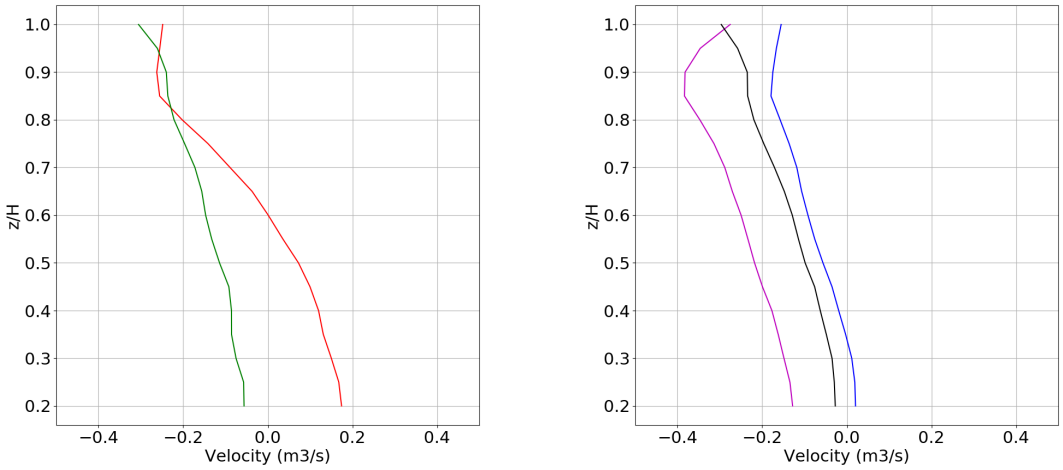

Figure 2.10: a)Tidally averaged velocity profiles for neap (full red line) and spring (full green line) tides with low river discharge, b) Tidally averaged velocity profiles for three different river flow conditions : 391 $m^3.s^{-1}$ (pink line), 128 $m^3.s^{-1}$ (black line), and 89 $m^3.s^{-1}$ (blue line).

2.2 Stratification influence on the turbulent properties

The previous section revealed the complex vertical salinity structure and circulation taking place in the Adour estuary. This first result needs to be investigated further with a turbulent property analysis, to get a better understanding of the interaction between stratification and turbulent mixing. The representation of the Richardson number profile as $log_{10}(Ri/0.25)$ is used in figures 2.11 and 2.12 to estimate the stability of the water column more easily: stable (unstable) flows are expected for positive (negative) values. In addition, high-resolution high-frequency velocity profiles are used to infer the turbulent properties of the flow. Figures 2.11 and 2.12 show the tidal evolution of the vertical distribution of turbulent properties at the survey station SF2 for the low (LD-ST18) and high (HD-ST18) river discharge experiments, respectively.

2.2.1 Low river discharge conditions

Figure 2.11 depicts the data recovered during spring tide and low discharge conditions (LD-ST18). At 08:15, the water column is slightly stratified and the production of turbulence is focused in a very thin layer above the bed, linked to weak turbulent diffusion in most of the water column. The water column becomes homogeneous and the ebb current accelerates during the estuary flushing. The turbulence spreads into the water column except in the 2 m surface layer. The turbulent mixing overcomes the buoyancy forces and the water column becomes fully unstable ($log_{10}(Ri/0.25) < 0$). Maximal values of P_{tke} and ν_t are associated with maximum ebb currents. The eddy viscosity is maximal in the bottom 4 m and reaches typical values (about 1.5 10^{-2} $m^2.s^{-1}$) measured in estuaries for similar velocity and stratification conditions [107]. These measurements also confirms that the eddy viscosity decreases toward the surface [84]. The slack water and the subsequent flow reversal are associated with a drastic drop in turbulence production. After 13:00, the sign change of the Richardson number indicates the

shift toward a stable stratified situation which further reduces the eddy viscosity. At the salt-wedge entrance (around 13:30), a stable stratification develops with no turbulent mixing except an increase of TKE production and eddy viscosity at the tip of the salt-wedge. High values of the Richardson number are associated with the edges of the pycnocline. Bursts of turbulent production seems to develop in the upper layer between 14:00 and 14:30, which may correspond to a local destabilisation of the sheared layer. As the tide rises, the water column turns stable up to the surface with no more turbulent mixing.

In addition, Ri calculations (not shown here) were carried out for neap tide conditions based on profiles shown in figure 2.6. As expected, the nearly permanent vertical salinity stratification promotes stability throughout the water column.

2.2.2 High river discharge conditions

Figure 2.12 presents similar data to that in figure 2.11, but applied on data collected under high river run-off conditions. It is first recalled that Richardson number should be considered with respect to the corresponding velocity and density profiles: nearly neutrally stratified conditions (i.e. unstable conditions) may appear stable in terms of the Richardson number when the velocity shear is very weak. This is for instance the case in the surface layer (Fig. 2.12). During high discharge conditions, the lower estuary is filled with fresh water for most of the tidal cycle, the only exception being the salt-wedge arrival just before high tide (15:00). Therefore, the turbulent property variations differ drastically from the low discharge case shown in figure 2.11. At the end of the ebb tide (before 10:00), the water column is fully fresh and has an almost constant velocity. High rate of TKE production and eddy viscosity are measured at the peak of ebb currents. The strong discharge is able to maintain the instability and a significant TKE production until 12:00 (i.e. more than two hours after low tide). Then, slack water (around 13:00) is associated to a strong drop in turbulence production and eddy viscosity, which remains very weak until the arrival of the salt wedge. However, the piston effect is clearly visible at rising, with nearly vertically uniform velocity profiles during most of the rising tide. The consequence, in terms of stability, is that the lower estuary remains unstable all the time until the salt-wedge is able to reach the measurement station (15:00). A first moderate rise of TKE production is observed near the bottom to a depth of 3m, which indicates that the tip of the salt-wedge is a mixing zone. From that moment, one notes the development of a 1 to 2 m high pycnocline, both strongly stratified and very sheared. Corresponding positive values of the Richardson number indicate the stability of the sheared layer. Peaks of Richardson number are observed near the edges of the pycnocline, associated with more stable areas, whereas the core of the sheared zone is very close to the instability threshold. The TKE production strongly rises near the bottom, but remains confined to the bottom layer because of the overlying stratification effect. It can be noticed that, even if the velocity of entering marine waters is much lower than in the low discharge case, a much stronger turbulent mixing is observed in the bottom layer. The salt-wedge arrival (15:00) is a striking example of a dynamic competition between turbulent mixing and stratification: turbulent diffusion is very active near the bottom and below the pycnocline, but entirely vanishes in the overlying fresh water layer.

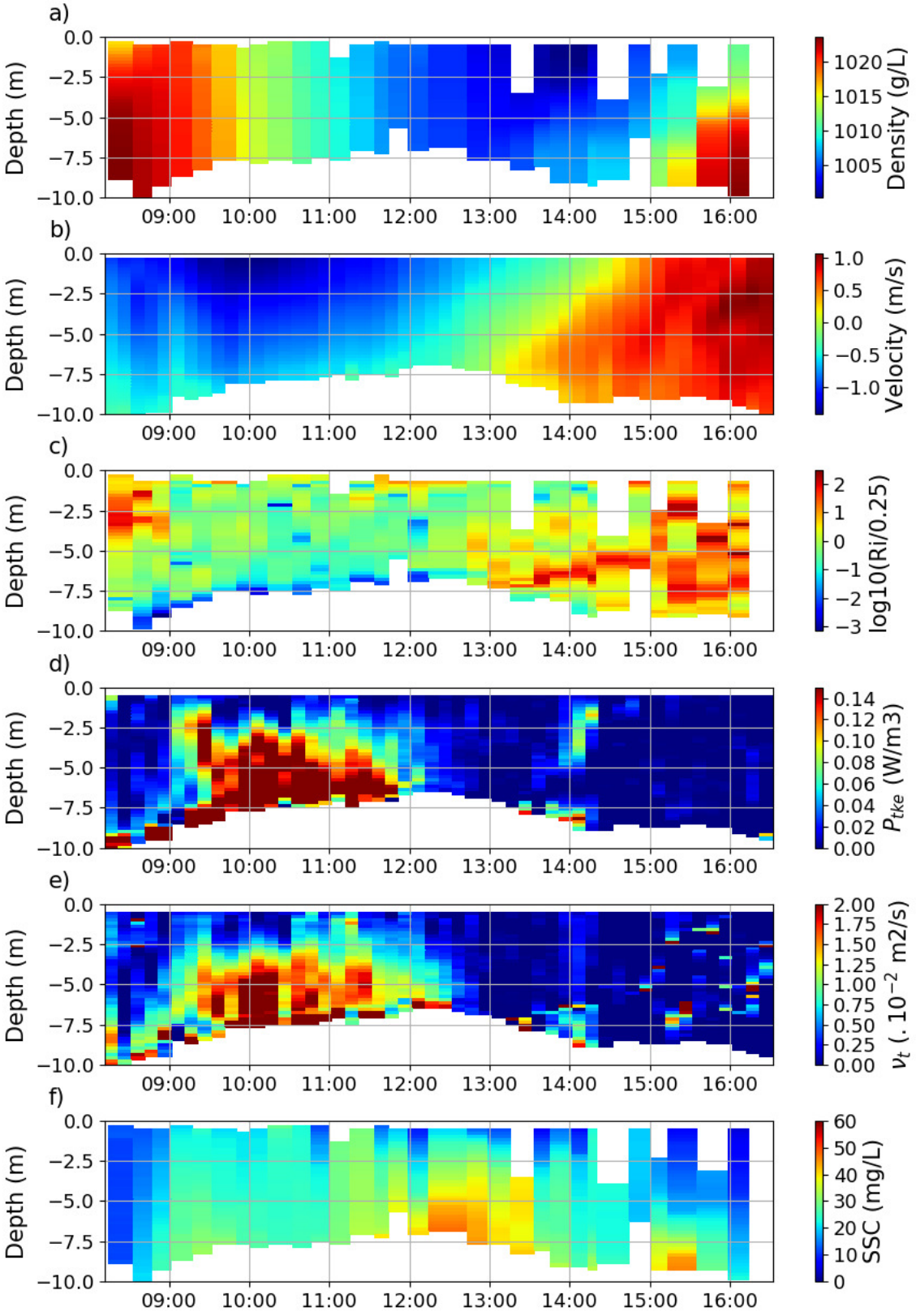

Figure 2.11: Tidal evolution during LD-ST18 experiment : (a) vertical structure of density, (b) time-averaged velocity, (c) Richardson number, (d) production rate of TKE, (e) eddy viscosity, and (f) suspended sediment concentration.

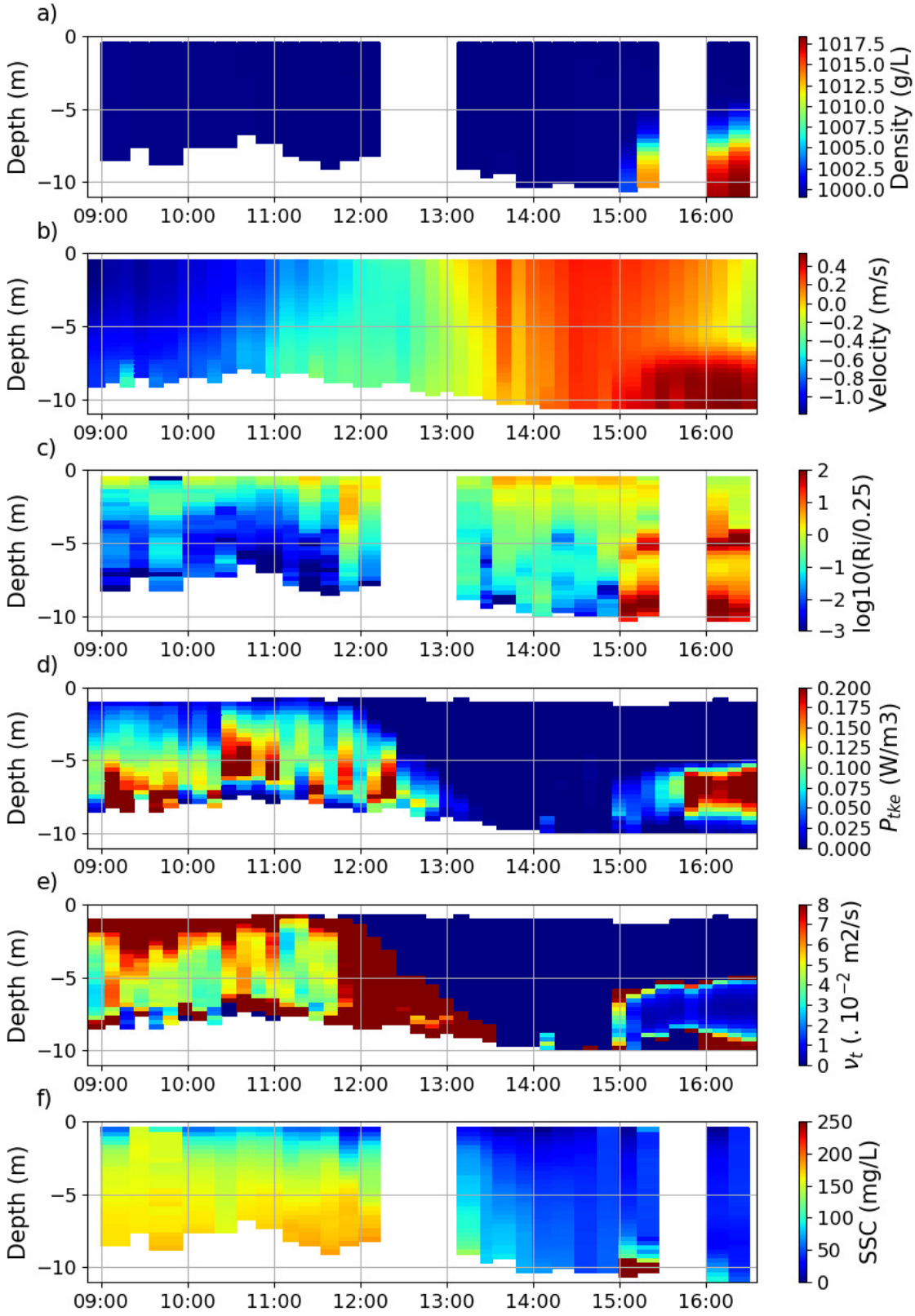

Figure 2.12: Tidal evolution during HD-ST18 experiment : (a) vertical structure of density, (b) time-averaged velocity, (c) Richardson number, (d) rate of TKE production, (e) eddy viscosity and (f) suspended sediment concentration. Note the difference in range compared to Figure 2.11.

Chapter 3

Suspended sediment dynamics

3.1 Variability of the suspended sediment dynamics

A major issue of estuarine dynamics is to understand the fate of the sediment load. Under the competing effects of turbulent suspension and gravitational settling, strong variations of suspended sediments concentration (SSC) are observed in both time (throughout the tidal cycle, the fortnightly cycle and seasons) and space (i.e. along the estuary) [132, 44]. This chapter is thus dedicated to the response of the sediment load to the complex hydrodynamics of the lower Adour estuary presented above.

3.1.1 Influence of tidal forcing

3.1.1.1 Tidal cycle

3.1.1.1.1 Erosion/advection/deposition cycle

In an estuary, throughout the tidal cycle, sediments are alternatively eroded from the bed, advected and deposited on the bed. From mid-ebb to low tide, the shear stress applied on the bed is strong enough to re-suspend sediments and even to erode the bed. The strong turbulent mixing keeps the particles in suspension, while they are advected seaward by the flow. The late ebb phase is associated to the expulsion of suspended sediments from the estuary. In Figure 2.4 d), it can be noticed that a horizontal gradient of SSC develops along the lower estuary, with the SSC decreasing seaward. The vertical mixing is strong enough to homogenize the SSC across the water column. Note the nil SSC surface layer observed in Figure 2.4 d) is a measurement artifact. At slack tide after low tide, i.e. when the velocity reaches a minimum, suspended material settle down , generating a vertical gradient of SSC. At the beginning of the flood (Fig. 2.4 e)) it can be noticed that the horizontal gradient of SSC is impacted by the salt-wedge entrance. The SSC decreases above the salt-wedge. This phenomenon of particles settling due to turbulence damping by the stratification has been observed and reproduced numerically [44, 134]. In addition, it can be clearly seen that the salt-wedge front corresponds to an accumulation of SPM. This accumulation may be caused by the re-suspension and advection of sediments by the salt-wedge entrance, and additionally to the settling of particles from the upper layer. During the flood, this area of high SSC is advected landward. In contrast to the ebb tide, during the flood tide the re-suspension of sediments is constrained by the pycnocline (Fig. 2.11). After the high tide, at the flood slack time, i.e. when the currents reach a minimum, deposition process occurs, generating a vertical gradient of SSC (Fig. 3.1). It can be hypothesized that a temporary pool of sediments is created at the limit of saline water entrance.

3.1.1.1.2 Turbulent mixing and suspended sediment concentration

Figures 2.11 and 2.12 reveal how the generation of turbulence is related to the suspended sediments concentration. It is straightforward during the ebb, when strong turbulent mixing

level can be linked to high values of SSC. At ebb slack, i.e. when currents are very low, no force is able to maintain particles in suspension, leading to strong deposition. During the flood, the turbulence is constrained by the pycnocline and consequently the SSC also.

3.1.1.1.3 No observed Estuarine Turbidity Maximum

Data collected during our field campaigns enables us to analyze the impacts of physical processes taking place inside the Adour estuary on the observed sediment transport. Based on the present dataset, no stable ETM has been observed in the lower Adour estuary (i.e. last 6km).

Further insight is provided by analyzing the main expected ETM drivers detailed in Section 1.3.3.2 of Part I. First, the tidal asymmetry in the Adour estuary has been studied based on the water elevations collected along the estuary. Figure 2.1 outlines that a slight tidal asymmetry of less than 20 minutes exists in the lower estuary. This feature appears too weak to generates an ETM when compared to the Charente estuary [116]. The second ETM driving process is the residual estuarine circulation. In general, no residual estuarine circulation has been observed in the lower estuary (Fig. 2.10). The mean ebbing velocities are stronger than the mean flooding velocities, resulting in a good flushing of water masses and suspended sediment. The only exception is during low riverine and tidal forcing conditions, as observed on the residual tidally-averaged velocity profiles depicted in Figure 2.10 a) (red line). In such conditions, a residual circulation is observed, but its effect in generating a well-developed ETM is likely compensated by limited resuspension due to reduced velocities. Note however than the bottom moored current profilers are not able to resolve the bottom 1.5 m (structure size and blanking zone), which can hide some near-bed processes.

Moreover, it should be noted that riverine input of sediment is very low compared to other tidal estuaries, based on SSC obtained in the present conditions. Even during high river discharge, during the ebb, when the water column is full of fresh riverine waters flowing out the estuary, the SSC is about 150 $mg.L^{-1}$. This very low supply in sediment even during high river discharge might be related to the marshy meadows located along the Adour river, which could be responsible for particle trapping. However, additional surveys are needed to complement the present data set with the first large freshets draining the whole watershed in fall.

3.1.1.2 Fortnightly cycle

A focus on the low river discharge reference case enables us to study the effect of tidal range on sediment dynamics. As previously stated, the tidal cycle has a huge influence on the erosion/advection/deposition cycle. In this chapter, the influence of the fortnightly cycle on the estuarine sediment dynamics is presented.

3.1.1.2.1 Spring tides

A focus on low river discharge conditions enables us to study the effect of tidal range on sediment dynamics. During spring tides, the tidal amplitude is bigger and tidal currents are stronger, thus the impacts of the tides over the erosion/advection/deposition cycle (presented above) are exacerbated. Increased tidal currents lead to a bigger erosion of the bed and a bigger advection of sediment, and reduced slack time results in smaller deposition rates.

On figures 2.11 and 2.3, it can be highlighted that the SSC ranges from 10 to 50 $mg.L^{-1}$. These values are very low, even if we consider they were collected during the dry season, compared to others French estuaries where SSC can reach several grams per liter.

In recent years, ADCPs have been deployed to investigate sediment load fluctuations [97, 113, 114]. The level of echo intensity measured by the ADCP is directly linked to the presence of backscatterers such as suspended matter, bubbles, or living organisms. This level of echo intensity is generally converted in SSC by what is called the "backscatter inversion", based on the Sonar Equation. Unfortunately, this method was applied without any good results on our data. Attempts of backscatter inversion are presented in Annex 2. However, a quantitative

insight can be provided by the raw echo intensity. In general, high level of echo intensity can be associated with high SSC. Figure 3.1 shows raw data of echo intensity measured by the RDI Workhorse sentinel ADCP moored at SF4 station during the dry season at spring (a) and neap (b) tides.

The stratification is clearly marked on the echo intensity data during the flood, as well as the peak of sediment re-susension and deposition (Fig. 3.1 a)). During the flood, it can be noticed that sediments are re-suspended and confined within the bottom layer by the pycnocline. Another striking feature is the decrease of SSC in the layer of fresh continental water flowing above the salt wedge (Fig. 2.11 and 2.4). This observation should likely be attributed to the stratification-induced damping of turbulence, leading to particles sinking. At the end of the flood tide, i.e. when the velocity is maximum, the pycnocline and the suspended sediments reach the surface. The high water slack time is characterized by a vertical gradient of SSC due to particles settling. It progressively leads to an overall SSC decrease. At mid-ebb, sediments are re-suspended up to the surface by the increasing gradient of velocity. In accordance with figure 2.4, a horizontal gradient of SSC is generated inside the estuary, in the opposite direction of the salinity gradient. The late ebb flow produces stronger and longer resuspension than the flood tide. A maximum of SSC is reached at the end of the ebb tide. During the ebb slack, sediments settle down and shortly are re-suspended by the salt-wedge entrance.

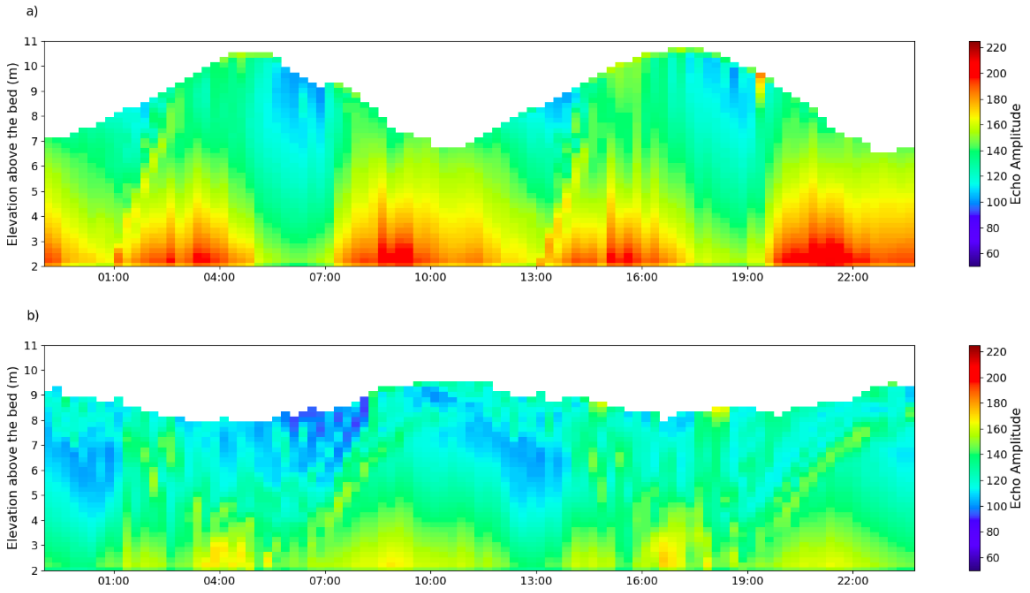

Figure 3.1: Tidal evolution at SF4 of the Echo intensity from moored ADCP station, during (a) LD-ST17 and (b) LD-NT17.

3.1.1.2.2 Neap tides

The influence of the tidal range on the sediment dynamics is straightforward, when comparing the echo intensity for neap and spring tides. During neap tides, levels of echo intensity are very low, in accordance with Figures 2.7 and 2.6. SSC is of about 10 $mg.L^{-1}$ (equivalent to SSC of marine waters), throughout the tidal cycle and quite homogeneous over the water column. Only small peaks of resuspension can be noticed during the flood and the ebb, but they are not able to reach the surface waters. The flood produces stronger and longer resuspension than the ebb tide, which is characterized by two small peaks of resuspension. This could be explained by the absence of re-suspension due to very low velocities and the permanent stable stratification leading to very low turbulent mixing. Those data, associated with reduced salt-wedge velocity and strong density stratification, highlight the incapacity of the estuary to flush out waters or sediment during the dry season at neap tides.

3.1.2 Influence of river discharge

3.1.2.1 Erosion and deposition mechanisms

Figures 2.12 f) and 2.11 f) represent the SSC profiles collected during high discharge (1400 $m^3.s^{-1}$) and low discharge (100 $m^3.s^{-1}$) conditions. Figure 3.2 show the tidal evolution of echo intensity from SF4 ADCP moored station. During high river discharge, the ebbing velocities are stronger and consequently is the sediment transport ability. SSC values are much more higher than those observed during low discharge conditions (Fig. 2.9 and 2.12). During the ebb, SSC is quite homogeneous in the water column, with values about 150 $mg.L^{-1}$. The low tide slack waters are associated to a progressive sedimentation. The SSC first decreases in the surface layers, similarly to the turbulent production. The bigger the river run-off, the shorter the slack duration. Sediments are thus kept in suspension much more longer during high river run-off. Peaks of SSC are stronger and longer. In comparison, during low river discharge, high water slack time are associated with very low values of SSC. Figures 2.12 f) and 2.11 f) reveal that the salt-wedge front passing corresponds to the higher measured SSC, reaching more than 850 $mg.L^{-1}$ in the bottom layer during high river discharge. This area of high concentration is generally associated to the convergence of sediment fluxes from the river directed seaward and from the ocean directed landward. High river discharge conditions result in strong riverine currents and thus it increases the convergence of sediments. Around one hour after the salt-wedge front passing, the SSC at the bottom of the water column decreases. This high turbidity area is thus supposed to follow the up estuary motion of the salt-wedge leading front.

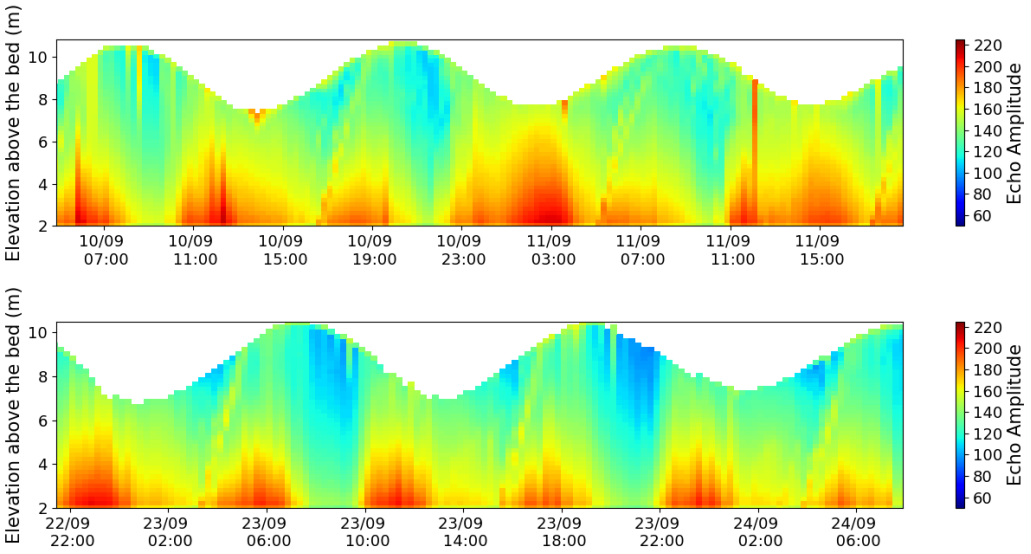

Figure 3.2: Tidal evolution at SF4 of the Echo intensity from moored ADCP station, during (a) high river discharge (400 $m^3.s^{-1}$) and (b) low river discharge (90 $m^3.s^{-1}$) conditions.

3.1.2.2 Suspended sediment transport

3.1.2.2.1 Suspended sediment fluxes

Based on velocity and suspended sediment concentration data collected during LD-ST18 and HD-ST18, sediment fluxes were calculated and they are presented on figure 3.3. The riverine forcing affects largely the sediment fluxes. During low riverine forcing, the sediment flux is directed seaward during the ebb, with transport concentrated on the surface, while during the flood, the flux is directed landward and it is focused on the bottom of the water column. It should be noted that the tidal cycle is not fully covered by the data presented on figure 3.3. However, the sediment flux expelled from the estuary during the ebb seems mostly compensated by the flood sediment input (Fig. 3.4).

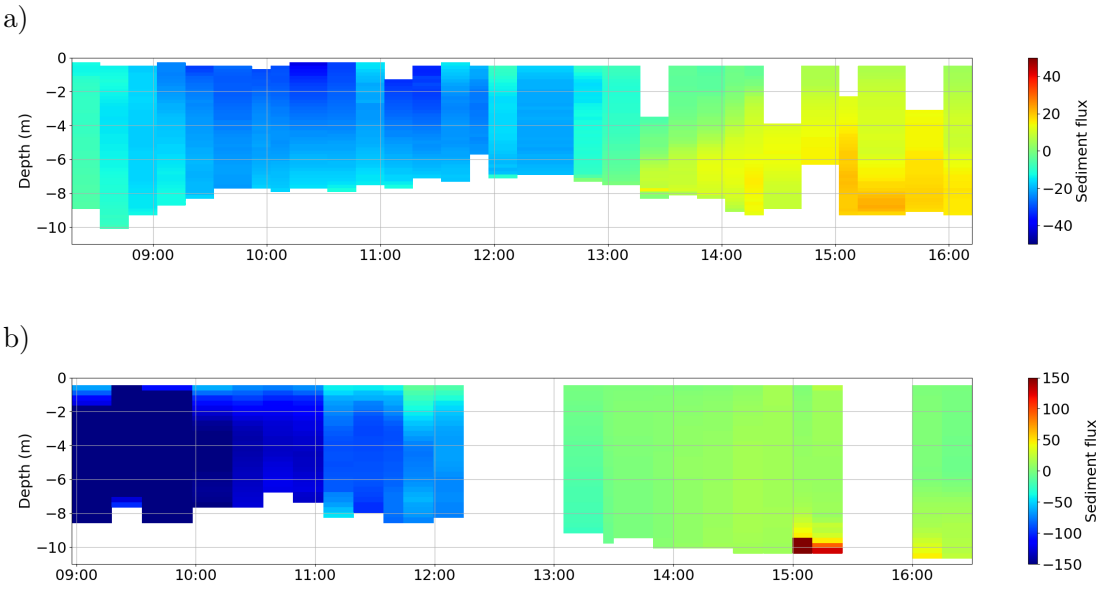

Figure 3.3: Tidal evolution of sediment fluxes per unit of cross-sectional area ($kg.m^2.s^{-1}$) at SF2 station during : a) LD-ST18 and b) HD-ST18.

A completely different dynamics was observed under high riverine forcing, with sediment fluxes much more homogeneous. During the ebb, the seaward sediment flux is four times more important than during low discharge conditions. The flux decreases progressively with the current reversal, at mid-flood the flux is almost nil throughout the water column. It keeps being very low during the rest of the flood, except at the salt-wedge passing, where a strong sediment flux directed landward occurs in the last 1m of the water column. The averaged sediment flux is mainly directed seaward (Fig. 3.4). This confirms the good sediment flushing capacity of the estuary during high river discharge.

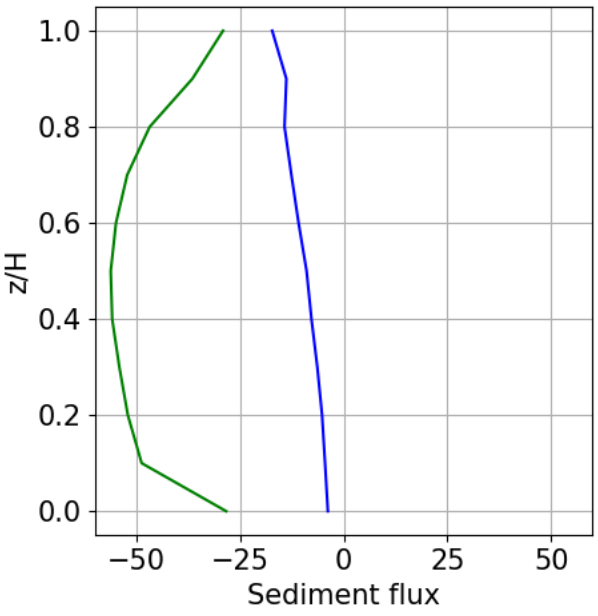

Figure 3.4: Averaged sediment flux for LD-ST18 (blue line) and HD-ST18 (green line). It should be noted that data was not collected during the full tidal cycle due to operating limitations.

3.1.2.2.2 Residual path

The residual path of suspended particles was calculated based on moored ADCP data. The residual path is considered to be the integral of the depth-averaged velocity over a tidal cycle (Fig. 3.5). The residual path during the dry season was estimated to about 5.5 km seaward. This residual path is largely influenced by both river discharge and tidal range. For a tidal amplitude of 3.3 m, the residual path is estimated to 10 and 5 km for 400 and 90 $m^3.s^{-1}$ discharges, respectively. For a river discharge slightly less than 100 $m^3.s^{-1}$, the residual path is estimated to 5 and 2 km for 3.6 and 1.1 m tidal amplitude, respectively. As expected, during spring tide and high river discharge conditions the residual path is longer than during neap tide and low river discharge conditions. In all cases, the residual path is directed seaward, it confirms the good flushing capacity of the lower Adour estuary, in particular during high discharge conditions.

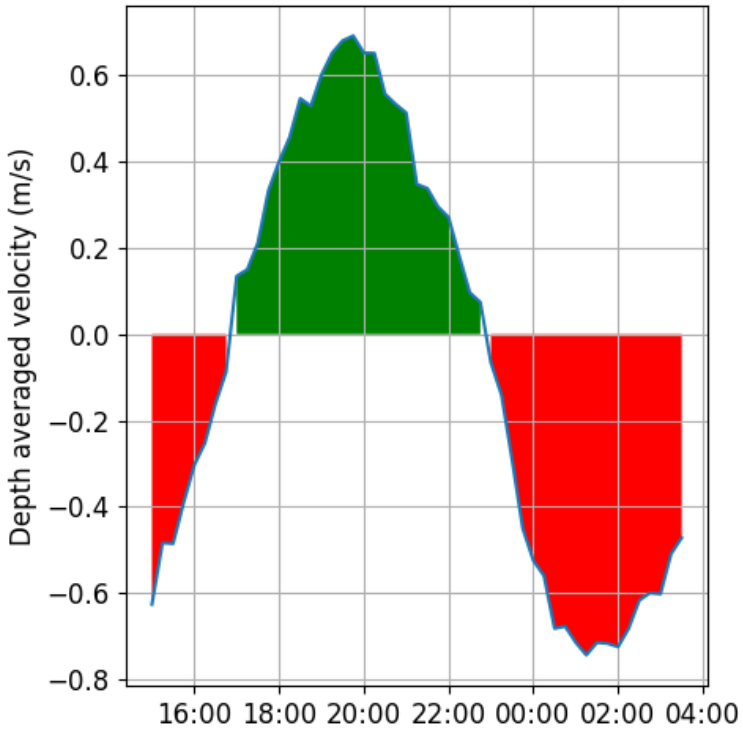

Figure 3.5: Depth averaged velocity over a tidal cycle, based on data collected by the bottom-moored ADCP at SF2 station. The green area represent the residual path traveled during the flood tide by a particle in suspension, while the red area is the residual path traveled during the ebb tide.

3.1.3 Adour river plume

The observed influence of tidal range on the lower estuary has also a strong effect on the ejected plume. At spring tide during the dry season, continental waters are blocked inside the estuary by the marine waters entrance for about three hours. This mechanism drives the pulsed behaviour of the plume of the Adour estuary already highlighted by Dailloux [23]. By contrast, at neap tide during low discharge conditions or under high discharge conditions, a layer of continental water is flowing seaward all along the tidal cycle at the top of the water column, almost constantly feeding the plume leaving the estuary with fresh water. The pulsed behaviour of the Adour estuary should therefore take place only when the tidal forcing is able to overcome the riverine forcing, and so the riverine waters are blocked into the estuary by the marine water entrance.

3.2 Suspended sediments characteristics

3.2.1 Size and density

During the boat survey, particle size profiles have been undertaken at spring and neap tides. Due to LISST limitations, almost all the data collected at neap tide, i.e. when the water column is strongly stratified, have been discarded. Particle sizes ranged mostly between 70 μm and 160 μm, whereas the excess density ranged from 200 to 1400. No relationship between the density of the ambient water and particles characteristics can be found.

Water samples were also collected during our first field campaign (September 2017) on spring and neap tides. They were analyzed by laser scattering at EPOC Laboratory (Fig. 3.6). The median diameter of particles ranged from 14 to 99 μm. These data comparable with the one collected with the LISST at similar period, taking into account as the method used by the EPOC laboratory breakdown the potential flocs contained in the water, leading to smaller D50 values. Various samples were contaminated with an unknown white and translucent substance, and thus these data are not presented in this study.

Figure 3.6 demonstrates the influence of tidal cycle on the type of particles in suspension. Post-slack times during flood and ebb are characterized by the smaller particle distributions, due to settling induced by low velocity. The increased velocities at high and low tides are associated with a shift of the distribution toward larger sizes. At high tide two populations of particles are observed near the bottom. The first dominant peak is typical of riverine sediments (silt-clay), while the second peak of larger particles, up to 2mm, reveals the present of sand coming into the estuary or re-suspended by the salt-wedge entrance. A vertical sorting is observed where surface data are available, with larger sizes near the bottom.

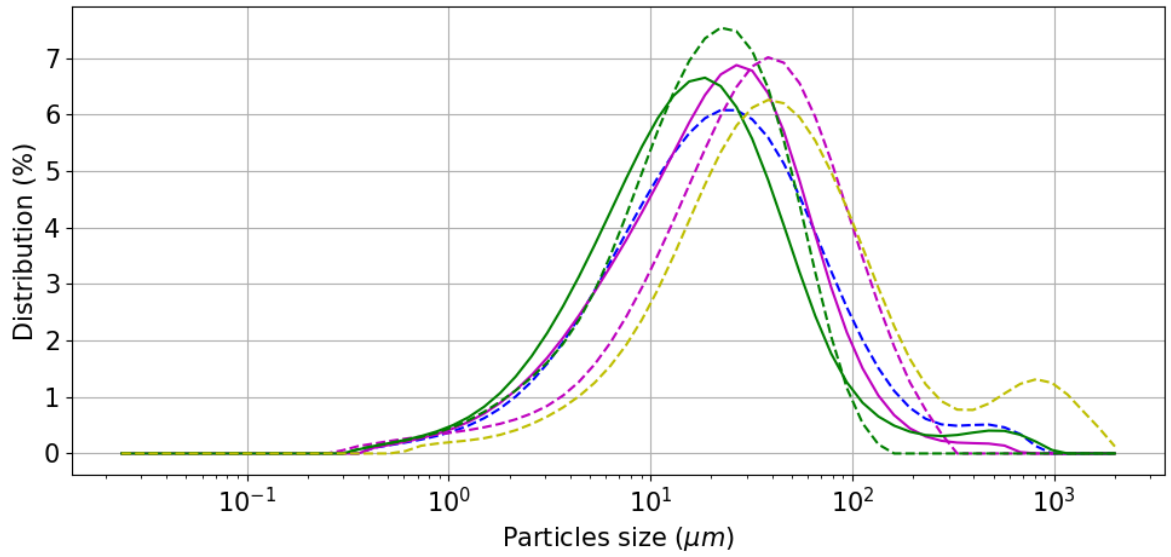

Figure 3.6: Particle size distribution analyzed by laser scattering at EPOC Laboratory and collected on spring tide at : high tide (yellow), mid-ebb (blue), low tide (magenta), and mid-flood (green), where dashed lines represent samples collected on the bottom of the water column and full lines represent the ones collected on the surface.

3.2.2 Hysteresis cycles

Turbidity data (from the YSI probe fixed on the floating pontoon) have been combined with daily Adour river discharge to compute hysteresis cycles (Fig. 3.7 and 3.8). These counter-clockwise cycles confirm the ones obtained with the former sets of data previously presented.

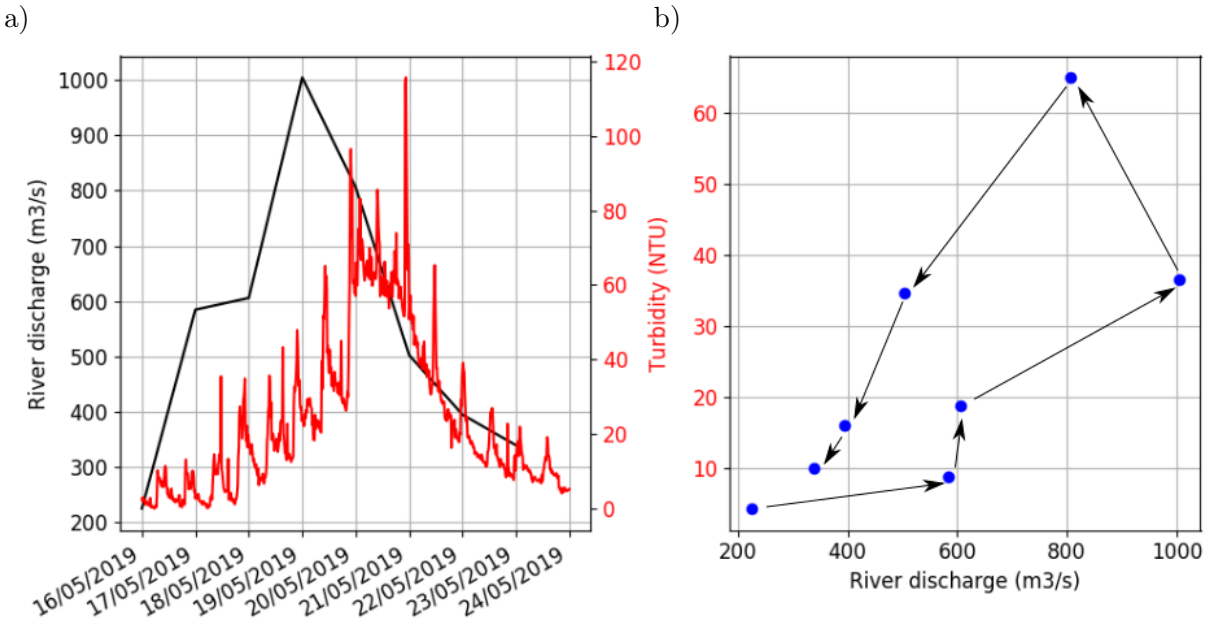

Figure 3.7: a) Turbidity (NTU) in red, and river flow ($m^3.s^{-1}$) in black, along the freshet period, b) Turbidity (NTU) in function of river flow ($m^3.s^{-1}$). ρ/ρ_0 (ρ_0 being the water density). Data collected in the lower Adour estuary on a floating pontoon (c.a. 5 km from the mouth of the estuary).

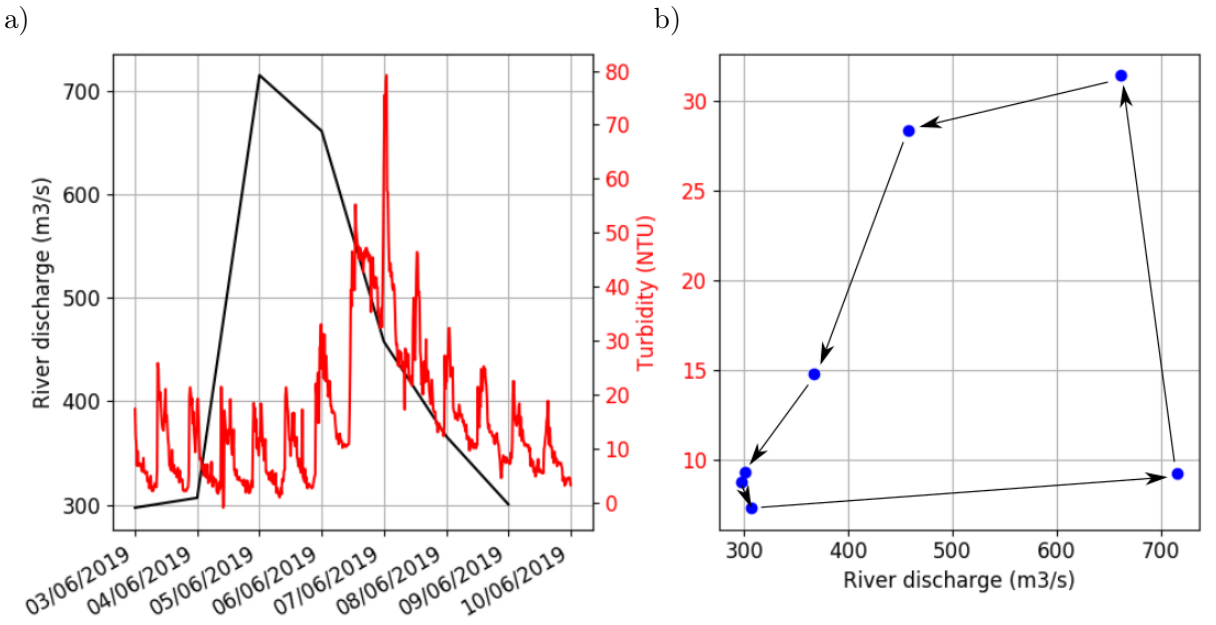

Figure 3.8: a) Turbidity (NTU) in red, and river flow ($m^3.s^{-1}$) in black, along the freshet period, b) Turbidity (NTU) in function of river flow ($m^3.s^{-1}$). Data collected in the lower Adour estuary on a floating pontoon (c.a. 5 km from the mouth of the estuary).

Different hypothesis that can explain counter-clockwise cycles were presented in Part I: "Different explanations can be given to such behavior : (1) a distant catchment of SPM, (2) some disturbance on the way which could slow down the dispersion of particles but not the water discharge, and (3) the water discharge of one tributary, richer in SPM, is delayed from the others." In order to confirm one or several of these hypothesis, we used the data collected by the MESsAGe network. The MESsAGE network was put in place in 2015, by the Adour-Garonne

Water Agency in collaboration with GEO-transfert. This network has been developed to follow up the sediment in suspension fluxes, as well as the pollutant fluxes. Two stations are located on the Adour river watershed, one located on the Adour river at Saint Vincent de Paul and the other one located on the Gave de Pau river at Labatut. In 2018, sediment fluxes were estimated to 368000 $t.yr^{-1}$ and 183900 $t.yr^{-1}$ for the Gave de Pau river and the Adour river, respectively. Values of SSC can reach up to 1.1 $g.L^{-1}$ in the Gave de Pau river, while they reach only 400 $mg.L^{-1}$ in Saint-Vincent de Paul.

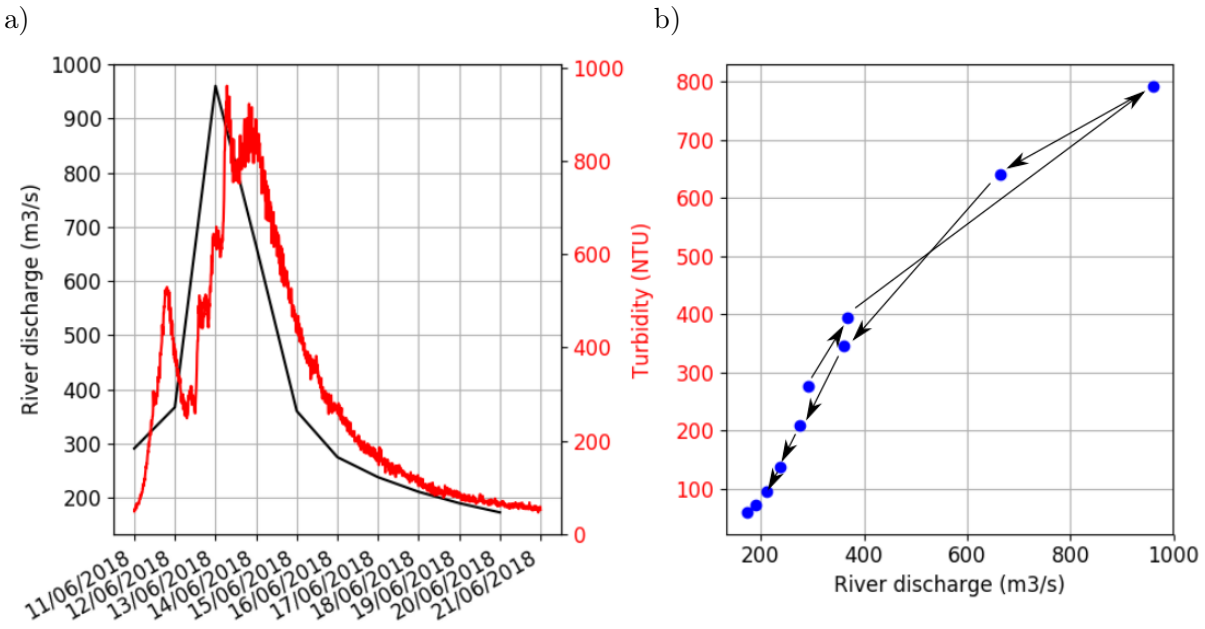

Figure 3.9: a) Turbidity (NTU) in red, and river flow ($m^3.s^{-1}$) in black, along the freshet period, b) Turbidity (NTU) in function of river flow ($m^3.s^{-1}$), based on data collected at Labatut.

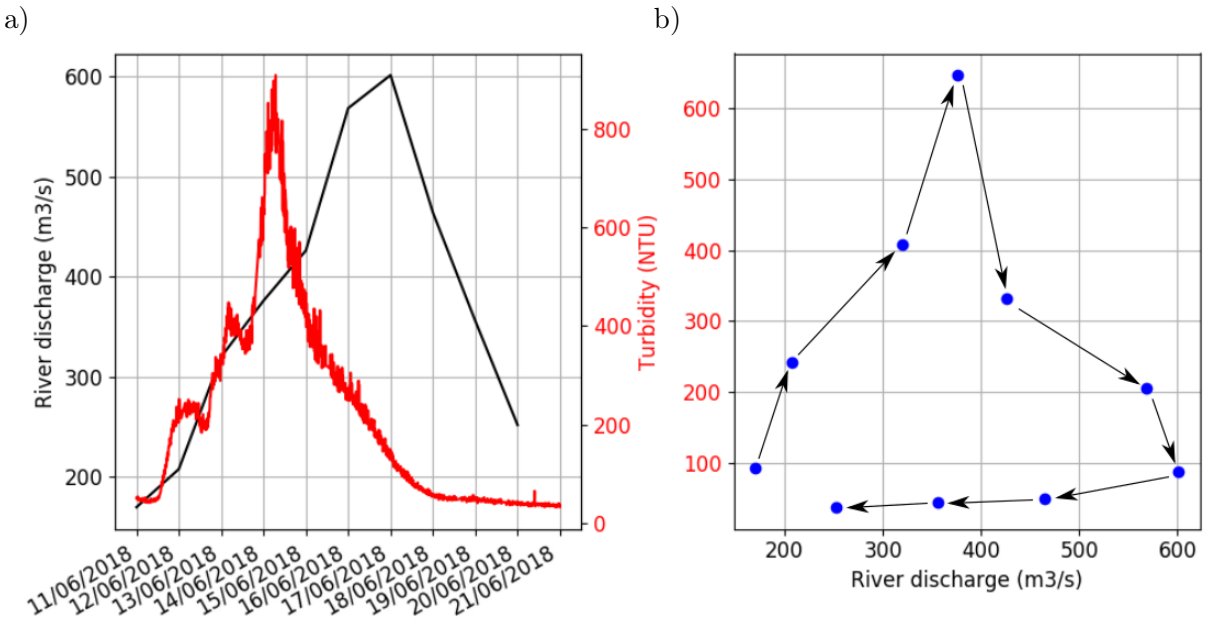

Figure 3.10: a) Turbidity (NTU) in red, and river flow ($m^3.s^{-1}$) in black, along the freshet period, b) Turbidity (NTU) in function of river flow ($m^3.s^{-1}$), based on data collected at Saint Vincent de Paul.

Figures 3.9 and 3.10 are hysteresis cycles realized with data collected respectively at Labatut (Gave de Pau river) and Saint Vincent de Paul (Adour river), for the same freshet event (June 2018). In Labatut, the hysteresis cycle has a single-line shape, i.e. both peaks of turbidity and river flow are almost simultaneous. On the other hand, the hysteresis cycle made with data from Saint Vincent de Paul is a clockwise cycle, i.e. the turbidity peak is reached before the river flow peak. For the same freshet, we can see that both turbidity peaks are reached on the same day (i.e. 14/06/2018), with a delay of only a few hours. However, river flow peaks are not reached at the same time and with different intensity on both sites. A 4-day delay can be noticed between them. This seems to indicate that hypothesis 3 is invalid, as the sediment peaks are reached simultaneously on the river and one of the major tributaries.

The single-line hysteresis cycle obtained with data from the Gave de Pau river and the fact that SSC could reached values up to 1.1 $g.L^{-1}$ could be explained by a sediment catchment located close by this station. A sediment catchment located in the Gave de Pau river could confirm hypothesis 1. The clockwise hysteresis cycle obtained with data collected in the upstream part of the Adour estuary could be the sign of a depletion of available sediment before the water discharge has peaked [137]. If we combined this with the relatively low values of SSC reached during the freshet, it seems to indicate that there is few sediment available in this reach of the estuary. During the high river discharge, such as the one observed during June 2018 of about 3000 $m^3.s^{-1}$ in the lower estuary, a lot of areas normally dry are submerged. These marshy meadow areas named Barthes are presented on the following page (blue areas). These areas could be responsible for particles trapping, that could explain that high values of SSC observed in the Gave de Pau river are not observed in the lower reach of the estuary (hypothesis 2). To confirm this hypothesis, the measurement of turbidity in the lower estuary with the YSI probe should be maintained and combined with the MESsAGe network measurement.

NATURA 2000

Association Barthes Nature

CPIE SEIGNANX ET ADOUR

Site Natura 2000
FR7200720 Barthes de l'Adour

Zone de Protections Réglementaires

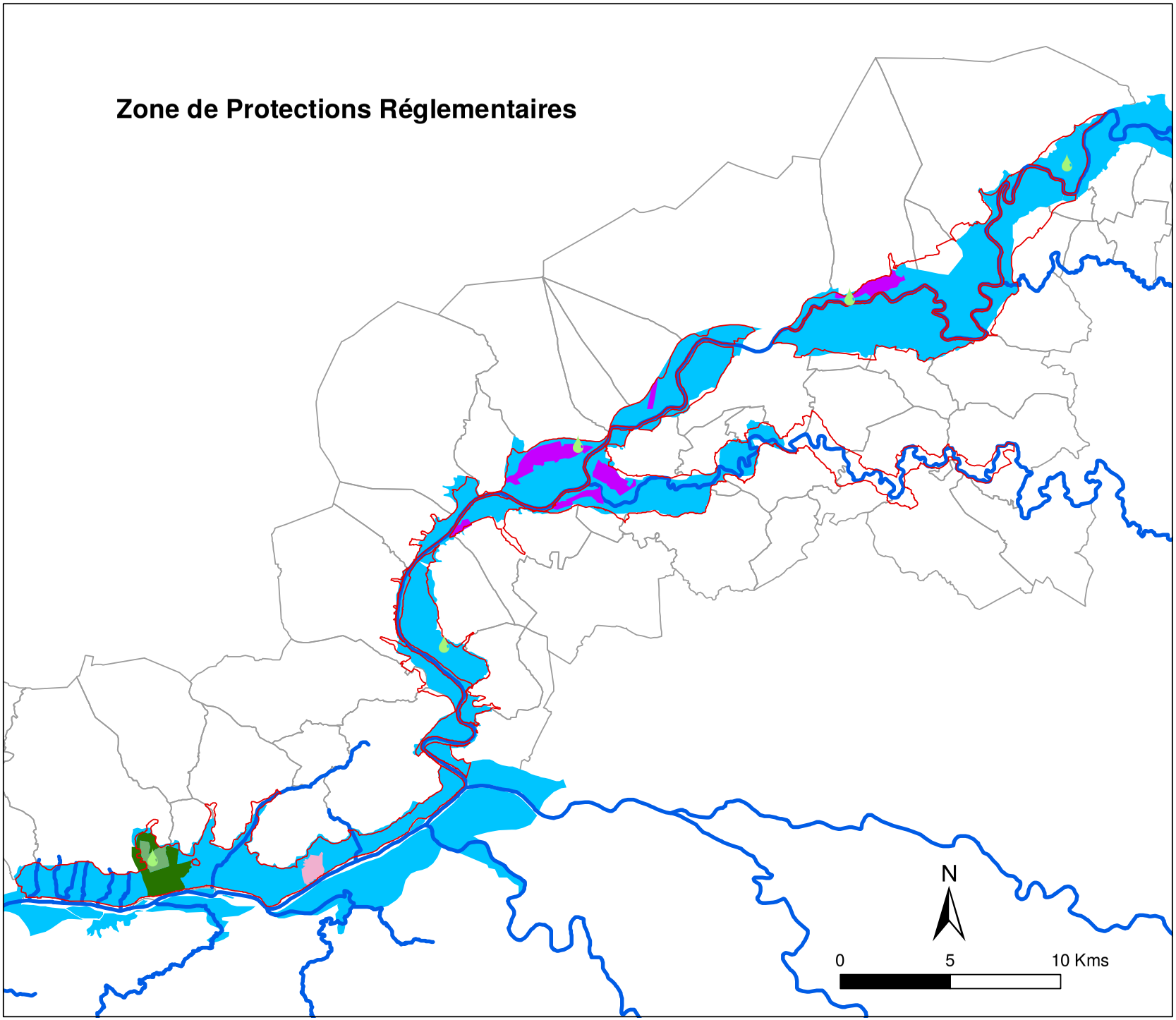

Périmètre du site

Limites communales

Réserves de Zone Humides
Fédération Des Chasseurs (40)

Axes prioritaires pour les poissons migrateurs
(SDAGE 2010-2015)

Zones humides associées à l'Adour à forts enjeux environnementaux
(SDAGE 2010-2015)

Espaces Naturels Sensibles (ENS)

Zone de préemption ENS - Tourbière de Passeben

Arrêté Préféctoral de Protection de Biotope (APPB)

Réserve de Lesgau (zone centrale) - St Martin de Seignanx

Réserve de Lesgau (zone périphérique) - St Martin de Seignanx

CPIE Seignanx et Adour

Source : IGN 2007 (DREAL Aquitaine)

Août 2011

Chapter 4

Synthesis & Discussion

4.1 Estuarine circulation

In this section, general features of the Adour estuary dynamics are presented and discussed. We start by presenting a general circulation of the water masses and salinity occurring in the Adour estuary. A second section details the high variability of the Adour estuary dynamics according to the hydrological conditions. Thirdly, the Adour estuary is classified according to different schemes presented in Part I. Finally, possible impacts of the human intervention are discussed.

4.1.1 General dynamics

4.1.1.1 Tidal wave and circulation

Figure 4.1 presents the schematics of the Adour estuary dynamics throughout a tidal cycle. The evolution of water elevation and velocity are presented, as well as the vertical structure of velocity, salinity and eddy viscosity, throughout a tidal cycle. At the mouth of the estuary, the tidal wave is symmetrical and it has a mean amplitude of 2.5 m (**mesotidal**) and a period of about 12h (**semi-diurnal**). The tidal wave is considered **quasi-progressive**, as the maximum velocity occurs one hour before high and low tide time, and minimum velocity is reached one hour before mid-tide. The maximum rising velocity is characterized by a logarithmic profile and a value of about 1 $m.s^{-1}$, while the maximum falling velocity is characterized by a sheared profile and a value of about 1.5 $m.s^{-1}$. Flood slack time is marked by a two-layer flow with a bottom layer moving landward and a surface layer moving seaward, while at the ebb slack time the full water column reverses to move seaward. Shortly after the ebb slack time, the marine water entrance prevents the riverine water from moving seaward, i.e. the flow goes from a two-layer structure to a one-layer structure.

4.1.1.2 Stratification and generation of turbulence

At the beginning of the flood, marine water entrance has a wedge shape, leading to both strong vertical and horizontal density stratifications, and a small turbulence at the salt-wedge front. As the tide rises, the bottom layer increases both in thickness and salinity, while the strong stratification damps down the generation of turbulence. The strong velocity shear produced at the falling tide generates turbulence all over the water column, resulting in a stratification break-down and almost vertical isohalines. At the end of the ebb, almost all the marine waters are expelled from the estuary and the estuarine structure is reset.

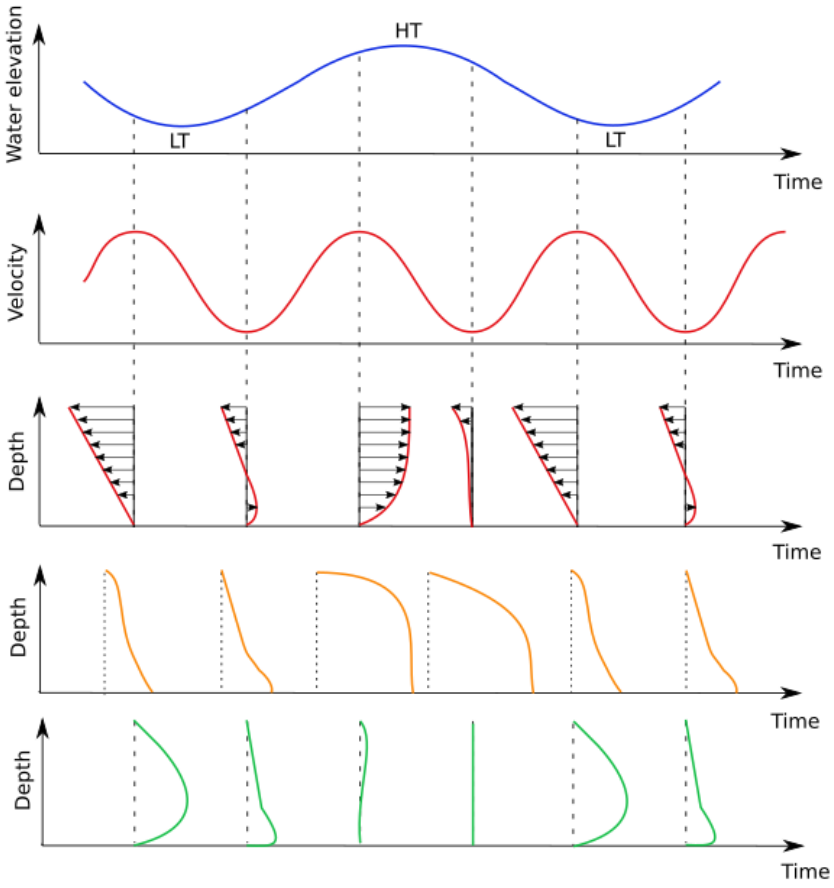

Figure 4.1: Schematic of the Adour estuary dynamics throughout a tidal cycle, with time series of water elevation (blue line) and velocity (red line), and vertical profiles of velocity (red lines), salinity (orange lines) and eddy viscosity (green lines).

4.1.2 High variability of the hydrodynamics

In addition to the typical pattern shown in Figure 4.1, the present in-situ dataset revealed the high variability of the Adour lower estuary, in terms of hydrological functioning (Fig. 4.2). A salt-wedge generally develops during the flood tide of the Adour lower estuary. This salt-wedge depends on river discharge, by being more steeply marked during the wet season due to strongly river forcing. In addition, the tidal forcing is also an important driver of the Adour estuary (mesotidal system) with a strong effect of the spring/neap cycles on the estuarine salinity structure. Under low discharge conditions, the neap tides are associated to fully vertically stratified estuary throughout tidal cycle, while during spring tide the salt-wedge shape is lost during the ebb, and a horizontal salinity gradient takes place. The analysis of the tidally averaged velocity revealed a switch of the driving force during the fortnightly cycle during the dry season, with a density-driven flow during neap tide and a tidally forced flow during spring tide.

Turbulent properties showed a significant response to the variations of salinity structure, with higher values when stratification is minimal. At spring tide, a tidal variation between mixing conditions on the ebb and the flood is revealed by ADCP measurements, with higher values extended up to the surface during the ebb. However, during neap tide, the permanent stratification leads to a very stable configuration.

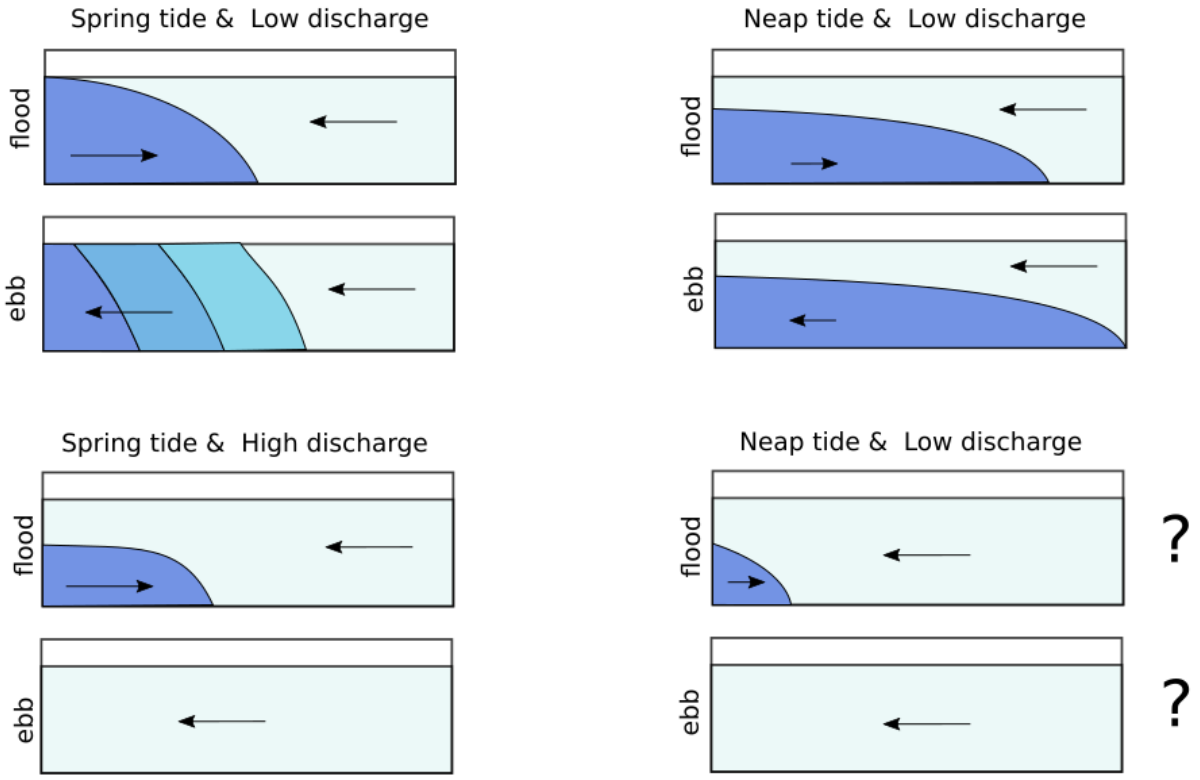

Figure 4.2: Schematic of the salinity stratification in the Adour estuary for the four forcing conditions : Spring tide & Low discharge, Neap tide & Low discharge, Spring tide & High discharge, and Neap tide & Low discharge, based on field data. The last configuration has "question marks", because no data are available for this configuration, it is an hypothesis.

4.1.3 Classification of the Adour estuary

It is of particular interest to know the extent to which the variability of the Adour estuary can be described by the different classification schemes and to evaluate how it can compare to other typical systems selected for their contrasted dynamics.

We have seen that the Adour estuary is subjected to a **semi-diurnal mesotidal** forcing. The tidal wave propagation is mostly impacted by bottom friction, resulting in a **hyposynchronous** estuary, except during neap tide, when the tidal asymmetry is flattened and the estuary can be considered as **synchronous**. According to its salinity stratification, which is reset at each tidal cycle, the Adour estuary has been classified as a **time-dependent salt wedge**.

An adaptation of Geyer and MacCready's regime diagram [46] is proposed in Figure 4.3, with the M and Fr_f ranges reached by some well-documented estuarine systems in order to easily compare with the Adour estuary. For the calculation of both parameters, we considered $\beta = 7.710^{-4} PSU^{-1}$, H to be a characteristic value of the water depth $H = 10m$, the salinity of ocean $s_{ocean} = 34.5$ PSU. A first remark should be made about the uncertainty surrounding the estimation of the mixing parameter M. This parameter shows a strong sensitivity to both U_T and C_D values, whose the estimation is not straightforward. In Geyer et al 2014 [46], U_T is defined as the amplitude of the depth-averaged tidal velocity, while it has been estimated as the rms velocity 3m above the bed in Geyer et al 2000 [48] and considered equivalent to the maximal velocity in Li et al 2014 [76]. For the present study, the reference value of U_T is provided by rms depth-averaged velocity measured at the SF2 bottom moored station (Fig. 1.10). The bottom drag coefficient C_D can also be strongly spatially variable inside an estuary, and is relatively challenging to estimate. In Geyer et al. 2014 [46], the authors consider that C_D generally varies between 1 and 2.5 10^{-3} inside an estuary, while Geyer et al. 2010 [50] mention a value of C_D

generally about 3 10^{-3} inside estuaries. As far as the Adour estuary is concerned, two-point current-meters deployed in the bottom layer were used by Sous et al [111] to estimate a C_D value about 1.5 10^{-3} at SF4 station, which is used here as a reference for the estimation of M.

Using data collected inside the Adour estuary, U_R estimation ranges from 0.05 to 0.75 $m.s^{-1}$, therefore Fr_f should range from 0.03 to 0.46 for low to high discharge conditions, respectively. The mixing parameter M, based on reference values for U_T and C_D, ranges from 0.36 to 0.66 for neap to spring tide conditions, respectively (Fig. 4.3, solid line rectangle). In order to illustrate the M sensitivity to U_R and C_D parameters, estimating now U_T as the maximal entering velocity together with a C_D value of 3 10^{-3} will shift the Adour's system toward higher ranges of mixing parameter values (0.68 to 1.13), cf. dashed line rectangle in Figure 4.3. In addition, the values of the mixing parameter might be increased further with data from neap tide conditions combined with high river run-off, which are not documented by the present dataset.

Keeping these limitations in mind, the estuarine parameter space diagram proposed by Geyer and MacCready [46] confirms the variability of the hydrological functioning of the Adour estuary in comparison to other typical systems (Fig. 4.3). It should be noted that the large area covered by the Adour river in this diagram is due to the highly contrasted hydrological conditions encountered during our measurements. Others systems may have been observed only during mean hydrological conditions, leading to reduced rectangles. Based on the collected data, presented in this paper, we can analyze the observed dynamics of the Adour estuary.

Under high tidal mixing conditions (i.e. high M value), the Adour river dynamic is quite similar to those of the Fraser [45], the Changjiang [76] and the Merrimack rivers [95], which are all considered as **time-dependent salt-wedge estuaries**. These energetic and stratified estuaries are characterized by strong tidal and riverine velocities and the dominance of tidal salt fluxes over residual circulation (Fig. 2.10). It results in a strengthened stratification during the flood, that weakens during the ebb tide, where the turbulence develops in the full water column.

Under low tidal mixing conditions (i.e. low M value), the Adour tends to show a behavior similar to that of the Ebro river. The latter has a similar shape and river discharge as the Adour, but the microtidal regime (associated to a low M) results in a stagnant salt-wedge under low river run-off ejected out of the estuary when the river discharge exceeds 500 $m^3.s^{-1}$ [60]. Measurements undertaken during neap tide and low river discharge in the Adour estuary reveal a similar pattern with an almost **stagnant salt-wedge** and strong stratification. Unfortunately, observations were not carried out during neap tide and high river discharge (around 1500 $m^3.s^{-1}$), but we can expect an absence of salt-wedge or at least a strong reduction of the saline intrusion.

The role of river discharge is, however, clearly identified for spring tides, corresponding to fluctuations along the Fr_f axis in Figure 4.3 for high values of M. **Under low river discharge conditions** (i.e. low Fr_f value), the influence of tidal mixing is more important, leading to a smoother vertical stratification and a **strongly stratified regime**. During the ebb, the peak of turbulence can be sufficient to break down the vertical stratification and generate a horizontal stratification. This horizontal stratification is a typical attribute of **partially mixed regime**. When the river discharge increases (i.e. higher Fr_f values), the vertical stratification appears to be stronger, with a sharper pycnocline and a salt-wedge restricted to the lower part of the water column.

Finally, Geyer and MacCready's study concludes that: *"Estuaries with intermediate mixing rates show marked transition between these regimes at timescales of the spring-neap cycle"*, which is in accordance with our observations made during the dry season in the Adour estuary, i.e. density-driven flows during neaps and tidally forced flows during springs.

Nevertheless, as previously stated in the subsection "Residual circulation" and mentioned by Geyer and MacCready, in estuaries subjected to energetic tidal forcing, the mixing is strong enough to destratify the water column during part of the tidal cycle, therefore to take the tidal average is an inherent limitation of this classification scheme.

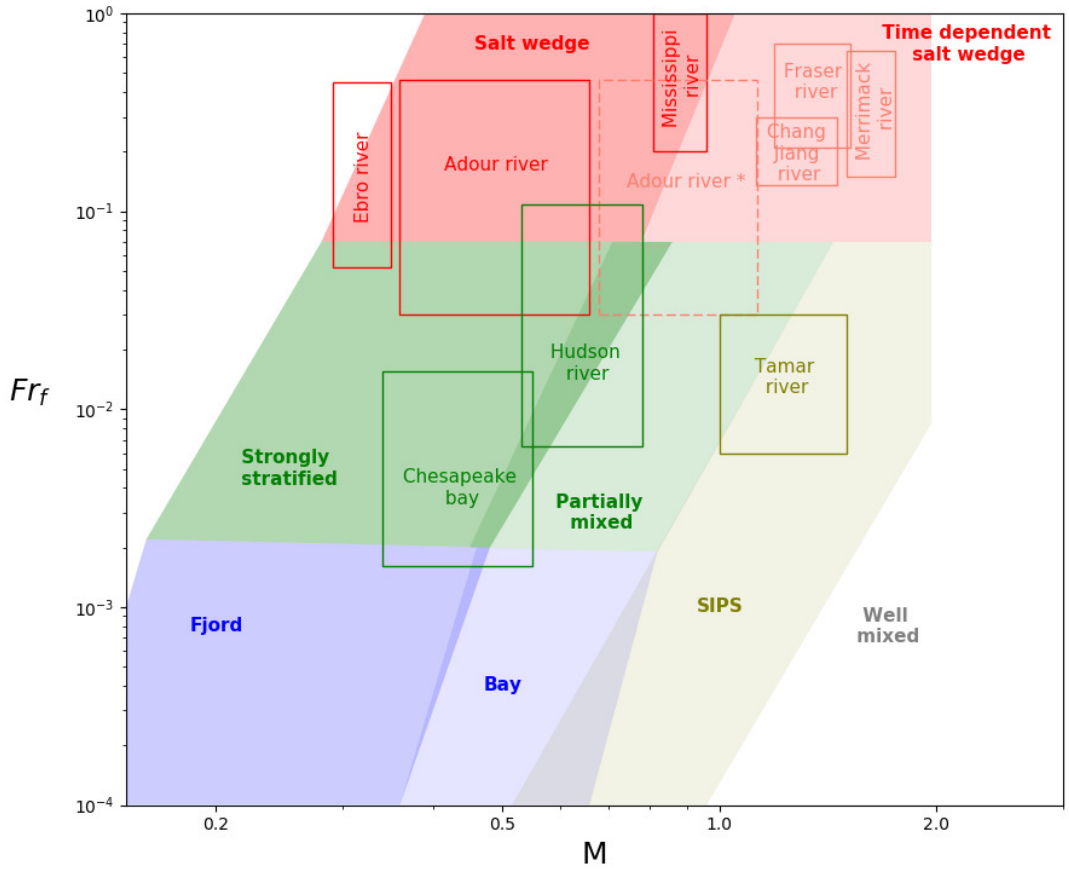

Figure 4.3: Estuarine classification based on the freshwater Froude number and mixing number, adapted from [46], Fig 6. (*) The dashed rectangle represent the location of the Adour river using other estimations of U_t and C_D.

4.1.4 Human interventions

The Adour estuary exhibits a strong variability of salinity, which has never been reported in the literature. It is highlighted by direct measurements in a wide range of conditions and confirmed by the Geyer and MacCready classification diagram [46]. Part of the observed variability is directly imposed by the fluctuations of the external forcing, i.e. a mesotidal regime associated with seasonal variations of river discharge driven by the oceanic climate and the close proximity to the Pyrenées mountains. However, such conditions are not usual and may not entirely explain the observed variability of the estuarine salinity circulation when comparing the Adour to other systems. It can be hypothesized that the artificial channelization of the lower estuary, coupled with strong dredging activities act to enhance the fluctuations in hydrological regimes. The Adour estuary is fully artificial since 1578, when the mouth of the estuary has been fixed in front of the Bayonne city by diking, under the decision of King Charles IX. In 1810, Napoleon decided to reduce the entrance of the estuary to 150 m in the aim of protecting the channel from sand accumulation by focusing the ebb energy. For a wider lower estuary, which would likely be the case in a more natural context, the U_R value would consequently decrease and so would Fr_f. This reduction of river flow velocity should reduce the stratification within the estuary which should promote the development of strongly stratified or partially mixed regimes. These

engineering works are complemented by dredging activities from 1896. Nowadays, the quantity of sediments to be dredged in the lower estuary per year is about 525000 m^3. The dredger of 1200 m^3 capacity operates almost everyday, except from June to September. This is also supposed to have a significant impact on the stratification, by making the channel deeper. In the absence of dredging, the depth reduction should strengthen the river flow, resulting in an enhanced mixing. Following the Geyer and MacCready classification [46], this would result in an increase in both parameters, likely leading to a more systematic time-dependent salt wedge regime. Such assumptions can certainly not be directly confirmed by the present or former datasets, and would require prospective scenarios with dedicated numerical modeling to be discussed further. However, while they are difficult to assess, the strong and continuous human interventions on the estuary's morphology are expected to lead to major changes in the salinity structure within the estuary, with strong consequences on biogeochemical processes controlled by mixing, residence time and water properties. Such issues should obviously not only concern the Adour system and call for a more extensive assessment of the impact of artificialisation and urbanisation of estuarine systems on the physical processes controlling the hydrodynamics and finally affecting the entire ecosystem.

4.2 Suspended sediment dynamics

The present study allows to analyze the impacts of physical processes taking place inside the Adour estuary on the observed sediment transport. The tidal and riverine forcing have been shown to be the major drivers of the estuarine dynamics, as well as of the sediment dynamics. The sediment dynamics is therefore strongly variable in time and space.

4.2.1 High variability of SSC into the estuary

Data collected in the lower Adour estuary enabled us to understand the SSC variations along the tidal cycle (Fig. 4.4). During the flood phase, the salt-wedge entrance generates bottom shear stress and turbulence, responsible of sediment re-suspension and landward advection. In the fresh water area, the river flow is responsible for re-suspension and seaward advection of sediment. This leads to a convergence of sediment at the salt-wedge front. The fresh water flowing over the salt-wedge is slowed down and the turbulence is damped, resulting in a fall of the sediments in the lower layer. During the flood stack, the sediment in suspension settle down on the river bed. It could be hypothesized that a temporary pool of sediment is created at the limit of the salt-wedge entrance. During the ebb phase, the shear stress is much more intense than during the flood phase, the re-suspension is then stronger and the advection is directed seaward. The sediment are expelled from the estuary. A gradient of SSC is generated in the opposite direction of the salinity gradient. The ebb slack is characterized by deposition processes.

This schematic of the sediment dynamics can strongly be modulated by the tidal range and the river discharge. An increase in one of these drivers or both enhances the re-suspension and advection mechanisms and reduces the deposition mechanism, while an decrease of the drivers results in a very low sediment transport.

It has been shown that the riverine forcing largely influences the tidally-averaged sediment fluxes. However, further field observations would be necessary to complete our understanding of the sediment flux in the lower estuary.

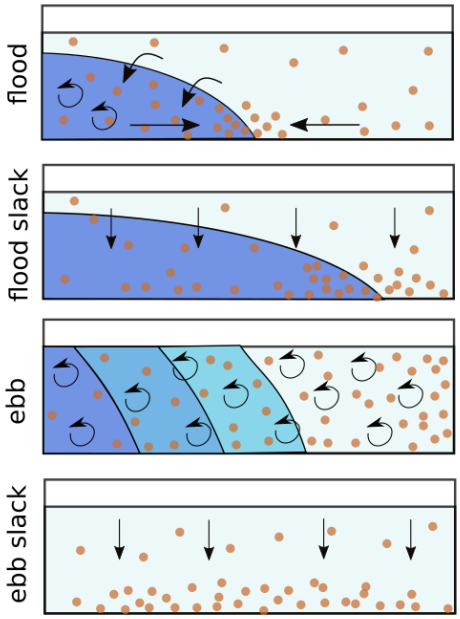

Figure 4.4: Schematic of the sediment dynamics throughout the tidal cycle.

4.2.2 No observed ETM

No stable ETM has been observed in the lower Adour estuary during our field experimentation or previous measurement. It has been established that the two majors drivers of ETM generation are not present in the lower estuary. However, the influence of human intervention and the potentiality of an ETM in an upper reach of the estuary need to be discussed.

4.2.2.1 Human activities

The question arises then on the role of estuary engineering (channelization and dredging) on the absence of observed ETM in the lower reach of the estuary, in particular when compared to other tidal estuaries. First, the width reduction at the estuary mouth to only 150 m certainly enhances the good flushing capacity of the lower Adour, by reinforcing the ebbing currents. Such hypothesis might be impossible to confirm due to the lack of available data collected before those engineering works, a numerical study could be necessary to discuss further this issue. In addition, it is hypothesized that the artificialization of the river mouth tends to maintain a low marine sediment input, thus participating to the absence of ETM. At the river mouth, along the Northern jetty, a sand pit has been artificially created and maintained by dredging operations, in order to avoid sand accumulation in the estuary entrance under storm conditions. Dubranna's numerical study [32] highlighted that the transport of sediment from the coastal area into the estuary is strongly limited by this man-engineered retention pit. In addition, Grasso and al [54] have shown the important contribution of energetic wave conditions to the ETM mass, by sediment resuspension action. However, it has been demonstrated that both jetties located at the estuary entrance, efficiently protect the port against incoming swell and sea waves with a reduction factor of 85 % compared to the offshore wave energy [6]. Finally the dredging operations taking place every day in the lower estuary may infer with the global sediment dynamics, by modifying the bed form and destabilizing the eventual consolidation of the river bed. All together, these interventions can further contribute to the absence of ETM in the Adour lower estuary. Nevertheless, the impacts of the artificialisation of the lower estuary on its hydrodynamics and sediment transport can not be quantified by the present study, and would require further investigations.

The plume generated by the brackish fresh waters flowing out the estuary is also influenced by the engineering works at the entrance of the estuary. As already mentioned the width reduction at the entrance of the estuary might be responsible for an intensification of the plume. In addition, the Northern jetty also affects the dispersion of the plume orienting the plume in the southwest direction. Such issue was not part of the scope of this study, however this could be the aim for additional research. Additional measurements upstream in the Adour estuary would be necessary to confirm such hypothesis.

4.2.2.2 Potential ETM in the upper reach of the estuary

Even though no ETM was observed in the lower estuary, the hypothesis of an ETM in the Adour estuary has already been advanced in Coynel's study [21]. The tidal asymmetry is too weak in the lower estuary to generate an ETM in the lower estuary, but a strongest asymmetry has be noticed in the upper part of the estuary (i.e. from Urt village). The tidal pumping mechanism might have an impact on sediment transport in this reach of the estuary. Extended measurements until Urt village or a dedicated numerical study should be foreseen as further work to estimate the impact of this tidal asymmetry on the sediment transport in the upper estuary. Further more, high values of SSC collected in the Gave de Pau river reaching 1 $g.L^{-1}$ (MESsAGe network) seems to indicate that a huge sediment catchment is available in the upper part of the estuary.

Part III

Numerical modeling

Chapter 1

Numerical tool presentation : TELEMAC 3D

Numerical models of increasing complexity have been developed in the past 30 years and are widely applied to the study of the hydrodynamics, sediment and associated contaminant transport in shallow waters. Their ability to describe physical processes is always improving. Nevertheless, each system is different and models require a good level of expertise to reproduce physical processes accurately. The perfect numerical model does not exist, which is why it essential to weigh the pros and cons of various existing models before opting for the one best suited, and more readily adaptable, to the specific context of one's study.

TELEMAC3D, which is part of the TELEMAC-MASCARET integrated suite of solvers, was selected for the present study. It is used in wide range of maritime applications from ocean circulation modeling, estuarine and coastal studies, to small scale simulation like effluents and pollutants discharges. TELEMAC3D is also used in continental waters applications, such as in lake and riverine studies. The influence of different phenomenon on the hydrodynamics and sediment transport can be studied such as tidal currents, wind, waves, Coriolis force, density gradients, among others. TELEMAC3D solves the 3D free surface flow equations. At every time step, it resolves the velocity field, the water elevation and tracers concentrations at each of the nodes of the 3D grid.

The system was developed by the Laboratoire National d'Hydraulique et Environnement (LNHE) in the Research and Development Division of EDF (EDF-R&D). It is now available as open source, and is developed by the Open Telemac-Mascaret Consortium, composed of Artelia (formerly Sogreah, France), BundesAnstalt für Wasserbau (BAW, Germany), Centre d'Etudes et d'Expertise sur les Risques, l'Environnement, la Mobilité et l'Aménagement (CEREMA, France), Daresbury Laboratory (United Kingdom), Electricité de France R&D (EDF, France), and HR Wallingford (United Kingdom). The source codes are written in FORTRAN 90 language, and can be modified by the user to fit a specific application. A large community of users shares new developments and applications through yearly Users Conferences and through an active forum (http://www.opentelemac.org/).

Over the past decades, the worldwide estuarine community has been using the TELEMAC suite of solvers more and more, to study hydrodynamics, sediment transport and morphodynamics. The range of issues to be addressed is wide: salinity distribution [115], tidal propagation/dissipation [80], sediment transport [31, 10], estuarine turbidity maximum [130], morphodynamics [51, 100, 126], flooding risk [109], water quality [31], climate change impacts [99, 98]. Even a flocculation model was coupled with TELEMAC to study estuarine muds [106]. Some of the major French estuaries have been studied using the TELEMAC model, such as the Loire estuary [20, 87, 129, 130], the Gironde estuary [58, 59, 124, 125, 127], the Seine estuary [16, 72] and the Rance estuary [31].

In addition to its high number of users in the estuarine community, the main asset of

TELEMAC 3D is its efficient and flexible finite element method, compared to other modeling systems (Delft 3D, Mike 21, MOHID, etc ..). The finite element method allows the use of an irregular grid and avoid the need of embedded models. This means that nearshore or other specific areas with complex bathymetry can achieve a high resolution, when deeper waters can have a coarser resolution. This optimizes the computation time and accuracy, in contrast to traditional finite difference models and with finite volume models [57, 126].

1.1 Finite element method

The finite element method is used to go from a continuous to a discrete problem. An interpolation method provides an approximate function of the one defined on the continuous domain, constructed from a finite number of real numbers. A variational method, named "weighted residuals", gives a finite number of equations to replace the ones defined on the continuous domain [57]. In TELEMAC 3D, the space is discretized in an **unstructured grid of prismatic elements**. The 2D mesh is composed of triangular elements. This 2D mesh is reproduced on each vertical layers, leading to prismatic elements. The vertical layers can be spread equally between the bed and the surface, or with given proportions (sigma transform coordinate grid). The sigma coordinate grid can also be combined with fixed planes, where a constant elevation is prescribed, then planes located below and above these fixed planes are evenly space (double sigma transform). A fourth method of horizontal planes distribution can also be used, where all the plane elevations are prescribed. If the elevation prescribed is located below the bottom or above the surface, the "MinMod" limiter will help maintain those planes slightly above the bottom or below the surface [57]. All the variables (velocity components, tracers concentrations, elevations etc ...) are defined at every point of the 3D mesh, except for the surface elevation and the bottom elevation which are 2D variables.

1.2 Hydrodynamics

1.2.1 Governing equations

The **mass conservation equation**, also known as the continuity equation, describes the conservation of a fluid mass. The continuity equation can be applied to any conservative quantity, such as energy or momentum. Let us define a domain of study Ω, and its boundary Γ. The fluid contained in Ω has a density ρ and a velocity $\vec{U}$. The expression of the conservation of the fluid mass can be expressed as :

$$\frac{d}{dt}\Big(\int_\Omega \rho d\Omega\Big) = 0 \tag{1.1}$$

With the consecutive application of the Leibnitz and Gauss theorems, we obtain :

$$\int_\Omega \frac{\partial \rho}{\partial t} d\Omega + \int_\Omega div(\rho \vec{U}) d\Omega = 0 \tag{1.2}$$

The local expression of this equation is given by :

$$\frac{\partial \rho}{\partial t} + div(\rho \vec{U}) = 0 \tag{1.3}$$

From Newton's second law, we can establish the **momentum conservation equation**.

$$\int_\Omega \frac{\partial(\rho \vec{U})}{\partial t} d\Omega + \int_\Omega \nabla(\rho \vec{U} \otimes \vec{U}) d\Omega = \int_\Omega \rho(\vec{g} + \vec{F}) d\Omega + \int_\Omega div(\underline{\underline{\sigma}}) d\Omega \tag{1.4}$$

Or

$$\frac{\partial(\rho\vec{U})}{\partial t} + \nabla(\rho\vec{U} \otimes \vec{U}) = \rho(\vec{g} + \vec{F}) + div(\underline{\underline{\sigma}}) \tag{1.5}$$

where $\underline{\underline{\sigma}}$ is the stress tensor and $\vec{F}$ represents forces other than acceleration of gravity $\vec{g}$, e.g the Coriolis force.

1.2.2 Hypothesis and approximations

In order to facilitate the resolution of such equations, some hypothesis and approximations must be formulated. This will also lead to a reduction of computation time.

Incompressible fluid hypothesis or Boussinesq approximation
In TELEMAC, variations of density are considered sufficiently minor for using the mass conservation equation in a incompressible form : $\rho = \rho_0 + \Delta\rho$.

The hydrostatic pressure hypothesis
It consists in neglecting the vertical velocity acceleration, diffusion and the source term in the conservation of momentum equation along the vertical (Eq. 1.6). This hypothesis can not be applied to any case, e.g. in a dam break application the vertical velocity acceleration can not be neglected.

$$\cancel{\frac{\partial W}{\partial t}} + U\cancel{\frac{\partial W}{\partial x}} + V\cancel{\frac{\partial W}{\partial y}} + W\cancel{\frac{\partial W}{\partial z}} = -\frac{1}{\rho}\frac{\partial p}{\partial z} + \cancel{\nu\triangle(W)} + \cancel{F_z} - g \tag{1.6}$$

where U, V, W are the velocity components, p is the pressure , ν is the coefficient of kinematic viscosity and F_z is the vertical component of forces other than acceleration of gravity.

Meterological forcing
Wind action and its associated surface friction and pressure gradient were not considered in the present computation.

1.2.3 Navier Stokes equations

When the previous hypothesis and approximations are applied to the governing equations, it results in a simplified form of the Navier-Stokes equations expressed as follows in Cartesian coordinates:

- **Conservation of mass :**

$$\frac{\partial U}{\partial x} + \frac{\partial V}{\partial y} + \frac{\partial W}{\partial z} = 0 \tag{1.7}$$

- **Conservation of momentum :**

$$\frac{\partial U}{\partial t} + U\frac{\partial U}{\partial x} + V\frac{\partial U}{\partial y} + W\frac{\partial U}{\partial z} = -\frac{1}{\rho}\frac{\partial p}{\partial x} + \nu\Delta(U) + fV \tag{1.8}$$

$$\frac{\partial V}{\partial t} + U\frac{\partial V}{\partial x} + V\frac{\partial V}{\partial y} + W\frac{\partial V}{\partial z} = -\frac{1}{\rho}\frac{\partial p}{\partial y} + \nu\Delta(V) - fU \tag{1.9}$$

$$\frac{\partial p}{\partial z} = -g\rho_0(1 + \frac{\Delta\rho}{\rho_0}) \tag{1.10}$$

where f is the Coriolis parameter : $f = 2\omega sin\phi$, $\omega = 7.292110^{-5} rad.s^{-1}$ is the Earth's angular rotation speed and ϕ is the latitude.

1.2.4 Turbulence

Different approaches to solve the Navier-Stokes equations exist :

- Direct Numerical Simulation (DNS) : resolves all scales (eddies) for a sufficient interval of time, in order to reach a statistical equilibrium.
- Large Eddy Simulation (LES) : based on space-filtered equations. Large eddy scales are explicitly calculated and smaller scales are modeled.
- Reynolds Averaged Navier-Stokes (RANS) : based on Reynolds averaged Navier-Stokes equations. All scales are modeled (i.e. none are explicitly calculated).

TELEMAC 3D system solves **Reynolds averaged Navier-Stokes equations**. Reynolds' average is based on the decomposition of each unknown x into its time-average $\overline{x}$ and its fluctuations x' : $x = \overline{x} + x'$. This leads to the Reynolds momentum equation:

$$\rho(\frac{\partial \overline{u_i}}{\partial t} + \Sigma \overline{u_j}(\frac{\partial \overline{u_i}}{\partial x_j})) = \Sigma \frac{\partial}{\partial x_j}(\sigma_{ij} - \rho \overline{u_i' u_j'}) + \rho \overline{g_i} \tag{1.11}$$

where

$$\sigma_{ij} = -\rho \delta_{ij} + \mu(\frac{\partial \overline{u_i}}{\partial x_j} + \frac{\partial \overline{u_j}}{\partial x_i}) \tag{1.12}$$

with δ_{ij} the Kronecker tensor or identity tensor which is equal to 1 when i=j and otherwise equal to 0, and μ is the coefficient of dynamic viscosity. The term $-\rho \overline{u_i' u_j'}$ is named the Reynolds tensor.

The RANS Navier-Stokes equations are an open system, which means that there are more unknown quantities than equations. It is necessary to introduce new information, such as physical hypothesis, in order to close the system: this is the **Closure Problem**. The introduction of a closure hypothesis related to turbulence is a common way to close the system.

Boussinesq hypothesis

The Boussinesq hypothesis or flux-gradient hypothesis comes from an analogy between the momentum transfer due to turbulence and the momentum transfer due to molecular motion in gas. With this analogy, an eddy viscosity ν_t was defined as the proportionality coefficient between the momentum flux $< u'w' >$ and the gradient of mean velocity $\frac{\partial U}{\partial z}$:

$$< u'w' > = -\nu_t \frac{\partial U}{\partial z} \tag{1.13}$$

Different turbulence models based on this hypothesis have been developed, and they differ in the way they compute ν_t. The choice of the turbulent model is directly linked to the type of information we want to obtain with the simulation. Turbulence models vary in their complexity from zero equation to 2 equations. Some turbulence models available in TELEMAC 3D are presented below. In TELEMAC 3D, the total eddy viscosity ν is considered as the sum of the eddy viscosity computed by the turbulence model ν_t and the molecular viscosity ν_{mol}:

$$\nu = \nu_t + \nu_{mol}. \tag{1.14}$$

In TELEMAC3D, the default value of the molecular viscosity is $\nu_{mol} = 10^{-6}\ m^2.s^{-1}$.

In oceanography numerical modeling, the computational grids are far to large to reach the isotropic scale of the turbulence. Furthermore, at large scale the geophysical flows are generally anisotropic due to the combined effect of vertical confinement (aspect ratio), density stratification and/or background rotation, and the numerical grids are generally built accordingly (vertical resolution being much higher than horizontal one). A distinction is often made between horizontal and vertical components of the eddy viscosity computed by the turbulence model.

Constant eddy viscosity models
These zero equation models are the simplest. They consider a constant turbulent viscosity : $\nu_t = cst$. This value is generally determined experimentally. Typical values of eddy viscosity in estuaries range from 10^{-4} to 10^{-2} $m^2.s^{-1}$.

Mixing length model
This model was introduced by Ludwig Prandlt in 1945. It links the turbulent viscosity directly to the gradient of the time-averaged velocity. This notion of mixing length was developed by analogy with the viscosity of a perfect gas and its mean free path. In this model, the turbulent viscosity is expressed as follows:

$$\nu_t = L_m^2 \sqrt{2 D_{ij} D_{ij}} \tag{1.15}$$

Where

$$D_{ij} = \frac{1}{2}\Big(\frac{\partial \overline{U_i}}{\partial x_j} + \frac{\partial \overline{U_j}}{\partial x_i}\Big) \tag{1.16}$$

and

$$\begin{aligned} L_m &= \kappa z \qquad if \quad z \leq 0.2h \\ L_m &= 0.2\kappa h \qquad if \quad z \geq 0.2h \end{aligned} \tag{1.17}$$

where $\kappa = 0.41$ is the Von Karman constant, z is the distance to the bottom and h the water elevation.

Other formulations have been developed for the mixing length calculation. Three of them are already hard-coded in TELEMAC 3D (Tab. 1.1).

Table 1.1: Different mixing length model formulations, where d is the distance to the free surface.

Prandlt	Nezu & Nakagawa	Quetin	Tsanis
$L_m = \kappa z \quad (if \quad z \leq 0.2h)$ $L_m = 0.2\kappa h \quad (if \quad z \geq 0.2h)$	$L_m = \kappa z \sqrt{1 - \frac{z}{h}}$	$L_m = \frac{1}{\frac{1}{\kappa z} + \frac{1}{0.65d}}$	$L_m = \kappa z \quad (if \quad z \leq 0.2h)$ $L_m = 0.2\kappa h \quad (if \quad z \geq 0.2h$ and $z \leq 0.8h)$ $L_m = \kappa d \quad (if \quad z \geq 0.8)$

However, the vertical length scale of turbulent eddies can be hugely impacted by stratification. High stratification is usually associated with strong reduction of eddy viscosity. Various closure models have been developed to reproduce the damping induced by stratification. The majority are based on the Richardson number, and the eddy viscosity along the vertical can be given as :

$$\nu_z = f(Ri) L_m^2 \sqrt{\Big(\frac{\partial U}{\partial z}\Big)^2 + \Big(\frac{\partial V}{\partial z}\Big)^2} \tag{1.18}$$

Various **damping functions** $f(Ri)$ have been developed based on experimental results - they always decrease with Ri (Fig. 4.7). One of the most commonly used damping function was proposed by Munk Anderson in 1948 [83], and it is hard-coded in TELEMAC3D :

$$f(Ri) = (1 + aRi)^{-b} \tag{1.19}$$

where a and b are coefficients determined experimentally (Tab. 1.2).

Since then, others empirical formulations have been introduced (Tab. 1.2). For example, the formulation of Lehfeldt and Bloss (1988) has been applied satisfactorily to the Seine estuary [8].

The subroutine 'DRICV.f' was then modified to include two new formulations: Mac Anally and Lehfeldt & Bloss [71].

Table 1.2: Different sets of damping function coefficients: Munk & Anderson, Mac Anally, and Lehfeldt & Bloss.

	Tracer		**Velocity**	
	a	b	a	b
Munk & Anderson	3.33	1.5	10.0	0.5
Mac Anally	3.33	3.5	10.0	4.0
Lehfeldt & Bloss	3.0	3.0	3.0	1.0

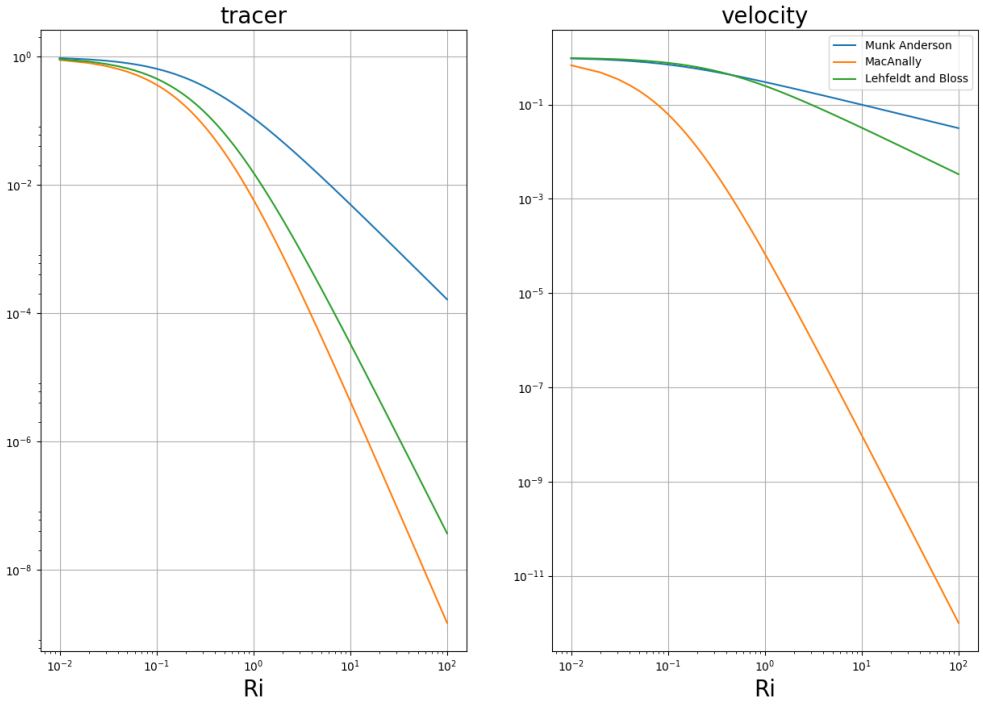

Figure 1.1: Representation of three different damping functions for tracer (on the left) and velocity (on the right) : Munk Anderson (blue line), MacAnally (orange line), and Lehfeldt & Bloss (green line).

Smagorinski model

The Smagorinski model is based on the mixing length model and it is included in the sub-grid turbulence models. The general idea is that small scale turbulence can not be adequately resolved if the size of finite elements is larger than small eddies. In this model, the eddy viscosity is defined as the product of characteristic scale Δ and a velocity scale $\Delta\sqrt{2D_{ij}D_{ij}}$. It can be given by equation 1.20, where the mixing length scale corresponds to the eddies smaller than the mesh size.

$$\nu_t = C_s^2 \Delta^2 \sqrt{2D_{ij}D_{ij}} \tag{1.20}$$

This model is used mostly in large scale ocean modeling, where the horizontal mesh size is large. In our case, the mesh is fine, and we focus on the vertical direction more than the horizontal direction. Therefore, this model was not used in our simulations, only constant viscosity model and $k-\varepsilon$ model were considered on the horizontal direction.

k-ε model

The k-ε model is part of the two-equation models, where two characteristic scales of the turbulence are defined to compute the turbulent viscosity. The first characteristic scale is common to all two-equation models: the turbulent kinetic energy k. The turbulent dissipation rate ε is the most largely used as second characteristic scale. This term appears in the transportation equation of the turbulent kinetic energy and allows to define the turbulent viscosity as:

$$\nu_t = C_\mu \frac{k^2}{\varepsilon} \tag{1.21}$$

The two equations for k and ε can be written as follows :

$$\frac{\partial k}{\partial t} + U\frac{\partial k}{\partial x} + V\frac{\partial k}{\partial y} + W\frac{\partial k}{\partial z} = \frac{\partial}{\partial x}\Big(\frac{\nu_t}{\sigma_k}\frac{\partial k}{\partial x}\Big) + \frac{\partial}{\partial y}\Big(\frac{\nu_t}{\sigma_k}\frac{\partial k}{\partial y}\Big) + \frac{\partial}{\partial z}\Big(\frac{\nu_t}{\sigma_k}\frac{\partial k}{\partial z}\Big) + P - G - \varepsilon \tag{1.22}$$

$$\begin{aligned}\frac{\partial \varepsilon}{\partial t} + U\frac{\partial \varepsilon}{\partial x} + V\frac{\partial \varepsilon}{\partial y} + W\frac{\partial \varepsilon}{\partial z} =& \frac{\partial}{\partial x}\Big(\frac{\nu_t}{\sigma_\varepsilon}\frac{\partial \varepsilon}{\partial x}\Big) + \frac{\partial}{\partial y}\Big(\frac{\nu_t}{\sigma_\varepsilon}\frac{\partial \varepsilon}{\partial y}\Big) + \frac{\partial}{\partial z}\Big(\frac{\nu_t}{\sigma_\varepsilon}\frac{\partial \varepsilon}{\partial z}\Big) + \\ & C_{1\varepsilon}\frac{\varepsilon}{k}[P + (1 - C_{3\varepsilon})G] - C_{2\varepsilon}\frac{\varepsilon^2}{k},\end{aligned} \tag{1.23}$$

where :

$$k = \frac{1}{2}\overline{u_i' u_i'} \tag{1.24}$$

and

$$\varepsilon = \nu \overline{\frac{\partial u_i'}{\partial x_j}}\,\overline{\frac{\partial u_i'}{\partial x_j}} \tag{1.25}$$

Terms P and G are respectively the turbulent energy production term and a source term due to the gravity forces. They can be expressed as :

$$P = \nu_t\Big(\frac{\partial \overline{U_i}}{\partial x_j} + \frac{\partial \overline{U_j}}{\partial x_i}\Big)\frac{\partial \overline{U_i}}{x_j} \tag{1.26}$$

$$G = -\frac{\nu_t}{Prt}\frac{g}{\rho}\frac{\partial \rho}{\partial z} \tag{1.27}$$

With Prt being the Prandt number in case of temperature gradient, or being the Schmidt number otherwise.

The new parameters introduced: C_μ, $C_{1\epsilon}$, $C_{2\epsilon}$, $C_{3\epsilon}$, σ_k and σ_ϵ, are constants determined experimentally. The following values have been defined in TELEMAC 3D:

Table 1.3: Constants of the $k-\epsilon$ model hard coded in TELEMAC 3D [57].

C_μ	$C_{1\epsilon}$	$C_{2\epsilon}$	$C_{3\epsilon}$	σ_k	σ_ϵ
0.09	1.44	1.92	1	1.0	1.3

1.2.5 Transport-diffusion equation

The transport of various tracers contained in water can be solved by TELEMAC 3D. Tracers can be categorized as active or passive. Active tracers are able to affect the flow through changes in the water density, such as temperature or salinity. Passive tracers are only transported by the flow. The transport of tracers depends on advection by the flow, diffusion mostly by turbulence and the presence of sources and sinks, it can be expressed in the developed form by :

$$\frac{\partial C}{\partial t} + U\frac{\partial C}{\partial x} + V\frac{\partial C}{\partial y} + W\frac{\partial C}{\partial z} = \frac{\partial}{\partial x}\Big(\nu_T\frac{\partial C}{\partial x}\Big) + \frac{\partial}{\partial y}\Big(\nu_T\frac{\partial C}{\partial y}\Big) + \frac{\partial}{\partial z}\Big(\nu_T\frac{\partial C}{\partial z}\Big) + Q \tag{1.28}$$

where C is the tracer concentration and Q is the source term.

In TELEMAC3D the eddy diffusivity for tracers is computed as : $\nu_T = \nu_t/Prt + K$, where ν_t is the turbulent viscosity for velocities, Prt is the Prandlt number and K is the coefficient for diffusion of tracers. The Prandlt number is set to 1.0 by default in TELEMAC3D.

1.2.6 Density law

Different density laws are available in TELEMAC 3D, where the density depends on the temperature and/or salinity and/or any other physical quantity (e.g. sediment). The general formulation depends on salinity and temperature and is given by :

$$\rho = \rho_{ref}[1 - (7(T - T_{ref})^2 - 750S)10^{-6}] \tag{1.29}$$

where T_{ref} is the temperature reference of 4°C and $\rho_{ref} = 999,972$ is the density reference at the temperature reference and at a salinity of zero. This formulation is valid for a temperature range from 0°C to 40°C and a salinity range from 0 to 42.

Chapter 2

Viollet test case

The aim of this study was to evaluate the capacity of TELEMAC 3D system to represent accurately the stratification inside a channel. This work is focused on the influence of different factors on the stratification, such as turbulence models and grid sizing. The stable configuration of Viollet's experiments [128] was chosen, in order to compare simulation results with experimental data.

2.1 Viollet's experimentation

The test case can be described as follows: a 10 m long and 1 m wide open channel, where a two-layer free-surface flow of water is simulated. The channel was considered to have a very small tilt of $5.30921\,10^{-6}$. The upper layer had a temperature T2 = 25,35°C and a initial velocity of $2/30\ m.s^{-1}$. The lower layer had a temperature T1 = 20°C and a initial velocity of $1/30\ m.s^{-1}$. The height of each layer was $h = 0.1m$. The configuration of Viollet's experimentation is shown in Figure 2.1.

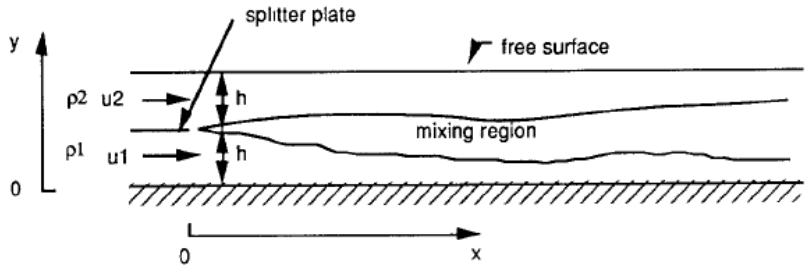

Figure 2.1: Scheme of Viollet experiments (1980), extracted from [128]

2.2 Numerical simulations

2.2.1 Grid size

In order to study the influence of grid sizing on the representation of the stratification, the four meshes presented by Rosales [102] were reproduced. A ratio of $\sqrt{2}$ was used between the cell size and the time step. The characteristics of the four meshes are presented in Table 2.1. These simulations were run with the $k - \varepsilon$ turbulence model.

In Figure 2.2, we can see that results obtained with Mesh 1, Mesh 2 and Mesh 3 converge to a solution, which is not in perfect agreement with the measurements. The general trend is that numerical results tend to underestimate the vertical diffusion. Unfortunately, mesh 3 is giving

Table 2.1: Different meshes used to evaluate the influence of grid sizing

	Nbr of points			Cell sizing (m)			time step (s)
	x	y	z	$\triangle x$	$\triangle y$	$\triangle z$	t
Mesh1	58	10	50	0.172	0.100	0.004	0.10
Mesh2	40	10	40	0.250	0.100	0.005	0.14
Mesh3	29	10	29	0.344	0.100	0.007	0.20
Mesh4	20	10	20	0.500	0.100	0.010	0.28

better results than meshes 1 and 2. Mesh 4 does not converge with the three other solutions. This highlights the need of a sensitivity study regarding the grid sizing.

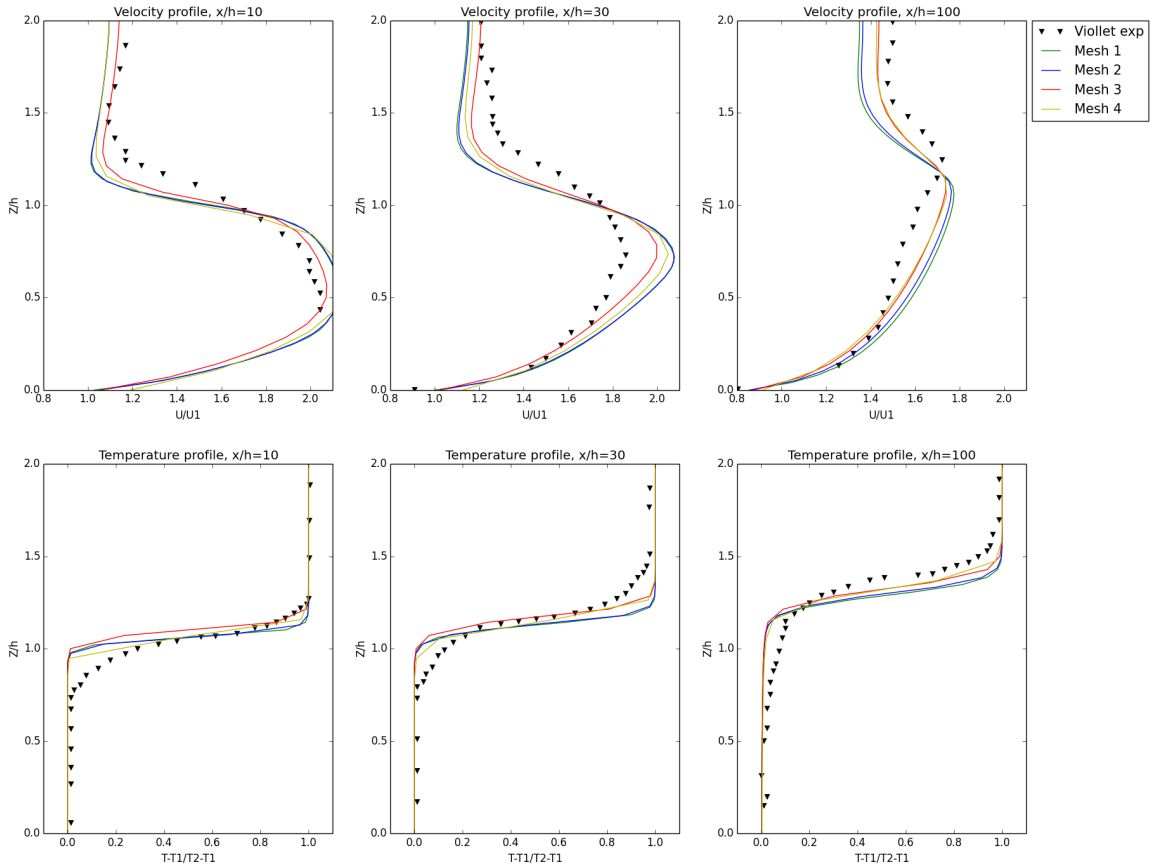

Figure 2.2: Comparison between Viollet experimental data and $k-\epsilon$ model with different grid sizing

2.2.2 Turbulence models

In order to evaluate the influence of turbulence models in the stratification modeling, we selected three type of turbulence models: constant viscosity, mixing length and $k-\epsilon$ models. The version V7p2r1 of Telemac 3D enables us to select different types of turbulence models along the vertical and the horizontal. Table 2.2 is a summary of all the configurations which were tested. The first line lists all the turbulence models used along the vertical and the first row summaries the turbulence models used along the horizontal. For the simulations run with

constant viscosity model, the eddy viscosity was fixed to 1.10^{-5} $m^2.s^{-1}$ in both directions.

Table 2.2: Turbulence models used on the vertical (first line) and on the horizontal (first row) during the simulations.

	Constant viscosity	Prandlt	Nezu	Quetin	Tsanis	$k-\epsilon$
Constant Viscosity	X	X	X	X	X	X
$k-\epsilon$	X					X

As it is shown on Figure 2.3, the results obtained with the constant viscosity model are satisfying, except on the last velocity profile (x/h=100) where the model is more diffusive than the experimental results.

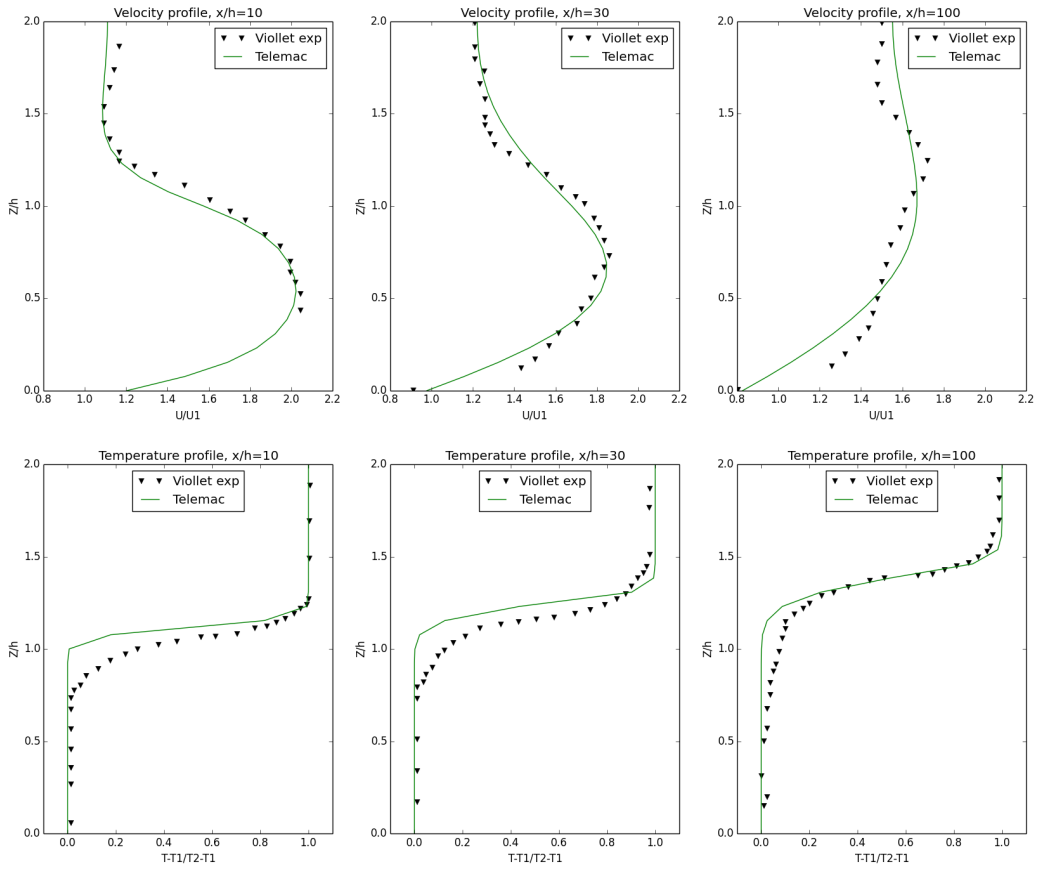

Figure 2.3: Velocity and temperature profiles for a model using constant viscosity model on both horizontal and vertical

Four different formulations of the mixing length model were tested. Munk and Anderson damping function was used in each case. The results are presented in Figure 2.4 here below. Prandlt and Tsanis models have a very similar formulation and thus gave similar results. All the mixing length models seem more diffusive than experimental data, for both velocity and temperature. Nevertheless, velocity and temperature profiles at x/h=100 are very close to Viollet's experimental data. Tsanis model seems the one giving the more promising results.

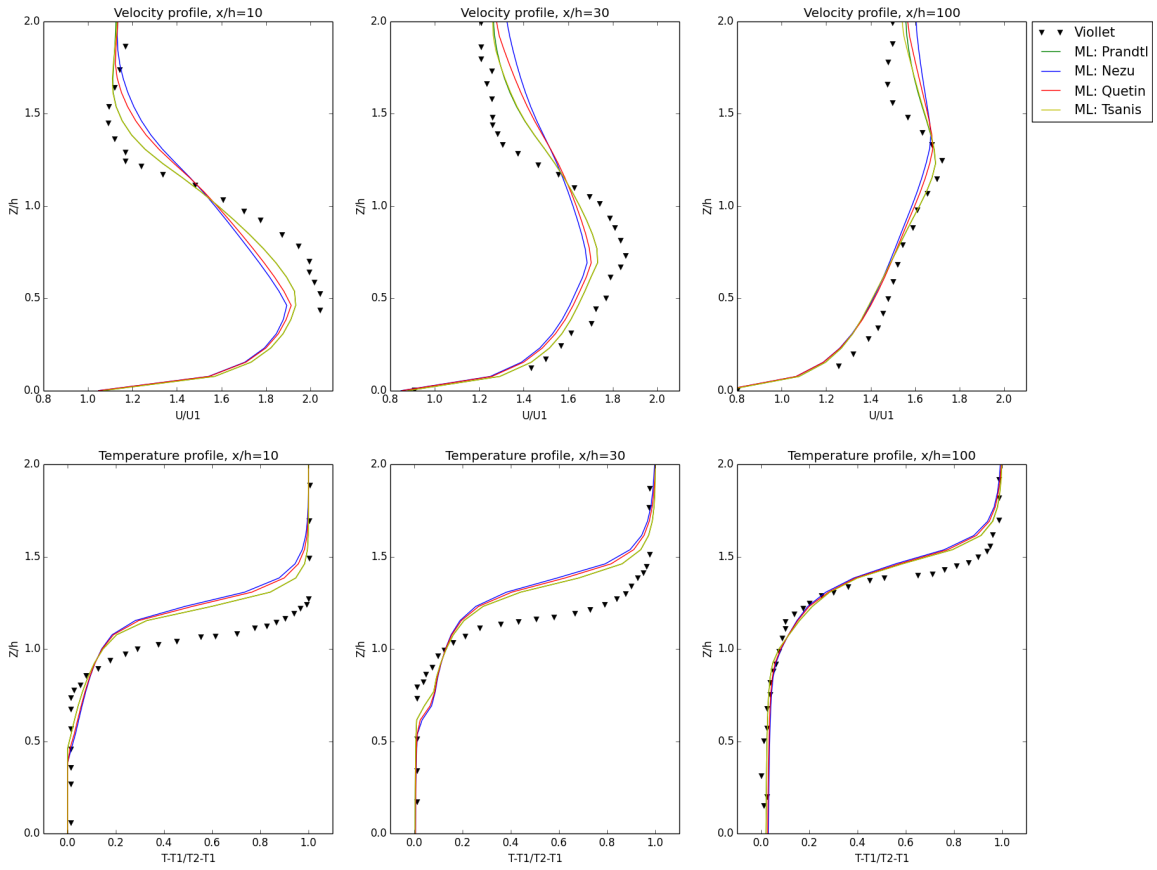

Figure 2.4: Comparison of velocity and temperature profiles between Viollet experimental data and different mixing length models

Two simulations were run with the models $k-\epsilon$ model, one using $k-\epsilon$ model on both directions and another using $k-\epsilon$ model on the vertical and constant viscosity model on the horizontal (Fig. 2.5). Both models gave similar results (i.e. blue line is covered by the red line), this can be explained by the fact that our study case is a 2D case, therefore the model used on the horizontal as few influence on the representation of the stratification inside the channel. However, it has a great influence on the computation time.

In conclusion, simulations were run with different turbulence models. They all showed promising results, as the stratification was well reproduced in each case. Nevertheless, the mixing length model is a slightly too diffusive, while the $k-\varepsilon$ model is not enough diffusive, for equivalent grid size. The results obtained with the $k-\varepsilon$ model were particularly in good agreement with the experimental data (Fig. 2.5).

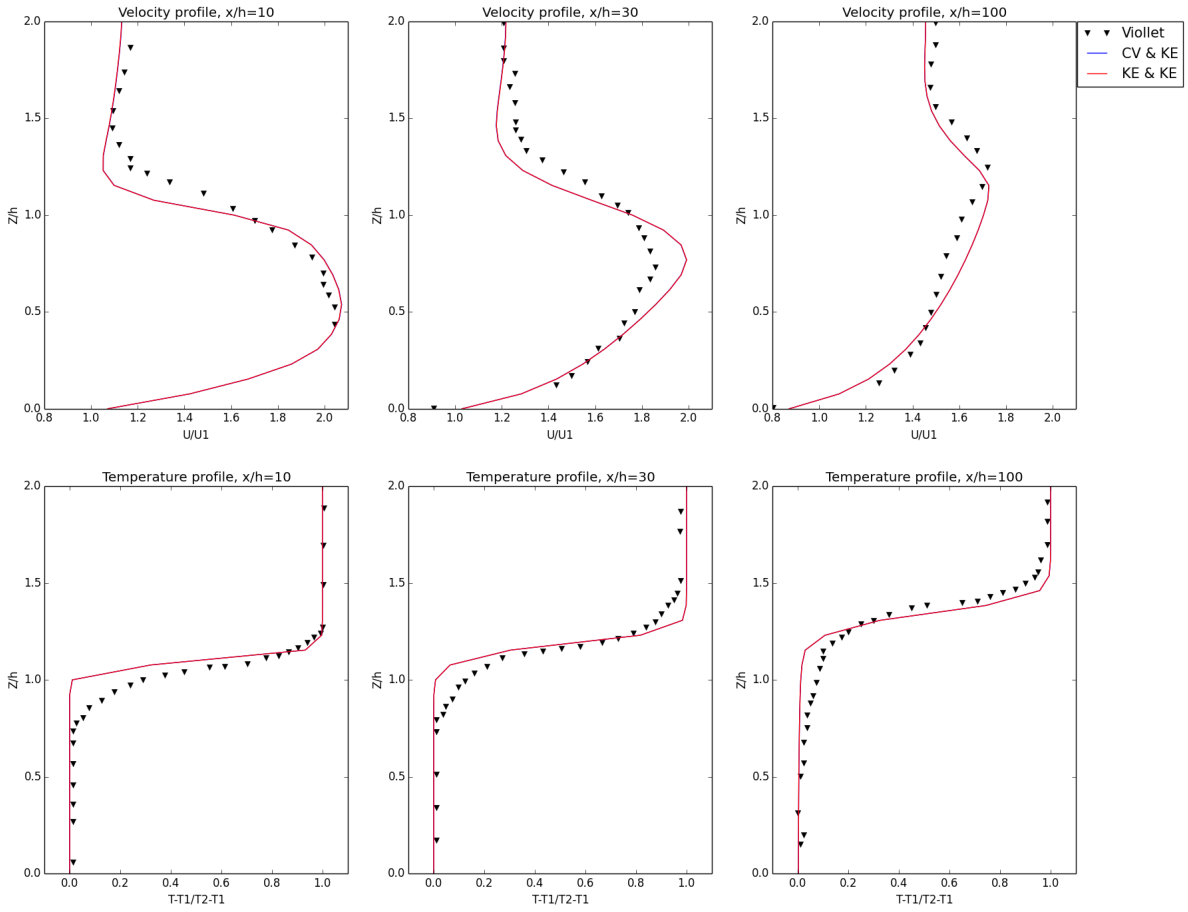

Figure 2.5: Results of TELEMAC3D simulations (red lines) compared to experimental data from Viollet experimentations (black triangles).

Chapter 3

Adour estuary numerical modeling

3.1 Mesh grid

The mesh was generated using the BLUEKENUE software, developed by the Hydraulic Canadian Center. Grids with regular and irregular triangular elements can be combined with BLUEKENUE. A file in SELAFIN format is generated by BLUEKENUE, containing the 2D mesh interpolated on the bathymetry data. Other variables can be added in this file, such as the bottom friction or wind values (if spatially variable). The boundary conditions file can also be generated by BLUEKENUE, if needed. Moreover, it can be used for results visualization.

3.1.1 Description

The mesh was created based on a new, high-resolution bathymetry data set provided by the Bayonne Harbor. The new data was collected in 2015, only in the lower part of the Adour estuary (i.e. last 6 km of the estuary) with a resolution of about 1m. For the oceanic area, different bathymetry data sets from the SHOM data base were combined. The grid covers the ocean up to 40 km from the estuary mouth and it goes up to 70 km into the Adour and 25 km into the Nive river. The river boundaries were extended in order to be able to damp the tidal wave. The upper parts of both rivers are not realistic in terms of bathymetry and bottom friction coefficient. The erratic coastline was simplified and linearized, because this study focuses on the lower estuary dynamics. This allows us to limit the number of cell needed for the coastline and it eases the computation. If the plume dispersion is to be studied with this numerical model in a further work, the coastline will have to be more realistic and detailed.

The final mesh is composed of several refinement areas to resolve the lower estuary in detail, such as measurement sites, dikes, embankments and islands. The lower Adour estuary is the area of the utmost importance; it is composed of small cells (30 m), on the other hand the maritime boundary composed of biggest cells (2 km). An intermediate region in the ocean, close to the estuary was refined with cells of 500 m (Fig. 3.1). In the Nive river and the upper part of the Adour river, regular meshes were created, ranging from 30 m to 200 m long, in order to reduce the computation time. The area around the two islands located close to Urt village was refined to fit this specific morphology.

The final mesh has the following characteristics :

- Unstructured grid and regular grid (from 30m to 2km)
- 20 equidistant sigma coordinate layers
- 16591 nodes and 28696 elements (2D mesh)
- Study Area : 2093.8 km^2

a)

b)

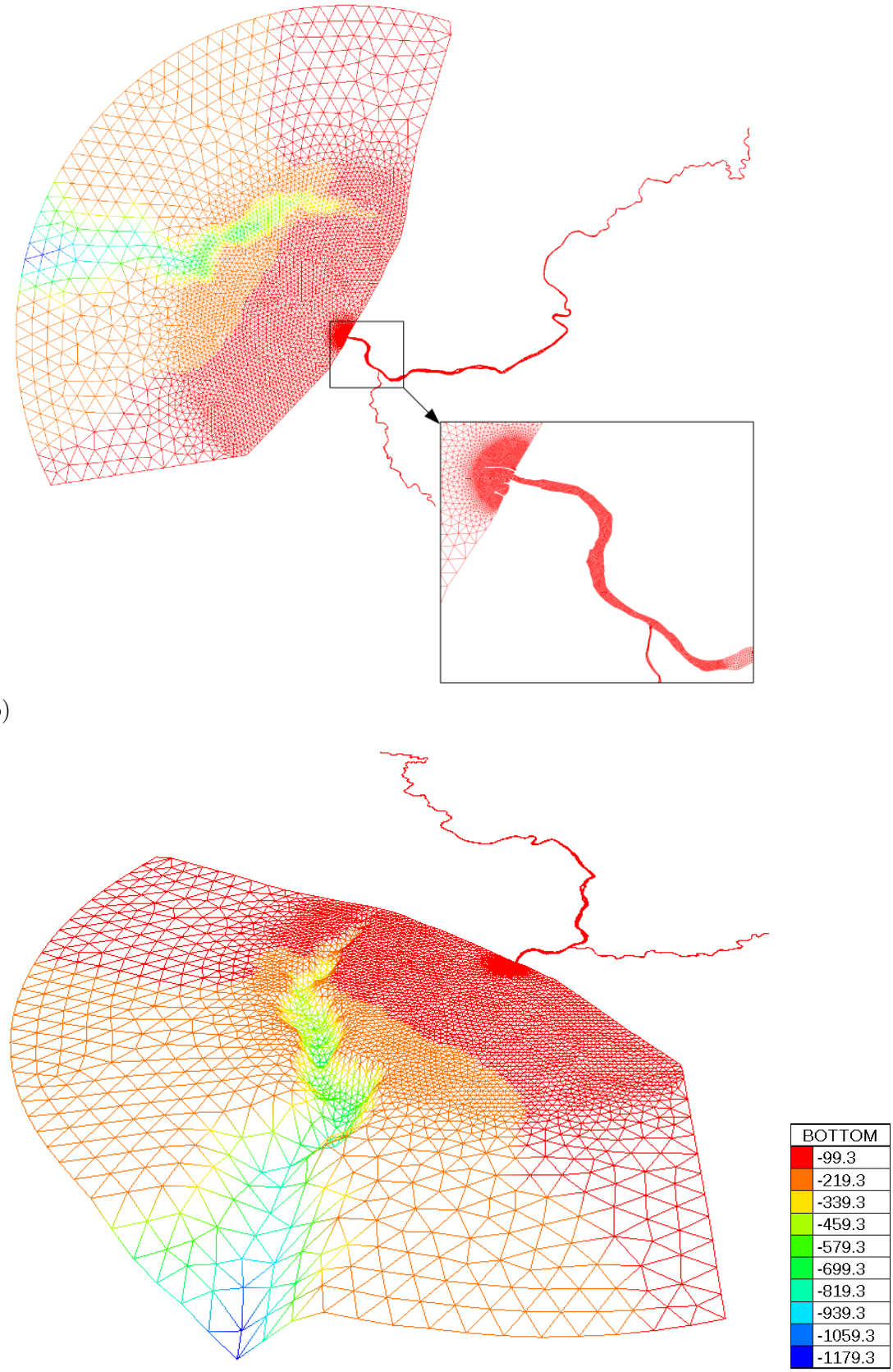

Figure 3.1: 2D view (a)) and 3D view (b)) of the interpolated mesh grid, with a zoom on the last 6 km of the estuary where the measurements took place. Colors correspond to the bathymetry in meter.

3.1.2 Sensitivity study to the grid resolution

The vertical density stratification inside the lower estuary being the cornerstone of this study, the sensitivity study was dedicated to the vertical refinement of the numerical modeling. The 2D mesh was refined in areas of particular interest and/or strong bathymetry changes, as presented in the previous paragraph. A fine vertical resolution is expected to provide a good reproduction of the steep salinity stratification inside the estuary. In general, the degree of refinement of a vertical mesh has to be balanced with the computation time. As we had no operational objective, we could afford the luxury of a relatively high computation time, if needed, for an accurate reproduction of the estuarine dynamics. To give an order of magnitude, a 30-day simulation with 10 vertical layers will require a computational time of 2H30, when the same simulation with 30 layers will take 7h30 to compute. Both simulations were run on 30 parallel processors. These computation times were obtained with a very simple turbulence model. A two-equation turbulence model may be twice to three times more time-consuming.

In the literature, numerical studies of stratified estuaries generally have between 8 and 30 vertical layers [7, 27, 94, 95, 116], for similar water depth values. In order to define the number of vertical plans necessary for a good representation of the salinity and velocity profiles, simulations with varying numbers of vertical plans (10, 15, 20, 25, 30, 35) were run. The simulations were run with a low river discharge forcing (i.e. 100 $m^3.s^{-1}$) and a strong tidal forcing (i.e. 3.1 m of tidal amplitude). These conditions were shown to produce the most contrasted density stratification, i.e. a vertical salinity gradient during the flood and a horizontal salinity gradient during the ebb (cf. experimental results presented below). RMSE values for water elevations, velocities and salinities were computed (Tab. 3.1). This sensitivity study shows that twenty levels are sufficient to resolve the density structure in the estuary, and beyond 25 plans numerical instabilities may appear on the velocity and salinity profiles.

Table 3.1: RMSE calculation (cf. next chapter) for the sensitivity study for water elevation (m), velocity ($m.s^{-1}$) and salinity ($g.L^{-1}$).

	10 layers vs 15 layers	15 layers vs 20 layers	20 layers vs 25 layers	25 layers vs 30 layers	30 layers vs 35 layers
Water elevation (m)	0.008	0.011	0.005	0.006	0.005
Velocity ($m.s^{-1}$)	0.09	0.035	0.033	0.024	0.023
Salinity ($g.L^{-1}$)	1.3	0.99	0.85	0.61	0.51

3.2 Forcing

3.2.1 Tidal forcing

Tides are produced by a combination of the motion of the Earth, the Moon, and the Sun. Harmonic analysis of tide shows that tide can be considered as a summation of a finite number of harmonic constituents. Constituents have different origins, therefore each one has its own phase angle, amplitude and periodicity. In the TELEMAC 3D system, several tidal databases are available : JMJ, NEA and TPXO, each with its own sets of harmonic constituents. In this study we focused on the JMJ and TPXO databases, because the NEA tidal base had not been fully tested at the beginning of this study according to the Telemac User Manual (v7p1).

The JMJ database was developed by Jean-Marc Janin and Xavier Blanchard, to determine current fields through harmonic constituents. This database is limited to the near Atlantic and the English Channel. It only takes four harmonic constituents into account: M2, S2, N2, and M4. It provides phase angles and amplitudes for water elevation, as well as horizontal velocity components. Water elevation and horizontal velocity components are expressed as follows, at a point M of the mesh and a time t :

$$F(M,t) = \sum_i F_i(M,t) \tag{3.1}$$

with :

$$F_i(M,t) = f_i(t) A_{F_i}(M) cos\Big(2\pi \frac{t}{T_i} - \varphi_{F_i}(M) + u_i^0 + v_i(t)\Big) \tag{3.2}$$

where :

- F : the water elevation h or one of the horizontal velocity components U or V,
- i : a harmonic constituent,
- T_i : the periodicity,
- A_{F_i} : the amplitude,
- φ_{F_i} : the phase angle
- u_i^0 : phase angle at t = 0
- $f_i(t)$ and $v_i(t)$: nodal factors

The Oregon State University (OSU) has developed a global solution for tide, named TPXO, and several local solutions, such as AO, covering the Atlantic Ocean or ES, covering the European Shelf (http://volkov.oce.orst.edu/tides/region.html). The global solution considers eleven harmonic constituents : M2, S2, N2, K2, K1, O1, P1, Q1, M4, MS4 and MN4, and local solutions consider thirteen harmonic constituents adding Mf and Mm. These solutions give amplitudes and phase angles for the water elevation and transport terms (i.e. a product of the water elevation and the velocity components). The theory used by the OSU is slightly different, as it uses complex numbers :

$$F_j(M,t) = f_j(t) Re\left(A_{F_j}(M) exp\left(i\Big(2\pi \frac{t}{T_j} + \varphi_{F_j}(M) + u_j^0 + v_j(t)\Big)\right)\right) \tag{3.3}$$

Based on the harmonic analysis (cf. page 69) of water elevations collected at the mouth of the estuary, we decided to use Atlantic Ocean local solution of the TPXO data base. Indeed, the K2 harmonic constituent, which appears to have a significant influence in our study site, is not considered in the JMJ data base.

3.2.2 Riverine forcing

Values of river flows to be imposed at the riverine boundaries are extracted from the Banque Hydro database (http://www.hydro.eaufrance.fr/). The Nive river discharge is directly accessible on the Banque Hydro website, while for the Adour river we had to add the river flow collected at Saint Vincent de Paul (Adour) and all the downstream tributaries except the Nive river, i.e. both Gaves rivers, the Bidouze river and the Luy river. The daily average river discharge is imposed in the "liquid boundaries file". The value to be imposed at each time step is calculated by interpolation.

3.2.3 Coriolis

The Coriolis force is caused by the rotation of the Earth on its own axis. On a point of latitude λ, the Coriolis force can be expressed as follows:

$$\vec{F}_{Coriolis} = -2\vec{\omega} \wedge \vec{V} \quad where \quad \vec{\omega} = \begin{pmatrix} 0 \\ \omega cos(\lambda) \\ \omega sin(\lambda) \end{pmatrix} \tag{3.4}$$

As the Coriolis parameter $f = 2\omega sin\phi$ depends on the latitude ϕ, it has to be given in the configuration file. In our case, the Coriolis parameter was estimated to be $f = 0.0001$.

Even if the Adour estuary is too narrow for the Coriolis force to play a role in the estuarine hydrodynamics, it has been shown that it can have an major impact on the plume dispersion in the coastal area [23].

3.3 Boundary conditions

The boundary conditions file was generated with BLUEKENUE and can be easily modified with a text editor, if needed.

3.3.1 Solid boundaries

Bottom and lateral boundaries were defined as solid boundaries, where the impermeability condition applies : $\vec{U}.\vec{n} = 0$ and a tangential stress $\mu\frac{\partial\vec{U}}{\partial n}$ due to friction on the wall is specified.

3.3.2 Liquid boundaries

At the maritime boundary, a tidal forcing is imposed. Velocity components (U and V) and the water elevation (H) are extracted from TPXO data base. Salinity values are left free. The vertical velocity profile is defined as logarithmic.

At riverine boundaries, river flow and salinity values are imposed. River flow values are extracted from the Banque hydro data base, and the salinity value is set at 0. The water elevation and velocity components are left free. The vertical velocity profile is defined as logarithmic.

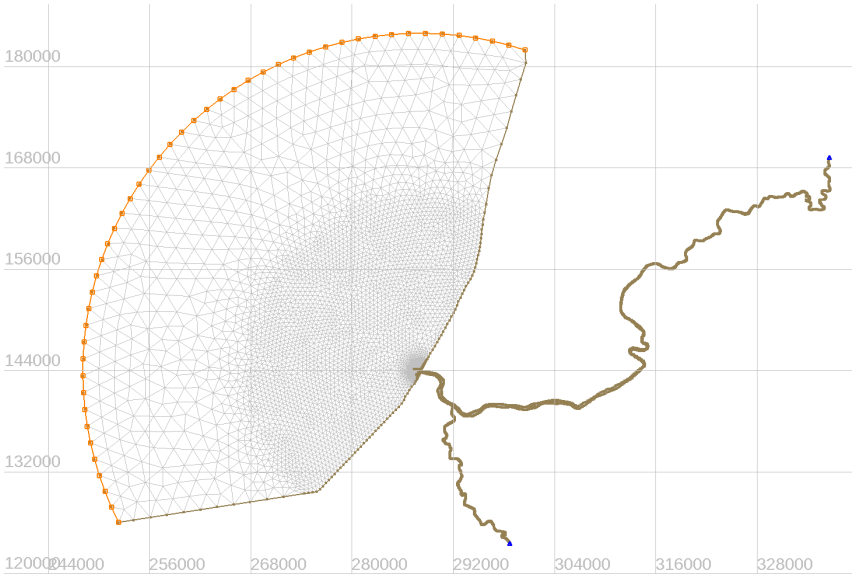

Figure 3.2: Liquid boundary conditions generated with BLUEKENUE software.

3.4 Initial conditions

The riverine part of the domain is set with a zero salinity value, while the maritime part is set with a salinity value collected by the SOMLIT network (http://somlit.epoc.u-bordeaux1.fr/fr/): on September 2017 : 34.5, on June 2018 : 34.7, and on sept 2018 : 35.2. This configuration was implemented in the source code (i.e. subroutine 'CONDIM.f'), in order to save some spin-up time.

The TPXO initial condition was used for the simulation, in order to initialize the model easily. It imposes an initial elevation and velocity extracted from the TPXO model. One drawback of this TPXO initial condition is that the initial elevation and velocity are not available for the upstream part of the rivers, therefore a zero velocity and a mean elevation are imposed in these reaches of the rivers. It results in a jump of the initial velocity and elevation values at the boundaries between those two areas, at the first time step.

In order to facilitate the initialization of the model, simulations always begin at a high tide on a neap tide. Beginning at high tide means that the water will move in the same direction in the whole domain, with waters coming from rivers and ocean moving towards the maritime boundary at the first time steps. Beginning on neap tide makes the transition easier, with waters moving slowly at the beginning and increasing in velocity progressively.

3.5 Spin-up time

The spin-up time is the number of simulated days necessary for a numerical model to establish the flow. In our case, we estimated the spin-up time based on four combinations of maritime and hydrological conditions, i.e. ST/LD, NT/LD, ST/HD and NT/HD. The initial conditions were set to constant elevation with no velocity, which is the stringent initial conditions to be imposed. The salinity is the parameter which requires a longer spin-up time, compared to water elevation and velocity. In the basic configuration of TELEMAC 3D, a unique salinity value is defined in the whole domain at the initial time step. As salinity is the parameter which requires the biggest spin up time, the source code (subroutine 'CONDIM.f') was modified to impose fresh water inside the rivers and salty waters everywhere else. We estimated that we saved 5 days in spin-up time, thanks to this modification of the initial conditions. Another way to reduce the spin-up time is to begin the simulation on a high tide. The spin-up time was finally estimated at about 20 days.

Chapter 4

Calibration and validation

Numerical models are very powerful tools, however, it is critical to have an accurate understanding of the system, based on field data, to develop a numerical model able to reproduce in a reliable manner the hydrodynamics of a specific system. It needs to be properly calibrated and validated with field observations. In order to estimate errors introduced by the numerical model, different indicators can be used.

Error estimations
The statistics presented below were used to evaluate the performance of the numerical modeling system. In the following section, $< . >$ represents the average and $|.|$ the modulus. The Root Mean Square Error (RMSE) is the standard deviation of the prediction errors. It is frequently used to evaluate the differences between observed values and predicted values. It is a measure of how close to data points a fitted line is. The lower the RMSE, the better the prediction. The RMSE is generally not used on its own to assess a model because it is largely influenced by the outliers. RMSE is expressed as :

$$RMSE = \sqrt{< (m-o)^2 >} \tag{4.1}$$

where m is the simulated data and o is the data collected on site.

RMSE values have units, for this reason we normally can not compare RMSE values for two different parameters, e.g. temperature and velocities.

Willmott (1981) proposed an "index of agreement" [138] defined as :

$$WS = 1 - \frac{< (m-o)^2 >}{< (|m- < o > | + |o- < o > |)^2 >} \tag{4.2}$$

A Willmott skill score (WS) of 1 indicates that model and measurements "agree" perfectly. The smaller the WS, the bigger the difference between the numerical model and the observations. This score is dimensionless, and in this sense it complements the information contained in RMSE. This score has been used in various recent estuarine studies [27, 77, 79, 116, 131].

The strategy employed to calibrate the model is first to compare the water elevations simulated to the ones collected by the tidal gauges along the estuary. Friction coefficients were chosen to get the best fit between numerical and experimental data. In a second step, simulated velocities were compared with the moored-ADCP data collected during one month in December of 2017. The third step dedicated to the vertical salinity structure is more complex, due to the important role of turbulent mixing. Simulated velocity and salinity profiles are compared to the ones collected in June and September 2018. Finally, the capacity to reproduce the along-estuary salinity structure is analyzed based on the MINIBAT data collected in September 2017.

4.1 Water elevation

The bottom friction coefficient was calibrated based on the water elevation measured by five tidal gauges spread along the Adour and Nive rivers : Convergent, Quai de lesseps, Pont bLanc, Villefranque and Urt (Fig. 4.1). Data from these tidal gauges are available on the SHOM website (https://data.shom.fr/). Simulations were all run with the same turbulence model, namely Prandlt formulation of mixing length turbulence model with Munk & Anderson damping function, as it has little impact on the water elevation values.

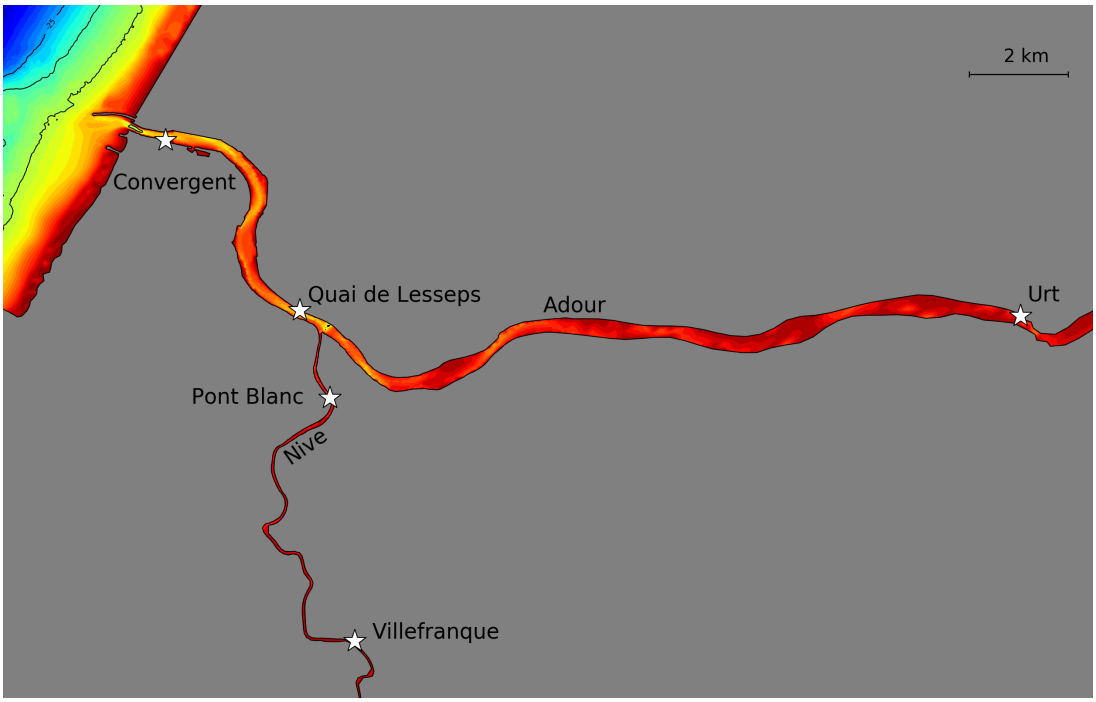

Figure 4.1: Location of the five tidal gauges (white stars) along the Adour and Nive rivers.

The bottom friction coefficient imposed in the lower part of the estuary has a small influence on the water elevation for the three downstream control points. However, the friction coefficient imposed on the rest of the two rivers largely impacts the phase and the amplitude of the tidal wave for both Urt and Villefranc control points. After a series of tests including uniform and spatially variable coefficients, the best performance is obtained with two different Strickler friction coefficients imposed in the numerical model, namely S=35 $m^{1/3}.s^{-1}$ in the lower reach and an unrealistic friction coefficient of S=5 $m^{1/3}.s^{-1}$ in the upper reach (Strickler law). With such coefficients, the simulated water elevation was consistent with the observations, with an RMSE of less than 10 cm in the lower estuary (Tab. 4.1). For upstream tidal gauges: Urt and Villefranque, an unrealistic friction coefficient was used to calibrate the phase of the tidal wave. During the calibration tests, different friction coefficients were tested, none of them was able to reproduce the phase and amplitude of the tidal wave accurately. It was decided to choose a friction coefficient which favored the phase over the amplitude.

Table 4.1: Error calculations between modeled and observed water elevations at five tidal gauges locations : Convergent, Quai de lesseps, Pont bLanc, Villefranque and Urt.

	Conv.	Q. Lesseps	P. Blanc	Villefr.	Urt
RMSE (m)	0.06	0.09	0.13	0.22	0.28
W.S. (%)	99.9	99.7	99.4	98.1	96.7

The numerical model developed in this study only takes into account the astronomical tide, i.e. the water elevation variation due to the gravitational pull of the Moon and the Sun. Nevertheless, the water elevation measured by tidal gauges is affected by phenomena other than gravitational pull, such as the large scale variations of atmospheric pressure. Such meteorological mechanisms can modify the water elevation, with a difference that can reach up to 50 cm in extreme conditions. This effect was ignored in the present simulations and must be implemented in future works.

Another source of errors in the water elevation estimations is the siltation of the water stabilizer tube for the radar sensor used by the tidal gauges. Regular maintenance operations are needed to keep this tube clear of sediment. When the bottom of the tube has silted up, errors can appear in the measurement of the low tide, specifically during spring tides.

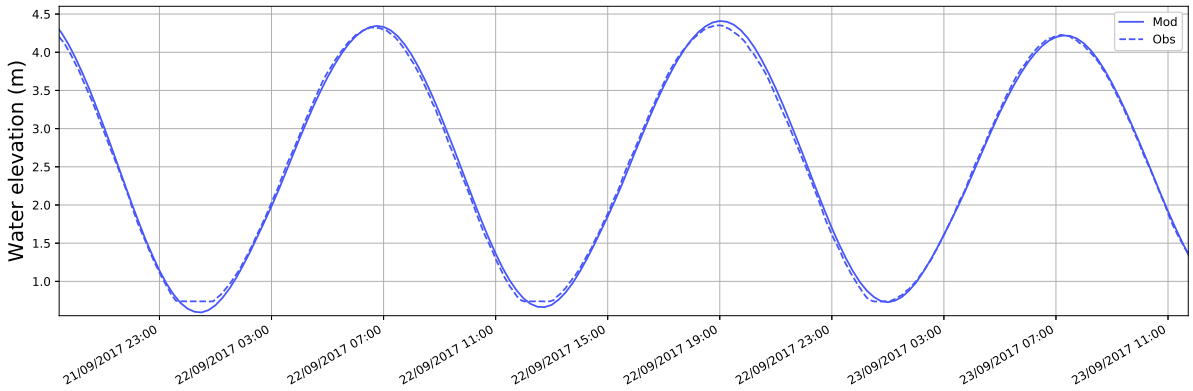

Figure 4.2: Timeseries of observed (dashed line) and modeled (full line) water elevation at Convergent tidal gauge.

4.2 Velocity

Data collected by both bottom-moored ADCPs deployed during one month in September of 2017 were used for the calibration and validation of the velocity predicted by the numerical model (Fig. 4.3). Error estimations are presented in Table 4.2. A good overall agreement is obtained in terms of magnitude and timing. The numerical model tends to overestimate the rising velocity on the surface. The velocity is better reproduced during spring tide than neap tides.

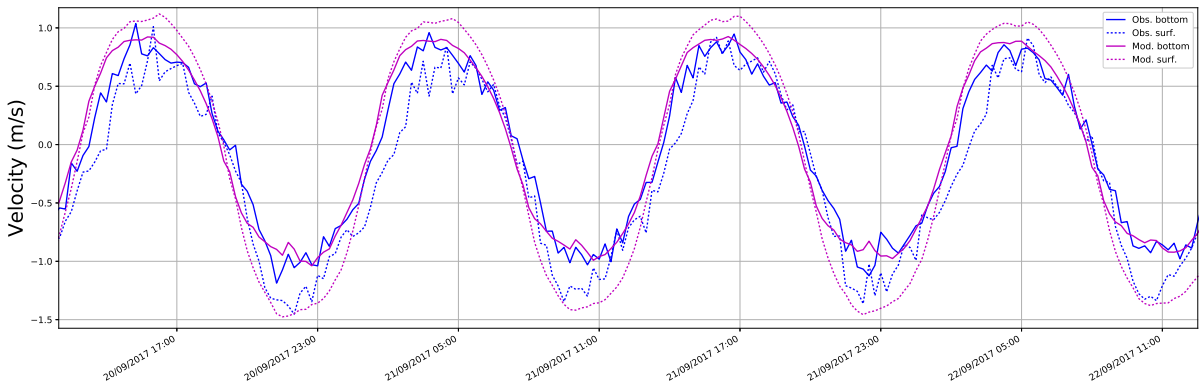

Figure 4.3: Timeseries of observed (blue) and modeled (pink) velocity at SF2 station.

Table 4.2: Error calculations between modeled and observed velocities at SF2 and SF4 stations.

	SF2		**SF4**	
	Bottom	Surface	Bottom	Surface
RMSE ($m.s^{-1}$)	0.31	0.39	0.25	0.39
W.S. (%)	90.0	82.2	92.2	84.5

4.3 Vertical salinity structure

In a salt-wedge estuary study, such as this study, the vertical salinity stratification is of the foremost importance. It has been demonstrated with the Viollet test case that a permanent stratification can be correctly reproduced with TELEMAC3D. However, according to field data collected inside the lower estuary, it has been shown that the salt-wedge structure is reset at the end of almost each tidal cycle. The question arises on the capacity of the numerical model to reproduce such unsteady stratification, variable both in time and space. Bottom-moored velocity profiles combined with salinity profiles collected during the boat surveys were used to calibrate the vertical structure (Fig. 4.4). In order to improve the reproduction of the vertical salinity structure different turbulence models, damping functions, advection schemes, and Prandlt number values were tested. Some of the simulations results are presented below, others were placed in Annex 2.

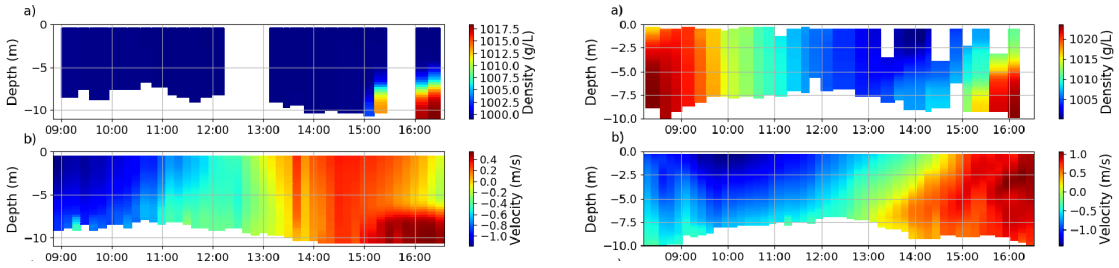

Figure 4.4: Tidal evolution of: (a) vertical structure of density, (b) time-averaged velocity, and during HD-ST18 (on the left) and LD-ST18 (on the right) experiments (extracted from Fig. 2.12 and 2.11)

4.3.1 Turbulence models

Different vertical turbulence models were tested in order to investigate which one would be the more efficient to reproduce the different patterns of stratification. Simulations were run with constant viscosity, mixing length and $k-\varepsilon$ turbulence models on the vertical axis. The constant viscosity model was used along the horizontal. This study revealed that the vertical salinity structure is very sensitive to the choice of turbulence model. The constant viscosity model, when used with $\nu_t = 10^{-6}$, tends to well reproduce the stratification during the rising tide, and to underestimate the mixing during the falling tide, as expected with a turbulence model which as a constant value throughout the tidal cycle (cf. Annex 2). This kind of turbulent model is thus not able to reproduce the intense mixing period during the falling tide and the low mixing periods during the rising tide. Different formulations of the mixing length model were tested: Prandlt, Tsanis, and Quetin, all with a Munk & Anderson damping function. In general manner, mixing length model does not mix enough during the ebb, with remaining salt in HD-ST18 simulations and no vertically homogeneous density profiles, and it mixes too much during the flood where the stratification should be steeper. The salt-wedge structure observed during HD-ST18 , with a layer of fresh water flowing over the salt-wegde is never reproduced. During the ebb, the salt has a global tendency to stay longer in the estuary than the observations. For example the results

obtained with Quetin formulation of the mixing length model are presented in Figure 4.5. The $k-\varepsilon$ turbulence model seems to mix too much throughout the tidal cycle, resulting in vertically homogeneous density profiles even during the flood (cf. Annex 2).

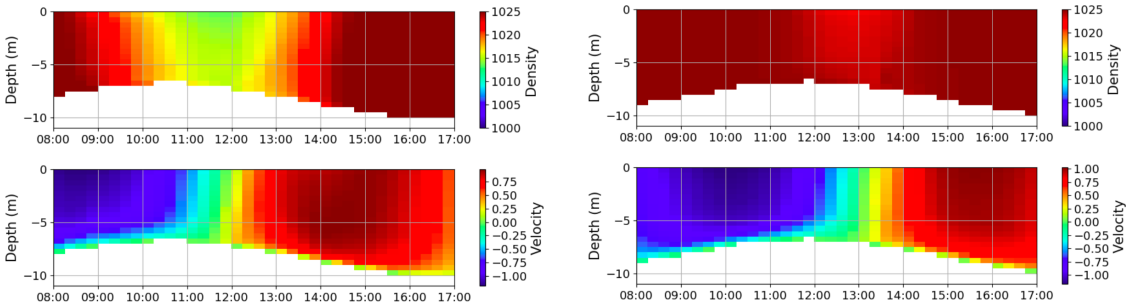

Figure 4.5: Tidal evolution of the: vertical structure of density (two subplots on top), velocity (two subplots underneath), results obtained with a simulation of HD-ST18 (on the left) and LD-ST18 (on the right) with Quetin mixing length model.

Best results were obtained with the **Prandlt mixing length model** which are shown here in Figure 4.6. Nevertheless, those results do not reproduce the salt-wedge entrance accurately, as the stratification is not as steep as it was observed and the two-layer flow is not reproduced. The salt-wedge reaches the measurement site one hour before what it was measured during HD-ST18. In the same simulation, during the ebb some salt persists inside the estuary after 09:00. In LD-ST18 simulation, the horizontal gradient of density observed during the ebb is not well reproduced, as well as the stratification generated during the flood. Too much salt persists in the estuary during the slack time, i.e. the salt-wedge is not fully flushed at the end of the ebb tide as observed.

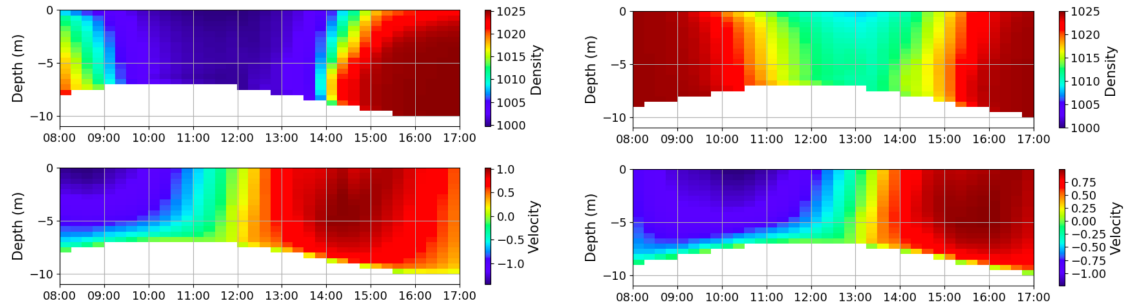

Figure 4.6: Tidal evolution of the: vertical structure of density (two subplots on the top), velocity (two subplots underneath), results obtained with a simulation of HD-ST18 (on the left) and LD-ST18 (on the right) with Prandlt mixing length model.

4.3.2 Damping functions

The best results were obtained with Prandlt mixing length model, and they were unable to reproduce the stratification accurately during the flood, i.e. when the stratification is strong. Therefore, we decided to test other damping functions than the Munk & Anderson, in order to improve the representation of the stratification during the flood. The two damping functions, Mac Anally and Lehfeldt & Bloss, were presented in the first Chapter of this Part. These two damping functions were supposed to help us to make the stratification steeper during the flood, as they tend to strongly damp the eddy viscosity when Ri values are high (stable stratified configuration). However, the results were not as expected (Fig. 4.7), the turbulent mixing seems to be even more important than with Munk & Anderson damping function. Best results were obtained with the Munk & Anderson damping function (Fig. 4.6).

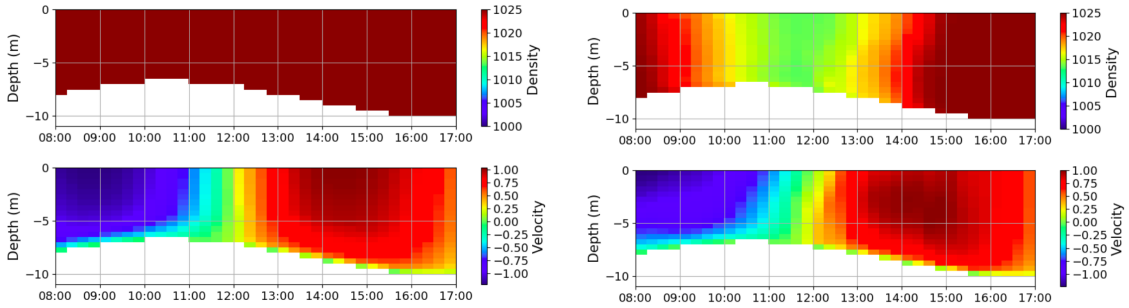

Figure 4.7: Tidal evolution of the: vertical structure of density (two subplots on the top), velocity (two subplots underneath), results obtained with a simulation of HD-ST18 with Lehfeldt & Bloss (on the left) and Mac Anally (on the right) damping functions.

4.3.3 Advection scheme

The choice of the advection scheme plays a major role in the performance of numerical models. In numerical simulations, the energy can be dissipated by three mechanisms: bottom friction, turbulent dispersion and numerical diffusion [80]. The bottom friction is generally calibrated with water elevation data. In order to resolve velocity and salinity gradients properly, the mesh is supposed to be fine enough and the turbulent model to be accurately chosen. The aim of the present study is obviously not to extensively present and assess the various numerical strategies for advection schemes, but to present our choice in the existing options in TELEMAC3D. It has been demonstrated that SUPG scheme is the best suited for narrow rivers or estuaries in TELEMAC2D simulations [80]. In TELEMAC3D the advection scheme for velocities used by default (and therefore used in the previous mentioned simulations) is the characteristic scheme. Therefore we decided to run simulations with the SUPG advection scheme for velocities (Fig. 4.8). The results have revealed a moderate sensitivity to the choice of the advection scheme for velocities. If we compare the results of the HD-ST18 simulation run with SUPG scheme (Fig. 4.8) and the results obtained with the characteristic scheme (Fig. 4.6), we can see that the salt tends to stay longer inside the estuary during the ebb with SUPG scheme and the stratification is steeper during the flood with the characteristic scheme. It can be concluded that the characteristics scheme gives the best results.

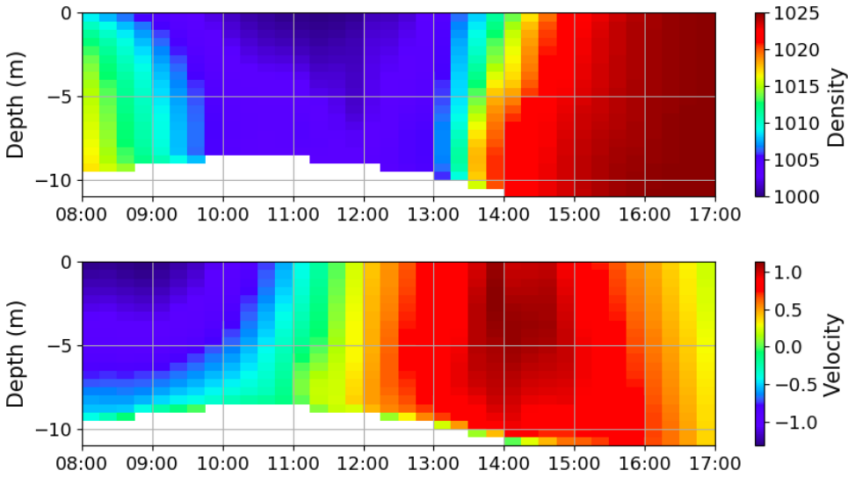

Figure 4.8: Tidal evolution of the: vertical structure of density (on the top), velocity (underneath), results obtained with a simulation of HD-ST18 with the SUPG advection scheme for velocities.

4.3.4 Prandtl number

As previously introduced the eddy diffusivity for tracers is computed as : $\nu_T = \nu_t/Prt + K$, therefore we may be able to reduce the tracer diffusion playing with the Prandlt number values. Different values of the Prandlt number were tested: 0.5, 1.2, and 1.5. Results of these simulations have not shown any improvement as presented by Figure 4.9. Best results were obtained with the default value, i.e. $Prt = 1.0$ (Fig. 4.6).

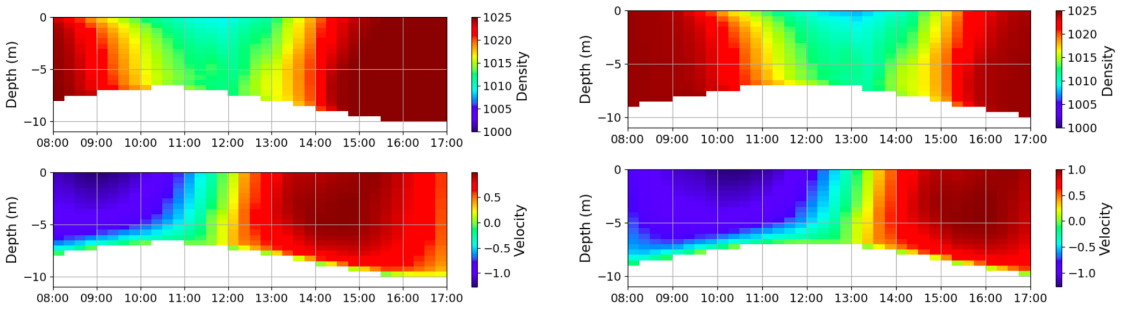

Figure 4.9: Tidal evolution of the vertical structure of density and velocity, results obtained with simulations of HD-ST18 (on the left) and LD-ST18 (on the right) with $Prt = 1.2$.

4.3.5 No tracer diffusion

All the previously mentioned results of simulations are too diffusive, therefore we decided to entirely damp the diffusion of tracers. The KEYWORD "SCHEME FOR DIFFUSION OF TRACERS" monitors the choice of the diffusion scheme for the tracers, when equal to zero no diffusion is computed. When this keyword was combined with the $k - \varepsilon$ turbulence model, the results obtained for high discharge conditions were satisfactory (Fig. 4.10). The piston like behavior with homogeneous profile of velocity at the beginning of the rising tide and the two layer flow from 15:00 is relatively well reproduced with this simulation. However, the simulation results under LD-ST18 conditions are not consistent with the observation. The salt is not flushed of the estuary at the end of the ebb and the horizontal gradient of salinity is not reproduces (Fig. 4.10).

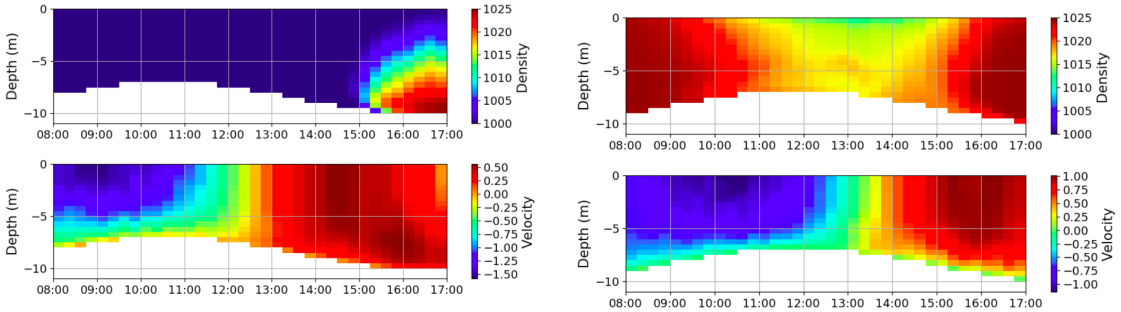

Figure 4.10: Tidal evolution of the vertical structure of density and velocity, results obtained with simulations of HD-ST18 (on the left) and LD-ST18 (on the right) with $k - \varepsilon$ turbulence model and no diffusion of tracers.

4.4 Longitudinal salinity structure

The vertical salinity structure is also variable along the estuary, as shown in the previous Part. Longitudinal sections of salinity recorded with the MINIBAT (Fig. 4.11 and 4.12) can be qualitatively compared to the modeling results. It should be noted that figures extracted from

the model are instantaneous, while it lasts c.a. 40 minutes to collect the MINIBAT data along a longitudinal transect.

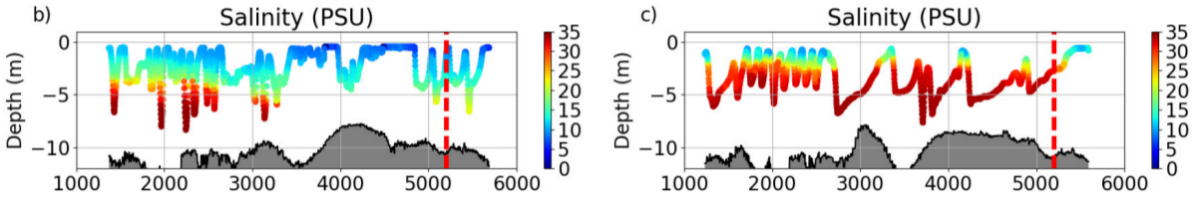

Figure 4.11: Longitudinal and vertical structure across the lower estuary from Minibat measurement during LD-NT17 experiment.(b) and (c): salinity data for rising and falling tide. The bed of the estuary is represented in grey. The red dashed line represents the SF2 station location. Extracted from Fig. 2.7

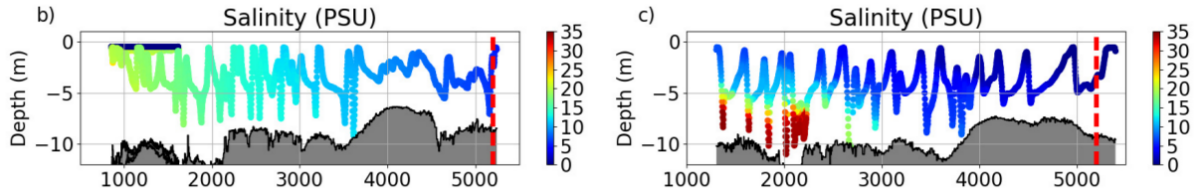

Figure 4.12: Longitudinal and vertical structure across the lower estuary from Minibat measurement during LD-ST17 experiment.(b) and (c): salinity data for falling and rising tide. The bed of the estuary is represented in grey. The red dashed line represents the SF2 station location. Extracted from Fig. 2.4

In the previous section we were not able to find a single set-up which reproduces the observed features of the saline structure under all forcing conditions. The Prandlt formulation of the mixing length model with Munk & Anderson damping function was the best set up to reproduce the dry season conditions, while the $k - \varepsilon$ model with no diffusion of the tracer produces the best results in the wet season conditions. Along-estuary sections were extracted from both simulations in order to be compared with the MINIBAT data (Fig. 4.13 and 4.14). As expected best result were obtained with the mixing length configuration, as the MINIBAT data were collected during the dry season. As shown by Figure 4.13, the $k - \varepsilon$ model configuration is able to reproduce the persistent salt-wedge structure during neap tide, while the results obtained on spring tide are not consistent with the observations. On the other hand, with the mixing length configuration, all the sections retrieved from the simulations are in very good agreement with the observations. During spring tide, the horizontal gradient of salinity is clearly reproduced by the numerical model on the ebb, as well as the salt-wedge entrance on the flood. During neap tide, the permanent salt-wedge is accurately simulated.

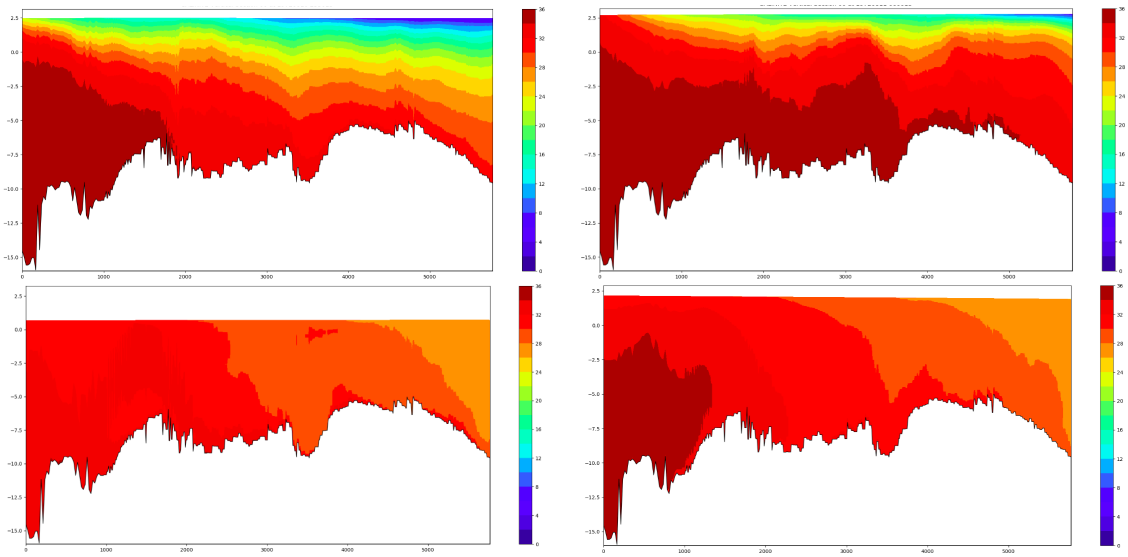

Figure 4.13: Longitudinal and vertical structures across the lower estuary, from simulation run with $k-\varepsilon$ model and no diffusion of the tracer, under LD-ST17 + LD-NT17 experiment conditions: during flood (top left) and ebb on neap tide (top right), and during ebb (bottom left) and flood (bottom right) on spring tide.

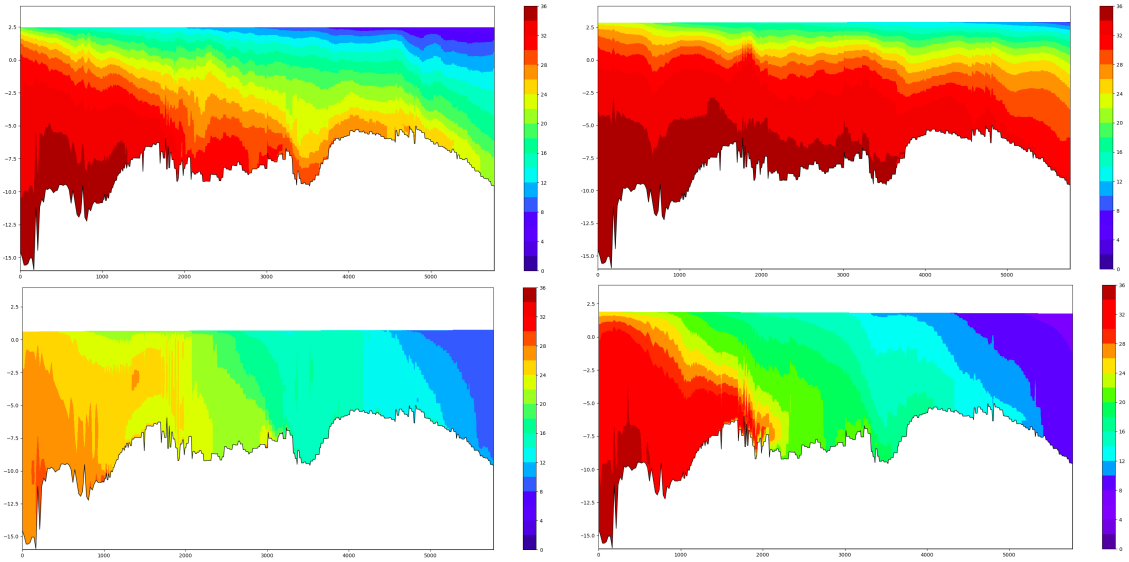

Figure 4.14: Longitudinal and vertical structures across the lower estuary, from simulation run with Prandlt formulation of the mixing length model and Munk & Anderson damping function, under LD-ST17 + LD-NT17 experiment conditions: during flood (top left) and ebb on neap tide (top right), and during ebb (bottom left) and flood (bottom right) on spring tide.

4.5 Stability of the water column and turbulent mixing

The density stratification has been shown to be in competition with tidal turbulent mixing, resulting in the lower Adour estuary in a strengthened stratification during the rising tide and a peak of turbulent mixing during the falling tide. In order to evaluate the capacity of the numerical modeling to reproduce this pattern, the eddy viscosity estimated during the simulations (Fig. 4.16 and 4.18) were compared to measurements (Fig. 4.15 and 4.17). The gradient Richardson number was also estimated based on simulated velocity and density fields.

Figures 4.15 and 4.16 represent the tidal evolution of the eddy viscosity and gradient Richardson number, among others, for the HD-ST18 experiment, estimated based on observations and simulation, respectively. The simulation was run with the $k-\varepsilon$ model with no diffusion of the tracer. This setup produces the best results for freshet conditions. Figure 4.16 reveals that the instability of the water column ($Ri < 0.25$) during the falling tide is well reproduced by the numerical modeling, as well as the stability during the rising tide. However, it seems that the eddy viscosity data retrieved from simulation results are irrelevant.

Figures 4.17 and 4.18 represent similar data for the LD-ST18 experiment. The simulation was run with the Prandlt formulation of the mixing length model with Munk & Anderson damping function. This setup produces the best results for dry season conditions. As the density and velocity fields are not accurately reproduced by the numerical modeling, the consequent estimation of the gradient Richardson number is not accurate either. Regarding the eddy viscosity, a peak of turbulent mixing is reproduced during the ebb tide as observed during the experiment, but it is slightly underestimated.

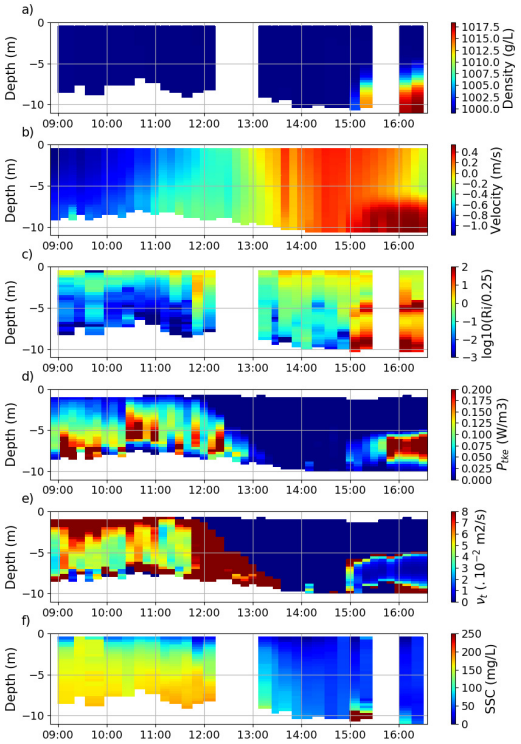

Figure 4.15: Tidal evolution during HD-ST18 experiment : (a) vertical structure of density, (b) time-averaged velocity, (c) gradient Richardson number, (d) rate of TKE production, (e) eddy viscosity and (f) suspended sediment concentration.

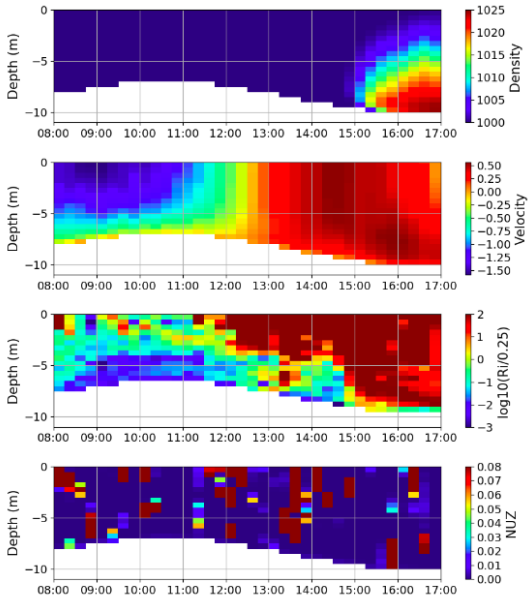

Figure 4.16: Tidal evolution obtained with simulation of HD-ST18 experiment : vertical structure of density, velocity, gradient Richardson number, and eddy viscosity.

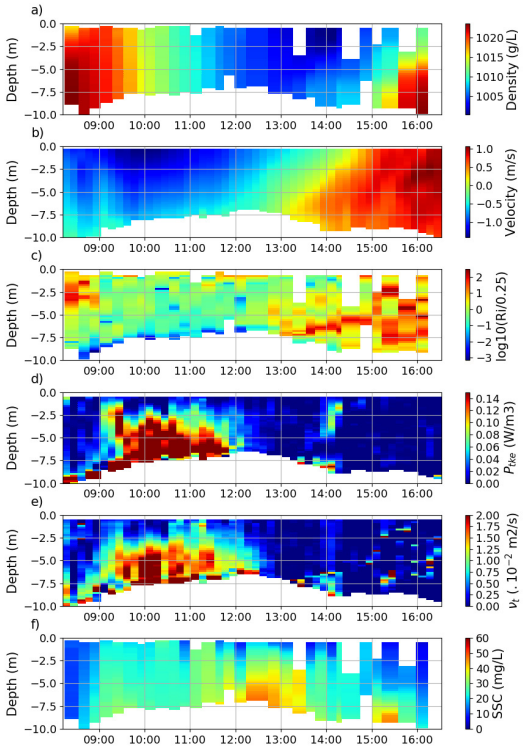

Figure 4.17: Tidal evolution during LD-ST18 experiment : (a) vertical structure of density, (b) time-averaged velocity, (c) gradient Richardson number, (d) rate of TKE production, (e) eddy viscosity and (f) suspended sediment concentration.

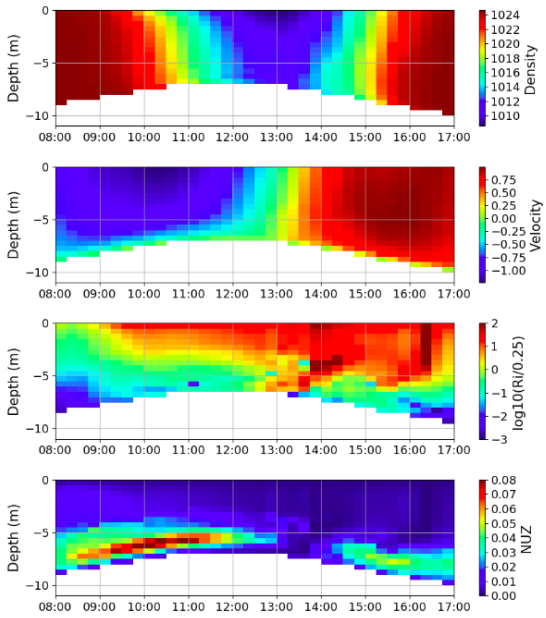

Figure 4.18: Tidal evolution obtained with simulation of LD-ST18 experiment : vertical structure of density, velocity, gradient Richardson number, and eddy viscosity.

Chapter 5

Synthesis & Discussion

It has been demonstrated with the Viollet test case that a permanent stratification can be correctly reproduced with TELEMAC3D. However, according to field data collected inside the lower estuary, it has been shown that the salt-wedge structure is reset at the end of almost each tidal cycle. The Adour estuary is thus characterized by a unsteady stratification, varying in both time and space. Such complex hydrodynamics is not easy to reproduce numerically. A 3D realistic numerical model of the Adour estuary was developed with TELEMAC 3D. This numerical model was calibrated and validated with the data collected during this study. Even if the water levels and velocities were in good agreement with the observations, the vertical and longitudinal salinity structure were difficult to reproduce. The vertical salinity structure shows a great sensitivity to the choice of a wide range of physical and numerical parameters. We were not able to find a single set-up which reproduces the observed features of the saline structure under all forcing conditions. The Prandlt formulation of the mixing length model with Munk & Anderson damping function was the best set up to reproduce the dry season conditions, while the $k-\varepsilon$ model with no diffusion of the tracer produces the best results in the wet season conditions.

Regarding the longitudinal structure, data were available only for the dry season. The configuration with Prandlt formulation of mixing length model with the Munk & Anderson damping function then gave a good agreement with the observations. All the pattern of horizontal gradient, non-permanent salt-wedge and stagnant salt-wedge were effectively reproduced.

A complex hydrodynamics, such as the one of a time-dependent salt-wedge, numerically reproduce with TELEMAC3D has not been found in the literature. However in the Loire estuary, where a strong stratification can develop under certain forcing conditions, a multi-layer mixing length model was developed to be adapted to a stratified flow [130]. The idea is to have a characteristic length which is not based on the water depth but based on the layer thickness. This new turbulence model showed good results on the Loire estuary simulations, and it was able to reduce the computational time in comparison with complex turbulence model such as $k-\varepsilon$ model.

In the literature, the effect of numerical mixing in the reproduction of the estuarine hydrodynamics is often discussed [94, 95]. All types of numerical model produce numerical mixing which is not easy to estimate and damp. This numerical mixing is generally produced at the same space and time as turbulent mixing. One solution is thus to damp artificially the turbulent mixing computed by the numerical model, which will be compensated by numerical mixing. Other solutions are to make the vertical resolution as fine as possible and the vertical mesh can also be adapted to follow the gradient of density. Advection schemes are also responsible for diffusion, advection scheme of the higher order is generally recommended. The implementation of such solutions could be considered for further work.

Part IV

Conclusion and prospects for future work

Chapter 1

Estuarine circulation and suspended sediment dynamics

This study aimed to investigate the hydro-sedimentary behavior of the lower Adour estuary by means of field experiments. A series of hydrodynamical processes are documented through bottom-moored, hull-mounted and vertical profiling instrumentation. It has been shown that its functioning is strongly influenced by both river and tidal forcing, resulting in a wide range of density stratification. The stratification variations show different time scales : from flood to ebb tides, from neap to spring tides, even from dry to wet seasons. It has been demonstrated that stratification is strengthened during the flood tide and weakened during the ebb tide. During low river discharge, neap tides promote stable a salt-wedge in the lower estuary, while spring tides allow full flushing of the salt-wedge. On the other hand, wet season has a tendency to constrain the salt-wedge in a thin bottom layer, enhancing the vertical stratification. This strong variability in the flow structure has a huge influence on the flushing capacity of the estuary.

The tidal evolution of the gradient of Richardson number has revealed the straight influence of the salinity structure on the turbulent mixing. Flood tide is generally associated with reduced turbulence production and stable stratification, while ebb tide is characterized by strong turbulent mixing. Through stratification and mixing characteristics of the Adour estuary, a recent classification scheme has been applied to compare it to other salt-wedge estuaries. Based on the Geyer and MacCready classification [46], the Adour estuary varies from salt-wedge to partially mixed estuary. This regime change could be attributed to a switch of major forcing between different hydrological conditions, i.e. fortnightly cycle and river discharge variations. It also has been hypothesized that the artificial channelization of the lower estuary coupling with strong dredging activities act to enhance the fluctuations in hydrological regimes.

Based on the collected data, it was established that both tides and river flow are the major drivers of sediment inside the estuary. During the tidal cycle, sediments are alternatively eroded from the bed by shear stress, advected by the flow and deposited by gravitation. Periods of maximum of velocity, i.e. one hour before high tide and low tide, are associated with strong erosion and advection, while periods of minimum of velocity, i.e. slack time, are associated with deposition processes. The tidal amplitude variations, during the fortnightly cycle, tend to enhance and/or to damp these mechanisms of erosion, advection and deposition. During spring tide, tidal currents are stronger and slack time shorter, resulting in an important erosion and advection, and in a reduced deposition. The opposite pattern can be observed during neap tides. It was demonstrated that variations of river discharge also influence the erosion/advection/deposition cycle. During high river discharge, ebbing currents are stronger, flooding currents are weaker, and slack time are shorter. This condition will favor erosion and advection during the ebb, resulting in a good flushing capacity of the estuary.

Density effects, salt-wedge displacement and the competition between stratification and mixing processes have a strong impact on the suspended matter displacement : longitudinal con-

vergence at the salt tip, sinking of particles due to stratification induced turbulence damping, and re-suspension due to the salt-wedge passing. However, the major mechanism associated with ETM generation has not been observed in the lower estuary : tidal asymmetry. The second major mechanism, the residual estuarine circulation, has been observed only under specific hydrological conditions: neap tides during dry season, when the velocity, turbulence and thus SSC are very low. The absence of the two major mechanisms responsible for ETM generation combined with low sediment input from both river and ocean could explain why no stable ETM was observed during our field campaigns. However, tidal pumping mechanism may be responsible for an ETM in the upper part of the estuary.

The **lateral dynamics**, which has not been explored in the present data analysis, may play an additional important role in the estuarine circulation and salinity structure. Both local curvature of the lower estuary and cross-sectional bathymetric gradient are expected to favor a degree of three-dimensionality in the estuarine flow structure. This calls for further dedicated experimental campaign to better understand the contributions of along-channel and lateral components. It could be explored with **ADCP transects at different section inside the estuary**. These ADCP transects should be combined with turbidity and salinity profiles, as well as water samples, in order to study the along-channel and lateral sediment fluxes variations.

The analysis of the tidal wave propagation inside the Adour estuary reveals a **significant tidal asymmetry in the upper part of the estuary**. It is expected to favor the generation of **an ETM in this reach of the estuary**. Field experimentations should be extended to the upper part of the estuary, at least until Urt village to confirm or invalidate this hypothesis. Data from the MESsAGe network may also be used to complement our understanding of the estuary. This network collects turbidity and SSC data in Saint Vincent de Paul city (about 70 km from the estuary mouth in the Adour river) and in Labatut village (about 40 km from the estuary mouth in the Gave de Pau river). An extension of the MESsAGe network with **continuous data collection in the lower estuary**, based on our experience with the YSI probe fixed to a floating pontoon, could be a good way to understand the estuarine dynamics. This kind of network are especially useful to study extreme hydrological conditions, when conventional field campaigns can not be carried out, and to cover an extended area, such as a 70km-long estuary. Such networks have been developed with success in the Seine estuary (SYNAPSES network) and in the Gironde estuary (MAGEST network).

The sediments expelled from the estuary, generally associated with pollutants and bacterias, are dispersed in the maritime area. The Adour river coastal area is composed of recreational, fishing, and protected natural areas (e.g. NATURA 2000). A specific field campaign should be carried out to understand this dispersion of sediment and the way each sensitive areas can be impacted. In Dailloux's study [23] it has been established that the wind and Coriolis force are part of the major forcing impacting the plume dispersion. However, it is expected that waves generate sufficient mixing to breakdown the plume stratification and impact the sediment dispersion in the coastal area. ADCP measurements coupled with salinity and turbidity profiles could help us to estimate the **role of waves in the plume dispersion**.

These new data would help us to get a better understanding of the estuarine dynamics, and it would also be helpful with the calibration and validation of the numerical model developed during this thesis.

Chapter 2

Numerical development

A 3D realistic numerical model of the Adour estuary was developed with TELEMAC 3D. This numerical model was calibrated and validated with the data collected during this study. The water levels and velocities were in good agreement with the observations. The vertical and longitudinal salinity structure were found to be very complex and not easy to reproduce numerically. The vertical salinity structure shows a great sensitivity to the choice of a wide range of physical and numerical parameters, such as the turbulence model, the Prandlt number or advection scheme. No single set-up was found to be able to reproduce the observed patterns of the salinity structure under all forcing conditions. The Prandlt formulation of the mixing length model with Munk & Anderson damping function was the best set-up to reproduce the dry season conditions, while the $k - \varepsilon$ model with no diffusion of the tracer produces the best results in the wet season conditions. In order to find a unique set-up different numerical tests can be foreseen with others advection schemes, or turbulence models already hard-coded in TELEMAC or available in the literature. A good start could be to update the version of TELEMAC3D to be used to pass to the version 8 recently released. A new turbulence model is available in this version 8, as well as new advection schemes. A new mesh which is adjusted to the density gradient could be another way to improve our numerical results [19].

Once a single set-up will be found to reproduce satisfactorily all the pattern observed in the Adour estuary, this model will be a powerful tool to gain understanding on the hydrodynamics of the estuary under conditions which have not been explored experimentally, such as extreme hydrological events.

In order to go further in the understanding of **the role of engineering works on the estuarine dynamics**, it could be interesting to simulate the estuary with different bathymetries and geometries. Simulation with no reduction of the section at the mouth of the estuary could enable us to estimate the reinforcement of the ebbing current due to this reduction, as well as the potential consequent lower water elevation at low tide. Other simulations with smaller depth and "natural shoals" could also enable us to estimate the role of dredging activities on the estuarine dynamics. Finally, the role of the Northern jetty on the plume dispersion could be investigated by simulations with a geometry without any jetty at the mouth of the estuary.

A second step would be to add some suspended sediments as passive tracers in the model. In order to do so, the sediment concentration in the upstream part of the Adour and Nive rivers should be known, as well as the along-channel variation of the cross-sectional sediment fluxes. To go deeper in the **sediment transport analysis**, a morphodynamic solver, such as the brand new GAIA module [40] (part of the TELEMAC suite of solvers) could be coupled to the TELEMAC3D model. This new module, based on the former sediment transport module SISYPHE, is able to model complex sediment and morphodynamic processes in coastal areas, rivers, lakes and estuaries, accounting for spatial and temporal variability of sediment size classes (uniform, graded or mixed), properties (cohesive and non-cohesive) and transport modes (suspended, bedload and both simultaneously). Gaia can also be coupled with the modules for sediment dredging Nestor

[1].

To go further and to analyze the **sediments dispersion in the coastal area**, wind and wave forcing should added to the model. They are the major forcing influencing the plume river dispersion. The wind can be added in the model by the modification of one subroutine and the creation of a data file containing the two component of the wind velocity. However, the wave forcing requires to couple the numerical model with a wave module named TOMAWAC (part of the TELEMAC suite of solvers).

One of the major issue linked to the Adour river discharge is the transport of bacterias from the **sewage plant discharge** to the adjacent beaches. Two discharge points are located inside the last 5km of the estuary, and could be added in the numerical model. Waters from these discharge points could be followed by a passive tracer concentration, as a first step. A second step could be to couple the present numerical model with a **water quality model**, such as WAQTEL. This much more complex step will require a strong knowledge of chemistry. This would also require a new data set with chemical data.

Communications

Paper

• Defontaine, S., Sous, D., Morichon, D., Verney, R., Monperrus, M., 2019. Hydrodynamics and SPM transport in a man-engineered tidal estuary: the Adour river (France). Estuarine and Coastal Shelf Science.

Oral communications

• Defontaine, S., Sous, D., Morichon, D., Monperrus, M., 2018. A combined numerical/experimental approach to understand stratification and mixing processes in the Adour estuary. 16th International Symposium on Oceanography of the Bay of Biscay, Anglet, France.

• Defontaine, S., Sous, D. , Maron, P. , Morichon, D., 2019. Density stratification and turbulent mixing in a salt-wedge estuary : The Adour river. 26th annual Telemac-Mascaret Users conference, Toulouse, France.

Posters

• Defontaine, S., Sous, D., Morichon, D., 2019. Water masses and salinity circulation in a man-engineered tidal estuary : the Adour river (France). Advances in Coastal and Estuarine Physics from Nearshore to Continental-Margin Scales, Gordon Research Conference.

• Sous, D., Defontaine, S., Morichon, D., Bhairy, N., Lanceleur, L., Monperrus, M., 2018. Turbulence measurements in a stratified man-controlled estuary : The adour case. 16th International Symposium on Oceanography of the Bay of Biscay.

Bibliography

[1] *Introducing GAIA, the brand new sediment transport module of the TELEMAC-MASCARET system*, 2019.

[2] Stéphane M Abadie, Christophe Brière, Jean Dubranna, Philippe Maron, and Didier Rihouey. Erosion generated by wave-induced currents in the vicinity of a jetty: case study of the relationship between the adour river mouth and anglet beach, france. *Journal of Coastal Research*, pages 59–69, 2008.

[3] E Eric Adams, Keith D Stolzenbach, Jeng-Jong Lee, J Caroli, and D Funk. Deposition of contaminated sediments in boston harbor studied using fluorescent dye and particle tracers. *Estuarine, Coastal and Shelf Science*, 46(3):371–382, 1998.

[4] YC Agrawal and HC Pottsmith. Instruments for particle size and settling velocity observations in sediment transport. *Marine Geology*, 168(1-4):89–114, 2000.

[5] GP Allen, JC Salomon, P Bassoullet, Y Du Penhoat, and C De Grandpre. Effects of tides on mixing and suspended sediment transport in macrotidal estuaries. *Sedimentary Geology*, 26(1-3):69–90, 1980.

[6] Florian Bellafont, Denis Morichon, Volker Roeber, Gael André, and Stéphane Abadie. Infragravity period oscillations in a channel harbor near a river mouth. *Coastal Engineering Proceedings*, 1(36):8, 2018.

[7] L Boudet, F Sabatier, and O Radakovitch. Modelling of sediment transport pattern in the mouth of the rhone delta: Role of storm and flood events. *Estuarine, Coastal and Shelf Science*, 198:568–582, 2017.

[8] I Brenon and P Le Hir. Modelling the turbidity maximum in the seine estuary (france): identification of formation processes. *Estuarine, coastal and shelf science*, 49(4):525–544, 1999.

[9] Christophe Brière. *Etude de l'hydrodynamique d'une zone côtière anthropisée: l'embouchure de l'Adour et les plages adjacentes d'Anglet.* PhD thesis, Pau, 2005.

[10] JM Brown and AG Davies. Flood/ebb tidal asymmetry in a shallow sandy estuary and the impact on net sand transport. *Geomorphology*, 114(3):431–439, 2010.

[11] Louise C Bruce, Perran LM Cook, Ian Teakle, and Mathew R Hipsey. Hydrodynamic controls on oxygen dynamics in a riverine salt wedge estuary, the yarra river estuary, australia. *Hydrology and Earth System Sciences*, 18(4):1397–1411, 2014.

[12] Dailloux D. Bur R. Premier bilan sur la qualité des eaux de l'estuaire de l'adour, 2012.

[13] Hans Burchard and Helmut Baumert. The formation of estuarine turbidity maxima due to density effects in the salt wedge. a hydrodynamic process study. *Journal of Physical Oceanography*, 28(2):309–321, 1998.

[14] Hans Burchard and Robert D Hetland. Quantifying the contributions of tidal straining and gravitational circulation to residual circulation in periodically stratified tidal estuaries. *Journal of Physical Oceanography*, 40(6):1243–1262, 2010.

[15] Hans Burchard, Henk M Schuttelaars, and David K Ralston. Sediment trapping in estuaries. *Annual review of marine science*, 10:371–395, 2018.

[16] J.P. Lemoine C. Fisson. Les niveaux d'eau en estuaire de seine : Risque inondation et changement climatique, 2016.

[17] Aurélien Callens. Analyse des forçages physiques et climatiques influant sur le transport des micropolluants dans l'estuaire de l'adour, 2017.

[18] WM Cameron and DW Pritchard. Estuaries. in 'the sea, vol. 2'.(ed. mn hill.) pp. 306–324, 1963.

[19] Chris Cawthorn, Sébastien Bourban, Chris Mead, Matthew Wood, and Michael Turnbull. Adaptive vertical layering in telemac-3d. *Proceedings of the XVIIIth Telemac & Mascaret User Club 2011, 19-21 October 2011, EDF R&D, Chatou*, pages 137–141, 2011.

[20] C Cheviet, D Violeau, and M Guesmia. Numerical simulation of cohesive sediment transport in the loire estuary with a three-dimensional model including new parameterisations. In *Proceedings in Marine Science*, volume 5, pages 529–543. Elsevier, 2002.

[21] Alexandra Coynel. *Erosion mécanique des sols et transferts géochimiques dans le bassin Adour-Garonne*. PhD thesis, Bordeaux 1, 2005.

[22] R. Pedreros D. Idier. Modélisation hydrodynamique de la côte basque. partie 1 : marées, courants de marée et surcotes, 2005.

[23] Damien Dailloux. *Video measurements of the Adour plume dynamic and its surface water optical characteristics.* PhD thesis, Université de Pau et des Pays de l'Adour, 2008.

[24] Foulquier C. Dailloux D. Etude physico-chimique, chimique et bacteriologique de la qualite des eaux de l'estuaire de l'adour, 2014.

[25] JL Davies. A morphogenic approach to world shorelines. *Zeitschrift fur Geomorphologie*, 8:127–142, 1964.

[26] Victor N de Jonge, Henk M Schuttelaars, Justus EE van Beusekom, Stefan A Talke, and Huib E de Swart. The influence of channel deepening on estuarine turbidity levels and dynamics, as exemplified by the ems estuary. *Estuarine, Coastal and Shelf Science*, 139:46–59, 2014.

[27] Michel AJ de Nijs and Julie D Pietrzak. Saltwater intrusion and etm dynamics in a tidally-energetic stratified estuary. *Ocean Modelling*, 49:60–85, 2012.

[28] Michel AJ de Nijs, Johan C Winterwerp, and Julie D Pietrzak. The effects of the internal flow structure on spm entrapment in the rotterdam waterway. *Journal of Physical Oceanography*, 40(11):2357–2380, 2010.

[29] Kent L Deines. Backscatter estimation using broadband acoustic doppler current profilers. In *Current measurement, 1999. proceedings of the ieee sixth working conference on*, pages 249–253. IEEE, 1999.

[30] Yves Deler. Esquisse morphologique de la cote basque francaise entre l'embouchure de l'adour et celle de la bidassoa. *Revue géographique des Pyrénées et du Sud-Ouest. Sud-Ouest Européen*, 3(1):18–63, 1932.

[31] Thierry Denot and Pierre Lang. Apports de la modélisation numérique à l'étude de la dynamique hydro-sédimentaire de l'estuaire de la rance. *Journées Nationales Génie Civil Génie Côtier*, pages 147–154, 2000.

[32] Jean Dubranna. *Etude des échanges sédimentaires entre l'embouchure de l'Adour et les plages adjacentes d'Anglet*. PhD thesis, Pau, 2007.

[33] JC Duinker, M Th J Hillebrand, RF Nolting, St Wellershaus, and N Kingo Jacobsen. The river varde å: processes affecting the behaviour of metals and organochlorines during estuarine mixing. *Netherlands Journal of Sea Research*, 14(3-4):237–267, 1980.

[34] Keith R Dyer. Sediment transport processes in estuaries. In *Developments in Sedimentology*, volume 53, pages 423–449. Elsevier, 1995.

[35] KR Dyer. Circulation and mixing in stratified estuaries. *Marine Chemistry*, 32(2):111–120, 1991.

[36] KR Dyer and K Ramamoorthy. Salinity and water circulation in the vellar estuary. *Limnology and Oceanography*, 14(1):4–15, 1969.

[37] C Enjalbert, B Castelle, D Rihouey, and D Dailloux. High-frequency video observation of a geologically-constrained barred-beach: La grande plage de biarritz (france). *Journal of Coastal Research*, pages 70–74, 2011.

[38] Huan Feng, J Kirk Cochran, Honoratha Lwiza, Bruce J Brownawell, and David J Hirschberg. Distribution of heavy metal and pcb contaminants in the sediments of an urban estuary: the hudson river. *Marine environmental research*, 45(1):69–88, 1998.

[39] John F Festa and Donald V Hansen. Turbidity maxima in partially mixed estuaries: A two-dimensional numerical model. *Estuarine and Coastal Marine Science*, 7(4):347–359, 1978.

[40] Jacques Fontaine, Boris Glander, Nicolas Huybrechts, Rebekka Kopmann, Agnès Leroy, Sara Pavan, Chi-Tuân Pham, Florent Taccone, Pablo Tassi, and Regis Walther. Introducing gaia, the brand new sediment transport module of the telemac-mascaret system.

[41] METEO FRANCE. Fiche climatologique, statistiques 1981-2010 et records, biarritz pays basque (64). Technical report, 2018.

[42] RE Francois and GR Garrison. Sound absorption based on ocean measurements: Part i: Pure water and magnesium sulfate contributions. *The Journal of the Acoustical Society of America*, 72(3):896–907, 1982.

[43] RE Francois and GR Garrison. Sound absorption based on ocean measurements. part ii: Boric acid contribution and equation for total absorption. *The Journal of the Acoustical Society of America*, 72(6):1879–1890, 1982.

[44] W Rockwell Geyer. The importance of suppression of turbulence by stratification on the estuarine turbidity maximum. *Estuaries*, 16(1):113–125, 1993.

[45] W Rockwell Geyer and David M Farmer. Tide-induced variation of the dynamics of a salt wedge estuary. *Journal of Physical Oceanography*, 19(8):1060–1072, 1989.

[46] W Rockwell Geyer and Parker MacCready. The estuarine circulation. *Annual Review of Fluid Mechanics*, 46:175–197, 2014.

[47] W Rockwell Geyer and DK Ralston. A mobile pool of contaminated sediment in the penobscot estuary, maine, usa. *Science of the Total Environment*, 612:694–707, 2018.

[48] W Rockwell Geyer, John H Trowbridge, and Melissa M Bowen. The dynamics of a partially mixed estuary. *Journal of Physical Oceanography*, 30(8):2035–2048, 2000.

[49] W Rockwell Geyer, Jonathan D Woodruff, and Peter Traykovski. Sediment transport and trapping in the hudson river estuary. *Estuaries*, 24(5):670–679, 2001.

[50] WR Geyer. Estuarine salinity structure and circulation. *Contemporary issues in estuarine physics*, pages 12–26, 2010.

[51] Alessio Giardino, Elsy Ibrahim, Stefanie Adam, Erik A Toorman, and Jaak Monbaliu. Hydrodynamics and cohesive sediment transport in the ijzer estuary, belgium: Case study. *Journal of waterway, port, coastal, and ocean engineering*, 135(4):176–184, 2009.

[52] Louis Glangeaud. Transport et sédimentation dans l'estuaire et à l'embouchure de la gironde. caractères pétrographiques des formations fluviatiles, saumâtres, littorales et néritiques. *Bulletin de la Societe Geologique de France, Paris*, 7(5):599–630, 1938.

[53] Louis Gostiaux and Hans Van Haren. Extracting meaningful information from uncalibrated backscattered echo intensity data. *Journal of Atmospheric and Oceanic Technology*, 27(5):943–949, 2010.

[54] F Grasso, R Verney, P Le Hir, B Thouvenin, E Schulz, and Y Kervella. Suspended sediment dynamics in the macrotidal seine estuary (france): 1. numerical modeling of turbidity maximum dynamics. *Journal of Geophysical Research: Oceans*, 123:558–577, 2018.

[55] Donald V Hansen and Maurice Rattray. New dimensions in estuary classification. *Limnology and Oceanography*, 11(3):319–326, 1966.

[56] Miles O Hayes. Morphology of sand accumulation in estuaries: an introduction to the symposium. In *Geology and Engineering*, pages 3–22. Elsevier, 1975.

[57] Jean-Michel Hervouet. *Hydrodynamics of free surface flows: modelling with the finite element method*, volume 360. Wiley Online Library, 2007.

[58] Nicolas Huybrechts and Catherine Villaret. Large-scale morphodynamic modelling of the gironde estuary, france. In *Proceedings of the Institution of Civil Engineers-Maritime Engineering*, volume 166, pages 51–62. Thomas Telford Ltd, 2013.

[59] Nicolas Huybrechts, Catherine Villaret, and Florent Lyard. Optimized predictive two-dimensional hydrodynamic model of the gironde estuary in france. *Journal of Waterway, Port, Coastal, and Ocean Engineering*, 138(4):312–322, 2011.

[60] Carles Ibañez, Didier Pont, and Narcís Prat. Characterization of the ebre and rhone estuaries: A basis for defining and classifying salt-wedge estuaries. *Limnology and Oceanography*, 42(1):89–101, 1997.

[61] David A Jay. Estuarine variability. *Contemporary issues in estuarine physics*, pages 62–99, 2010.

[62] David A Jay and Jeffery D Musiak. Particle trapping in estuarine tidal flows. *Journal of Geophysical Research: Oceans*, 99(C10):20445–20461, 1994.

[63] David A Jay, Philip M Orton, Thomas Chisholm, Douglas J Wilson, and Annika MV Fain. Particle trapping in stratified estuaries: Application to observations. *Estuaries and Coasts*, 30(6):1106–1125, 2007.

[64] TD Jickells, JE Andrews, DJ Parkes, S Suratman, AA Aziz, and YY Hee. Nutrient transport through estuaries: the importance of the estuarine geography. *Estuarine, Coastal and Shelf Science*, 150:215–229, 2014.

[65] J-M Jouanneau, O Weber, N Champilou, P Cirac, I Muxika, A Borja, A Pascual, J Rodríguez-Lázaro, and O Donard. Recent sedimentary study of the shelf of the basque country. *Journal of Marine Systems*, 72(1-4):397–406, 2008.

[66] Jens Kappenberg and Iris Grabemann. Variability of the mixing zones and estuarine turbidity maxima in the elbe and weser estuaries. *Estuaries*, 24(5):699–706, 2001.

[67] WM Kemp, JM Testa, DJ Conley, D Gilbert, and JD Hagy. Temporal responses of coastal hypoxia to nutrient loading and physical controls. *Biogeosciences*, 6(12):2985–3008, 2009.

[68] Martin Kerner. Effects of deepening the elbe estuary on sediment regime and water quality. *Estuarine, coastal and shelf science*, 75(4):492–500, 2007.

[69] RA Kostaschuk, MA Church, and JL Luternauer. Sediment transport over salt-wedge intrusions: Fraser river estuary, canada. *Sedimentology*, 39(2):305–317, 1992.

[70] RA Kostaschuk and JL Luternauer. The role of the salt-wedge in sediment resuspension and deposition: Fraser river estuary, canada. *Journal of Coastal Research*, pages 93–101, 1989.

[71] R Lehfeldt and S Bloss. Algebraic turbulence model for stratified tidal flows. In *Physical processes in estuaries*, pages 278–291. Springer, 1988.

[72] J.P. Lemoine. Analyse par modélisation de l'impact de l'élévation du niveau marin sur les niveaux de pleine mer dans l'estuaire de la seine, 2015.

[73] JP Lemoine and R Verney. Fonctionnement hydro-sédimentaire de l'estuaire de la seine, 2015.

[74] James A Lerczak and W Rockwell Geyer. Modeling the lateral circulation in straight, stratified estuaries. *Journal of Physical Oceanography*, 34(6):1410–1428, 2004.

[75] Roy Lewis. *Dispersion in estuaries and coastal waters*. Wiley, Chichester ; New York, 1997.

[76] Lu Li, Hui Wu, James T Liu, and Jianrong Zhu. Sediment transport induced by the advection of a moving salt wedge in the changjiang estuary. *Journal of Coastal Research*, 31(3):671–679, 2014.

[77] Ming Li, Liejun Zhong, and William C Boicourt. Simulations of chesapeake bay estuary: Sensitivity to turbulence mixing parameterizations and comparison with observations. *Journal of Geophysical Research: Oceans*, 110(C12), 2005.

[78] Youyu Lu and Rolf G Lueck. Using a broadband adcp in a tidal channel. part ii: Turbulence. *Journal of Atmospheric and Oceanic Technology*, 16(11):1568–1579, 1999.

[79] Gangfeng Ma, Fengyan Shi, Shuguang Liu, and Dingman Qi. Hydrodynamic modeling of changjiang estuary: Model skill assessment and large-scale structure impacts. *Applied Ocean Research*, 33(1):69–78, 2011.

[80] Andreas Malcherek. Application of telemac-2d in a narrow estuarine tributary. *Hydrological processes*, 14(13):2293–2300, 2000.

[81] Robert H Meade. Landward transport of bottom sediments in estuaries of the atlantic coastal plain. *Journal of Sedimentary Research*, 39(1):222–234, 1969.

[82] Ole Mikkelsen and Morten Pejrup. The use of a lisst-100 laser particle sizer for in-situ estimates of floc size, density and settling velocity. *Geo-Marine Letters*, 20(4):187–195, 2001.

[83] W.H. Munk and E.R. Anderson. Notes on a theory of the thermocline. *Journal of Marine Research*, 7(3):276–295, 1948.

[84] Iehisa Nezu and Wolfgang Rodi. Open-channel flow measurements with a laser doppler anemometer. *Journal of Hydraulic Engineering*, 112(5):335–355, 1986.

[85] MM Nichols and Robert B Biggs. Estuaries. in 'coastal sedimentary environments'.(ed. ra davies jr.) pp. 77–173, 1985.

[86] FO Nitsche, TC Kenna, and M Haberman. Quantifying 20th century deposition in complex estuarine environment: An example from the hudson river. *Estuarine, Coastal and Shelf Science*, 89(2):163–174, 2010.

[87] C Le Normant. Three-dimensional modelling of cohesive sediment transport in the loire estuary. *Hydrological processes*, 14(13):2231–2243, 2000.

[88] Caroline Petus. *Qualité des eaux côtières du Sud du Golfe de Gascogne par télédétection spatiale*. PhD thesis, Université de Pau et des Pays de l'Adour, 2009.

[89] Paul R Pinet. *Invitation to oceanography*. Jones & Bartlett Publishers, 2009.

[90] H Postma and K Kalle. Die entstehung von trübungszonen im unterlauf der flüsse, speziell im hinblick auf die verhältnisse in der unterelbe. *Deutsche Hydrografische Zeitschrift*, 8(4):137–144, 1955.

[91] Donald W Pritchard. Estuarine hydrography. In *Advances in geophysics*, volume 1, pages 243–280. Elsevier, 1952.

[92] Donald W Pritchard. Salinity distribution and circulation in the chesapeake bay estuarine system. *Journal of Marine Research*, 11(2):106–123, 1952.

[93] DW Pritchard. Estuarine circulation patterns. In *Proceedings of the American Society of Civil Engineers*, volume 81, pages 1–11. ASCE, 1955.

[94] David K Ralston, Geoffrey W Cowles, W Rockwell Geyer, and Rusty C Holleman. Turbulent and numerical mixing in a salt wedge estuary: Dependence on grid resolution, bottom roughness, and turbulence closure. *Journal of Geophysical Research: Oceans*, 122(1):692–712, 2017.

[95] David K Ralston, W Rockwell Geyer, and James A Lerczak. Structure, variability, and salt flux in a strongly forced salt wedge estuary. *Journal of Geophysical Research: Oceans*, 115(C6), 2010.

[96] David K Ralston, W Rockwell Geyer, and John C Warner. Bathymetric controls on sediment transport in the hudson river estuary: Lateral asymmetry and frontal trapping. *Journal of Geophysical Research: Oceans*, 117(C10), 2012.

[97] G Reichel and HP Nachtnebel. Suspended sediment monitoring in a fluvial environment: advantages and limitations applying an acoustic doppler current profiler. *Water Research*, 28(4):751–761, 1994.

[98] Peter Robins and Alan Davies. Application of telemac-2d and sisyphe to complex estuarine regions to inform future management decisions. *Proceedings of the XVIIIth Telemac & Mascaret User Club 2011, 19-21 October 2011, EDF R&D, Chatou*, pages 86–91, 2011.

[99] Peter E Robins, Matt J Lewis, John H Simpson, Eleanor R Howlett, and Shelagh K Malham. Future variability of solute transport in a macrotidal estuary. *Estuarine, Coastal and Shelf Science*, 151:88–99, 2014.

[100] Peter Edward Robins and Alan G Davies. Morphological controls in sandy estuaries: the influence of tidal flats and bathymetry on sediment transport. *Ocean Dynamics*, 60(3):503–517, 2010.

[101] Collin S Roesler and Emmanuel Boss. In situ measurement of the inherent optical properties (iops) and potential for harmful algal bloom detection and coastal ecosystem observations, 2008.

[102] Victor ROSALES, Antoine GARAPON, and Daniel LEVACHER. Simulation numérique d'un écoulement stratifié turbulent. *VII journées nationales Génie Civil–Génie Côtier*, pages 105–115, 2002.

[103] Lauren Ross, Arnoldo Valle-Levinson, Aldo Sottolichio, and Nicolas Huybrechts. Lateral variability of subtidal flow at the mid-reaches of a macrotidal estuary. *Journal of Geophysical Research: Oceans*, 122(9):7651–7673, 2017.

[104] J. R. Schubel and D. W. Pritchard. The estuarine environment, part 1. *Journal of Geological Education*, 20(2):60–68, 1972.

[105] Malcolm E Scully and W Rockwell Geyer. The role of advection, straining, and mixing on the tidal variability of estuarine stratification. *Journal of Physical Oceanography*, 42(5):855–868, 2012.

[106] Xiaoteng Shen, Byung Joon Lee, Michael Fettweis, and Erik A Toorman. A tri-modal flocculation model coupled with telemac for estuarine muds both in the laboratory and in the field. *Water research*, 145:473–486, 2018.

[107] JH Simpson, E Williams, LH Brasseur, and JM Brubaker. The impact of tidal straining on the cycle of turbulence in a partially stratified estuary. *Continental Shelf Research*, 25(1):51–64, 2005.

[108] John H Simpson, Juan Brown, John Matthews, and Graham Allen. Tidal straining, density currents, and stirring in the control of estuarine stratification. *Estuaries*, 13(2):125–132, 1990.

[109] S Smolders, T Maximova, J Vanlede, and MJ Teles. Implementation of controlled reduced tide and flooding areas in the telemac 3d model of the scheldt estuary. 2014.

[110] Dehai Song, Xiao Hua Wang, Zhenyi Cao, and Weibing Guan. Suspended sediment transport in the deepwater navigation channel, yangtze river estuary, china, in the dry season 2009: 1. observations over spring and neap tidal cycles. *Journal of Geophysical Research: Oceans*, 118(10):5555–5567, 2013.

[111] D Sous, S Defontaine, D Morichon, N Bhairy, L Lanceleur, and M Monperrus. Turbulence measurements in a stratified man-controlled estuary : The adour case, 2018. 16th International Symposium on Oceanography of the Bay of Biscay.

[112] Mark T Stacey and David K Ralston. The scaling and structure of the estuarine bottom boundary layer. *Journal of Physical Oceanography*, 35(1):55–71, 2005.

[113] Caroline Tessier, Pierre Le Hir, Xavier Lurton, and Patrice Castaing. Estimation de la matière en suspension à partir de l'intensité rétrodiffusée des courantomètres acoustiques à effet doppler (adcp). *Comptes Rendus Geoscience*, 340(1):57–67, 2008.

[114] PD Thorne, CE Vincent, PJ Hardcastle, Salim Rehman, and Nicolus Pearson. Measuring suspended sediment concentrations using acoustic backscatter devices. *Marine Geology*, 98(1):7–16, 1991.

[115] Chaofeng Tong, Jinhai Zheng, Cheng Zhang, and Claude Guilbaud. Salinity response to the runoff from yangtze river basin at qingcaosha reservoir area in yangtze estuary. In *ASME 2010 29th International Conference on Ocean, Offshore and Arctic Engineering*, pages 247–255. American Society of Mechanical Engineers, 2010.

[116] F Toublanc, I Brenon, and T Coulombier. Formation and structure of the turbidity maximum in the macrotidal charente estuary (france): Influence of fluvial and tidal forcing. *Estuarine, Coastal and Shelf Science*, 169:1–14, 2016.

[117] Mayeur D. Trut G. Etude de la qualité des eaux de l'estuaire de l'adour (suivi 2001-2003), 2004.

[118] John Stewart Turner. *Buoyancy effects in fluids*. Cambridge University Press, 1979.

[119] RJ Uncles, JA Stephens, and RE Smith. The dependence of estuarine turbidity on tidal intrusion length, tidal range and residence time. *Continental Shelf Research*, 22(11-13):1835–1856, 2002.

[120] Arnoldo Valle-Levinson. Density-driven exchange flow in terms of the kelvin and ekman numbers. *Journal of Geophysical Research: Oceans*, 113(C4), 2008.

[121] Arnoldo Valle-Levinson. *Contemporary issues in estuarine physics*. Cambridge University Press, 2010.

[122] Arnoldo Valle-Levinson and Carlos AF Schettini. Fortnightly switching of residual flow drivers in a tropical semiarid estuary. *Estuarine, Coastal and Shelf Science*, 169:46–55, 2016.

[123] DS Van Maren, T Van Kessel, K Cronin, and L Sittoni. The impact of channel deepening and dredging on estuarine sediment concentration. *Continental Shelf Research*, 95:1–14, 2015.

[124] C Villaret, JM Hervouet, N Huybrechts, LA Van, and AG Davies. Effect of bed friction on morphodynamic modelling: Application to the central part of the gironde estuary. In *Proceedings of the River, Coastal and Estuarine Morphodynamics Conference*, pages 899–90, 2009.

[125] C Villaret, N Huybrechts, AG Davies, O Way, et al. Effect of bed roughness prediction on morphodynamic modelling: Application to the dee estuary (uk) and to the gironde estuary (france). In *Proceedings of the 34th World Congress of the International Association for Hydro-Environment Research and Engineering: 33rd Hydrology and Water Resources Symposium and 10th Conference on Hydraulics in Water Engineering*, page 1149. Engineers Australia, 2011.

[126] Catherine Villaret, Jean-Michel Hervouet, Rebekka Kopmann, Uwe Merkel, and Alan G Davies. Morphodynamic modeling using the telemac finite-element system. *Computers & Geosciences*, 53:105–113, 2013.

[127] Catherine Villaret, Lan Anh Van, Nicolas Huybrechts, Damien Pham Van Bang, and Olivier Boucher. Consolidation effects on morphodynamics modelling: application to the gironde estuary. *La Houille Blanche*, (6):15–24, 2010.

[128] PL Viollet. On the numerical modelling of stratified flows. In *Physical processes in estuaries*, pages 257–277. Springer, 1988.

[129] Régis Walther, Cyrielle Cayrol, Luc Hamm, A Delouis, and D Lehay. Evaluation of an offshore disposal site in the loire estuary through field monitoring and 3d numerical modeling. *Coastal Engineering Proceedings*, 1(34):24, 2014.

[130] Regis Walther, Julien Schaguene, Luc Hamm, and Eric David. Coupled 3d modeling of turbidity maximum dynamics in the loire estuary, france. *Coastal Engineering Proceedings*, 1(33):22, 2012.

[131] John C Warner, W Rockwell Geyer, and James A Lerczak. Numerical modeling of an estuary: A comprehensive skill assessment. *Journal of Geophysical Research: Oceans*, 110(C5), 2005.

[132] St Wellershaus. Turbidity maximum and mud shoaling in the weser estuary. *Archiv fur Hydrobiologie*, 92(2), 1981.

[133] Chester K. Wentworth. A scale of grade and class terms for clastic sediments. *The Journal of Geology*, 30(5):377–392, 1922.

[134] JR West, KOK Oduyemi, and K Shiono. Some observations on the effect of vertical density gradients on estuarine turbulent transport processes. *Estuarine, Coastal and Shelf Science*, 32(4):365–383, 1991.

[135] Karen Wild-Allen and John Andrewartha. Connectivity between estuaries influences nutrient transport, cycling and water quality. *Marine chemistry*, 185:12–26, 2016.

[136] Eirwen Williams and John H Simpson. Uncertainties in estimates of reynolds stress and tke production rate using the adcp variance method. *Journal of Atmospheric and Oceanic Technology*, 21(2):347–357, 2004.

[137] Garnett P Williams. Sediment concentration versus water discharge during single hydrologic events in rivers. *Journal of Hydrology*, 111(1-4):89–106, 1989.

[138] Cort J Willmott. On the validation of models. *Physical geography*, 2(2):184–194, 1981.

Annexes

Annex 1 : Backscatter inversion issue

ADCP echo intensity data have been used in attempt to estimate the suspended sediment concentration (SSC) inside the water column based on both turbidity profiles and water samples from boat survey. To link the echo amplitude to the quantity of particles in suspension, an energy balance should be established through the Sonar Equation [29, 53]. To estimate the received intensity, we used the equation proposed by Gostiaux and Van Haren [53]. The transmission loss is calculated as a sum of the spherical spreading loss and the attenuation of acoustic signal by the estuarine waters. Due to low suspended sediment concentration ($< 100\ mg.L^{-1}$) during the field observations, the particles attenuation has been neglected. The water attenuation has been estimated by the formulation given by François and Garrison [42, 43]. An empirical calibration can then usually be established between $10log_{10}(SSC)$ and the backscatter index BI.

Figures 2.1, 2.2, 2.3 and 2.4 show the relationship between the suspended sediment concentration (in log scale) and the backscatter index for spring/neap tide conditions and ebb/flood tidal phase. The first striking observation is the absence of a single linear determination, except for LD-ST18 (Fig.2.4). This precludes the possibility to obtain a robust calibration of the ADCP backscatter signal and the subsequent estimation of SSC fluxes. However, a more careful analysis reveals interesting features. On figure 2.1, the neap conditions are associated to similar relationships between SSC and BI, whatever the tidal phase. The spring flood tide shows also a close dependency. A quite different relationship is observed during spring ebb conditions. On figure 2.3, a similar pattern with two different relationships between spring flood and spring ebb conditions can be observed. This suggests the presence of sediment from different origin or composition in the Adour lower estuary.

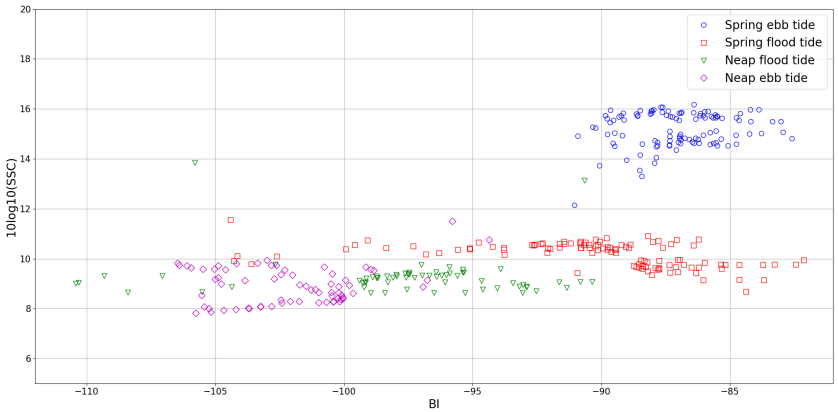

Figure 2.1: Suspended sediment concentration ($10 * log10(SSC)$) versus backscatter index BI, for data collected at SF4 during LD-NT17 flood (green symbols) and ebb (magenta symbols) tides and during LD-ST17 flood (red symbols) and ebb (blue symbols) tides.

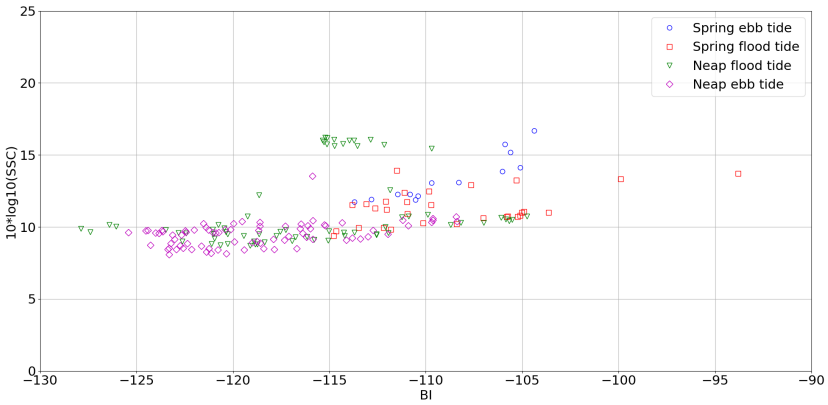

Figure 2.2: Suspended sediment concentration $(10 * log10(SSC))$ versus backscatter index BI, for data collected at SF2 during LD-NT17 flood (green symbols) and ebb (magenta symbols) tides and during LD-ST17 flood (red symbols) and ebb (blue symbols) tides.

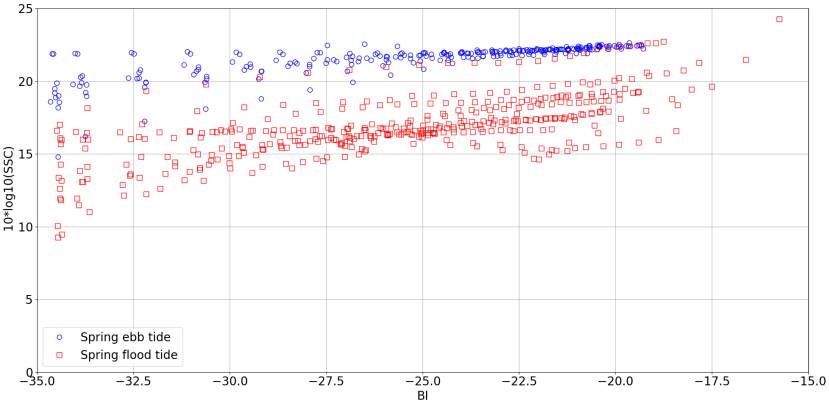

Figure 2.3: Suspended sediment concentration $(10 * log10(SSC))$ versus backscatter index BI, for data collected at SF2 during HD-ST18 flood (red symbols) and ebb (blue symbols) tides.

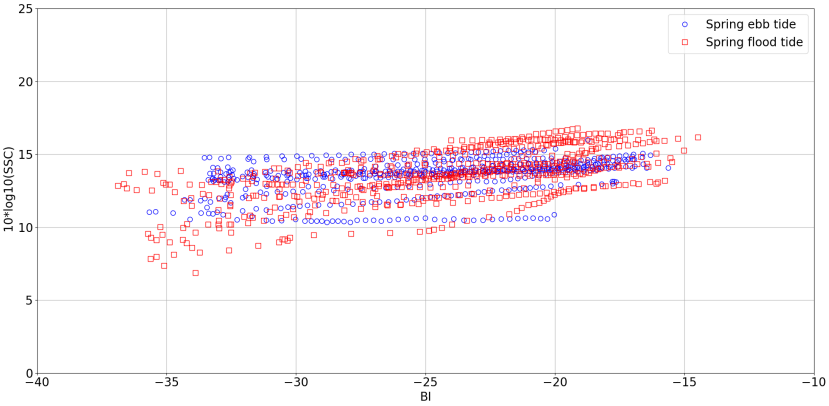

Figure 2.4: Suspended sediment concentration $(10 * log10(SSC))$ versus backscatter index BI, for data collected at SF2 during LD-ST18 flood (red symbols) and ebb (blue symbols) tides.

Annex 2 : Additional numerical results

- Results obtained with constant viscosity model:

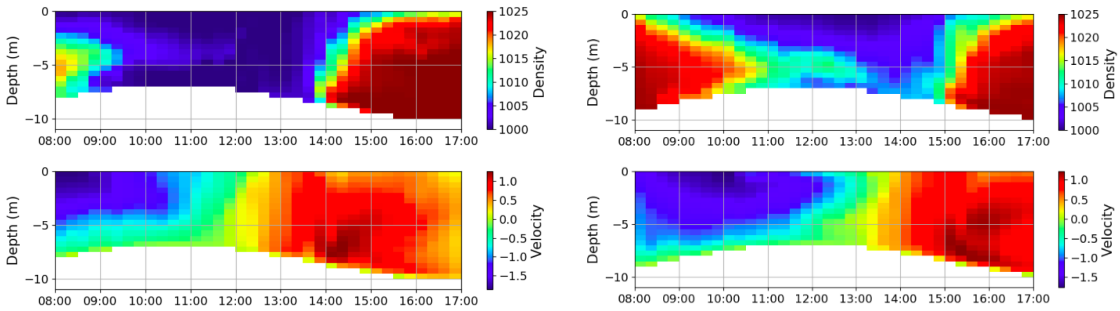

Figure 2.5: Tidal evolution of the: vertical structure of density (two subplots on top), velocity (two subplots underneath), results obtained with a simulation of HD-ST18 (on the left) and LD-ST18 (on the right) with constant viscosity model.

- Results obtained with $k - \varepsilon$ model:

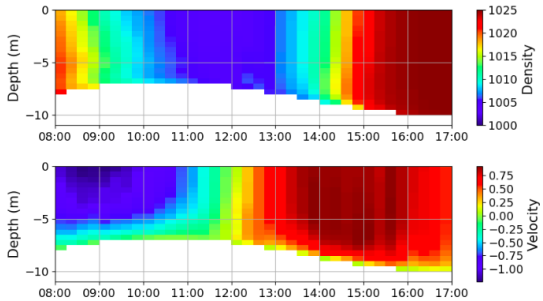

Figure 2.6: Tidal evolution of the: vertical structure of density (on top), velocity (underneath), results obtained with a simulation of HD-ST18 with $k - \varepsilon$ model.

- Results obtained with Tsanis formulation of mixing length model:

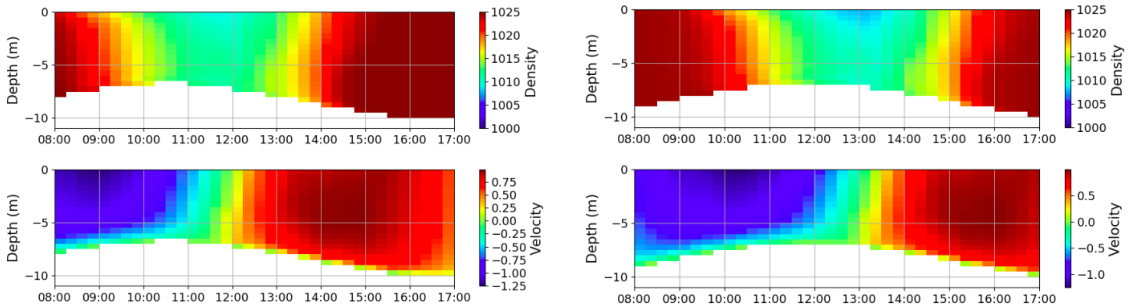

Figure 2.7: Tidal evolution of the: vertical structure of density (on top), velocity (underneath), results obtained with a simulation of HD-ST18 (on the left) and LD-ST18 (on the right) with Tsanis formulation of mixing length model.

- Results obtained with Prandlt number values of 0.5 and 1.5:

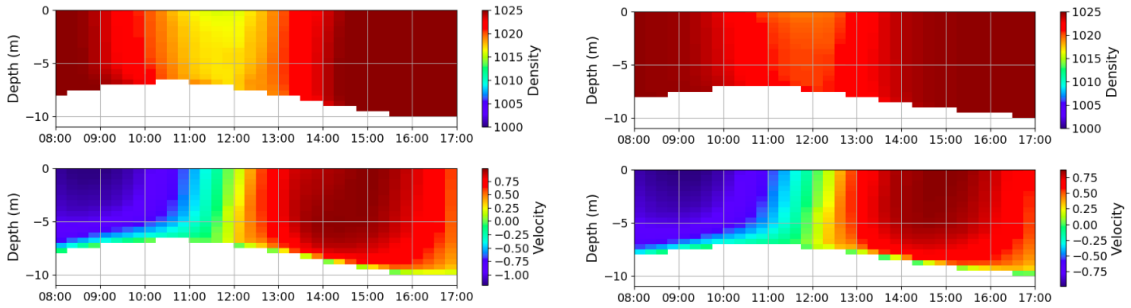

Figure 2.8: Tidal evolution of the: vertical structure of density (two subplots on top), velocity (two subplots underneath), results obtained with a simulation of HD-ST18 (on the left) and LD-ST18 (on the right) with $Prt = 0.5$

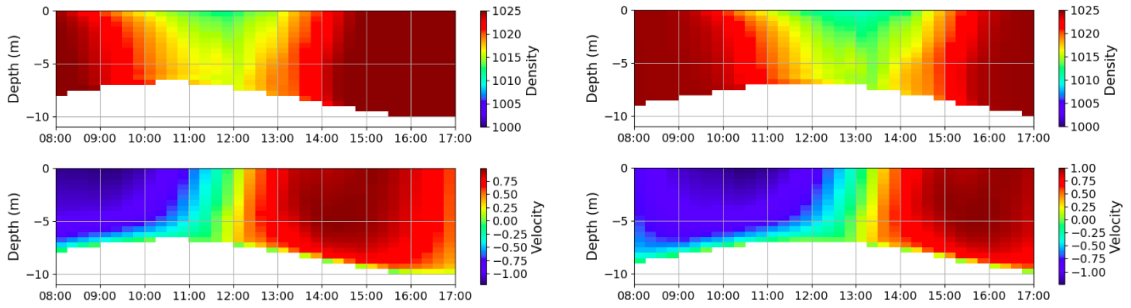

Figure 2.9: Tidal evolution of the: vertical structure of density (two subplots on top), velocity (two subplots underneath), results obtained with a simulation of HD-ST18 (on the left) and LD-ST18 (on the right) with $Prt = 1.5$

Annex 3 : Poster presented at the Gordon conference

WATER MASSES AND SALINITY CIRCULATION IN A MAN-ENGINEERED TIDAL ESTUARY : THE ADOUR RIVER (FRANCE)

S.Defontaine[(a)], D.Sous[(b,c)], D.Morichon[(c)]

[(a)] CNRS / Univ. Pau & Pays Adour/ E2S UPPA, Laboratoire de Mathématiques et de leurs Applications de Pau,
[(b)] Université de Toulon, Aix Marseille Université, CNRS, IRD, Mediterranean Institute of Oceanography (MIO), La Garde, France,
[(c)] Univ. Pau & Pays Adour / E2S UPPA, Laboratoire des Sciences de l'Ingénieur Appliquées à la Mécanique et au Génie Electrique (SIAME)

INTRODUCTION

Estuaries are complex **transfer areas** of water masses and suspended particulate matters (SPM) between ocean, land and continental waters. A key issue of the preservation of estuarine and marine ecosystems is to improve our knowledge of the **hydrodynamical processes** controlling the dynamics and renewal of water masses in estuaries and their ability to transport, expel or retain sediments, contaminants, nutrients and living organisms. **Density gradients** generated by the continental waters inter-playing with marine waters, and interactions between tides and estuarine morphology have been shown to be the major mechanisms governing the estuarine dynamics.

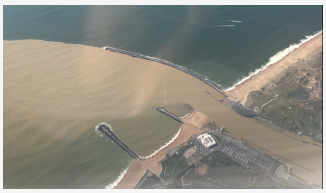

STUDY SITE

- Site location : South of Bay of Biscay (SW of France)
- Study site : the last 6 km of the estuary, from Nive confluence to estuary entrance
- Adour river : it originates in the Pyrenées mountains at an altitude of 2200 m, and flows about 300 km before pouring into the Atlantic Ocean
- Watershed area : 17000 km^2
- Dimension : 10m depth, between 150 and 400 m wide
- River flow : from 70 to 3000 $m^3.s^{-1}$, with annual mean river flow of 340 $m^3.s^{-1}$
- Tide : mean tidal range of 2.5 m, with tidal amplitude from 1 m to 4.5 m (mesotidal), semi-diurnal
- Limit of tidal influence : St Vincent-de-Paul (70 km upstream)
- Maximum of saline entrance : Urt village (22 km upstream)

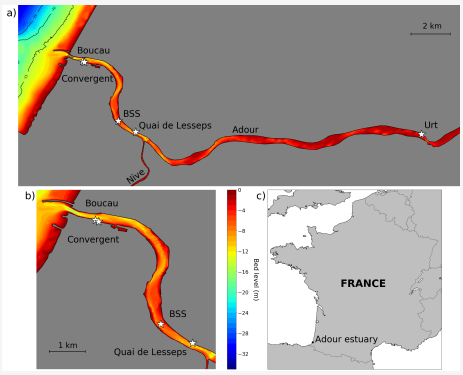

FIELD CAMPAIGN

OBJECTIVES

To understand the tidally-driven hydrodynamics inside the lower estuary, including **density stratification, mixing and SPM dynamics**.

Provide **high-resolution in-situ data** for model validation.

INSTRUMENTATION

Bottom-moored station (BSS) : velocity profiles were recorded by a Flowquest ADCP (600 kHz) every 15 min (time averaged 5-min burst data at 4Hz)

Anchored boat station (BSS) : vertical profiles of velocity, salinity, temperature and turbidity were recorded every 15 min.

Longitudinal section : an OSIL Minibat under-water towed vehicle, equipped with a multi-parameter probe recorded salinity, temperature, pressure and turbidity.

RESULTS

- **High variability of water masses and salinity circulation** :

	Low River Disch.	High River Disch.
Neap Tide	Almost stagnant salt-wedge	/
Spring Tide	Flood = vert. strat. Ebb = horiz. strat.	Strong vert. strat. Salt-wedge = 3 m bottom layer Reduced saline entrance

- **Stratification induced turbulence damping** :

	Low River Disch.	High River Disch.
Neap Tide	No turbulence	/
Spring Tide	Flood = turb. at salt-wedge front Ebb = turb. from bottom to mid water column	Flood = under the pycnocline Ebb = turb. in full water column

- **Impacts on suspended sediment dynamics** :
  - Flood = Accumulation at the salt-wedge tip during the flood and advection of SPM upstream.
  - Ebb = Strong turbulent mixing implies high SSC in the water column.
  - Ebb slack time = Reduced velocity and turbulent mixing results in sedimentation.
  - No stable ETM has been observed in the lower estuary

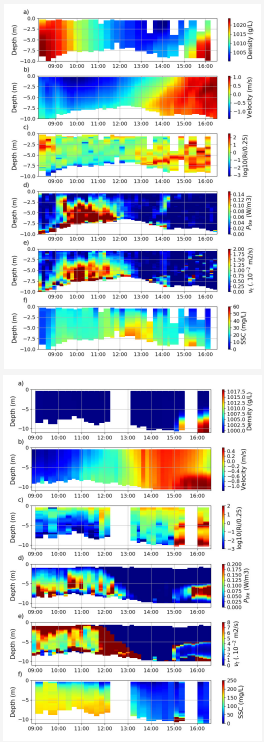

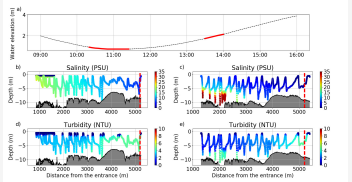

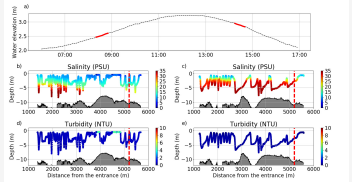

Paper (in revision) : Hydrodynamics and SPM transport in a man-engineered tidal estuary: the Adour river (France), S. Defontaine, D. Sous, D. Morichon, R. Verney, M. Monperrus. Estuarine and Coastal Shelf Science.

NUMERICAL STUDY

OBJECTIVES

To test the ability of TELEMAC3D to represent **salt-wedge dynamics**

To provide **comprehensive spatio-temporal description** of the estuarine hydrodynamics

TELEMAC 3D modeling

Free surface **Navier-Stokes equations**.

Hypothesis : non-hydrostatic, incompressible fluid, Boussinesq approximation, turbulence models (constant viscosity, mixing length, $k-\epsilon$)

Mesh : unstructured grid combined with regular grid with cell from 30m to 2km, 30 equidistant sigma coordinate layers, 16591 nodes and 28696 elements.

Forcing : Tide (TPXO tidal data base) and river discharge (Banque Hydro data base), Coriolis force

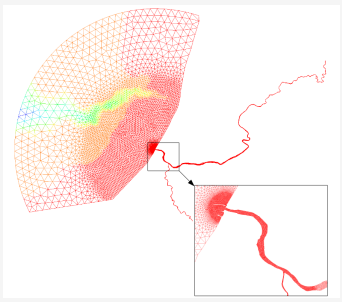

RESULTS

Water level calibration :

5 tidal gauges along the Adour and Nive rivers are used for water levels calibration : **Convergent**, Quai de Lesseps, Pont blanc, Villefranque and Urt

	Conv.	Q. Lesseps	P. Blanc	Villefr.	Urt
RMSE (m)	0.06	0.09	0.13	0.22	0.28
W.S. (%)	99.9	99.7	99.4	98.1	96.7

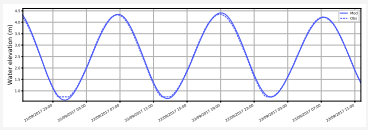

Velocity calibration :

Bottom moored ADCP data (**BSS**) have been used for velocity calibration

	Surface	Bottom
RMSE (m/s)	0.39	0.31
W.S. (%)	82.2	90.0

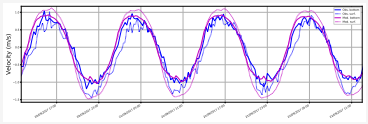

Vertical structure :

Bottom moored velocity profiles combined with salinity profiles collected during the boat surveys are used to calibrate the vertical structure

The varying stratification inside the estuary being difficult to reproduce, different turbulence models have been tested : constant viscosity, mixing length and $k-\epsilon$

Spring tide /Low river discharge :

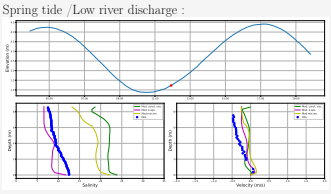

Neap tide /Low river discharge :

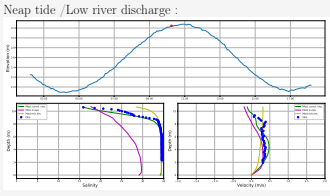

Longitudinal section :

Longitudinal sections of salinity recorded with the Minibat can be qualitatively compared to the modeling results

Spring tide / Low river discharge / Low tide :

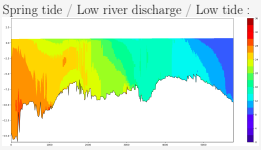

Spring tide / Low river discharge / Flood tide :

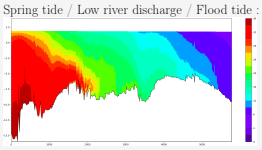

Neap tide / Low river discharge / Low tide :

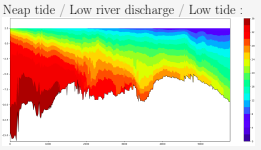

Neap tide / low river discharge / Flood tide :

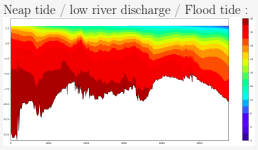

CONCLUSIONS

- Adour river functioning is strongly influenced by both river and tidal forcing, resulting in a **wide range of density stratification**
- Turbulent properties showed a significant response to the variations of salinity structure, with higher values when stratification is minimal
- Suspended sediment concentration is linked to **turbulent mixing** during the ebb. During the flood, the suspended sediment concentration (SSC) seems related to the salt-wedge entrance re-suspension and **stratification-induced turbulence damping**
- No stable Estuarine Turbidity Maximum (**ETM**) has been observed in the lower Adour estuary
- The strong variability of salinity structure observed in the Adour estuary is challenging to reproduce with the numerical modeling
- **TELEMAC3D** allows to reproduce at least qualitatively the observed physical processes
- The choice of the **turbulence model** is of the foremost importance for a good representation of the interaction between water masses

ACKNOWLEDGEMENTS

- This study was sponsored by the **MICROPOLIT project** (European Regional Development Fund - ERDF) and Adour-Garonne Water Agency).
- Field experimentation were funded by the **EC2CO PANACHE program** (CNRS INSU). The port of Bayonne, the Gladys group, MIO and EPOC supported the experimentation.

Annex 3 : ECSS paper

Estuarine, Coastal and Shelf Science 231 (2019) 106445

Contents lists available at ScienceDirect

Estuarine, Coastal and Shelf Science

journal homepage: http://www.elsevier.com/locate/ecss

Hydrodynamics and SPM transport in an engineered tidal estuary: The Adour river (France)

Sophie Defontaine [a,*], Damien Sous [b,c], Denis Morichon [c], Romaric Verney [d], Mathilde Monperrus [e]

[a] CNRS / Univ. Pau & Pays Adour/ E2S UPPA, Laboratoire de Mathématiques et de leurs Applications de Pau - Fédération MIRA, UMR5142, Pau, 64000, France
[b] Université de Toulon, Aix Marseille Université, CNRS, IRD, Mediterranean Institute of Oceanography (MIO), La Garde, France
[c] Univ. Pau & Pays Adour / E2S UPPA, Laboratoire des Sciences de l'Ingénieur Appliquées à la Mécanique et au Génie Electrique (SIAME) - MIRA, EA4581, 64600, Anglet, France
[d] IFREMER, DYNECO/DHYSED, CS10070, Plouzané, 29280, France
[e] CNRS / Univ. Pau & Pays Adour/ E2S UPPA, Institut des Sciences Analytiques et de Physico-Chimie pour l'Environnement et les Matériaux - Fédération MIRA, UMR5254, 64600, Anglet, France

ARTICLE INFO

Keywords:
Salt-wedge estuary
Estuarine circulation
Stratification
Turbulence
Suspended particles transport
Adour river

ABSTRACT

The present paper reports on a series of field experiments aiming to characterise the functioning of a man-engineered strongly forced salt-wedge estuary: the lower estuary of the Adour river, France. Bottom-moored velocity measurements and surface boat surveys have been performed under low river discharge conditions, for both neap and spring tides, in order to provide a well-documented reference framework to understand the dynamics of water masses, turbulence and suspended particulate matter (SPM) transport in the lower estuary. An additional campaign has been carried out in high river discharge conditions. This first documented *in-situ* study of the Adour lower estuary demonstrates its variability in terms of hydrological regimes, from salt-wedge to partially mixed regimes depending on tidal and discharge conditions. Turbulent properties showed a significant response to the variations of salinity structure, with higher values when stratification is minimal. At spring tide, a tidal variation between mixing conditions on the ebb and the flood is revealed by ADCP measurements, with higher values extended up to the surface during the ebb. The link between turbulent mixing and suspended sediment concentration is straightforward during the ebb. During the flood, the suspended sediment concentration (SSC) seems related to the salt-wedge entrance re-suspension and stratification-induced turbulence damping. No stable Estuarine Turbidity Maximum (ETM) has been observed during the field experiment in the lower Adour estuary.

1. Introduction

Estuaries are complex transfer areas of water masses and suspended particulate matters (SPM) between ocean, land and continental waters (Duinker et al., 1980). They constitute unique habitats for a large variety of living organisms and essential nurseries for many marine species. In the overall context of climate change and growing anthropogenic pressure, a key issue of the preservation of estuarine ecosystems is to improve our knowledge of the hydro-dynamical processes controlling the dynamics and renewal of water masses in estuaries and their ability to transport, expel or retain sediments, contaminants, nutrients and living organisms.

Many studies investigated estuarine dynamics from *in-situ* measurements (Dyer and Ramamoorthy, 1969; Simpson et al., 2005; de Nijs et al., 2010; Scully and Geyer, 2012) and/or numerical modelling (Lerczak and Rockwell Geyer, 2004; Burchard and Hetland, 2010; Ralston et al., 2010; de Nijs and Pietrzak, 2012). From a physical point of view, estuaries are exchange areas between fresh brackish continental water and salty marine waters, mainly driven by river run-off, tides and wind forcing. Density gradients generated by the continental waters inter-playing with marine waters, and interactions between tides and estuarine morphology have been shown to be the major mechanisms governing the estuarine dynamics. Those mechanisms are known as: (i) gravitational circulation induced by horizontal density gradient, (ii)

* Corresponding author.
E-mail address: sophie.defontaine@univ-pau.fr (S. Defontaine).

https://doi.org/10.1016/j.ecss.2019.106445
Received 14 January 2019; Received in revised form 7 October 2019; Accepted 18 October 2019
Available online 23 October 2019

tidal pumping generated by an ebb-flood asymmetry, (iii) tidal straining caused by advection. The vertical salinity gradient plays also an essential role by influencing the turbulent mixing inside the water column. Note that a wide number of additional processes can also act on the estuarine dynamics and mixing, including bed morphology (Dyer and Ramamoorthy, 1969), lateral circulation (Dyer, 1974; Dyer, 1991; Lacy et al., 2003; Lerczak and Rockwell Geyer, 2004; Scully et al., 2009), wind (Scully et al., 2005; Ralston et al., 2008), Earth rotation (Lerczak and Rockwell Geyer, 2004; Valle-Levinson, 2008), internal waves (Uittenbogaard, 1995; Dyer, 1991; Dyer et al., 2004) and sediment load (Winterwerp, 2001).

A growing interest in classifying estuaries developed along the years, in order to gain a unified view of the physics of estuaries. Different classification schemes have been proposed based on water balance, geomorphology (Pritchard, 1952), vertical salinity structure (Cameron and Pritchard, 1963) or hydrodynamics (Hansen and Rattray, 1966; Valle-Levinson, 2008; Geyer and MacCready, 2014). One of the commonly used classification has been proposed by Cameron and Pritchard (1963). It is based on water column stratification, in which estuaries can be classified as salt-wedge, strongly stratified, weakly stratified or well mixed. However, the horizontal and vertical salinity gradients can show important variations in time (e.g. from neap to spring tide, or from wet to dry season) and space within a given estuary, such as stratification might not be systematically used to classify estuaries. Therefore this type of qualitative classification has been progressively forsaken, to be replaced by more quantitative methods. One recent approach has been proposed by Geyer and MacCready (2014), discussing the respective contributions of tide and river flow in mixing and stratification processes. It is based on two dimensionless parameters. The former is the freshwater Froude number Fr_f (Geyer, 2010) which expresses the ratio between the river flow inertia and the buoyancy due to salinity gradient. The second is the mixing parameter M which quantifies the effectiveness of tidal mixing in stratified estuaries. Geyer and MacCready proposed a mapping of various estuaries based on those two parameters, demonstrating the efficiency to discriminate different classes of estuary. For example, salt-wedge estuaries, such as the Mississippi, The Fraser and the Ebro rivers are located near the top of the Fr_f/M diagram (i.e. high values of Fr_f); while partially stratified estuaries are on the centre of the diagram (e.g. James river and San Fransisco Bay) and fjords and well mixed estuaries are on the bottom part (e.g. Puget Sound). This research effort for a quantitative classification of estuaries needs to be deepened and sustained, in particular by providing relevant in-situ data from additional and contrasted case studies.

In addition to the hydrodynamic structure, a major issue of estuarine dynamics is to understand the fate of the sediment load. Under the competing effects of turbulent suspension and gravitational settling, strong variations of Suspended Particulate Matter (SPM) concentrations are observed in both time, along the tidal cycle, and space, along the estuary (Wellershaus, 1981; Geyer, 1993). In the past decades, many studies, see e.g. (de Nijs and Pietrzak, 2012; Toublanc et al., 2016; Burchard and Baumert, 1998), have revealed the presence and the mechanisms responsible for the generation of a zone of high turbidity, the so-called Estuarine Turbidity Maximum (ETM) in salt-wedge estuaries. Three major mechanisms have been highlighted in the formation of ETM. First, the estuarine circulation, due to longitudinal salinity gradient, associated with the river run-off drive a convergent SPM transport at the salt intrusion limit, that can lead to the formation of an ETM. Second, the asymmetry between the ebb and flood duration and peak velocities can also contribute to the formation of an ETM. Third, damping of turbulent mixing, due to stable stratification, can also be responsible for a sinking of particles from the upper part of the water column to the lower part. Those particles will then be advected upward by the lower layer. In addition, a recent study (Grasso et al., 2018) also revealed that energetic wave conditions can influence the ETM mass by increasing the mass by a factor of 3 during mean tides. The presence or the absence of an ETM in a given estuary is a major concern when trying to understand and predict the dispersion or the retention of SPM and related biochemical issues.

A significant research effort has thus been engaged during the last two decades to perform field observations of turbulence, mixing and stratification in order to provide a basis for theoretical analysis and numerical modelling of estuarine dynamics and sediment transport (Stacey et al., 2001, 2010; Stacey and Ralston, 2005; Burchard and Hetland, 2010; Geyer and MacCready, 2014). The present study has been specifically designed to advance knowledge on hydrodynamics and sediment transport in a man-engineered channel-shape estuary, subjected to strong tidal and fluvial forcing, with few intertidal areas and small watershed; as very few is known about such estuaries. The selected field site is the Adour river estuary, located at the bottom of the Bay of Biscay. It is a highly developed estuary with several kilometres of its downstream part completely channelised in order to secure the Bayonne harbour operations. This specific morphology is reinforced by a man-engineered reduction of the section at the last reach, in order to ease the expulsion of water and sediment. The dynamics of estuarine water masses and sediments is further affected by human interventions aiming to facilitate the navigation by dredging activities and wave protection. In addition to this very specific morphology, the Adour estuary is also subjected to important fluvial and tidal forcing, due to the location nearby the Pyrénées (heavy rainfall and snow melt freshet) and the Atlantic ocean. Despite serious economic and environmental issues related to water quality and sediment supply, very little is known about the functioning of the Adour estuary and the influence of human interventions on its internal dynamics. Most known studies have focused on the dynamics of the turbid plume and its area of influence in ocean waters (Brière, 2005; Dubranna, 2007; Dailloux, 2008; Petus, 2009; Jouanneau et al., 2008).

The aim of our study is to gain a detailed insight on the behaviour of the current and salinity structure within the Adour river and their influence on particle matters dynamics. The present paper reports therefore on the first field experimentation conducted in the lower Adour estuary, where the marine waters play a primary role and the hydrological system remains simple enough to be monitored. The methods and instrumentation are presented in section 2. The results are detailed in section 3 and discussed in section 4. The last section is devoted to the conclusion.

2. Study site and data set

2.1. Study site

The Adour river originates in the Pyrenées mountains at an altitude of 2200 m, and flows about 300 km before pouring into the Bay of Biscay (SW of France). The catchment area is of about 17000 km^2. The annual average river discharge is of about 300 $m^3.s^{-1}$, and can reach up to more than 3000 $m^3.s^{-1}$ during extreme flood events. The Adour river is characterised by a turbulent pulsed transport with about 75% of annual solid flux exported within 30–40 days (Point et al., 2007). The estuary is exposed to a mesotidal regime, with a tidal range varying between 1 m and 4.5 m. The tidal regime is mostly composed of semi-diurnal components (M2: 1.22 m, S2: 0.42 m, N2: 0.25 m, K2: 0.12 m). The tide wave propagates until St Vincent-de-Paul (70 km upstream), and the saline intrusion limit is nearby Urt village (22 km upstream). The lower Adour river estuary (i.e. the lower 6 km), which is our zone of primary interest, is a fully man-engineered channel of 150 m–400 m width. The main channel depth is maintained by dredging to about 10 m depth along the dock in the Bayonne harbour, to ease navigation. The estuary mouth has been straightened and channelised by embankments in order to accelerate water flow and to facilitate the sediment expulsion out of the estuary. In addition, a 700 m long jetty has been constructed at the north

side of the river mouth to protect the Bayonne harbour from swells mainly coming from the northwest sector (Fig. 1).

2.2. Field experiments

The objective of the present field experiments is to study the tidally-driven hydrodynamics inside the lower estuary, including salt-wedge, stratification, mixing and SPM dynamics. The field campaigns are based on a series of operations aiming to investigate the effect of river discharge and tidal range on the estuarine dynamics. For the sake of simplicity, the experimental results will be organised and named following the forcing conditions: LD/HD will refer to low/high river discharge and ST/NT will refer to spring/neap tide conditions, respectively, while the year is added at the end. For instance, LD-ST17 will refer to data recover in low discharge and spring tide conditions in 2017. A summary of conditions during the boat survey measurements is given in Table 1, while each type of measurement is described herebelow. The measurements have been undertaken only in the last 6 km of the estuary, in between the mouth and the confluence with the Nive river (Fig. 1 a)).

Table 1
Experimental conditions. LD/HD refer to low/high discharge conditions, respectively. ST/NT refer to spring/neap tide, respectively. T.R. and Disch. are the tidal range and river discharge, respectively.

Conditions	Date	T.R. (m)	Disch. (m^3/s)
LD-ST17	Sept, 19–20 2017	3.2–3.8	84–86
LD-NT17	Sept, 28–29 2017	1.2–1.3	112–128
LD-ST18	Sept, 25 2018	3.3	103
HD-ST18	June, 12 2018	3.2	1421

2.2.1. Bottom moored measurements

A bottom-moored station has been deployed, at about 5 km from the entrance of the estuary, at the same location than the boat survey station (BSS on Fig. 1), in September 2017. Velocity profiles were recorded by a Flowquest ADCP (600 kHz) every 15 min (time averaged 5-min burst data at 4Hz), with a vertical resolution of 0.5m. The ADCP was located at 0.56 m above the bed. Velocity profiles recorded during LD-NT17 are

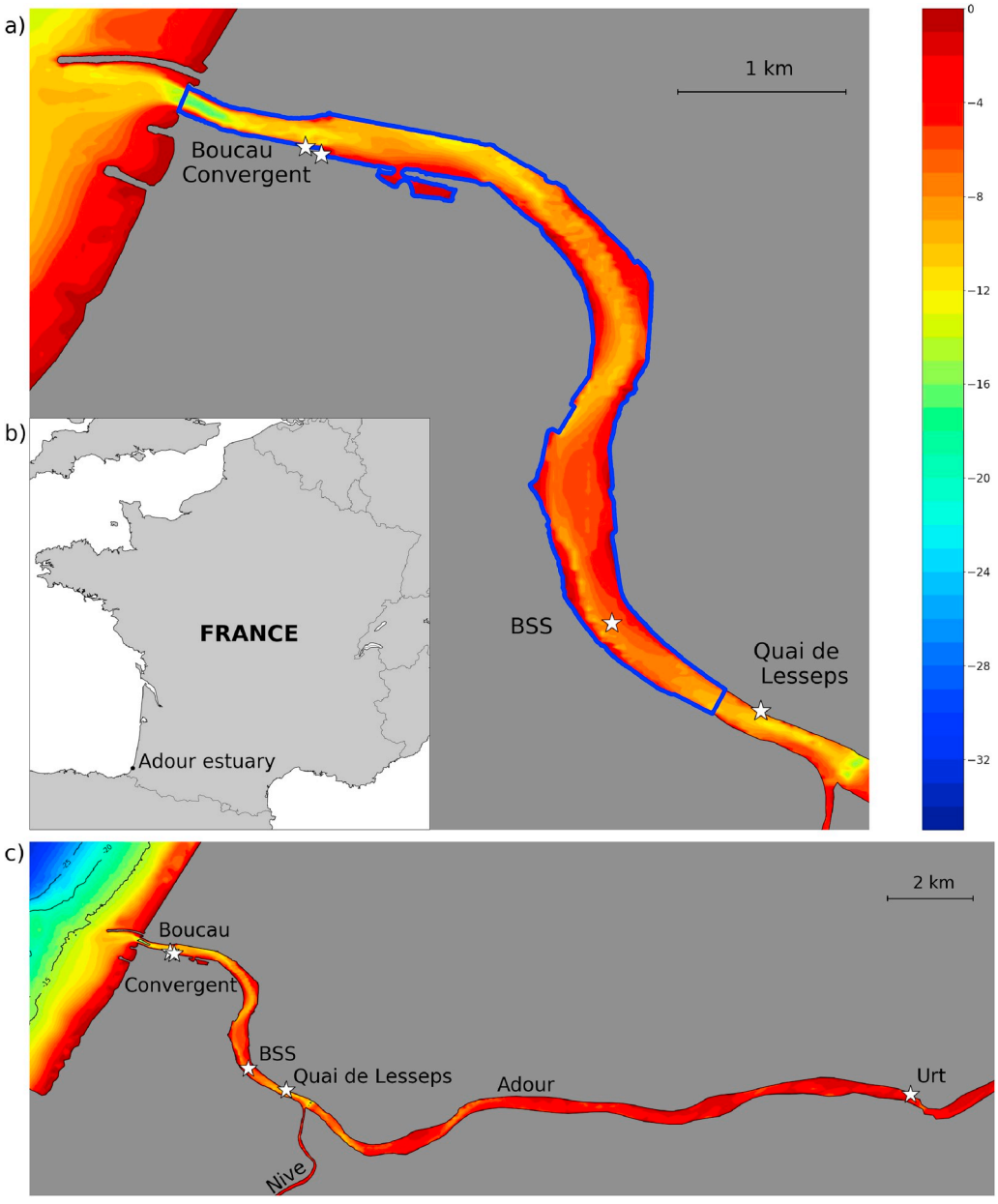

Fig. 1. a) The study area, i.e. the last 6 km of the estuary, with the Bayonne Harbour in blue. b) The location of the Adour estuary along the French coast. c) The Adour estuary from the entrance to Urt village. BSS white star is the boat survey station location. Boucau, Convergent, Quai de Lesseps and Urt white stars are the tide gauges locations. Colors represent the bathymetry in meter below the chart datum. (For interpretation of the references to color in this figure legend, the reader is referred to the Web version of this article.)

presented in Fig. 4.

2.2.2. Fixed boat surveys

The fixed boat surveys were dedicated to the vertical structure of velocity, salinity, temperature and turbidity. Measurements were performed from an anchored boat (BSS on Fig. 1).

The salinity, temperature and turbidity measurements were carried out by a Seabird C19plus CTD sensor or a YSI 6920 probe. For each experiment, 5-L water samples have been taken to calibrate the instruments. Forty kilograms weights were attached to the measurements line in order to ensure the verticality. Probe measurements were recorded at 4Hz for the Seabird C19plus and 1Hz for the YSI 6920. Temperature data will not be discussed in this paper, due to negligible contributions in the density variations compared to salinity effect.

In addition to water properties measurements (1 profile every 15 min), high-frequency velocity profiles were recorded, for LD-ST18 and HD-ST18 only, by a Nortek Signature 1000 current profiler (ADCP) secured along the hull. The ADCP was continuously sampling at a rate of 8Hz with 20–30 cm cells.

2.2.3. Longitudinal sections

Longitudinal transects were realised across the control area (from 1 km to 5.5 km, from the entrance of the estuary) with an OSIL Minibat under-water towed vehicle, equipped with a multi-parameter probe. Salinity, temperature, pressure and turbidity have been recorded by the Minibat. Deployments have been carried out during LD-ST17 and LD-NT17 experiments (see Figs. 3 and 5, respectively). While the Minibat provides useful spatial information, its deployment remains a very delicate operation in such a shallow and vertically sheared navigation channel. The transects were surveyed following the centre axis of the estuary, i.e. not always in the main channel due to navigation constraints near the docks.

2.2.4. Water levels

The tide gauge data presented hereafter have been collected either by Convergent or Bayonne-Boucau tide gauges, due to episodic malfunctioning. Both are operated by the Service Hydrographique et Océanographique de la Marine (SHOM) and located near to the entrance of the estuary (Fig. 1). In this paper, those data will be presented in water elevation above the local chart datum (in m C.D.).

2.3. Data processing

2.3.1. Velocity measurements

For each profiler, the velocity data are projected into a local coordinate system with the x axis directed along the channel with positive values landward, the y axis directed laterally towards the right bank, and the z axis directed upward. For simplicity, the generic term "velocity" generally refers later on to the x-component of velocity, otherwise clarification will be given.

High frequency velocity data from LD-ST18 and HD-ST18 are used to analyse turbulence properties. The 8Hz, 1s averaged, ADCP data of opposing beams (b_i) have been split into a mean ($\overline{b_i}$) and a fluctuating part (b_i'), using a sampling interval of 10 min. An additional high-pass filter is applied to remove low frequency fluctuations due to ship motion. The along-beam velocities have been used to estimate the components of Reynolds stress (Lu and Lueck, 1999; Williams and Simpson, 2004; Simpson et al., 2005), as follows:

$$-\overline{u'w'} = \frac{\overline{b_3'^2} - \overline{b_1'^2}}{4sin(\theta)cos(\theta)} \quad (1)$$

$$-\overline{v'w'} = \frac{\overline{b_2'^2} - \overline{b_4'^2}}{4sin(\theta)cos(\theta)} \quad (2)$$

where θ represent the angle of each beam from the axis of the instrument ($\theta = 25^o$ for Nortek Signature 1000 ADCP).

The eddy viscosity is classically computed following the flux-gradient hypothesis:

$$\nu_t = -\frac{\overline{u'w'}}{\partial\overline{u}/\partial z} \quad (3)$$

The rate of Turbulent Kinetic Energy (TKE) production is expressed as a product of stress and shear:

$$P = -\rho\overline{u'w'}\frac{\partial\overline{u}}{\partial z} - \rho\overline{v'w'}\frac{\partial\overline{v}}{\partial z} \quad (4)$$

2.3.2. Richardson number

The non-dimensional Richardson number *Ri* is often used to quantify the stability of the density stratification in sheared flow (Turner, 1979). A threshold value of 0.25 is commonly applied to distinguish stable stratification from unstable situation due to the breakdown of

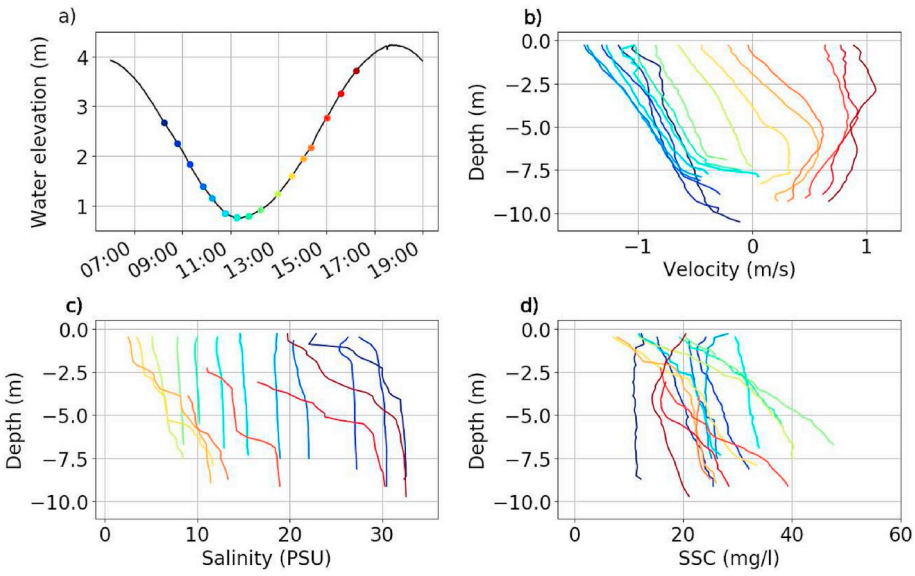

Fig. 2. Tidal dynamics from LD-ST18 fixed boat surveys during low discharge spring tide conditions. (a) Water level and timing of measurements. (b), (c), and (d): velocity, salinity and SSC profiles. Note that the same data is presented in contour plots in Fig. 7.

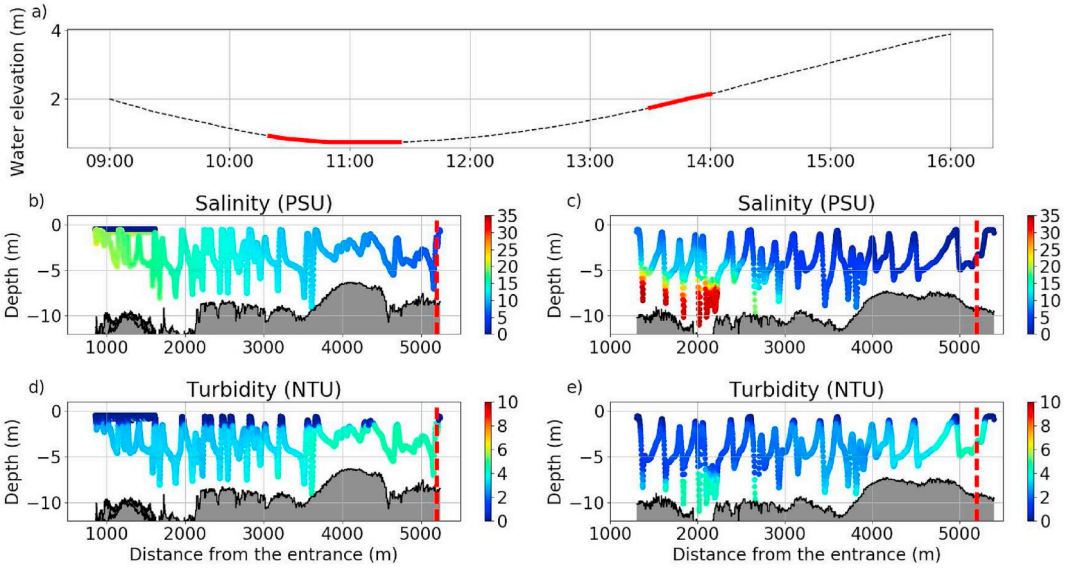

Fig. 3. Longitudinal and vertical structure across the lower estuary from Minibat measurement during LD-ST17 experiment. (a): Water elevation with measurement periods highlighted in red. (b) and (c): salinity data for falling and rising tide. (d) and (e): turbidity data for falling and rising tide. The bed of the estuary is represented in grey. The red dashed line represents the BSS location. (For interpretation of the references to color in this figure legend, the reader is referred to the Web version of this article.)

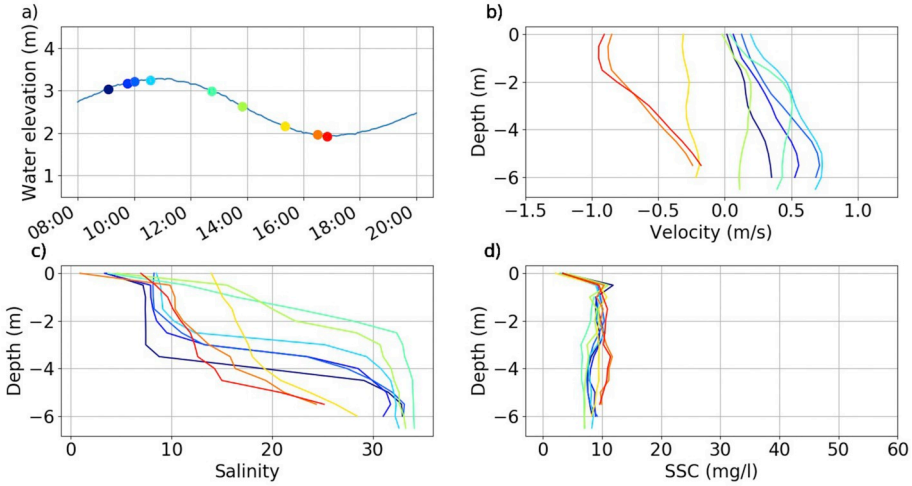

Fig. 4. Tidal dynamics from LD-NT17 fixed boat surveys during low discharge neap tide conditions. (a) Water level and timing of measurements. (b), (c), and (d): velocity, salinity and SSC profiles.

stratification by turbulent mixing. For high values of *Ri*, the buoyancy forces driven by the vertical density gradient are expected to overcome and suppress turbulent mixing. The Richardson number formulation is here calculated from the ratio between density and mean velocity gradients:

$$Ri = -\frac{g}{\rho_0}\frac{\partial\rho/\partial z}{(\partial\overline{u}/\partial z)^2} \quad (5)$$

where ρ_0 is the depth-averaged density. For the calculation of the Richardson number, density is estimated according to UNESCO formula and density profiles are interpolated over the ADCP regular measurement positions. It should be noted that in Fig. 2, the top of the water column is missing in some salinity and SSC profiles due to the malfunctioning of our multi-parameters probe.

2.3.3. Turbidity and SSC

Turbidity profiles from boat surveys during LD-NT17, LD-ST18 and HD-ST18 have been converted into suspended sediment concentration (SSC) using a series of 5-L water samples and pre-weighted glass fiber filters.

3. Results

The presentation of the field results will first focus on salinity structure and circulation, based on the time evolution of the vertical profiles of the measured parameters (Figs. 2, 4 and 6 for LD-ST18, LD-NT17 and HD-ST18 cases, respectively) together with longitudinal sections (Figs. 3 and 5 for LD-ST17 and LD-NT17 cases, respectively). The LD-ST18 and HD-ST18 data are also depicted as temporal contour plots in Figs. 7 and 8, respectively. For theses cases, additional turbulence data over the whole water column, including estimates of eddy viscosity and rate of TKE production, are then presented from hull-mounted ADCP measurements, to analyse the competition between turbulence and stratification. SPM dynamics is finally explored in the view of previous observations on estuarine dynamics.

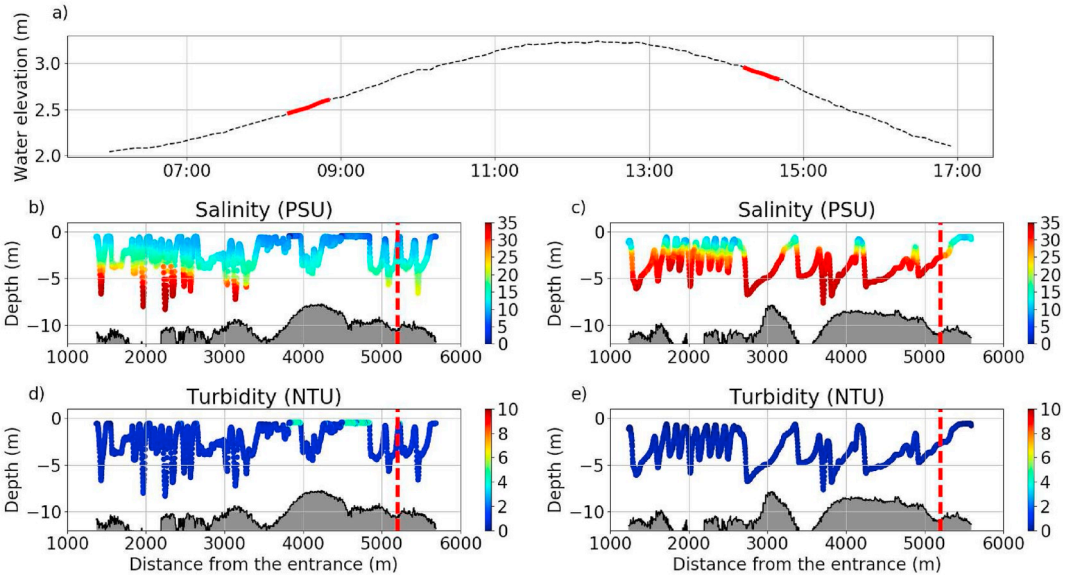

Fig. 5. Longitudinal and vertical structure across the lower estuary from Minibat measurement during LD-NT17 experiment. (a): Water elevation with measurement periods highlighted in red. (b) and (c): salinity data for falling and rising tide. (d) and (e): turbidity data for falling and rising tide. The bed of the estuary is represented in grey. The red dashed line represents the BSS location. (For interpretation of the references to color in this figure legend, the reader is referred to the Web version of this article.)

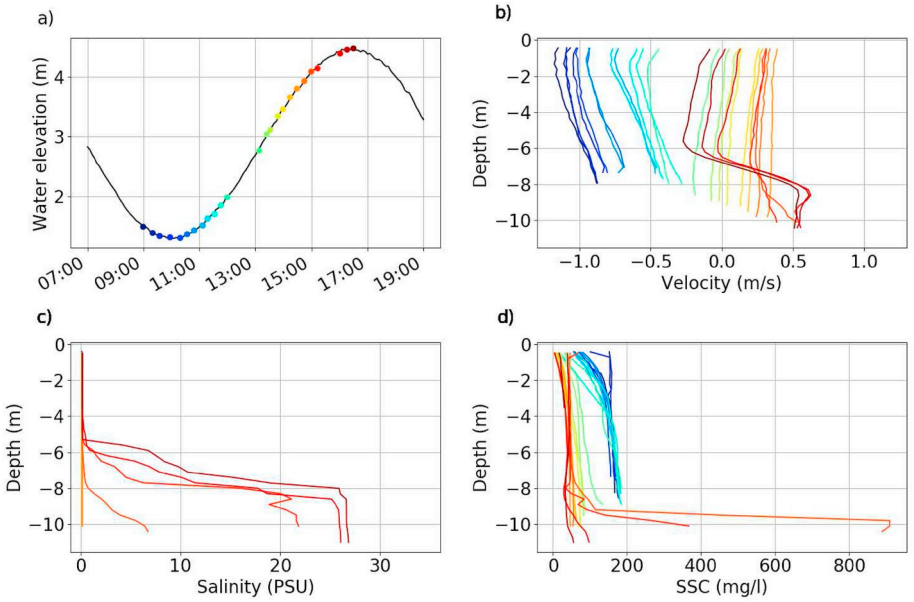

Fig. 6. Tidal dynamics from HD-ST18 fixed boat surveys during high discharge spring tide conditions. (a) Water level and timing of measurements. (b), (c), and (d): velocity, salinity and SSC profiles. Note that the same data is presented in contour plots in Fig. 8.

3.1. Estuarine salinity structure and circulation

Figs. 2, 4 and 6 present the tidal evolution of velocity, salinity and Suspended Sediment Concentration (SSC) profiles, during the dry season, for spring (LD-ST18) and neap (LD-NT17) tide conditions, and during the wet season for spring tide (HD-ST18) respectively. Figs. 3 and 5 display vertical salinity and turbidity structure along the last 6 km of the estuary, from Minibat measurement during LD-ST17 and LD-NT17 experiments, respectively.

The data analysis is first focused on the spring tide condition during the dry season (Figs. 2 and 3). The ebbing tide is characterised by a horizontal salinity gradient (Figs. 2 (c) and Fig. 3 (b)), with a homogeneous water column flowing out the estuary. As the ebb progresses, the water column becomes fresher and flows faster. At low water (11:36), the seaward current shows a strongly sheared structure, with a nearly linear profile across the water column. Progressively, the water column slows down and the salinity still decreases homogeneously along the water column. As the tide rises, the salinity at the top of the water column goes on decreasing, while, at the bottom of the water column the salinity increases. Salinity profiles are not homogeneous anymore, and the salinity gradient increases. The current reversal occurred around 13:30 (i.e. almost 2 h lagged from the low water time). The velocity profile reveals a typical salt-wedge profile, when the salty marine waters flow into the estuary. A fast landward salty bottom layer is observed in the lower 3m, while an oppositely fresh upper layer is still flowing seaward with a sheared profile. The salinity reaches its minimal value in

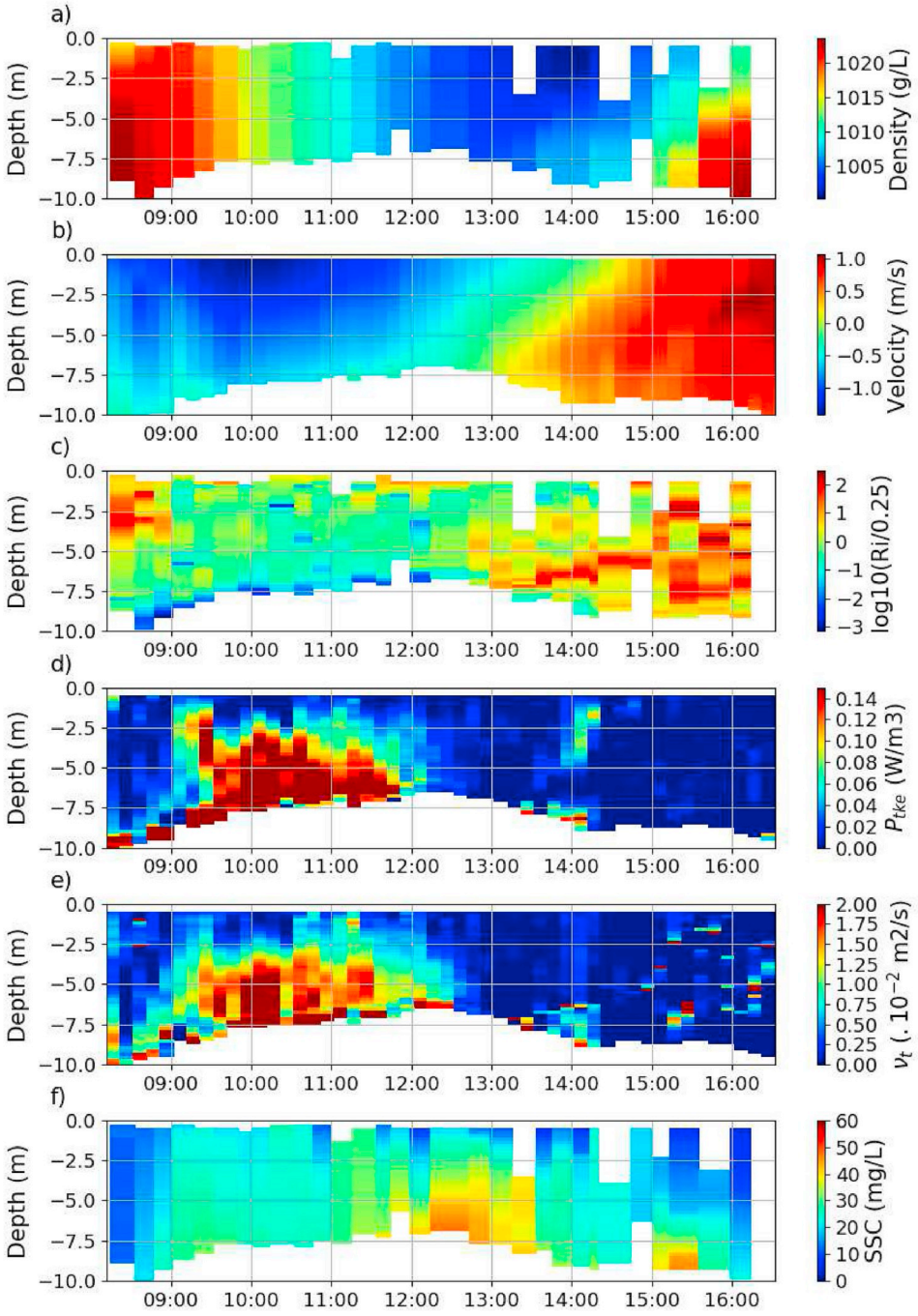

Fig. 7. Tidal evolution during LD-ST18 experiment: (a) vertical structure of density, (b) time-averaged velocity, (c) Richardson number, (d) production rate of TKE, (e) eddy viscosity, and (f) suspended sediment concentration.

the surface layer, when the salt-wedge starts entering the estuary. The salty bottom layer, which is rather well-mixed, increases both in thickness and salinity as the tide rises. At the end of the flood tide, the full water column is salty and flows upstream, blocking the fresh water inside the upper part of the estuary. The continental waters blocked into the upper part of the estuary during the flood, are then released during the ebb. This mechanism, named "pulsed plume mechanism", has already been highlighted by Dailloux (2008).

The contrast between spring tide and neap tide (Figs. 4 and 5) is straightforward, as during neap tide the salinity stratification is maintained all along the tidal cycle and the velocity magnitudes are reduced. At the end of the flood (11:00), a sharp pycnocline separates a two-layer flow, with denser marine water flowing upstream underneath fresh continental water. The bottom saline layer grows thicker until post-high tide slack water (14:00). Unlike spring tide, at neap tide the pycnocline is not able to reach the surface. The current reversal is lagged of almost 3h from the high water (10:49). As flow reverses seaward, the pycnocline thickens and deepens, while the surface and the bottom salinity remain relatively constant. This time the ebbing shear velocity profiles are associated with a vertical stratification. This permanent stratification leading to an inhibition of the salt-wedge flushing during neap tide is generally associated with stagnant waters and hypoxia (Kemp et al., 2009; Bruce et al., 2014).

A dedicated experiment (HD-ST18) was carried out during a high discharge event in order to explore the role of river runoff on the hydro and sediment dynamics compared to the reference low river discharge

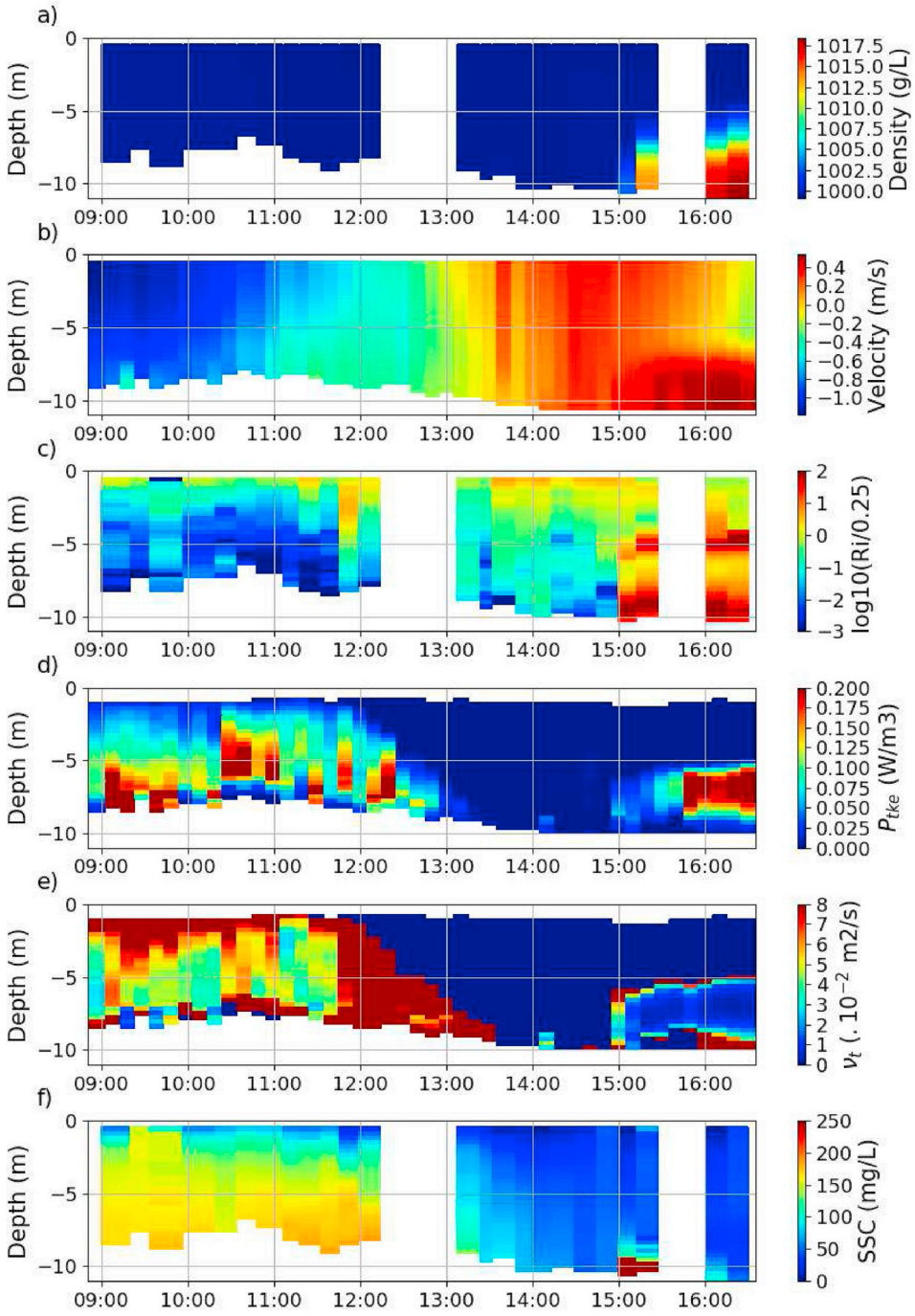

Fig. 8. Tidal evolution during HD-ST18 experiment: (a) vertical structure of density, (b) time-averaged velocity, (c) Richardson number, (d) rate of TKE production, (e) eddy viscosity and (f) suspended sediment concentration. Note the difference in range compared to Fig. 7.

dataset presented hereabove. Fig. 6 depicts the time evolution of velocity profiles, salinity and Suspended Sediment Concentration (SSC) profiles during high river discharge conditions. The comparison with low discharge conditions presented in Fig. 2 shows the drastic influence of river run-off on the estuarine dynamics. Similar maximal magnitudes are reached during the ebb, but the velocity profile is almost constant, and the water column is homogeneously fresh. As tide rises, the water column shows a piston-like behaviour, i.e. marine water impounding river water into the estuary with a quasi uniform velocity along the vertical. The current reversal (13:00) occurs much later for the high discharge case, i.e. almost 3 h after the low water (09:58), than for the low discharge case. The piston-like behaviour remains active all along the flow reversal and during the most part of the flood tide. This greatly differs from the low discharge case for which a vertical shear of velocity is systematic at the early stage of flood tide. At the very end of the flood (16:00), the salt-wedge is finally able to reach the measurement area. A 2 m thick bottom salty layer propagates upstream at about 0.5 m/s. The high river discharge is again responsible for a significant time lag compared to low discharge conditions for which the salt-wedge was able to reach boat survey station about 2 h earlier. A remarkable observation, at the salt-wedge arrival, is the rapid seaward reversal of the overlying fresh water layer. The water column forms, therefore, a two-layer vertical structure with strong vertical shear in velocity and a sharp pycnocline. Note that the seaward/landward velocity maxima are reached in the upper parts of the pycnocline and of the salt-wedge, respectively.

3.2. Turbulence properties

The previous section revealed the complex vertical salinity structure and circulation taking place into the Adour estuary. This first result needs to be further investigated by a turbulent properties analysis, to get a better understanding of the interaction between stratification and turbulent mixing. The representation of Richardson number profile as $log_{10}(Ri/0.25)$ is used in Figs. 7 and 8 to easily estimate the stability of the water column: stable (unstable) flows are expected for positive (negative) values. In addition, high-resolution high-frequency velocity profiles are used to infer turbulent properties of the flow. Figs. 7 and 8 shows the tidal evolution of the vertical distribution of turbulent properties at the survey station BSS for the low (LD-ST18) and high (HD-ST18) river discharge experiments respectively.

Fig. 7 depicts the data recovered during spring tide and low discharge conditions (LD-ST18). At 08:15, the water column is slightly stratified and the production of turbulence is focused in a very thin layer above the bed related with weak turbulent diffusion in most of the water column. As the water column becomes homogeneous and ebb current accelerates during the estuary flushing, the turbulence spreads into the water column aside from in the 2 m surface layer. The turbulent mixing overcomes the buoyancy forces and water column becomes fully unstable ($log_{10}(Ri/0.25) < 0$). Maximal values of P_{tke} and ν_t are associated with maximum ebb currents. The eddy viscosity is maximal in the bottom 4 m and reaches typical values (about $1.5\ 10^{-2}\ m^2.s^{-1}$) measured in estuary for similar velocity and stratification conditions (Simpson et al., 2005). Those measurements also confirm that the eddy viscosity decreases toward the surface (Nezu and Rodi, 1986). The slack water and the subsequent flow reversal are associated with a drastic drop of turbulence production. After 13:00, the sign change of the Richardson number indicates the shift toward a stable stratified situation which further reduces the eddy viscosity. At the salt-wedge entrance (around 13:30), a stable stratification develops with no turbulent mixing except an increase of TKE production and eddy viscosity at the tip of the salt-wedge. High values of Richardson number are associated to the edges of the pycnocline. Burst of turbulent production seems to develop in the upper layer between 14:00 and 14:30, which may correspond to a local destabilisation of the sheared layer. As the tide rises, the water column turns on stable up to the surface with no more turbulent mixing.

In addition, Ri calculations (not shown here) have been carried out for neap tide conditions based on profiles shown in Fig. 4. As expected, the nearly permanent vertical salinity stratification promotes stability throughout the water column.

Fig. 8 presents similar data than Fig. 7, but applied on data collected under high river run-off conditions. It is first recalled that Richardson number should be considered with respect to the corresponding velocity and density profiles: nearly neutrally stratified conditions (i.e. unstable conditions) may appear stable in terms of Richardson number when the velocity shear is very weak. This is for instance the case in the surface layer (Fig. 8). During high discharge conditions, the lower estuary is filled with fresh water for most of the tidal cycle, the only exception being the salt-wedge arrival just before high tide (15:00). Therefore, the turbulent properties variations drastically differ from the low discharge case shown in Fig. 7. At the end of the ebb tide (before 10:00), the water column is fully fresh and has an almost constant velocity. High rate of TKE production and eddy viscosity are measured at the peak of ebb currents. The strong discharge is able to maintain the instability and a significant TKE production until 12:00 (i.e. more than 2 h after low tide). Then, slack water (around 13:00) is associated to a strong drop of turbulence production and eddy viscosity, which remains very weak until the arrival of the salt-wedge. However, the piston effect is clearly visible at rising, with nearly vertically uniform velocity profiles during most of the rising tide. The consequence, in term of stability, is that the lower estuary remains unstable all the time until the salt-wedge is able to reach the measurement station (15:00). A first moderate rise of TKE production is observed near the bottom to a depth of 3m, which indicates that the tip of the salt-wedge is a mixing zone. From that moment, one notes the development of a 1–2 m high pycnocline, both strongly stratified and very sheared. Corresponding positive values of Richardson number indicates the stability of the sheared layer. Peaks of Richardson number are observed near the edges of the pycnocline, associated to more stable areas, whereas the core of the sheared zone is very close to the instability threshold. The TKE production strongly rises near the bottom, but remains confined near the bottom layer by the effect of overlying stratification. It can be noticed that, even if the velocity of entering marine waters is much lower than for the low discharge case, a much stronger turbulent mixing is observed in the bottom layer. The salt-wedge arrival (15:00) is a striking example of a dynamical competition between turbulent mixing and stratification: turbulent diffusion is very active near the bottom and below the pycnocline, but totally vanishes in the overlying fresh water layer.

3.3. Suspended sediment dynamics

This section is dedicated to the response of the sediment load to the complex hydrodynamics of the lower Adour estuary presented above. Figs. 2 (d), 4 (d) and 6 (d) represent the SSC profiles collected during LD-ST18, LD-NT17 and HD-ST18 respectively. Figs. 7 (f) and 8 (f) display same data as presented in Figs. 2 (d) and 6 (d) under timeseries color plots. Fig. 3 (d), (e) and 5 (d), (e) show Minibat turbidity data collected during LD-ST17 and LD-NT17 respectively.

First, a focus on the low river discharge reference case allow us to study the effect of tidal cycle on sediment dynamics, such as erosion, advection and deposition mechanisms. In Figs. 2 and 7, it can be noticed that at mid-ebb, the full water column is flowing out the estuary and the vertical velocity gradient is increasing. It results in a sufficient bottom shear stress to re-suspend sediment around 08:30. The sediments are maintained in suspension and are able to reach the surface of the water column by the turbulent mixing appearing at 09:00. Fig. 3 shows that a horizontal gradient of SSC associated to the horizontal gradient of salinity develops, with SSC increasing as the water becomes fresher. These sediments in suspension are advected seaward by the flow, at a velocity that can reach $1.5\ m.s^{-1}$ in the surface. Approaching the slack water period (12:00), the ebbing velocity is less than 0.6 m/s (green profiles on Fig. 7) and the vertical gradient of velocity decreases. Consequently the re-suspension capacity of the flow decreases. The turbulence maintaining the sediment in suspension also drops down, and so the SSC develops a vertical gradient, which might be associated with settling. It progressively leads to an overall SSC decrease. Around 14:00, sediments accumulated at the bottom of the water column are advected landward by the entrance of the marine waters into the estuary, while sediments located at the surface are still advected seaward. At 15:00, an area of high turbidity is generated at the tip of the salt-wedge front. This trend is generally attributed to the accumulation of sediments due to the convergence of sediment fluxes from the river and the ocean. This peak of SSC is contained near the bottom by the pycnocline. Another striking feature is the decrease of SSC in the layer of fresh continental water flowing above the salt-wedge (Figs. 7 and 3). This observation should likely be attributed to the stratification-induced damping of turbulence, leading to particles sinking, as previously observed in other systems (West et al., 1991; Geyer, 1993). At 16:00, velocity profiles are much more homogeneous and the turbulence is damped by the stability of the two-layer flow, and so the SSC decreases.

The tidal range has also a striking effect on the above mentioned sediment dynamics, as shown by the comparison between Figs. 2 and 4. During neap tides, the SSC remains very low, about $10\ mg.L^{-1}$ all over the tidal cycle and quite homogeneous over the water column, while during spring tides, the SSC is generally stronger (up to $45\ mg.L^{-1}$) and slightly more variable throughout the tidal cycle. This very low SSC can be explained by a permanent stratification and a reduced velocity. Low

velocities impede the re-suspension of sediments and the permanent stratification damps down the turbulence. The sediments can therefore not remain in suspension. During neap tides the flushing capacity is drastically reduced by the absence of re-suspension and advection and the strong deposition.

The riverine forcing also influences the sediment dynamics, as highlighted by Figs. 6 and 8. During high river discharge, the ebbing currents are reinforced and the flow is much more turbulent, resulting in a stronger re-suspension and seaward advection. Consequently, SSC values are much more higher than those observed during low discharge conditions. In Fig. 8, it can be noticed that during the ebb, the SSC is quite homogeneous in the water column, with values about 150 $mg.L^{-1}$. These reinforced re-suspension and advection result in a very good flushing capacity of the estuary. At 11:30, both flow and turbulent mixing reduce in intensity. The particles are not anymore maintained in suspension and a progressive sedimentation can be observed. The SSC shows a pattern similar to the one of turbulent properties. Between 15:00 and 17:00, the piston-like behaviour occurs pushing slowly the full low SSC water column landward. Similarly to the low discharge conditions, the salt-wedge passing (15:00) corresponds to the higher measured SSC. However, during high river discharge, the SSC is able to reach up to 850 $mg.L^{-1}$ in the bottom layer. The increased river flow reinforces the convergence mechanism. These sediment in suspension are also contained by the pycnocline and advected landward, while the surface waters containing little sediments are advected seaward. Around 1 h after the salt-wedge front passing, the SSC at the bottom of the water column has decreased to about 100 $mg.L^{-1}$. This high turbidity area is thus supposed to follow the up estuary motion of the salt-wedge leading front.

4. Discussion

This article presents a set of field observations carried out to improve the knowledge about circulation and sediment transport in the lower Adour estuary. These results provide the first in-situ characterisation of the hydrological functioning of the Adour lower estuary, but also give rise to a number of questions. Discussion points have been organised under three main topics: estuarine circulation, sediment dynamics and impacts of engineering works.

4.1. Estuarine circulation

The present in-situ dataset revealed the high variability of the Adour lower estuary, in terms of hydrological functioning. A salt-wedge generally develops during the flood tide in the Adour lower estuary. This salt-wedge depends on river discharge, by being more steeply marked during the wet season due to intense river forcing. In addition, the tidal forcing is also an important driver of the Adour estuary (mesotidal system) with a significant effect of the spring/neap cycles on the estuarine salinity structure. Under low discharge conditions, the neap tides are associated to fully vertically stratified estuary along the tidal cycle, while during spring tide the salt-wedge shape is lost during the ebb, and an horizontal salinity gradient takes place. Such a versatility in the salinity circulation in response to the fluctuations of tidal and fluvial forcing can not be properly accounted for by usual descriptive estuary classifications, such as, e.g. the well-know scheme of Cameron and Pritchard (1963). More physical insight is provided by the recent quantitative scheme of classification developed by Geyer and MacCready (2014).

The scheme of classification developed by Geyer and MacCready (2014) investigates the respective contribution of tidal mixing and stratification by the means of a two parameters space: the freshwater Froude number $Fr_f = U_R/(\beta g s_{ocean} H)^{1/2}$ and the mixing parameter $M = \sqrt{(C_D U_T^2)/(\omega N_0 H^2)}$, where U_R is the net velocity due to river flow (i.e. the river volume flux divided by the estuarine section), β is the coefficient of saline contraction, g is the acceleration due to gravity, s_{ocean} is the ocean salinity, H is the water depth, C_D is the bottom drag coefficient, U_T is the amplitude of the tidal velocity, ω is the tidal frequency and $N_0 = (\beta g s_{ocean}/H)^{1/2}$ is the buoyancy frequency for maximum top-to-bottom salinity variation in an estuary. The former dimensionless parameter Fr_f compares the net velocity due to river flow and the maximum possible front propagation speed, while the later M assesses the role of tidal mixing and the influence of stratification on the vertical mixing. Due to spring/neap variations and wet/dry seasons changes, estuaries are not represented by a point in this classification scheme, but rather by rectangles covering the range of observed regimes. An adaptation of the Geyer and MacCready's regime diagram (Geyer and MacCready, 2014) is proposed in Fig. 9, with the M and Fr_f ranges reached by some well-documented estuarine systems in order to easily compare with the Adour estuary.

Of particular interest is to know the extent to which the variability of the Adour estuary can be described by such approach and to evaluate how it can compare to other typical systems selected for their contrasted dynamics. For the calculation of both parameters, we considered $\beta = 7.710^{-4} PSU^{-1}$, H to be a characteristic value of the water depth $H = 10m$, the salinity of ocean $s_{ocean} = 34.5$ PSU. A first remark should be made on the uncertainty on the estimation of the mixing parameter M. This parameter shows a strong sensitivity to both U_T and C_D values, which are not straightforward to estimate. In Geyer et al 2014 (Geyer and MacCready, 2014), U_T is defined as the amplitude of the depth-averaged tidal velocity, while it has been estimated as the rms velocity 3m above the bed in Geyer et al. (2000) and considered equivalent to the maximal velocity in Li et al. (2014). For the present study, the reference value of U_T is provided by rms depth-averaged velocity measured at the BSS bottom moored station (Fig. 1). The bottom drag coefficient C_D can also be strongly spatially variable inside an estuary, and relatively challenging to estimate. In Geyer et al., 2014 (Geyer and MacCready, 2014) authors consider that C_D generally varies between 1 and 2.5 10^{-3} inside an estuary, while Geyer et al., 2010 (Geyer, 2010) mentioned a value of C_D generally about 3 10^{-3} inside estuaries. For the Adour estuary, two point currentmeters deployed in the bottom layer have been used by Sous et al. (2018) to estimate a C_D value about 1.5 10^{-3} between Convergent and BSS stations, which is used here as a reference for the estimation of M. Using data collected inside the Adour estuary, U_R estimation ranges from 0.05 to 0.75 $m.s^{-1}$, therefore Fr_f should range from 0.03 to 0.46 for low to high discharge conditions, respectively. The mixing parameter M, based on reference values for U_T and C_D, ranges from 0.36 to 0.66 for neap to spring tide conditions, respectively (Fig. 9, solid line rectangle). In order to illustrate the M sensitivity to U_R and C_D parameters, estimating now U_T as the maximal entering velocity together with a C_D value of 3 10^{-3} will shift the Adour's system toward higher ranges of mixing parameter values (0.68–1.13), see dashed line rectangle in Fig. 9. In addition, the values of the mixing parameter might be further increased with data from neap tide conditions combined to high river run-off, which are not documented by the present dataset.

Keeping in mind these limitations, the estuarine parameter space diagram proposed by Geyer and MacCready (2014) confirms the variability of the hydrological functioning of the Adour estuary in comparison with other typical systems (Fig. 9). Noted that the large area covered by the Adour river in this diagram is due to the highly contrasted hydrological conditions encountered during our measurements. Other systems may have been observed only during mean hydrological conditions, leading to reduced rectangles. Based on collected data, presented in this paper, we can analyse the observed dynamics of the Adour estuary. Under high tidal mixing conditions (i.e. high M value), the Adour river dynamics is quite similar to those of Fraser (Geyer and Farmer, 1989), Changjiang (Li et al., 2014) and Merrimack rivers (Ralston et al., 2010), which are all considered as time-dependent salt-wedge estuaries. Those energetic and stratified estuaries are characterised by

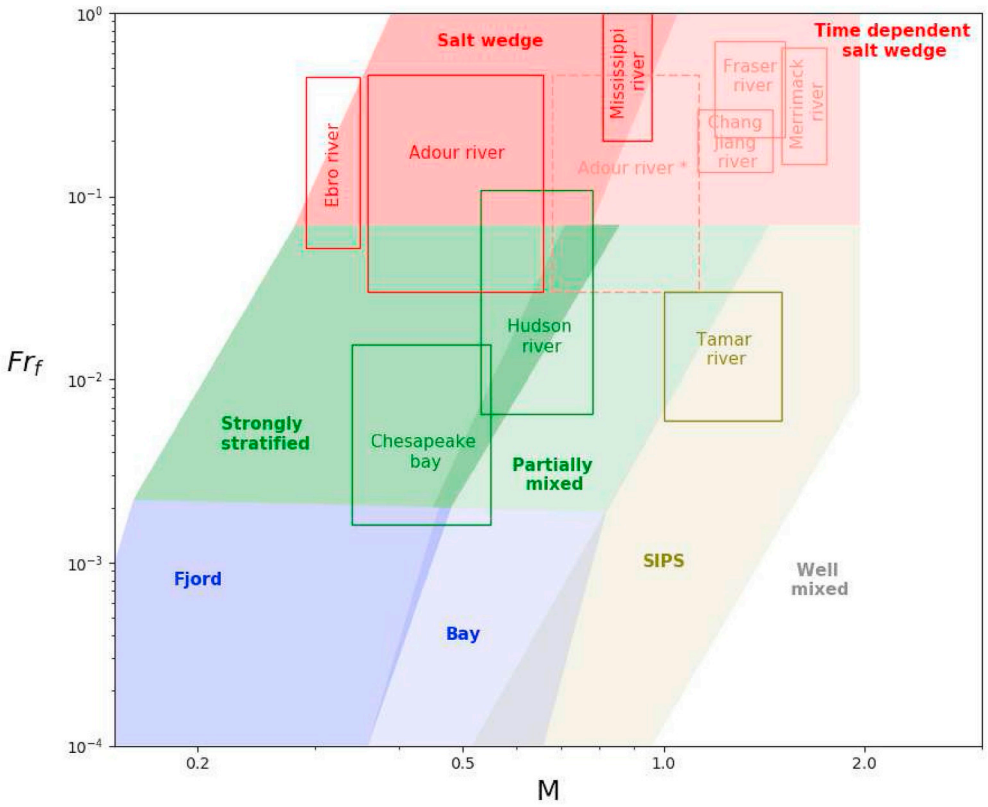

Fig. 9. Estuarine classification based on the freshwater Froude number and mixing number, adapted from (Geyer and MacCready, 2014), Fig. 6. (*) The dashed rectangle represent the location of the Adour river using other estimations of U_t and C_D.

strong tidal and fluvial velocities (Fig. 10). It results in a strengthened stratification during the flood, that weakens during the ebb tide, where the turbulence develops in the full water column. Under low tidal mixing conditions (i.e. low M value), the Adour tends to show a behaviour similar to the Ebro river. This latter has a similar shape and river discharge than the Adour, but the microtidal regime (associated to a small M) results in a stagnant salt-wedge under low river run-off ejected out of the estuary when the river discharge exceeds 500 $m^3.s^{-1}$ (Ibañez et al., 1997). Measurements undertaken during neap tide and low river discharge in the Adour estuary reveal a similar pattern with an almost stagnant salt-wedge and strong stratification. Unfortunately, observations were not carried out during neap tide and high river discharge (around 1500 $m^3.s^{-1}$), but we can expect an absence of the salt-wedge or at least a strong reduction of the saline intrusion. The role of river discharge is however clearly identified for spring tides, corresponding to fluctuations along the Fr_f axis in Fig. 9 for large value of M. Under low river discharge conditions (i.e. low Fr_f value), the influence of tidal mixing is more important, leading to a smoother vertical stratification and a strongly stratified regime. During the ebb, the peak of turbulence can be sufficient to break down the vertical stratification and generate an horizontal stratification. This horizontal stratification is a typical attribute of partially mixed regime. When the river discharge increases (i.e. higher Fr_f values), the vertical stratification appears to be stronger, with a sharper pycnocline and a salt-wedge restricted in the lower part of the water column.

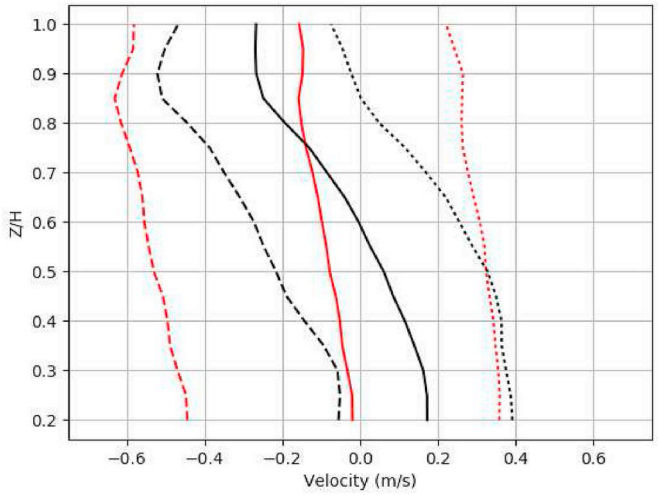

Fig. 10. Tidally averaged velocity profiles for neap (full black line) and spring (full red line) tides with low river discharge. Flood (dotted lines) and ebb (dashed lines) average velocity profiles for neap/spring low river discharge conditions. Data from bottom moored station located at BSS location (Fig. 1). (For interpretation of the references to color in this figure legend, the reader is referred to the Web version of this article.)

The lateral dynamics, which has not been explored in the present data analysis, may play an additional important role in the estuarine circulation and salinity structure. Both local curvature of the lower estuary and cross-sectional bathymetric gradient are expected to favor a degree of three-dimensionality in the estuarine flow structure (Lacy et al., 2003; Scully and Geyer, 2012). This calls for further dedicated experimental campaign to better understand the contributions of along-channel and lateral components in mixing processes, and their dependencies on tidal range and river discharge.

4.2. Suspended sediment dynamics

The present study allows to analyse the impacts of physical processes taking place inside the Adour estuary on the observed sediment transport. Since the Glangeaud's pioneering description of an Estuarine Turbidity Maximum (ETM) in the Gironde estuary in 1938 (Glangeaud,

1938), a series of numerical and experimental studies have revealed the importance of ETM in estuarine sediment dynamics (Burchard and Baumert, 1998; Jay et al., 2007; Uncles et al., 2002; Burchard et al., 2018) among others. ETM have strong impacts on the marine and estuarine ecosystems, being a major driver of sediments, contaminants and nutrients from continent to ocean. ETM formation is primarily driven by the hydrodynamical functioning of the estuary. In salt-wedge systems, and in particular in the presence of strong tidal forcing, two key mechanisms have been identified in the ETM dynamics: the residual gravitational circulation and the tidal asymmetry. Burchard and Baumert (1998) demonstrated that tidal asymmetry is of a bigger importance in the ETM formation than gravitational circulation in macrotidal salt-wedge estuaries. The gravitational circulation plays a part in sustaining and stabilising the ETM mass. In the Charente estuary, which shows similarities with the Adour in terms of dimension and salt-wedge regime but with a stronger tidal forcing, the tidal asymmetry is mostly responsible for the formation of the turbidity maximum, while the density gradient has an influence on its shape and its stratification (Toublanc et al., 2016). More recently, Olabarrieta et al. (2018) have highlighted the role of density gradient-driven subtidal flows in the sediment import and trapping into the estuary associated to near-bed flood tide dominance.

Based on the present dataset, no stable ETM has been observed in the lower Adour estuary. Further insight is provided by analysing the main expected ETM drivers. First, the tidal assymetry in the Adour estuary has been studied based on the water elevations collected by tidal gauges along the estuary. Fig. 11 outlines that a slight tidal asymmetry of less than 20 min exists in the lower estuary. Provided time lag appears too weak to generate an ETM when compared to the Charente estuary, where tidal asymetry can reach almost 3.8 h at the river mouth (Toublanc et al., 2015, 2016). A strongest asymmetry can be noticed in the upper part of the estuary (i.e. 20 km upstream at Urt village). Such mechanism might generate on ETM in this reach of the estuary. Extended measurements until Urt village or a dedicated numerical study are foreseen as further work to estimate the impact of this tidal asymmetry on the sediment transport in the upper estuary. The second ETM driving process is the residual estuarine circulation. In most cases, no residual estuarine circulation has been observed in the lower estuary. The mean ebbing velocities are stronger than the mean flooding velocities, resulting in a good flushing of water masses and suspended sediment. The only exception is observed during very low river flow and tidal forcing conditions, as revealed by the residual tidally-averaged velocity profiles depicted in Fig. 10, black solid line. In such conditions, a residual circulation is observed, but its effect in generating a well-developed ETM is likely compensated by limited resuspension due to reduced velocities. Note however that the bottom moored current profilers are not able to resolve the bottom 1.5 m (structure size and blanking zone), which can hide near-bed processes.

Moreover, it should be noted that riverine input of sediment is very low compared to other tidal estuaries, based on SSC obtained in the present conditions. Even during high river discharge, during the ebb, when the water column is full of fresh riverine waters flowing out the estuary, the SSC is about 150 $mg.L^{-1}$. This very low supply in sediment even during high river discharge might be related to the marshy meadows located along the Adour river, which could be responsible for particle trapping.

The observed influence of tidal range on the lower estuary has also a strong effect on the ejected plume. At spring tide during the dry season, continental waters are blocked inside the estuary by the marine waters entrance for about 3 h. This mechanism drives the pulsed behaviour of the plume of the Adour estuary already highlighted by Dailloux (2008). By contrast, at neap tide during low discharge conditions or under high discharge conditions, a layer of continental water is flowing seaward all along the tidal cycle at the top of the water column, almost constantly feeding the plume leaving the estuary with fresh water. The pulsed behaviour of the Adour estuary may take place only when the tidal forcing is able to overcome the riverine forcing, and so the riverine waters are blocked into the estuary by the marine water entrance.

4.3. Impacts of engineering works

The Adour estuary exhibits a strong variability of salinity, which has never been reported in the literature. This is highlighted by direct measurements in a range of conditions and confirmed by the Geyer and MacCready classification diagram (Geyer and MacCready, 2014). Part of the observed variability is directly imposed by the fluctuations of the external forcing, i.e. a mesotidal regime associated with seasonal variations of river discharge driven by the oceanic climate and the close proximity to the Pyrenées mountains. However, such conditions may not entirely explain the observed variability of estuarine salinity circulation

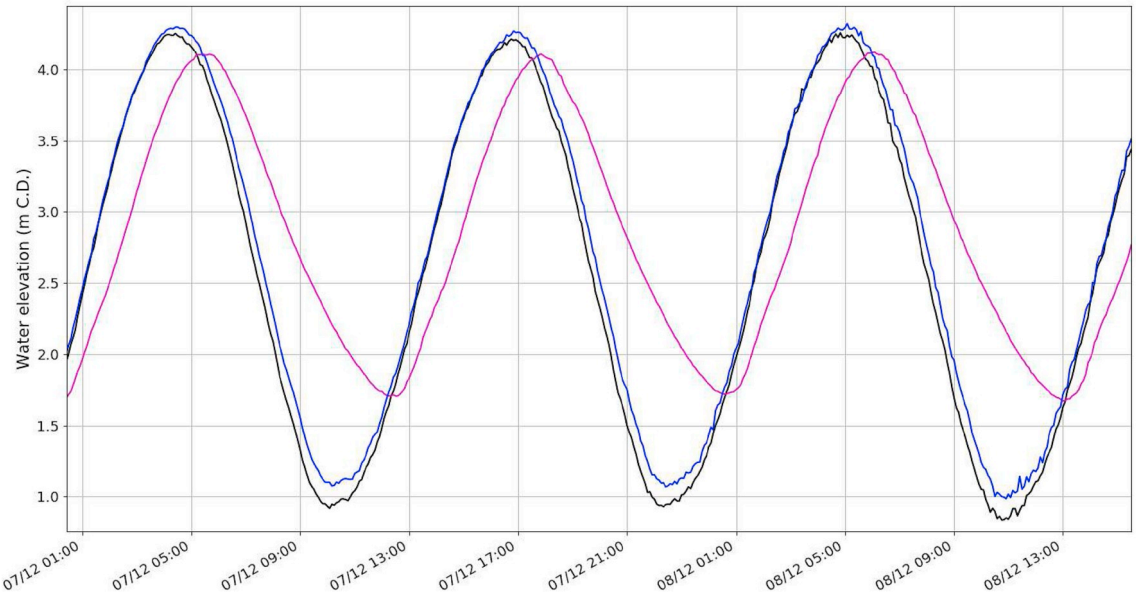

Fig. 11. Water elevation data collected at Urt village (22 km from the estuary mouth, in magenta), at Convergent (700 m from the estuary mouth,in black) and Quai de Lesseps (5.6 km from the estuary mouth, in bleu) tide gauges, during spring tide.

when comparing the Adour to other systems. It can be hypothesised that the artificial channelisation of the lower estuary coupling with strong dredging activities act to enhance the fluctuations in hydrological regimes. The Adour estuary is fully artificial since 1578, when the mouth of the estuary has been fixed in front of the Bayonne city by diking, under the decision of King Charles IX. In 1810, Napoleon decided to reduce the entrance of the estuary to 150 m in the aim of protecting the channel from sand accumulation by focusing the ebb energy. For a wider lower estuary, which would be likely the case in a more natural context, the U_R value would consequently decrease and so the Fr_f. This reduction of river flow velocity should reduce the stratification within the estuary which should promote the development of strongly stratified or partially mixed regimes. These engineering works are complemented by dredging activities from 1896. Nowadays, the quantity of sediments to be dredged in the lower estuary per year is about 525000 m^3. The dredger of 1200 m^3 capacity operates almost everyday, except from June to September. This is also supposed to have a significant impact on the stratification, by maintaining the channel deeper. In the absence of dredging, the depth reduction would strengthen the river flow and decrease the tidal propagation speed, resulting in an enhanced mixing. Following the Geyer and MacCready classification (Geyer and MacCready, 2014), this would result in an increase of both parameters likely leading to a more systematic time-dependent salt-wedge regime. Such assumptions can certainly not be directly assessed from the present or former dataset, and would require prospective scenarios with dedicated numerical modelling to be further discussed. The potential changes on estuarine salinity structure might have significant consequences on biogeochemical processes controlled by mixing, residence time and water properties. Such issues should obviously not only concern the Adour system and call for a more extensive assessment of the impact of artificialisation and urbanisation of estuarine systems on the physical processes controlling the hydrodynamics and finally affecting the entire ecosystem.

The question arises then on the role of estuary engineering (channelisation and dredging) on the absence of observed ETM in the lower reach of the estuary, in particular when compared to other tidal estuaries. First, the width reduction at the estuary mouth certainly enhances the good flushing capacity of the lower Adour by reinforcing the ebbing currents. Such hypothesis might be impossible to confirm due to the lack of available data collected before those engineering works, a numerical study could be necessary to discuss further this issue. In addition, it is hypothesised that the artificialisation of the river mouth tends to maintain a low marine sediment input, thus participating to the absence of ETM. At the river mouth, along the Northern jetty, a sand pit has been artificially created and maintained by dredging operations, in order to avoid sand accumulation in the estuary entrance under storm conditions. Dubranna's numerical study (Dubranna, 2007) highlighted that the transport of sediment from the coastal area into the estuary is strongly limited by this man-engineered retention pit. Grasso and al (Grasso et al., 2018) have shown the important contribution of energetic wave conditions to the ETM mass, by sediment resuspension action. However, it has been demonstrated that both jetties located at the estuary entrance, efficiently protect the port against incoming swell and sea waves with a reduction factor of 85% compared to the offshore wave energy (Bellafont et al., 2018). All together, these interventions may also contribute to the absence of ETM in the Adour lower estuary. Nevertheless, the impacts of the artificialisation of the lower estuary on its hydrodynamics and sediment transport can not be quantified by the present study, and would require further investigations.

The plume generated by the brackish fresh waters flowing out the estuary is also influenced by the engineering works at the entrance of the estuary. As already mentioned the width reduction at the entrance of the estuary might be responsible for an intensification of the plume. In addition, the Northern jetty also affects the dispersion of the plume orienting the plume in the southwest direction. Such issue was not part of the scope of this study, however this could be the aim for additional research. Additional measurements upstream in the Adour estuary would be necessary to confirm such hypothesis.

5. Conclusion

This study aimed to investigate the hydro-sedimentary behaviour of the lower Adour estuary by means of field experiments. A series of hydrodynamical processes are documented through bottom-moored, hull-mounted and vertical profiling instrumentation. It has been shown that its functioning is strongly influenced by both river and tidal forcing, resulting in a wide range of density stratification. The stratification variations show different time scales: from flood to ebb tides, from neap to spring tides, even from dry to wet seasons. It has been demonstrated that stratification is strengthened during the flood tide and weakened during the ebb tide. During low river discharge, neap tides promote stable salt-wedge in the lower estuary, while spring tides allow full flushing of the salt-wedge. On the other hand, wet season has a tendency to constrain the salt-wedge in a thin bottom layer, enhancing the vertical stratification. This strong variability in the flow structure has a huge influence on the flushing capacity of the estuary.

The tidal evolution of the gradient of Richardson number has revealed the straight influence of the salinity structure on the turbulent mixing. Flood tide is generally associated with reduced turbulence production and stable stratification, while ebb tide is characterised by strong turbulent mixing. Through stratification and mixing characteristics of the Adour estuary, a recent classification scheme has been applied to compare it to others salt-wedge estuaries. Based on the Geyer and MacCready classification (Geyer and MacCready, 2014), the Adour estuary varies from salt-wedge to partially mixed estuary.

Density effects, salt-wedge displacement and the competition between stratification and mixing processes have a strong impact on the suspended matter displacement: longitudinal convergence at the salt tip, sinking of particles due to stratification induced turbulence damping, and re-suspension due to the salt-wedge passing. However, both major mechanisms associated with ETM generation have not been observed in the lower estuary: tidal asymmetry and residual estuarine circulation.

Acknowledgments

This study was sponsored by the EC2CO PANACHE program (CNRS INSU) and the MICROPOLIT project (European Regional Development Fund (ERDF) and Adour-Garonne Water Agency). The port of Bayonne, the Gladys group, MIO and EPOC supported the experimentation. We are grateful to all the contributors involved in this experiment, in particular to Stéphane Gubert whose efforts were essential to the deployment and Nagib Bhairy for Minibat operations.

References

Bellafont, Florian, Morichon, Denis, Roeber, Volker, André, Gaël, Abadie, Stéphane, 2018. Infragravity period oscillations in a channel harbor near a river mouth. Coast. Eng. Proc. 1 (36), 8.
Brière, C., 2005. Etude de l'hydrodynamique d'une zone côtière anthropisée: l'embouchure de l'adour et les plages adjacentes d'anglet. Ph.D. thesis (Pau).
Bruce, L.C., Cook, P.L., Teakle, I., Hipsey, M.R., 2014. Hydrodynamic controls on oxygen dynamics in a riverine salt wedge estuary, the yarra river estuary, Australia. Hydrol. Earth Syst. Sci. 18 (4), 1397–1411.
Burchard, H., Baumert, H., 1998. The formation of estuarine turbidity maxima due to density effects in the salt wedge. a hydrodynamic process study. J. Phys. Oceanogr. 28 (2), 309–321.
Burchard, H., Hetland, R.D., 2010. Quantifying the contributions of tidal straining and gravitational circulation to residual circulation in periodically stratified tidal estuaries. J. Phys. Oceanogr. 40 (6), 1243–1262.
Burchard, H., Schuttelaars, H.M., Ralston, D.K., 2018. Sediment trapping in estuaries. Annu. Rev. Mar. Sci. 10, 371–395.
Cameron, W., Pritchard, D., 1963. Estuaries. In 'the Sea, 2', pp. 306–324 mn hill.
Dailloux, D., 2008. Video Measurements of the Adour Plume Dynamic and its Surface Water Optical Characteristics. Ph.D. thesis. Université de Pau et des Pays de l'Adour.
de Nijs, M.A., Pietrzak, J.D., 2012. Saltwater intrusion and etm dynamics in a tidally-energetic stratified estuary. Ocean Model. 49, 60–85.

de Nijs, M.A., Winterwerp, J.C., Pietrzak, J.D., 2010. The effects of the internal flow structure on spm entrapment in the rotterdam waterway. J. Phys. Oceanogr. 40 (11), 2357–2380.
Dubranna, J., 2007. Etude des échanges sédimentaires entre l'embouchure de l'adour et les plages adjacentes d'anglet. Ph.D. thesis (Pau).
Duinker, J., Hillebrand, M.T.J., Nolting, R., Wellershaus, S., Jacobsen, N.K., 1980. The river varde å: processes affecting the behaviour of metals and organochlorines during estuarine mixing. Neth. J. Sea Res. 14 (3–4), 237–267.
Dyer, K., 1974. The salt balance in stratified estuaries. Estuar. Coast Mar. Sci. 2 (3), 273–281.
Dyer, K., 1991. Circulation and mixing in stratified estuaries. Mar. Chem. 32 (2–4), 111–120.
Dyer, K., Christie, M., Manning, A., 2004. The effects of suspended sediment on turbulence within an estuarine turbidity maximum. Estuar. Coast Shelf Sci. 59 (2), 237–248.
Dyer, K., Ramamoorthy, K., 1969. Salinity and water circulation in the vellar estuary. Limnol. Oceanogr. 14 (1), 4–15.
Geyer, W., 2010. Estuarine salinity structure and circulation. Contemp. Issues Estuar. Phys. 12–26.
Geyer, W.R., 1993. The importance of suppression of turbulence by stratification on the estuarine turbidity maximum. Estuaries 16 (1), 113–125.
Geyer, W.R., Farmer, D.M., 1989. Tide-induced variation of the dynamics of a salt wedge estuary. J. Phys. Oceanogr. 19 (8), 1060–1072.
Geyer, W.R., Trowbridge, J.H., Bowen, M.M., 2000. The dynamics of a partially mixed estuary. J. Phys. Oceanogr. 30 (8), 2035–2048.
Geyer, W.R., MacCready, P., 2014. The estuarine circulation. Annu. Rev. Fluid Mech. 46, 175–197.
Glangeaud, L., 1938. Transport et sédimentation dans l'estuaire et à l'embouchure de la gironde. caractères pétrographiques des formations fluviatiles, saumâtres, littorales et néritiques. Bull. Soc. Geol. France, Paris 7 (5), 599–630.
Grasso, F., Verney, R., Le Hir, P., Thouvenin, B., Schulz, E., Kervella, Y., 2018. Suspended sediment dynamics in the macrotidal seine estuary (France): 1. numerical modeling of turbidity maximum dynamics. J. Geophys. Res.: Oceans 123, 558–577.
Hansen, D.V., Rattray, M., 1966. New dimensions in estuary classification. Limnol. Oceanogr. 11 (3), 319–326.
Ibañez, C., Pont, D., Prat, N., 1997. Characterization of the ebre and rhone estuaries: a basis for defining and classifying salt-wedge estuaries. Limnol. Oceanogr. 42 (1), 89–101.
Jay, D.A., Orton, P.M., Chisholm, T., Wilson, D.J., Fain, A.M., 2007. Particle trapping in stratified estuaries: application to observations. Estuar. Coasts 30 (6), 1106–1125.
Jouanneau, J.-M., Weber, O., Champilou, N., Cirac, P., Muxika, I., Borja, A., Pascual, A., Rodríguez-Lázaro, J., Donard, O., 2008. Recent sedimentary study of the shelf of the Basque country. J. Mar. Syst. 72 (1–4), 397–406.
Kemp, W., Testa, J., Conley, D., Gilbert, D., Hagy, J., 2009. Temporal responses of coastal hypoxia to nutrient loading and physical controls. Biogeosciences 6 (12), 2985–3008.
Lacy, J.R., Stacey, M.T., Burau, J.R., Monismith, S.G., 2003. Interaction of lateral baroclinic forcing and turbulence in an estuary. J. Geophys. Res.: Oceans 108 (C3).
Lerczak, J.A., Rockwell Geyer, W., 2004. Modeling the lateral circulation in straight, stratified estuaries. J. Phys. Oceanogr. 34 (6), 1410–1428.
Li, L., Wu, H., Liu, J.T., Zhu, J., 2014. Sediment transport induced by the advection of a moving salt wedge in the changjiang estuary. J. Coast. Res. 31 (3), 671–679.
Lu, Y., Lueck, R.G., 1999. Using a broadband adcp in a tidal channel. part ii: Turbulence. J. Atmos. Ocean. Technol. 16 (11), 1568–1579.
Nezu, I., Rodi, W., 1986. Open-channel flow measurements with a laser Doppler anemometer. J. Hydraul. Eng. 112 (5), 335–355.
Olabarrieta, M., Geyer, W.R., Coco, G., Friedrichs, C.T., Cao, Z., 2018. Effects of density-driven flows on the long-term morphodynamic evolution of funnel-shaped estuaries. J. Geophys. Res.: Earth Surf. 123 (11), 2901–2924.
Petus, C., 2009. Qualité des eaux côtières du Sud du Golfe de Gascogne par télédétection spatiale. Ph.D. thesis. Université de Pau et des Pays de l'Adour.
Point, D., Bareille, G., Amouroux, D., Etcheber, H., Donard, O.F., 2007. Reactivity, interactions and transport of trace elements, organic carbon and particulate material in a mountain range river system (adour river, France). J. Environ. Monit. 9 (2), 157–167.
Pritchard, D.W., 1952. Salinity distribution and circulation in the chesapeake bay estuarine system. J. Mar. Res. 11 (2), 106–123.
Ralston, D.K., Geyer, W.R., Lerczak, J.A., 2008. Subtidal salinity and velocity in the hudson river estuary: observations and modeling. J. Phys. Oceanogr. 38 (4), 753–770.
Ralston, D.K., Geyer, W.R., Lerczak, J.A., 2010. Structure, variability, and salt flux in a strongly forced salt wedge estuary. J. Geophys. Res.: Oceans 115 (C6).
Scully, M.E., Friedrichs, C., Brubaker, J., 2005. Control of estuarine stratification and mixing by wind-induced straining of the estuarine density field. Estuaries 28 (3), 321–326.
Scully, M.E., Geyer, W.R., 2012. The role of advection, straining, and mixing on the tidal variability of estuarine stratification. J. Phys. Oceanogr. 42 (5), 855–868.
Scully, M.E., Geyer, W.R., Lerczak, J.A., 2009. The influence of lateral advection on the residual estuarine circulation: a numerical modeling study of the hudson river estuary. J. Phys. Oceanogr. 39 (1), 107–124.
Simpson, J., Williams, E., Brasseur, L., Brubaker, J., 2005. The impact of tidal straining on the cycle of turbulence in a partially stratified estuary. Cont. Shelf Res. 25 (1), 51–64.
Sous, D., Defontaine, S., Morichon, D., Bhairy, N., Lanceleur, L., Monperrus, M., 2018. Turbulence measurements in a stratified man-controlled estuary. In: The Adour Case. 16th International Symposium on Oceanography of the Bay of Biscay.
Stacey, M.T., Brennan, M.L., Burau, J.R., Monismith, S.G., 2010. The tidally averaged momentum balance in a partially and periodically stratified estuary. J. Phys. Oceanogr. 40 (11), 2418–2434.
Stacey, M.T., Burau, J.R., Monismith, S.G., 2001. Creation of residual flows in a partially stratified estuary. J. Geophys. Res.: Oceans 106 (C8), 17013–17037.
Stacey, M.T., Ralston, D.K., 2005. The scaling and structure of the estuarine bottom boundary layer. J. Phys. Oceanogr. 35 (1), 55–71.
Toublanc, F., Brenon, I., Coulombier, T., Moine, O.L., 2015. Fortnightly tidal asymmetry inversions and perspectives on sediment dynamics in a macrotidal estuary (charente, France). Cont. Shelf Res. 94, 42–54.
Toublanc, F., Brenon, I., Coulombier, T., 2016. Formation and structure of the turbidity maximum in the macrotidal charente estuary (France): influence of fluvial and tidal forcing. Estuar. Coast Shelf Sci. 169, 1–14.
Turner, J.S., 1979. Buoyancy Effects in Fluids. Cambridge University Press.
Uittenbogaard, R., 1995. The Importance of Internal Waves for Mixing in a Stratified Estuarine Tidal Flow. Ph.D. thesis, PhD thesis. Delfl University of Technology.
Uncles, R., Stephens, J., Smith, R., 2002. The dependence of estuarine turbidity on tidal intrusion length, tidal range and residence time. Cont. Shelf Res. 22 (11–13), 1835–1856.
Valle-Levinson, A., 2008. Density-driven exchange flow in terms of the kelvin and ekman numbers. J. Geophys. Res.: Oceans 113 (C4).
Wellershaus, S., 1981. Turbidity maximum and mud shoaling in the weser estuary. Arch. Hydrobiol. 92 (2).
West, J., Oduyemi, K., Shiono, K., 1991. Some observations on the effect of vertical density gradients on estuarine turbulent transport processes. Estuar. Coast Shelf Sci. 32 (4), 365–383.
Williams, E., Simpson, J.H., 2004. Uncertainties in estimates of Reynolds stress and tke production rate using the adcp variance method. J. Atmos. Ocean. Technol. 21 (2), 347–357.
Winterwerp, J., 2001. Stratification effects by cohesive and noncohesive sediment. J. Geophys. Res.: Oceans 106 (C10), 22559–22574.